

# Non-Linear Pattern Generation By Swimming Micro-Organisms

Martin Alan Bees

Submitted in accordance with the requirements for the degree of PhD.

*University of Leeds*

*Department of Applied Mathematical Studies*

THE CANDIDATE CONFIRMS THAT THE WORK SUBMITTED  
IS HIS OWN AND THAT APPROPRIATE CREDIT HAS BEEN GIVEN  
WHERE REFERENCE HAS BEEN MADE TO THE WORK OF OTHERS.

January 22, 1998

## Abstract

This thesis explores the non-linear effects of gyrotaxis on the bioconvection patterns formed in a suspension of swimming micro-organisms. The cells are denser than the medium in which they swim and the patterns are formed spontaneously by aggregations of cells which drive bulk fluid motion. The micro-organisms under consideration are orientated by a balance between a gravitational torque, due to them being bottom heavy, and a viscous torque arising from local fluid velocity gradients. This mechanism is known as gyrotaxis. A wide range of investigative techniques are employed, from experiments in the laboratory to computer algebra and bifurcation analysis using amplitude equations.

Firstly, a series of experiments is described in which images of bioconvection patterns are captured and Fourier analysed. The most unstable pattern wavelength is extracted as a function of suspension concentration, depth and time. Ideas from surface geometry are exploited to produce a measure of pattern. Some other experiments are also discussed.

Secondly, a full linear analysis of a stochastic, gyrotactic continuum model in a suspension of finite depth is conducted and an extension of the theory to include the random nature of the micro-organisms' swimming speeds is proposed.

Thirdly, an approximation to the steady Fokker-Planck equation describing the stochastic nature of the micro-organism swimming direction using surface spherical harmonics is investigated. The limitations of this method are explored.

Finally, the non-linear mechanisms involved in a gyrotactic instability are elucidated by exploiting the long vertical scale for descending plumes in a deep suspension. Initially, a weakly non-linear analysis provides an amplitude equation that implies that the bifurcation to instability is supercritical. Secondly, non-linear solutions are seen to undergo a Hopf bifurcation when there is a weak background vorticity. The resulting limit cycle provides the basis for horizontally travelling, vertical plume solutions. Equations describing the slow vertical variations along plume solutions admit travelling waves, for which the wavespeed is found. The travelling waves are thought to describe the varicose instabilities seen on bioconvection plumes in experiments.

This thesis is dedicated  
to my parents,  
Valerie and Alan Bees.

## Acknowledgements

Thanks first and foremost go to Nick Hill for being my supervisor. His enthusiasm and helpful guidance made my work at the University of Leeds stimulating and enjoyable. Thanks go to all the members of the biomaths group who have consistently helped to broaden my horizons. You know who you are!

I would never hear the last of it if I did not thank Steve, Rich, Bob, Simon, Matt, Sue, Julian and Jonny and all the lesser members of the lunch time group with whom I have had such stimulating conversations. Thanks to all the people that have ever brought me a drink.

Thanks go to Rachel for putting up with me and for her care and support.

How could I not thank my climbing friends especially Jon and Stef without whom I would not have learnt to fall gracefully in the Verdon. Nick also helped me enjoy climbing with his vast belay testing skills.

Thanks to all the participants of GFD 1994 in Woods Hole, in particular Joe, Alex and especially Ed Spiegel for his “soon to be in press” paper with me on speciation in evolution but more so for his wife’s cooking.

And last but not least, thanks go to my mum and dad for their belief in me and for always being there.

This research was supported by the Engineering and Physical Sciences Research Council.

# Contents

<b>1</b>	<b>General Introduction</b>	<b>2</b>
1.1	Introduction . . . . .	2
1.2	Taxes - what are they? . . . . .	3
1.3	Micro-organisms and how they swim . . . . .	4
1.4	Bioconvection - a brief history of observations . . . . .	9
1.5	Geotaxis and Gyrotaxis - why bother? . . . . .	10
1.6	A review of modelling techniques . . . . .	12
1.6.1	Pure upswimming models . . . . .	13
1.6.2	Modelling gyrotaxis . . . . .	15
1.6.3	A new continuum model . . . . .	17
1.7	What this thesis is about . . . . .	19
<b>2</b>	<b>An Experimental Investigation of Bioconvection</b>	<b>21</b>
2.1	Introduction . . . . .	21
2.2	Culturing and concentrating the algae . . . . .	22
2.3	Parameter measurement and control . . . . .	24
2.4	Experimental arrangement . . . . .	26
2.5	Image processing and characterization . . . . .	27
2.5.1	Discrete Fourier transforms . . . . .	28
2.5.2	Fourier spectrum estimation and analysis . . . . .	29
2.5.3	Dominant wavenumber analysis . . . . .	32
2.5.4	Error analysis . . . . .	33
2.6	Experimental examples . . . . .	34
2.6.1	Tables . . . . .	35

2.6.2	Images . . . . .	37
2.7	Dominant wavenumber results . . . . .	37
2.7.1	The initial disturbance . . . . .	37
2.7.2	The well developed pattern . . . . .	56
2.7.3	Transitory mode interaction . . . . .	58
2.8	A measure of pattern . . . . .	61
2.8.1	Preprocessing . . . . .	65
2.8.2	Numerical gradients . . . . .	66
2.8.3	Interpretation . . . . .	66
2.9	Varying the density of the suspending fluid . . . . .	72
2.9.1	Theoretical predictions . . . . .	73
2.9.2	Experimental observations . . . . .	75
2.10	Discussion . . . . .	76
<b>3</b>	<b>Finite Depth Stochastic Gyrotactic Bioconvection - Linear Analysis</b>	<b>79</b>
3.1	Introduction . . . . .	79
3.2	Linear Solution of the Fokker-Planck Equation . . . . .	80
3.2.1	The Fokker-Planck equation on a sphere . . . . .	80
3.2.2	Solution for zero flow . . . . .	82
3.2.3	First order perturbation . . . . .	84
3.2.4	First order perturbation for spherical cells: $\alpha_0 = 0$ . . . . .	84
3.2.5	First order perturbation for aspherical cells: $\alpha_0 \neq 0$ . . . . .	87
3.2.6	Summary . . . . .	89
3.3	Linearizing the main model equations . . . . .	92
3.4	The effect of leading order non-Newtonian stress terms . . . . .	100
3.5	Asymptotic analysis . . . . .	103
3.5.1	Shallow layer analysis ( $0 < d \ll 1$ ) . . . . .	104
3.5.2	Deep layer analysis ( $d \gg 1$ ) . . . . .	114
3.5.3	A summary of the asymptotic results . . . . .	120
3.6	Numerical analysis . . . . .	122
3.7	The effect of swimming speed as a random variable . . . . .	131
3.8	Numerical analysis for our best parameter measurements . . . . .	135
3.9	Comparison with experiments . . . . .	135

3.10	Discussion . . . . .	139
<b>4</b>	<b>Spherical Harmonic Expansion of the Fokker-Planck Equation</b>	<b>141</b>
4.1	Introduction . . . . .	141
4.2	The coordinate system . . . . .	143
4.3	Calculating the mean quantities . . . . .	145
4.4	Recursion relations . . . . .	146
4.5	Simplification . . . . .	147
4.5.1	Left hand side . . . . .	148
4.5.2	Right hand side - vorticity terms . . . . .	148
4.5.3	Right hand side - rate of strain terms . . . . .	148
4.6	Special cases - extremal terms . . . . .	150
4.7	Implementation . . . . .	151
4.8	Results for $\alpha_0 = 0$ . . . . .	152
4.9	Results for $\alpha_0 \neq 0$ . . . . .	158
4.9.1	$\xi$ varies while $\zeta = 0$ and $\chi = 0$ . . . . .	158
4.9.2	$e_{13}$ varies where $\omega = 0$ and $e_{11} = 0$ . . . . .	162
4.9.3	Combining vorticity and rate-of-strain . . . . .	163
4.9.4	Regions of validity . . . . .	167
4.9.5	Including swimming speed as a random variable . . . . .	168
4.10	Extension to a three dimensional flow field . . . . .	170
4.11	Discussion . . . . .	172
<b>5</b>	<b>Non-Linear Analysis</b>	<b>174</b>
5.1	Introduction . . . . .	174
5.2	Linear analysis . . . . .	179
5.3	Long vertical wavelength approximation ( $m \sim \epsilon$ ) for 2-d non-linear solutions . . . . .	181
5.4	Amplitude equations for the non-linear saturation of initial disturbances from the homogeneous solution . . . . .	183
5.5	Steady state solution . . . . .	188
5.6	Travelling wave solution . . . . .	193
5.7	Vertical variation of the steady state solutions . . . . .	199

5.8	Discussion and future improvements . . . . .	203
5.8.1	Similarity solutions . . . . .	204
5.8.2	Extension to a three-dimensional flow field . . . . .	206
<b>6</b>	<b>Conclusions</b>	<b>208</b>
<b>A</b>	<b>Special functions</b>	<b>212</b>
A.1	Identities for associated Legendre polynomials . . . . .	212
A.2	The gamma function . . . . .	213
<b>B</b>	<b>An integral identity</b>	<b>214</b>
<b>C</b>	<b>Maple program for the spherical harmonic expansion of the Fokker-Planck equation</b>	<b>217</b>
<b>D</b>	<b>Some operator expressions</b>	<b>223</b>

# List of Figures

1	A micro-organism soup - “Not even Martin’s imagination can reproduce the variety seen in life”, N. A. Hill, October 1995. . . . .	1
1.1	A typical labyrinth pattern formed in a suspension of <i>Chlamydomonas nivalis</i> , for a concentration of $1.5 \times 10^7$ cells per $cm^3$ and a depth of 2 mm, viewed from above after several minutes. The dark regions indicate a high cell concentration and the scale on the left is in cm. . . . .	3
1.2	<i>Chlamydomonas nivalis</i> - anatomy. . . . .	6
1.3	The forces acting on <i>Chlamydomonas nivalis</i> . . . . .	7
1.4	How <i>Chlamydomonas nivalis</i> swims. a) The power stroke in which the micro-organism moves forward as the flagella are thrust back, and b) the recovery stroke in which ground is lost but the flagella are returned to their initial positions. . . . .	8
1.5	Gyrotaxis in Poiseuille flow through a U-tube. Cells swim towards relatively downwards flowing fluid and away from upward flowing fluid. This forms a “focused” plume on the left hand side of the U-tube and cells gather on the wall of the right hand side. . . . .	10
1.6	An overturning Rayleigh-Taylor type instability. Cells swim to the top and form a suspension layer of greater density than that below. . . . .	11
1.7	A gyrotactic instability. Cells swim towards downwelling fluid making it denser and, hence, sink faster. . . . .	12
1.8	Nutrient uptake from pond bed in a suspension of gyrotactic micro-organisms. Streamlines indicate high wall shear stress and large regions of upwelling fluid on the pond bed, increasing the area of nutrient uptake. . . . .	13

2.1	Two methods of concentrating the cells: a) cells swim up through absorbent cotton wool in a thin necked flask and remain in the suspension above the cotton wool; b) cells swim up through a floating raft of absorbent cotton wool and become trapped within it at the surface. . . . .	23
2.2	Experimental setup for cell concentration measurements. . . . .	26
2.3	Experimental setup for recording images of bioconvection in a petri dish. . . . .	27
2.4	Example of a bioconvection image as initially recorded. . . . .	28
2.5	The same image as before but after the first image, where bioconvection does not occur, has been subtracted. . . . .	29
2.6	Aliasing and how it affects the Fourier spectrum. The energy from higher wavenumbers beyond the cutoff wavenumber is reflected back onto the discrete Fourier spectrum. . . . .	30
2.7	Discrete image and Fourier transformed space: an example of a hexagonal pattern. The upper square indicates the input image and the lower square (with a thick boundary) indicates the form of the fast Fourier transformed output space and how it is to be interpreted (the square with a thin boundary). . . . .	31
2.8	An example of curve fitting using the unnormalised double Gaussian distribution to an image's Fourier spectrum. The horizontal axis measures wavenumber and the vertical axis is the Fourier density. . . . .	33
2.9	Key. Order in which images are recorded. Pictures taken one every 10 seconds unless otherwise stated. . . . .	37
2.10	Experiment number x208m. Concentration = $1.89 \times 10^6 \text{ cm}^{-3}$ , depth = $7.23 \text{ mm}$ . Pictures taken one every 10 seconds. . . . .	41
2.11	Experiment number x120h. Concentration = $2.47 \times 10^6 \text{ cm}^{-3}$ , depth = $5.28 \text{ mm}$ . Pictures taken one every 10 seconds. . . . .	42
2.12	Experiment number x120h. Fourier spectra of images. Horizontal axis is wavenumber and vertical axis is Fourier density. Concentration = $2.47 \times 10^6 \text{ cm}^{-3}$ , depth = $5.28 \text{ mm}$ . Pictures taken one every 10 seconds. . . . .	43
2.13	Experiment number x208l. Concentration = $1.89 \times 10^6 \text{ cm}^{-3}$ , depth = $4.69 \text{ mm}$ . Pictures taken one every 10 seconds. . . . .	44

2.14	Experiment number x108d. Concentration = $3.06 \times 10^6 \text{ cm}^{-3}$ , depth = $4.44 \text{ mm}$ . Pictures taken one every 10 seconds. . . . .	45
2.15	Experiment number x209e. Concentration = $2.09 \times 10^6 \text{ cm}^{-3}$ , depth = $3.55 \text{ mm}$ . Pictures taken one every 10 seconds. . . . .	46
2.16	Experiment number x208c. Concentration = $1.89 \times 10^6 \text{ cm}^{-3}$ , depth = $3.18 \text{ mm}$ . Pictures taken one every 20 seconds. . . . .	47
2.17	Experiment number y02k. Concentration = $12.2 \times 10^6 \text{ cm}^{-3}$ , depth = $3.00 \text{ mm}$ . Pictures taken one every 30 seconds. . . . .	48
2.18	Experiment number y02k. Fourier spectra of images. Horizontal axis is wavenumber and vertical axis is Fourier density. Concentration = $12.2 \times 10^6 \text{ cm}^{-3}$ , depth = $3.00 \text{ mm}$ . Pictures taken one every 10 seconds. . . . .	49
2.19	Experiment number x215g. Concentration = $4.19 \times 10^6 \text{ cm}^{-3}$ , depth = $2.91 \text{ mm}$ . Pictures taken one every 10 seconds. . . . .	50
2.20	Experiment number y02i. Concentration = $4.6 \times 10^6 \text{ cm}^{-3}$ , depth = $2.28 \text{ mm}$ . Pictures taken one every 10 seconds. . . . .	51
2.21	Experiment number y12d. Concentration = $15.0 \times 10^6 \text{ cm}^{-3}$ , depth = $1.95 \text{ mm}$ . Pictures taken one every 10 seconds. . . . .	52
2.22	Experiment number x215h. Concentration = $4.19 \times 10^6 \text{ cm}^{-3}$ , depth = $1.86 \text{ mm}$ . Pictures taken one every 10 seconds. . . . .	53
2.23	Experiment number y12e. Concentration = $11.8 \times 10^6 \text{ cm}^{-3}$ , depth = $1.18 \text{ mm}$ . Pictures taken one every 10 seconds. . . . .	54
2.24	Dominant wavelengths of the initial disturbance from a fully mixed suspension of <i>Chlamydomonas nivalis</i> against concentration and suspension depth. The diameter of the circles represent the most unstable wavelength measured on a continuous scale in <i>cm</i> . . . . .	55
2.25	Pattern type of the initial disturbance from a fully mixed suspension of <i>Chlamydomonas nivalis</i> against concentration and suspension depth. The regions correspond to the dominant pattern present where <i>D</i> = dots, <i>L</i> = lines, <i>X</i> = dots joined by lines in <i>X</i> or <i>Y</i> shapes and <i>M</i> = mixed. The subscript <i>T</i> means that the pattern evolves through a torus stage and the subscripts <i>H</i> and <i>S</i> mean clear evidence of hexagonal or square arrays respectively. . . . .	57

2.26	Dominant wavelengths of the final observed pattern in a suspension of <i>Chlamydomonas nivalis</i> against concentration and suspension depth. The diameter of the circles represent the most unstable wavelength measured on a continuous scale in <i>cm</i> . The dots represent experiments performed where a final pattern was not recorded. . . . .	58
2.27	How the dominant pattern wavenumber varies with time. Three identical experiments where the initial instability is highly dependent on the initial conditions. . . . .	59
2.28	A contour plot of the Fourier spectrum of experiment y02k varying with time. Different modes generally become unstable to modes of larger wavenumber. . . . .	60
2.29	Unstable wavenumbers varying with time. a) a discretely varying dominant wavenumber. b) a continuously varying dominant wavenumber. . .	61
2.30	A sketch to illustrate how clear fluid can be entrained in a plume and an annulus pattern can be formed when viewed from above. a) cells swim up to the top and overturn due to a Rayleigh-Taylor instability. b) gyrotaxis produces thin plumes. c) the plumes hit the bottom of the dish and spread out forming a ring vortex. d) clear fluid is entrained in the wake of the plume and an annulus is set up. . . . .	62
2.31	Possible mode interactions. Patterns can become unstable to other new modes. In particular, two dimensional patterns can become unstable to three dimensional patterns. These dot patterns can form annuli. When large enough, the annuli are essentially two dimensional patterns and can again become unstable to three dimensional patterns. Eventually the pattern settles down to a regular array of dots. In general the pattern wavelength decreases with time. . . . .	63
2.32	Bending and stretching a plane to produce a line pattern or a dot pattern.	64

2.33	Different combinations of $\kappa_m$ and $\kappa_g$ imply different local surface structures. In particular, if $\kappa_g < 0$ then the principal curvatures have different signs and we have a saddle point. If $\kappa_g > 0$ then the principal curvatures have the same sign and we have a local minimum or maximum. The sum of the principal curvatures, $\kappa_m$ , provides the extra information required to determine the form of the local surface structure. . . . .	67
2.34	An example (experiment x120h) of image characteristic curvatures varying with time. Key: Blue = cell concentration maximums or black dots; Red = cell concentration minimums or white dots; White = high cell concentration saddles or black lines; Green = low cell concentration saddles or white lines; Black = flat. . . . .	69
2.35	x120h. Image pattern coefficients varying with time. Dash-dotted line: $C_{bd}$ , black dot coefficient; Dashed line: $C_{bl}$ , black line coefficient; Solid line: $C_{wd}$ , white dot coefficient; Dotted line: $C_{wl}$ , white line coefficient. . . . .	70
2.36	An example (experiment x2081) of image characteristic curvatures varying with time. Key: Blue = cell concentration maximums or black dots; Red = cell concentration minimums or white dots; White = high cell concentration saddles or black lines; Green = low cell concentration saddles or white lines; Black = flat. . . . .	71
2.37	x2081. Image pattern coefficients varying with time. Dash-dotted line: $C_{bd}$ , black dot coefficient; Dashed line: $C_{bl}$ , black line coefficient; Solid line: $C_{wd}$ , white dot coefficient; Dotted line: $C_{wl}$ , white line coefficient. . . . .	72
3.1	Regions of the parameter space covered by the leading order balances of the linear equations for bioconvection in a shallow layer ( $d \ll 1$ ). There are four major balances. . . . .	105
3.2	Graph of Equation (3.187) against $w$ indicating its roots. . . . .	111
3.3	Graph of $F$ against $w$ from Equation (3.202). . . . .	113
3.4	Regions of parameter space corresponding to leading order balances of the linear equations for bioconvection in a deep layer ( $d \gg 1$ ). The shading indicates the self consistent region of parameter space where a neutral curve can exist. . . . .	116

3.5	A monotonically increasing function, $4k(k - \sinh k \cosh k)/(k^2 - \sinh^2 k)$ , of $k$ . . . . .	120
3.6	Curves of neutral linear stability for a shallow layer ( $d = 0.1$ and $\alpha_0 = 0.2$ ) and varying $d^2\eta$ . Dotted lines are curves from the asymptotic results and solid lines are from the numerical results. . . . .	123
3.7	Curves of neutral linear stability for a deep layer ( $d = 40$ and $\alpha_0 = 0.2$ ) and varying $d^2\eta$ . Dotted lines are curves from the asymptotic results and solid lines are from the numerical results. . . . .	124
3.8	Curves of neutral linear stability for a deep layer ( $d = 200$ and $\alpha_0 = 0.2$ ) and varying $d^2\eta$ . Dotted lines are curves from the asymptotic results and solid lines are from the numerical results. . . . .	125
3.9	Numerical curves of neutral linear stability for a deep layer ( $d = 200$ ), with $d^2\eta = 4$ and varying $\alpha_0$ . Increasing $\alpha_0$ stabilizes modes with long horizontal wavelengths. . . . .	126
3.10	Numerical curve of neutral linear stability for a deep layer ( $d = 200$ ), with $d^2\eta = 3.3$ , $\alpha_0 = 0$ . Here we see a combination of both zero and non-zero dominant unstable wavenumbers. For every $d$ we find that there is a critical $\eta$ that determines the bifurcation between there being a zero and a non-zero most unstable wavenumber. . . . .	127
3.11	Profiles of neutrally stable numerical solutions for a shallow layer ( $d = 0.1$ ) with $\eta = 0.1$ , $\alpha_0 = 0.2$ and $k = 10$ , for which it is found that $R \approx 1155$ . This is a mode one solution. . . . .	128
3.12	Profiles of neutrally stable numerical solutions for a deep layer ( $d = 10$ ) with $\eta = 0.1$ , $\alpha_0 = 0.2$ and $k = 10$ , for which it is found that $R \approx 22024$ . This is a mode one solution. . . . .	129
3.13	Profiles of neutrally stable numerical solutions for a deep layer ( $d = 200$ ) with $d^2\eta = 8$ , $\alpha_0 = 0.2$ and $k = 100$ , for which it is found that $R \approx 8.5 \times 10^9$ . This is a mode one solution. . . . .	130
3.14	Neutral curves for a deep layer ( $d = 200$ ) where $d^2\eta = 4$ , $\alpha_0 = 0.2$ and $\mathcal{N}$ varies. . . . .	134
3.15	The Gamma distribution $P(V = x)$ where $V_s$ is its mean. . . . .	135

3.16	Neutral curves for $d = 40$ using parameter estimates and measurements of $\alpha_0 = 0.4$ and $\mathcal{N} = 1.34$ . . . . .	136
4.1	The choice of coordinate system on a sphere. . . . .	143
4.2	Graph of the coefficient $A_1^0$ with $\zeta$ for orders of approximation of 2, 3 and 4. . . . .	152
4.3	Graph of the coefficient $A_1^1$ with $\zeta$ for orders of approximation of 2, 3 and 4. . . . .	153
4.4	Graph of the coefficient $A_2^0$ with $\zeta$ for orders of approximation of 2, 3 and 4. . . . .	155
4.5	Graph of the coefficient $A_2^1$ with $\zeta$ for orders of approximation of 2, 3 and 4. . . . .	155
4.6	Graph of the coefficient $A_2^2$ with $\zeta$ for orders of approximation of 2, 3 and 4. . . . .	156
4.7	A third order approximation to the probability density function, $f(\theta, \phi)$ for $\alpha_0 = 0$ when $\zeta = 0$ , $\xi = 0$ and $\chi = 0$ . . . . .	156
4.8	A third order approximation to the probability density function, $f(\theta, \phi)$ for $\alpha_0 = 0$ when $\zeta = 1$ , $\xi = 0$ and $\chi = 0$ . . . . .	157
4.9	A third order approximation to the probability density function, $f(\theta, \phi)$ for $\alpha_0 = 0$ when $\zeta = 2$ , $\xi = 0$ and $\chi = 0$ . . . . .	157
4.10	A third order approximation to the probability density function, $f(\theta, \phi)$ for $\alpha_0 = 0$ when $\zeta = 5$ , $\xi = 0$ and $\chi = 0$ . . . . .	158
4.11	Graph of the coefficient $A_1^0$ versus $\xi$ for a third order approximation. $\zeta = \chi = 0$ . . . . .	159
4.12	Graph of the coefficient $A_1^0$ versus $\xi$ for a seventh order approximation. $\zeta = \chi = 0$ . . . . .	159
4.13	Graph of the coefficient $A_1^0$ versus $\xi$ for a tenth order approximation. $\zeta = \chi = 0$ . . . . .	160
4.14	Streamlines at the stagnation point of a pure straining flow, acting on a swimming cell (where $\omega = e_{13} = 0$ ). Here, $e_{11}$ is positive and, hence, $e_{33}$ is negative. . . . .	160
4.15	A seventh order approximation to the probability density function, $f(\theta, \phi)$ for $\alpha_0 = 0$ when $\zeta = 0$ , $\xi = 1$ and $\chi = 0$ . . . . .	161

4.16	A seventh order approximation to the probability density function, $f(\theta, \phi)$ for $\alpha_0 = 0$ when $\zeta = 0$ , $\xi = 2$ and $\chi = 0$ . . . . .	161
4.17	A seventh order approximation to the probability density function, $f(\theta, \phi)$ for $\alpha_0 = 0$ when $\zeta = 0$ , $\xi = 4$ and $\chi = 0$ . . . . .	162
4.18	Graphical representation of a combined straining flow with vorticity. . .	163
4.19	Streamlines for a combination of a straining flow with vorticity. Here $e_{11} = \omega$ . Doubling $\omega$ would give a pure shear flow. . . . .	163
4.20	A seventh order approximation to the probability density function, $f(\theta, \phi)$ for $\alpha_0 = 0$ when $\zeta = 9$ , $\xi = 2$ and $\chi = 0$ . . . . .	164
4.21	A seventh order approximation to the probability density function, $f(\theta, \phi)$ for $\alpha_0 = 0$ when $\zeta = 9$ , $\xi = 4$ and $\chi = 0$ . In this case, the cell is almost always pointing downwards, due to the “barrier” formed by the large values of $\xi$ . . . . .	165
4.22	A seventh order approximation to the probability density function, $f(\theta, \phi)$ for $\alpha_0 = 0$ when $\zeta = 9$ , $\xi = 5$ and $\chi = 0$ . There are regions where $f$ has become negative and the method has broken down. . . . .	165
4.23	A fifth order approximation of $A_1^0(\zeta, \xi)$ with $\chi = 0$ ( $\propto e_{13}$ ). . . . .	166
4.24	A close up, at the origin, of Figure (4.23). A fifth order approximation of $A_1^0(\zeta, \xi)$ with $\chi = 0$ ( $\propto e_{13}$ ) showing the smooth solution surface close to the origin. . . . .	166
4.25	$\omega$ and $e_{11}$ space - highlighting the regions of validity. The solid lines indi- cate the possibility of spurious singularities and the surrounding shaded regions indicate unreliable results. . . . .	167
4.26	A graph of $D_{xx}$ with varying $\zeta$ and $\mathcal{N}$ for a second order approximation to $f(\theta, \phi)$ with $\alpha_0 = 0$ . $\mathcal{N}$ increases with $D_{xx}(0)$ from 1.0 to 2.0. . . . .	168
4.27	A graph of $D_{yy}$ with varying $\zeta$ and $\mathcal{N}$ for a second order approximation to $f(\theta, \phi)$ with $\alpha_0 = 0$ . $\mathcal{N}$ increases with $D_{yy}(0)$ from 1.0 to 2.0. . . . .	169
4.28	A graph of $D_{zz}$ with varying $\zeta$ and $\mathcal{N}$ for a second order approximation to $f(\theta, \phi)$ with $\alpha_0 = 0$ . $\mathcal{N}$ increases with $D_{zz}(0)$ from 1.0 to 2.0. . . . .	169
4.29	A graph of $D_{xz}$ with varying $\zeta$ and $\mathcal{N}$ for a second order approximation to $f(\theta, \phi)$ with $\alpha_0 = 0$ . $\mathcal{N}$ increases from 1.0 to 2.0. . . . .	170

5.1 *Chlamydomonas nivalis* being cultured in flasks. Plumes with long vertical scales can be clearly seen. Pulses are generally observed travelling down the plumes. . . . . 176

5.2 Curves of marginal stability for a homogeneous suspension of large depth. Two cases are indicated. If  $m = 0$  then the bifurcation is stationary and the growth rate is zero along the solid diagonal line and the line  $k = 0$ . If  $m \neq 0$  then we have a Hopf bifurcation in which the real part of the linear growth rate is zero along the dotted line. . . . . 180

5.3 A plot of the linear growth rate for a mode with  $m = 0$  and horizontal wavenumber  $k$ , for a value of the parameter  $K$  slightly above the critical value of 0. Here,  $\text{Re} = 10^{-3}$  and  $K = 0.1$ . . . . . 181

5.4 Orbits for  $K^* = 0.1$  going clockwise with increasing  $x$ . . . . . 189

5.5 Profiles of the orbits given in Figure 5.4. Examples of  $q (= \ln(n^0))$  varying in the  $x$  direction for  $K^* = 0.1$ . . . . . 190

5.6 Orbits for  $K^* = 1$  going clockwise with increasing  $x$ . . . . . 191

5.7 Profiles of the orbits given in Figure 5.6. Examples of  $q (= \ln(n^0))$  varying in the  $x$  direction for  $K^* = 1$ . . . . . 192

5.8 Nullclines for a typical travelling wave system where  $c + E(p_0) \leq 0$ . The saddle point, B, allows the possibility of a homoclinic orbit around the focus, A, and as the focus, A, changes stability a limit cycle can develop. This ensures the existence of a Hopf bifurcation. The equilibrium point C is not within the region of realistic cell concentrations. . . . . 194

5.9 Travelling wave solutions exist for a small range of wavespeeds,  $c$ , given the parameters  $\text{Re}$ ,  $K^*$  and  $p^0$ . Here  $K^* = 0.1$ ,  $\text{Re} = 0.4$  and  $p^0$  is plotted along the  $x$  axis. The hatched region indicates where travelling wave solutions exist. Here, the value of  $\text{Re}$  is artificially large in order to indicate the hatched region. Normally  $\text{Re} \sim 10^{-4}$  and the region is much smaller. . . . . 196

5.10 Trajectories for the travelling wave system (clockwise with  $\Xi$ ) where an unstable limit cycle is clearly observed. The + indicates the location of the saddle point.  $K^* = 0.1$ ,  $p_0 = 0.4$ ,  $\text{Re} = 0.4$  and  $c = 0.15$ . . . . . 197

- 5.11 Cell concentration varying with  $x - ct$  for waves travelling to the right.  
 $K^* = 0.1$ ,  $p_0 = 0.4$ ,  $Re = 0.4$  and  $c = 0.15$ . . . . . 198
- 5.12 Perturbation,  $p_1$ , to  $p_0$  varying with  $x$  for a vertically travelling pulse.  
 Here  $K^* = 0.01$  with the initial conditions  $n_0 = 5$ ,  $p_0 = 0$ ,  $n_1 = 13.8$   
 and  $p_1 = 0$ . . . . . 202
- 5.13 Perturbation,  $n_1$ , to the cell concentration,  $n_0$ , varying with  $x$  for a  
 vertically travelling pulse. Here  $K^* = 0.01$  with the initial conditions  
 $n_0 = 5$ ,  $p_0 = 0$ ,  $n_1 = 13.8$  and  $p_1 = 0$ . . . . . 203

# List of Tables

2.1	Table of experimental measurements where the subscript 0 means the first unstable mode to be measured and $\infty$ means the final pattern mode. Wavenumbers (waves per width of dish) are indicated by $k$ and the dimensional wavelength by $\lambda$ . For the final pattern, n/a indicates that the images are not available. . . . .	36
2.2	Table of experimental measurements (continued) where the subscript 0 means the first unstable mode to be measured and $\infty$ means the final pattern mode. Wavenumbers are indicated by $k$ and the dimensional wavelength by $\lambda$ . For the final pattern, n/a indicates that the images are not available. . . . .	38
2.3	Experimental initial and final patterns observed. The types of patterns are indicated by $D =$ dots, $L =$ lines, $X =$ dots joined by lines in $X$ or $Y$ shapes and $M =$ mixed. The subscript $T$ means that the pattern evolves through a torus stage and the subscripts $H$ and $S$ mean clear evidence of hexagonal or square arrays respectively. . . . .	39
2.4	Experimental initial and final patterns observed. Continued.... . . . .	40
2.5	Observations of suspensions of <i>Chlamydomonas nivalis</i> and Percoll in different ratios. . . . .	75
3.1	Values of the $K$ and $J$ constants, for varying values of $\lambda$ , from Pedley & Kessler (1990) with corrections for $K_4$ . . . . .	91
3.2	Parameter estimates and measurements (from [42, 85, 53, 41]). . . . .	93
3.3	The values of the constants $P$ for typical values of $\lambda$ and $\alpha_0$ . . . . .	99
3.4	Calculations of parameters from original and more recent measurements and estimates of $B$ and $\tau$ . . . . .	138

3.5	Experimental measurements of wavenumbers and corresponding calculations of $d$ and $R$ depending on the value of $\tau$ . Seven experiments have been chosen with similar depths so that they can be compared with the theoretical predictions. . . . .	138
5.1	Parameter expressions and estimates. . . . .	178
5.2	Table of constants for the mean cell swimming direction vector and diffusion tensor (to 5 s.f.). . . . .	178

## Nomenclature

## Chapter 1

$a$	cell length
$b$	cell breadth
$B$	gyrotactic orientation parameter
$c$	cell concentration (as in [19])
$\mathbf{D}$	cell diffusion tensor
$D_h$	horizontal component of orthotropic cell diffusion
$D_v$	vertical component of orthotropic cell diffusion
$D_r$	rotational cell diffusion
$\mathbf{e}$	dimensionless rate-of-strain tensor
$\mathbf{E}$	rate-of-strain tensor
$f(\mathbf{p})$	cell swimming direction probability density function
$g$	acceleration due to gravity
$h$	displacement of cells center of mass from geometrical center along $\mathbf{p}$
$H$	suspension depth
$\mathbf{i}, \mathbf{j}, \mathbf{k}$	coordinate system - unit vectors
$\mathbf{J}$	cell concentration flux
$\mathbf{L}_g$	gravitational couple acting on a cell
$\mathbf{L}_T$	total couple acting on a cell
$\mathbf{L}_v$	viscous torque acting on a cell
$m$	mass of micro-organism
$n$	cell concentration
$p$	pressure
$p_e$	excess pressure above hydrostatic
$\mathbf{p}$	unit vector in direction of swimming cell
$\langle \mathbf{p} \rangle$	mean value of $\mathbf{p}$
$\mathbf{P}, \mathbf{Y}, \mathbf{R}$	tensors depending on surface geometry of cell
$\mathbf{q}, \mathbf{r}$	unit vectors perpendicular to cell swimming direction

$S$	surface of unit sphere
$t$	time
$\mathbf{u}$	fluid velocity
$U(c, z)$	cell swimming speed (as in [19])
$v$	mean volume of a cell
$\mathbf{v}$	cell swimming velocity
$\mathbf{V}_r$	velocity of cell relative to its mean value
$V_s$	cell swimming speed
$\alpha_e$	extra density of a cell relative to the fluid (as in [19])
$\alpha_{  }$	dimensionless resistance coefficient for rotation about $\mathbf{p}$
$\alpha_{\perp}$	dimensionless resistance coefficient for rotation about an axis perpendicular to $\mathbf{p}$
$\alpha_0$	cell eccentricity
$\delta_{ij}$	Kronecker delta
$\epsilon_{ijk}$	Levi-Civita tensor (or alternating tensor)
$\lambda$	parameter
$\mu$	coefficient of viscosity
$\nu$	kinematic viscosity of fluid
$\phi$	cell orientation angle in horizontal plane
$\rho$	fluid density
$\Delta\rho$	extra density of a cell relative to the fluid (as in [83])
$\Sigma$	stress tensor
$\tau$	direction correlation time
$\theta$	cell orientation angle from vertical
$\boldsymbol{\omega}$	dimensionless vorticity vector
$\boldsymbol{\Omega}$	vorticity vector
$\boldsymbol{\omega}^c$	angular velocity of cell
$\partial_{\bullet} \equiv \frac{\partial}{\partial \bullet}$	abbreviation
$\partial_i \equiv \frac{\partial}{\partial x_i}$	abbreviation
$l$	differentiation with respect to the dependent variable

## Chapter 2

All notation is as before, plus the following.

$A_{ij}$	surface curvature area statistic
$C_{ij}$	normalised surface curvature area statistic
$d(k_x, k_y)$	measure of distance in Fourier space from zero wavenumber
$\mathcal{D}_p$	a measure of pattern dimension
$E, F, G$	coefficients of first fundamental form
$\mathcal{E}_{KS}$	Kolmogorov-Smirnov statistic
$\mathcal{E}_M$	sum modulus error statistic
$h(x, y)$	image space
$h_x$	horizontal length scale between pixels
$h_y$	vertical length scale between pixels
$H(k_x, k_y)$	discrete Fourier transformed space
$I_n$	bins defining discrete Fourier spectrum domain
$I_w$	image width
$k$	wavenumber
$k_0$	initial dominant wavenumber
$k_\infty$	final dominant wavenumber
$L, M, N$	coefficients of second fundamental form
$\mathcal{L}$	leakage due to application of discrete Fourier transform on a finite window
$\mathbf{n}(x, y)$	unit normal to image surface in Euclidean 3-space
$N$	image size
$\mathcal{P}_n$	discrete Fourier spectrum at wavenumber $n$
$\mathbf{r}(x, y)$	( $\equiv (x, y, z(x, y))$ ) image surface of $z(x, y)$ in Euclidean 3-space
$s$	frequency offset in bins
$\mathcal{W}(x)$	windowing function for discrete Fourier transform
$\mathcal{W}_s$	$N \times$ sum squared intensity of window function
$\mathcal{W}_H(x, y)$	two-dimensional Hann windowing function

$\alpha_i$	internal angles of a domain on a general surface
?	Gaussian distribution
$\bar{?}$	unnormalized double Gaussian distribution
$\lambda_0$	initial dominant wavelength
$\lambda_\infty$	final dominant wavelength
$\kappa_g$	Gaussian curvature of a surface
$\kappa_m$	mean curvature of a surface
$\kappa_n$	normal curvature of a curve

### Chapter 3

All notation is as before, plus the following.

$a_i, b_i, A_i,$	constants
$B_i$	
$a_{ij}, b_{ij}$	constants in linear expansion of the Fokker-Planck equation
$\tilde{a}_{ij}, \tilde{b}_{ij}$	constants in linear expansion of the Fokker-Planck equation
$\bar{a}_{ij}, \bar{b}_{ij}$	constants in linear expansion of the Fokker-Planck equation
<b>A</b>	column vector of constants for Case II of asymptotics
$d$	layer depth parameter
$F(P_i, k, \eta)$	function from Case IV of the asymptotics
$f^0(\theta, \phi)$	zero flow component of cell swimming probability density function, $f(\theta, \phi)$
$f^1(\theta, \phi)$	first order perturbation to $f(\theta, \phi)$
$f^{1*}(\theta, \phi)$	first order perturbation to $f(\theta, \phi)$ , arising from the asymmetry of the cell
$g_i(\theta, \phi)$	components of $f^1(\theta, \phi)$
$H$	suspension depth
$H_i(\alpha_0, \eta)$	functions of $J_i, K_i, \eta$ and $\alpha_0$ involved in the linearization of the governing equations

$J_i, K_i$	functions of $\lambda$ for the mean swimming direction vector and the diffusion tensor
$\mathbf{M}$	matrix of coefficients for Case II of asymptotics
$N$	multiplier of cell concentration steady state distribution
$\mathcal{N}$	cell swimming speed, variance ratio
$\bar{n}$	mean concentration of cells in the suspension
$P_m^n(x)$	associated Legendre polynomials
$P_i$	functions in linear governing equations which are only dependent on $K_i, J_i$ and $\alpha_0$
$R$	Rayleigh number based on suspension depth
$\hat{R}$	Rayleigh number based on sublayer depth
$S_c$	Schmidt number
$\mathbf{V}$	random variable in both cell swimming speed and direction
$W(z)$	amplitude of fluid velocity perturbation
$\alpha_0, \alpha_F$	parameters depending on geometry and locomotion of the cell
$\gamma_f$	mean angle of flagella from the direction of swimming
$\epsilon$	perturbation parameter
$\eta$	dimensionless gyrotaxis number
$\hat{\eta}$	scaled gyrotaxis number ( $= d^2\eta$ )
$\kappa^{-1}$	sublayer depth
$\lambda$	$= (2D_r B)^{-1}$
$\mu_\lambda$	function of $\lambda$
$\Phi(z)$	amplitude of cell concentration perturbation
$\hat{\phi}$	unit vector in direction of varying $\phi$ .
$\sigma$	linear growth rate
$\hat{\theta}$	unit vector in direction of varying $\theta$ .
$\chi^{sd}$	coefficient of non-dimensional stresses, due to the intrinsic stresslets of the cells, and the effective particle rotation, as a result of rotational diffusion
$\bullet^i$	perturbation of order $i$
$\bullet_I$	internal to boundary layer or inner region
$\bullet_\zeta$	intermediate region in matched asymptotics

Chapter 4

All notation is as before, plus the following.

$A_n^m$	spherical harmonic expansion coefficients
$C^m$	notation for $\cos m\phi$
$F_n^m$	terms in spherical harmonic expansion ( $= A_n^m C^m P_n^m$ )
$\mathcal{F}_n^0$	Equation (4.46)
$\mathcal{F}_n^1$	Equation (4.49)
$\mathcal{G}_n^m$	Equation (4.51)
$P_n^m(x)$	associated Legendre polynomials
$Q_n^m(\theta, \phi)$	spherical harmonics ( $= C^m P_n^m$ )
$R$	truncation order for spherical harmonic expansion
$R_n^m$	$= A_n^m C^m$
$S^m$	notation for $\sin m\phi$
$X_{cos}$	operators for expanding the Fokker-Planck equation in terms of
$X_{sin}$	spherical harmonics
$X_c$	(see Section 4.4 for definitions)
$X_{ss}$	
$X_{ssp}$	
$X_{su}$	
$X_{sd}$	
$X_{spu}$	
$X_{spd}$	
$\zeta$	gyrotaxis-vorticity parameter, $= \eta\omega$
$\xi$	gyrotaxis-strain-rate, $e_{11}$ , parameter, $= \alpha_0 \eta e_{11}$
$\chi$	gyrotaxis-strain-rate, $e_{13}$ , parameter, $= \alpha_0 \eta e_{13}$

Chapter 5

All notation is as before, plus the following.

$a_j^i, b_j^i, r_i$	constants defining $E$ and $A$
$A(\eta\omega)$	horizontal diffusion function ( $= \mathbf{D}^{xx}$ )
$B$	function of $p$ in the analysis of the equation describing slowly varying solutions in the vertical direction
$\mathcal{B}$	constant in the analysis of the equation describing slowly varying solutions in the vertical direction
$c$	wavespeed
$c_-, c_+$	bounds on wavespeed
$E(\eta\omega)$	horizontal gyrotaxis function ( $= -\langle \mathbf{p} \rangle^x$ )
$f(X, T)$	amplitude modulation of linear solutions for weakly nonlinear analysis
$F$	poloidal velocity field
$\mathcal{H}$	Hamiltonian, with respect to the $x$ direction, for the steady state system
$J(n, \psi)$	Jacobian
$K$	$= \text{Ra Re } \eta$
$K^*$	$= K\Lambda$
$k$	wavenumber in the $x$ direction
$l$	wavenumber in the $y$ direction
$m$	wavenumber in the $z$ direction
$M(Z, T)$	small amplitude modulation in vertical direction
$n$	normalized cell concentration
$N$	rescaled cell concentration ( $= n/\Lambda$ )
$p$	gyrotaxis-vorticity variable ( $= \eta\omega + O(\epsilon)$ )
$q$	log of rescaled cell concentration ( $= \ln(N)$ )
Ra	Rayleigh number for a fluid in an infinite domain
Re	Reynolds number based on the micro-organism
$X$	scaled horizontal distance
$Z$	scaled vertical distance

$\delta$	small parameter for expansion in horizontal direction
$\epsilon$	small scale for expansion in vertical direction
$\eta$	gyrotactic orientation parameter
$\Lambda$	horizontal space average of normalized cell concentration
$\psi$	stream function
$\Xi$	variable for travelling wave and similarity solutions
$\bullet^i$	expansion for small vertical variation
$\bullet$	weakly nonlinear expansion near neutral curve
$\bullet$	at a point on the neutral curve

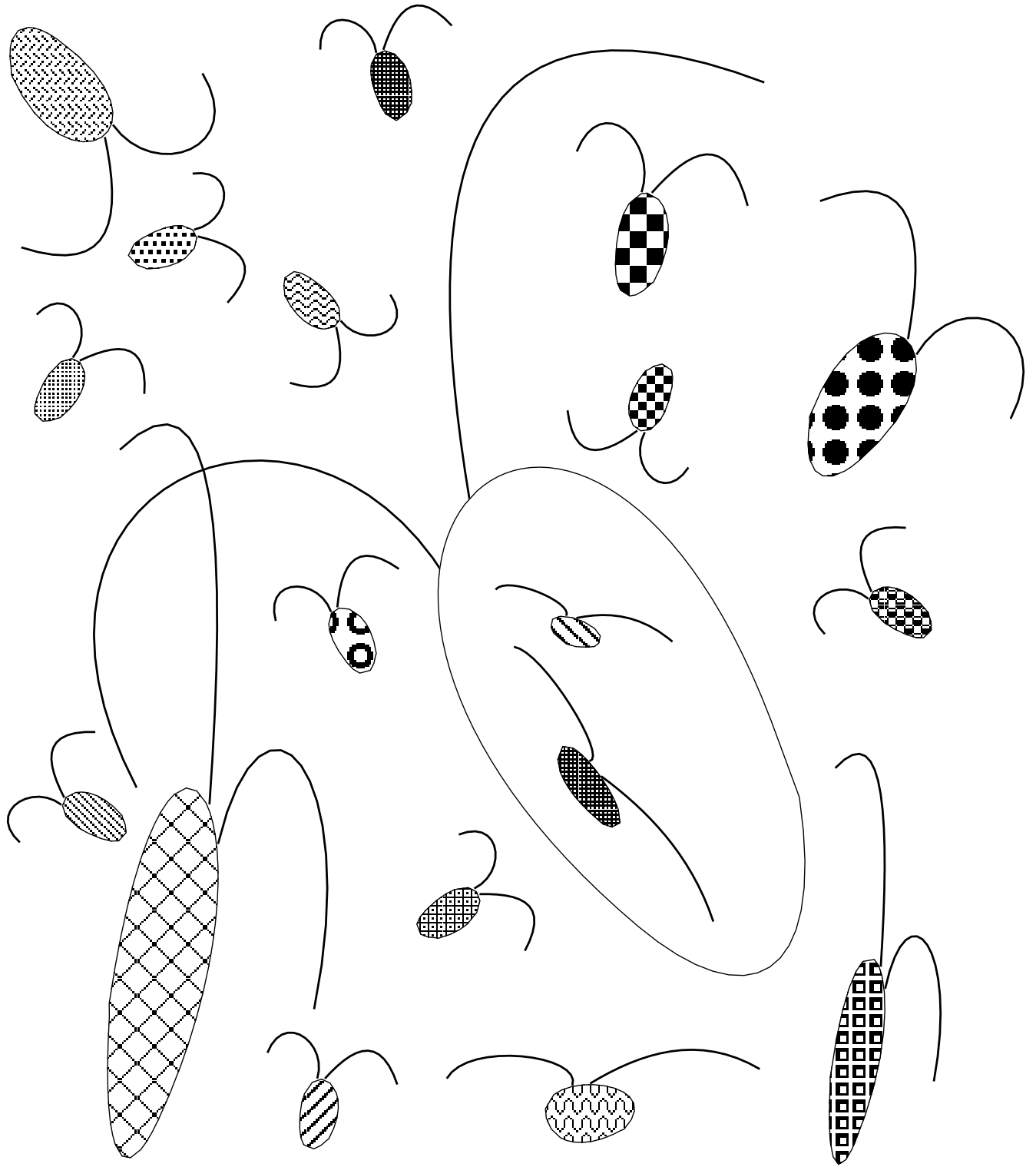


Figure 1: A micro-organism soup - "Not even Martin's imagination can reproduce the variety seen in life", N. A. Hill, October 1995.

# Chapter 1

## General Introduction

### 1.1 Introduction

Why study patterns formed by swimming micro-organisms (see Figure 1.1)? Surely the micro-organisms and their patterns are so small as to be insignificant to our daily lives. The lengthscales for these micro-organisms are of the order of  $1\mu m$  for bacteria and  $10\mu m$  for algae, and  $1cm$  for the patterns that they produce (see Figures 2.10 to 2.23). Even if the micro-organisms are important, we should be studying how they feed, mate and die. This is what pattern formation is all about. Over millions of years these organisms have evolved (they are some of the oldest species known to man) to fill niches, whether they are in your stomach or affecting the global weather by photosynthesizing in the sea. The patterns that they form are there for a reason, that may not be obvious, but definitely an essential part of the organism's life cycle. It is crucial that we understand how and why these organisms, at the base of the whole food chain, behave (at least under ideal conditions in the laboratory). After all, they consist of the majority of the Earth's biomass and a variation in their numbers could have catastrophic consequences (e.g. positive or negative feedback effects in global warming, Goodess & Palutikof 1992 [37] pp. 53–55, or species extinction due to high levels of bacteria in our rivers).

There is also the possibility of harnessing the power of micro-organisms. Some algae and bacteria produce alcohol as an unwanted byproduct but to us this is a valuable commodity not least for its use as a fuel. Plastics, fertilizers, waste treatment plants and solid fuels are other possible applications for algae, bacteria and their byproducts.

Figure 1.1: A typical labyrinth pattern formed in a suspension of *Chlamydomonas nivalis*, for a concentration of  $1.5 \times 10^7$  cells per  $cm^3$  and a depth of 2 mm, viewed from above after several minutes. The dark regions indicate a high cell concentration and the scale on the left is in cm.

If we can understand the patterns formed by some of the simplest organisms on Earth then maybe we could understand patterns formed by more complex organisms such as insects (e.g. locusts, ants and bees), fish and even humans (their migration and immune systems). This thesis aims to explain the patterns observed in suspensions of swimming micro-organisms whose behaviour is determined by a set of simple rules.

## 1.2 Taxes - what are they?

Taxis is Greek for an arrangement. Henderson's dictionary of biological terms, [48], defines it as

“a movement of a freely motile, usually simple organism, especially Pro-

tista, or part of an organism, towards (positive), or away from (negative), a source of stimulation, such as light, temperature, chemicals; an orientation behaviour related to a directional stimulus.”

Taxes represent simple rules for biasing the direction in which organisms move. Typical examples of taxes include chemotaxis (where organisms sense gradients in chemical concentrations around them and can change their swimming direction in response to them), phototaxis (which could be sensitivity to light intensity, direction or polarisation) and geotaxis (which is also known as gravitaxis and is where gravity gives a bias to the direction of movement). Taxes represent both the measurement of the surrounding environment and the physical mechanisms by which individuals move in response to that physical stimulus. Without taxes, organisms would move in a random manner in the hope that their situation will improve. Most organisms use a combination of random movement and taxes. Natural selection ensures that the optimal tactics are always employed (see Weiner 1994 [120]; Futuyma 1994 [34]).

The algae *Chlamydomonas nivalis* are “negatively geotactic” (they have a tendency to swim *upwards* due to being bottom heavy, Kessler 1985 [61]), phototactic (they need light for photosynthesis and hence swim towards it; Boscov & Feinlieb 1979 [9]; Foster & Smyth 1980 [33]; Kessler 1986 [63]; Witman 1993 [123]; Vincent 1995 [116]) and gyrotactic (a term coined by Kessler (1984) [60] to describe the phenomenon in which cells swim towards regions of down-flowing fluid and away from up-flowing fluid). Gyrotaxis (*gyro* is Greek for circle) is due to the cells’ geometry and mass distribution and describes the balance between viscous and gravitational torques. Rheotaxis (from the Greek *rheein* meaning to flow) is a similar taxis that represents the alignment of cells along streamlines because of their shape but is independent of gravity.

In this thesis gyrotaxis will be shown to be a significant mechanism for pattern formation.

### 1.3 Micro-organisms and how they swim

The term *organism* represents anything with animal or plant-like characteristics. *Protista* was originally defined ([48]) as a kingdom of living organisms including bacteria, protozoans (Greek, meaning first animals, and representing “a subkingdom and phylum

of microscopic animals whose body is equivalent to a single cell” [48]), algae and fungi. More recently the term is used for unicellular and colonial algae (or fungi) or for organisms showing both plant and animal characteristics, and is used as a collective noun for the groups protozoa and protophyta (Greek, meaning first plants, and representing all unicellular plants). The term *algae* is from the Latin word *alga* meaning seaweed. Henderson’s dictionary of biological terms defines algae as

“a major division of the plant kingdom consisting of simple non-vascular photosynthetic plants with a unicellular, colonial, filamentous, or thalloid body, and being aquatic in marine or fresh water or found in damp habitats on land.”

The label *plankton* (from the Greek, *plangkton*, meaning wandering) is in common use for a class of micro-organisms. Plankton also produce both small and large scale patterns (Steele & Henderson, 1979 [104]; Truscott & Brindley, 1994 [109]; Solow & Steele, 1995 [102]) but the mechanisms may be very different. Henderson’s dictionary defines plankton as

“the usually small marine or freshwater plants (*phyto-*) and animals (*zoo-*) drifting with the surrounding water, including animals with weak locomotory power.”

Clearly, *swimming* algae and bacteria are not subsets of plankton. However, the same publication mentions that unicellular motile flagellates can be classified in a section of the animal kingdom. This thesis is chiefly a mathematical thesis and we are free of such semantic restrictions and we may generalise our arguments to the idealized swimming micro-organism, paying attention purely to its mechanical and behavioural characteristics independently of its genealogical background. Bearing in mind the possible extensions of this work to other micro-organisms, we choose to study in detail the green biflagellated algae *Chlamydomonas nivalis* (Figure 1.2).

There are a number of forces acting on the algae, some external but others internally influenced. Figure (1.3) describes the main forces affecting the cell, under the assumption that the method of swimming contributes only a propulsive force to the cell and does not affect the flow field or the cell otherwise. Gyrotaxis is caused by the balance between gravitational and viscous torques. The micro-organisms’ geometry

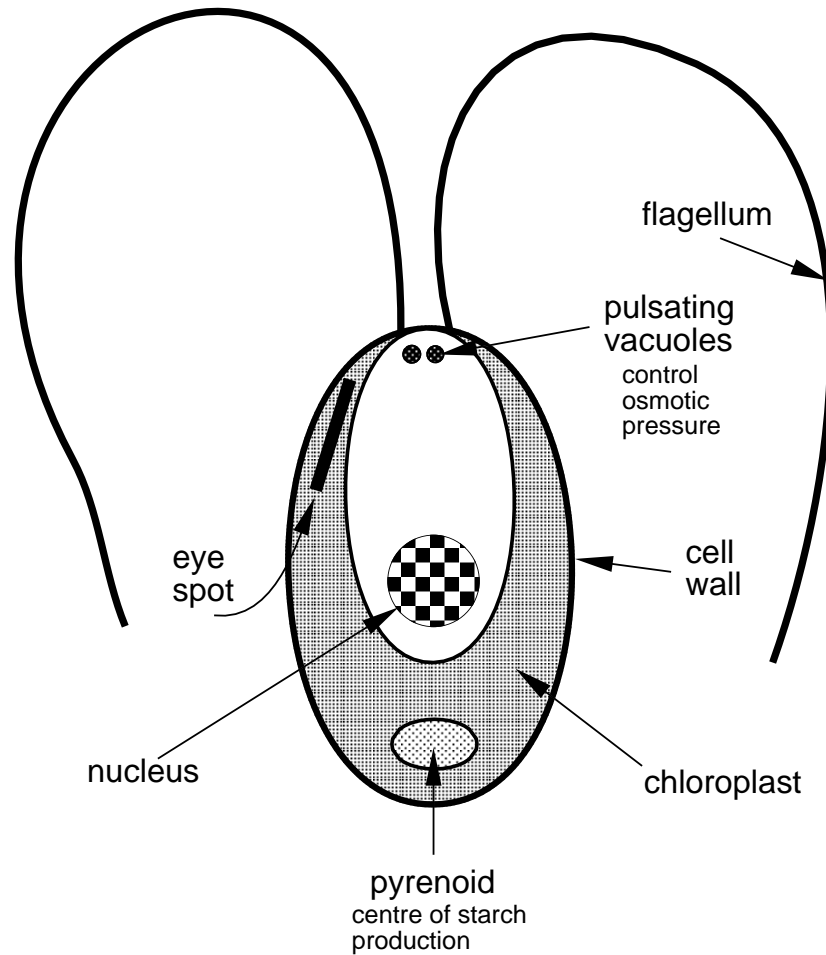


Figure 1.2: *Chlamydomonas nivalis* - anatomy.

and mass distribution imply that they swim towards regions of down flowing suspension and away from up flowing suspension. The viscous torques can effectively bias the direction in which the micro-organism swims and can lead to the cells aggregating. *Chlamydomonas nivalis* have a higher density than the medium in which they swim and so aggregations of cells will cause bulk fluid motion and lead to more cells swimming towards cell rich down flowing regions.

Jones *et al.* (1994) [55] has looked into the effects of biflagellar swimming in greater detail and has come to the conclusion that more realistic models can be approximated by assuming that the micro-organism is a self propelled spheroidal cell. They recommend that an adjustment should be made to the measured parameters of geometry and mass distribution to allow for the effects of the flagella.

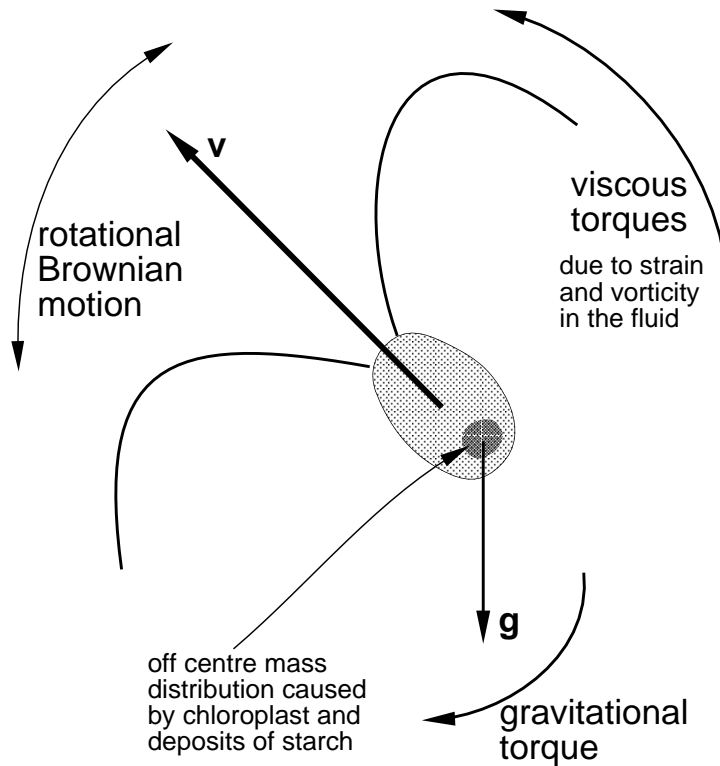


Figure 1.3: The forces acting on *Chlamydomonas nivalis*.

Swimming at small Reynolds number is very different to the way that we swim (Purcell 1977 [91]; Lighthill 1975 [76]). It has been likened to us swimming through thick syrup or “a vat of warm pitch” (Childress 1981 [18]). One of the keys to being able to swim is to have a stroke that is not symmetric in time otherwise the reversible viscous fluid flow prevents ground from being gained (Childress 1981 [18], pages 16–21). Figure (1.4) explains the breast stroke like swimming style of *Chlamydomonas nivalis*. There are two stages: an effective or power stroke in which the micro-organism gains ground, and a recovery stroke in which the flagella are returned to their original positions at the expense of losing some ground (see the analysis of Jones *et al.* 1994 [55]). The flagella do not perform their stroke symmetrically and hence the cells revolve about an axis with the swimming direction. It has been proposed by Crenshaw (1993) [25] and Hill & Vincent (1993) [43] that the cell takes advantage of this rotation in that its eye spot is able to survey the surrounding light field and hence control its phototaxis ([116, 117]). The typical swimming speed of *Chlamydomonas nivalis* is  $60\mu\text{m s}^{-1}$  (or 6 bodylengths  $\text{s}^{-1}$ ). The sedimentation velocity of a spheroidal cell with the dimensions of *Chlamydomonas nivalis* is found from analysis by Van de Ven

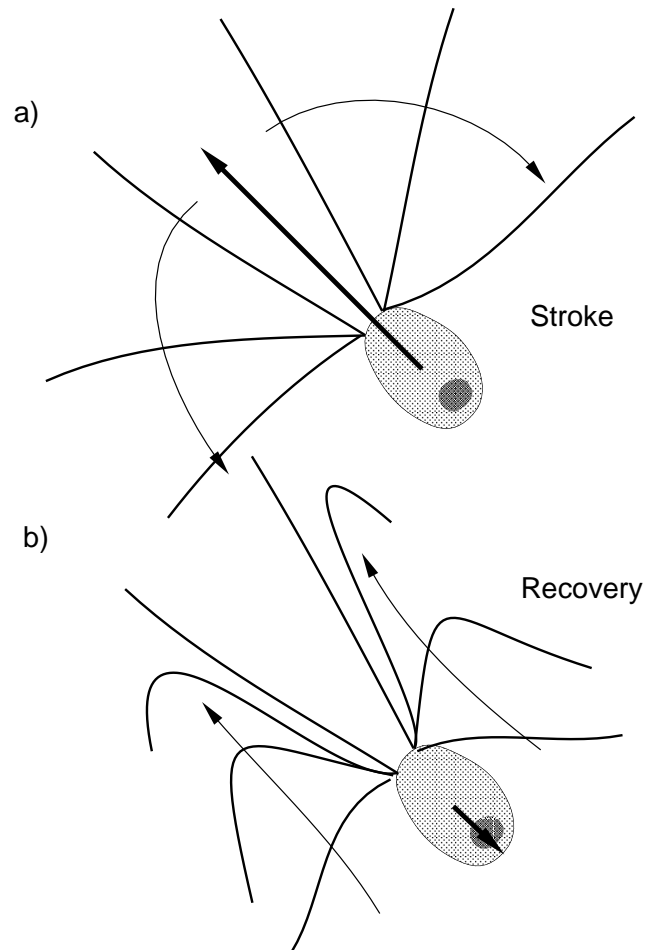


Figure 1.4: How *Chlamydomonas nivalis* swims. a) The power stroke in which the micro-organism moves forward as the flagella are thrust back, and b) the recovery stroke in which ground is lost but the flagella are returned to their initial positions.

(1989) [113] to be about  $1\mu m s^{-1}$  (see Jones 1995 [54] and Batchelor 1972 [4]) and it is, therefore, reasonable to ignore sedimentation of the cells with respect to the cells swimming. However, the rotational torque due to sedimentation is not quite so easily dispensed with. It was proposed by A. M. Roberts (1995, personal communication), via Roberts (1970) [97] and Roberts (1975) [98], that the viscous drag of the flagella on the cell due to sedimentation is responsible (at least in part) for the upswimming of the micro-organism. A series of independent calculations by Hill, Pedley and Jones (1995, personal communication) indicate that the mechanism is of an order of magnitude less than that due to the bottom heaviness of the cell. In this thesis the upswimming will be modelled as due to the cell being bottom-heavy. Nonetheless, a section in Chapter 2

is dedicated to some experiments aimed at distinguishing the two mechanisms.

*Euglena gracilis* has one main flagellum along which it passes a helical wave to power its swimming. *Euglena* also exhibits upswimming tendencies (Wager 1911 [119]) but is mainly phototactic. Other organisms may use flagella or cilia to swim. Ramia (1991) [93] has investigated the swimming capabilities of *Spirillia* with single trailing or leading, and bipolar flagella by simulating its movement in a fluid using the boundary element method. Ramia & Swan (1993) [94] compare these results with rotations and velocities observed in experiments on *Spirillum volutans* and report good agreement. Ramia *et al.* (1993) [95] further consider a general boundary element method which they benchmark with slender body results. They use their model to investigate a micro-organism with a spherical cell body and one flagellum. They go on to explore the interaction of parallel swimming individuals and hydrodynamic interactions with plane boundaries. Their general conclusion is that hydrodynamic interactions are only significant when separation distances are smaller than or equal to the micro-organisms largest physical length scale. These results indicate that it is reasonable to ignore cell-cell interaction when suspension concentrations are low. The particular shape of the cells used in Ramia *et al.* (1993) [95] could be applicable to the swimming of *Euglena gracilis*.

## 1.4 Bioconvection - a brief history of observations

Far from being a recently discovered phenomenon, pattern formation in suspensions of swimming cells has been observed for some time. Ever since some common algae, such as *Chlamydomonas nivalis*, *Euglena viridis*, *C. cohnii* and the ciliated protozoan *Tetrahymena pyriformis* had been isolated, plumes of aggregating cells have been noticed in the culturing flasks. The term “bioconvection” was first coined by Platt in 1961 to describe the phenomenon of pattern formation in shallow suspensions of motile micro-organisms. However, this is by no means the first documentation, which in fact goes back to at least 1848 (see Wagner 1911 [119]). Other investigators have included Loeffler & Mefferd (1952) [77], Nultsch & Hoff (1973) [82], Plesset & Winet (1974) [87] and recently Kessler [61, 60].

In a series of papers, Kessler has looked into the pattern forming capabilities of

micro-organisms ([59, 61, 63, 64, 65, 66]). He noticed that the regions of downwelling fluid which contained large quantities of micro-organisms were narrower than the upwelling clear fluid. Kessler demonstrated the phenomenon of cell focusing ([62, 61]) by considering Poiseuille flow through a long vertical U-tube, as in Figure 1.5, and found that the cells “focused” into a thin plume in the centre of the tube only on the side of the U-tube where the fluid flowed downwards. Cells collected on the outside of the other half of the U-tube.

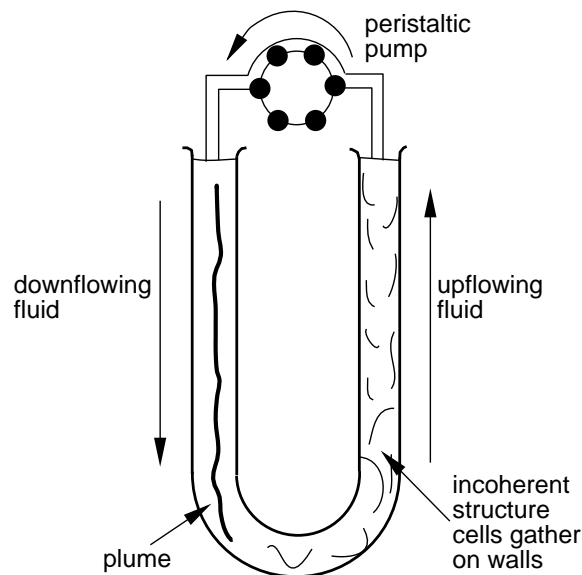


Figure 1.5: Gyrotaxis in Poiseuille flow through a U-tube. Cells swim towards relatively downwards flowing fluid and away from upward flowing fluid. This forms a “focused” plume on the left hand side of the U-tube and cells gather on the wall of the right hand side.

Kessler invented the term “gyrotaxis” to describe the mechanism behind this cell focusing.

## 1.5 Geotaxis and Gyrotaxis - why bother?

A possible explanation for the reason behind aggregation of cells in bioconvection patterns is provided by Tomson & Demets (1989) [108]. The micro-organisms mate sexually and as the volume fraction of the cells is very small (typically of the order of 0.001 for a cell concentration of 1 million per  $cm^3$ ) they need some mechanism so that they can

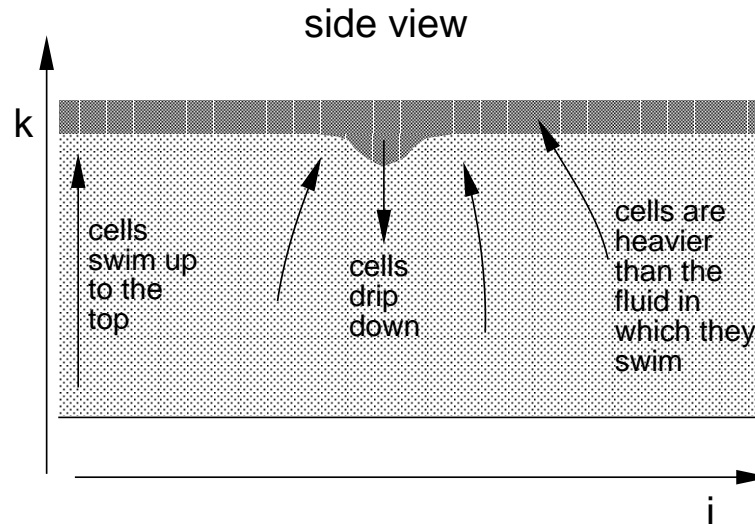


Figure 1.6: An overturning Rayleigh-Taylor type instability. Cells swim to the top and form a suspension layer of greater density than that below.

come into close proximity and, hence, chemotaxis can effectively drive sexual aggregation (see for example Clayton 1957 [22]). Tomson & Demets (1989) [108] call this the mating trap which they say “can only be effective at the beginning of the day, when the diurnally fluctuating sexual agglutinability is high and when the dark/light switch is *on*”. Only then, can the mating process begin. Geotaxis and gyrotaxis result in pattern formation and hence self-concentration and are two mechanisms that are available to *Chlamydomonas nivalis*. Gyrotaxis even works in the absence of an upper fluid boundary (see Figure 1.7) and drives the cells into increasingly concentrated regions. This increase in concentration is only halted by the diffusion of cells away from regions of high concentration. If the conditions for mating are wrong, then the cells are free to move as individuals, otherwise the cells become tactile and form pairs or much larger cell aggregates. Why then are the micro-organisms still geotactic and gyrotactic at times when they do not wish to mate? The reason could simply be that there is more sunlight at the surface of a pond for photosynthesis and in a murky pond, phototaxis may be ineffective. However, the cells also need nutrients and diffusion alone could not provide enough nutrients for a colony of cells living at the surface of a pond. Therefore it is perhaps beneficial for the cells to travel to the bottom of the pond once in a while. If they drive bulk motion at the same time then this may be helpful to the whole colony of cells by mixing the nutrients throughout the fluid. However, in all but very small

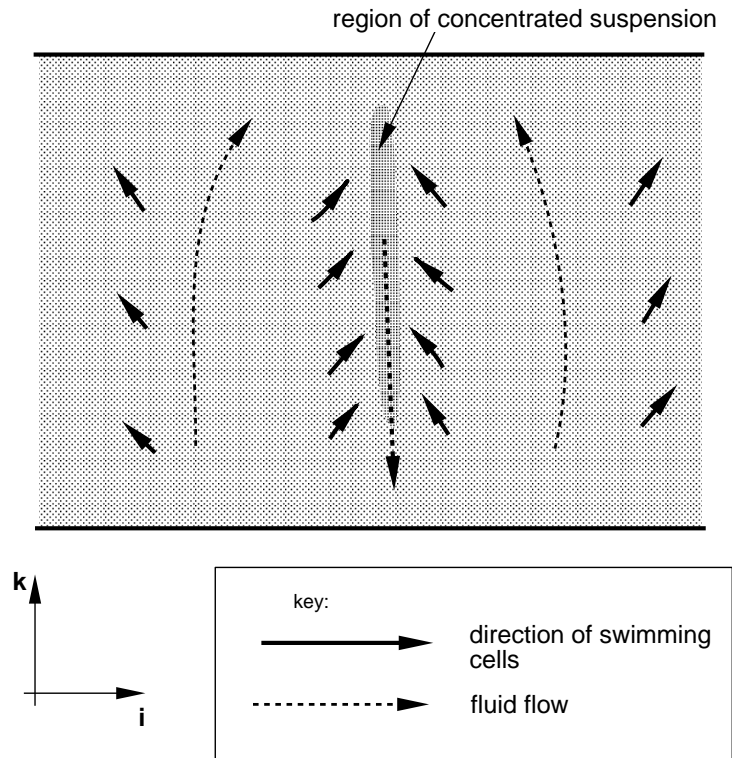


Figure 1.7: A gyrotactic instability. Cells swim towards downwelling fluid making it denser and, hence, sink faster.

puddles, mixing is likely to be driven by wind shear or thermal convection. Figure (1.8) shows how, in the absence of wind shear or thermal convection, gyrotaxis might work to extract more nutrients from the bed of a pond than a mere geotactic instability, involving organisms that do not exhibit gyrotaxis, by increasing the width of upflowing fluid and creating higher wall shear stress.

Maybe we are asking too much to explain an individual species' behaviour by considering them in isolation. Perhaps they have diversified into a niche that is only apparent when considering the wider ecosystem of a mixture of swimming micro-organisms and larger animals as will be found in nature (see Bees 1994 [5]; Bees & Spiegel 1996 [6]; Dawkins 1989 [27]).

## 1.6 A review of modelling techniques

Bioconvection is similar to the thermal convection problem between two horizontal plates (Chandrasekar 1961 [15]; Childress & Peyret 1976 [20]) but the energy input

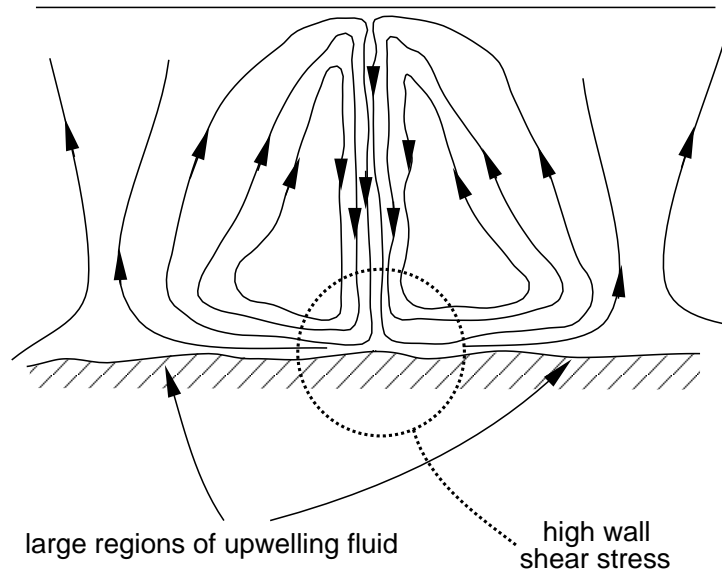


Figure 1.8: Nutrient uptake from pond bed in a suspension of gyrotactic micro-organisms. Streamlines indicate high wall shear stress and large regions of upwelling fluid on the pond bed, increasing the area of nutrient uptake.

is via the individual micro-organisms and not through the boundaries as in thermal convection (Whitehead 1988 [121]; Goldstein *et al.* 1993 [35]). However, much of the established linear and non-linear theory can be borrowed (Schlüter, Lortz & Busse 1965 [101]; Joseph 1971 [56]; Malkus & Veronis 1958 [78]; Proctor 1981 [90]), and of course, ideas from the comparable field of magnetohydrodynamics (Hughes & Proctor 1988 [49], 1992 [50]) can also be used. The necessary inclusion of fluid flow in convection and bioconvection modelling generally distances the theory from Turing type patterns (Turing 1952 [111]), however, many of the techniques involved in the analysis of both systems are common (Levin & Segel 1985 [75]; Eilbeck 1986 [30]). (See Spiegel & Zaleski 1984 [103] for a combination of shear flow and reaction diffusion.) On modelling the individual micro-organisms, existing theories for suspensions of particles can be exploited (Jeffrey 1922 [53]; Batchelor 1970 [3]; Leal & Hinch 1972 [71]) and ideas from the statistics of random walks employed (Hill & Häder 1996 [41]; Mardia 1972 [79]).

### 1.6.1 Pure upswimming models

The first models of bioconvection were developed by Plesset & Winet (1974) [87]. They considered a Rayleigh-Taylor instability in a continuously stratified, two-layer model

and were able to investigate the preferred pattern wavelength as a function of the upper layer depth and the cell concentration. Levandowsky *et al.* (1975) [74] investigated bioconvection and proposed a more realistic model (Childress *et al.* 1975 [19]) in which the micro-organisms could swim but were constrained to swim in the vertical direction only. They introduced an orthotropic diffusion,

$$\mathbf{D} = \begin{pmatrix} D_h & 0 & 0 \\ 0 & D_h & 0 \\ 0 & 0 & D_v \end{pmatrix}, \quad (1.1)$$

(with differing horizontal and vertical diffusion coefficients) to account for the random motions. Their model consisted of the Navier-Stokes equations, incorporating the Boussinesq approximation (e.g. Chandrasekar 1961 [15]),

$$\rho \frac{D\mathbf{u}}{Dt} + \nabla p - \mu \nabla^2 \mathbf{u} = -g\rho(1 + \alpha_e c)\mathbf{k} \quad (1.2)$$

and

$$\nabla \cdot \mathbf{u} = 0 \quad (1.3)$$

where  $\mathbf{u}$  is fluid velocity,  $\mu$  is viscosity,  $g$  is gravity,  $\rho$  is fluid density and  $\alpha_e c$  is the extra density due to micro-organisms of concentration  $c$  at a point. The Boussinesq approximation implies that the only way in which the cell concentration affects the fluid flow is through a change in the fluid density. Other effects of a change in viscosity and a non-Newtonian stress are considered negligible. Childress *et al.* (1975) [19] modelled the swimming cells with a cell conservation equation

$$\frac{\partial c}{\partial t} + \nabla \cdot \mathbf{J} = 0, \quad (1.4)$$

where the flux is given by

$$\mathbf{J} = cU(c, z)\mathbf{k} - \mathbf{D} \cdot \nabla c, \quad (1.5)$$

and  $U(c, z)$  is the cell swimming speed. These equations are very similar to the Rayleigh-Bénard equations for convection between two horizontal planes and a negative vertical temperature gradient (Chandrasekar 1961 [15]). However, in bioconvection, energy is provided internally by the action of swimming micro-organisms, which get their energy from nutrients in the medium and the incident light by photosynthesis. The Boussinesq vertical symmetry of the standard Rayleigh-Bénard problem is lost due to

the biased swimming behaviour of the micro-organisms. Linear analysis predicted that the most unstable wavenumber is zero, and Childress & Spiegel (1978) [21] were able to show from weakly non-linear theory that the bifurcation to instability was subcritical. This means that linear analysis cannot be used to predict a most unstable wavenumber. Harashima *et al.* (1988) [40] produced a simulation of bioconvection from the equations of [19] and found that in all cases the pattern wavelength increased with time, on a parallel with studies of weakly non-linear Rayleigh-Bénard convection with insulating boundaries (Chapman & Proctor 1980 [16]). It is found experimentally, in Chapter 2 of this thesis, that exactly the opposite occurs in bioconvection and indeed the first (linear) instability to occur has non-zero wavenumber.

### 1.6.2 Modelling gyrotaxis

We start, as in [84], by considering the total torque,  $\mathbf{L}_T$  on a cell, such as that in Figure 1.3.  $\mathbf{L}_T$  is the sum of two terms

$$\mathbf{L}_T = \mathbf{L}_g + \mathbf{L}_v \quad (1.6)$$

where  $\mathbf{L}_g$  is the gravitational torque and  $\mathbf{L}_v$  the viscous torque. For a bottom-heavy micro-organism such as *Chlamydomonas nivalis* then

$$L_{gi} = hmg \epsilon_{ijl} p_j k_l \quad (1.7)$$

where  $i, j$  and  $l$  are indices and the summation convention is assumed.  $h$  is the displacement of the centre of mass of the cell from its geometrical centre along the swimming direction  $\mathbf{p}$ ,  $m$  is the cell's mass,  $g$  is the magnitude of the acceleration due to gravity,  $\epsilon_{ijl}$  is the Levi-Civita tensor and  $\mathbf{k}$  is the unit vector in the vertical direction. Rallison (1978) [92] wrote the viscous torque on a solitary body with zero Reynolds number as

$$L_{vi} = -\mu v \left[ P_{ij}(v_j - u_j) + Y_{ij} \left( \omega_j^c - \frac{1}{2} \Omega_j \right) + R_{ijl} e_{jl} \right] \quad (1.8)$$

where  $\mu$  is fluid viscosity,  $v$  is the cell volume,  $\mathbf{v}$  is the cell velocity,  $\boldsymbol{\omega}^c$  is the cell's angular velocity,  $\mathbf{u}$  is the fluid velocity,  $\boldsymbol{\Omega}$  is the vorticity and  $\mathbf{e}$  is the rate-of-strain tensor. This is a linear expression assuming that the length scale for the changes in the flow is much larger than the cell diameter.  $\mathbf{P}$ ,  $\mathbf{Y}$  and  $\mathbf{R}$  are tensors depending only on the surface geometry and orientation of the cell. For a rigid prolate spheroid (Batchelor

1970 [3])

$$P_{ij} = 0, \quad (1.9)$$

$$Y_{ij} = \alpha_{\parallel} p_i p_j + \alpha_{-} (q_i q_j + r_i r_j) \quad (1.10)$$

and

$$R_{ijk} = -\alpha_0 Y_{il} (r_l p_j q_k - q_l p_k r_j), \quad (1.11)$$

where  $\mathbf{p}, \mathbf{q}, \mathbf{r}$  form an orthonormal right-handed set of coordinates and  $\alpha_0, \alpha_{\parallel}$  and  $\alpha_{-}$  are shape parameters.  $\alpha_0$  is the eccentricity and is given by

$$\alpha_0 = \frac{a^2 - b^2}{a^2 + b^2} \quad (1.12)$$

where  $a$  is length and  $b$  is breadth of the cell. As  $e_{ij}$  is symmetric we can write

$$L_{vi} = -\mu v \left[ Y_{ij} \left( \omega_j^c - \frac{1}{2} \Omega_j \right) - \alpha_0 Y_{il} \epsilon_{klm} p_m p_j e_{jk} \right]. \quad (1.13)$$

Putting  $L_T = 0$  gives

$$hmg \epsilon_{ijl} p_j k_l - \mu v \left[ (\alpha_{\parallel} p_i p_j + \alpha_{-} (q_i q_j + r_i r_j)) \left( \omega_j^c - \frac{1}{2} \Omega_j - \alpha_0 \epsilon_{kjm} p_m p_l e_{lk} \right) \right] = 0. \quad (1.14)$$

Multiplying this expression by  $\epsilon_{ist} p_s$  and using the identity

$$\epsilon_{ijk} \epsilon_{stk} = \delta_{is} \delta_{jt} - \delta_{it} \delta_{js} \quad (1.15)$$

where  $\delta_{ij}$  is the Kronecker delta, then

$$\frac{1}{2B} [\mathbf{k} - (\mathbf{k} \cdot \mathbf{p}) \mathbf{p}] = \boldsymbol{\omega}^c \wedge \mathbf{p} - \frac{1}{2} \boldsymbol{\Omega} \wedge \mathbf{p} - \alpha_0 (\mathbf{p} \wedge (\mathbf{E} \cdot \mathbf{p})) \wedge \mathbf{p} \quad (1.16)$$

where

$$B = \frac{\mu \alpha_{-}}{2h\rho g} \quad (1.17)$$

is the gyrotaxis number. Hence, as  $\dot{\mathbf{p}} = \boldsymbol{\omega}^c \wedge \mathbf{p}$ , so

$$\dot{\mathbf{p}} = \frac{1}{2B} [\mathbf{k} - (\mathbf{k} \cdot \mathbf{p}) \mathbf{p}] + \frac{1}{2} \boldsymbol{\Omega} \wedge \mathbf{p} + \alpha_0 [\mathbf{E} \cdot \mathbf{p} - \mathbf{p} \mathbf{p} \cdot \mathbf{E} \cdot \mathbf{p}]. \quad (1.18)$$

The above equation combines expressions from Leal & Hinch (1972) [71] and Hinch & Leal (1972) [47] which were both initially derived by Jeffrey (1922) [53].

### 1.6.3 A new continuum model

Pedley & Kessler (1990) [85] reasoned that by considering  $\mathbf{D}$  as isotropic and, hence, “strongly random” and independent of the mechanisms involved in gyrotaxis, Pedley *et al.* (1988) [83] were being inconsistent in that they were considering the determination of the swimming velocity,  $\mathbf{V}_s$ , as “weakly random”. That is to say that calculating the cell swimming direction, in a deterministic manner, for all of the cells, and then assuming that there was no bias in the direction of diffusion of these cells was inconsistent. Therefore, instead of assuming constant orthotropic diffusion tensor (as in [19]) they modelled the cell swimming direction in a probabilistic fashion. A model analogous to that of suspensions of colloidal particles subject to rotary Brownian motion was applied (Brenner & Weissmann 1972 [12]; Brenner [10, 11]; Hinch & Leal [46, 47, 70, 71]). From this, they calculated the average swimming direction and the cell diffusion tensor.

Consider a cell swimming direction probability density function (p.d.f.) defined on a sphere,  $f(\mathbf{p})$ , where

$$\mathbf{p} = \begin{pmatrix} \sin \theta \cos \phi \\ \sin \theta \sin \phi \\ \cos \theta \end{pmatrix}. \quad (1.19)$$

where  $\theta$  and  $\phi$  are the unit spherical polar angles.  $\theta$  is the colatitude measured relative to  $\mathbf{k}$ . The mean cell swimming direction,  $\langle \mathbf{p} \rangle$ , is defined by

$$\langle \mathbf{p} \rangle = \int_S \mathbf{p} f(\mathbf{p}) dS \quad (1.20)$$

where  $S$  is the surface of a unit sphere and

$$\mathbf{D}(t) = \int_0^\infty \langle \mathbf{V}_r(t) \mathbf{V}_r(t-t') \rangle dt', \quad (1.21)$$

where  $\mathbf{V}_r$  is the velocity of a cell relative to its mean value. The expression for  $\mathbf{D}$  is, of course, hard to calculate as it requires a knowledge of all previous cell velocities and, hence, we are forced to make an approximation for the sake of simplicity. If the cell swimming speed,  $V_s$ , is a constant as assumed by [85] (the effects of a non-constant  $V_s$  on the linear analysis will be considered in Section 3.7) and assume that it takes a cell  $\tau$  seconds to settle to a preferred direction (called the direction correlation time) then we have

$$\mathbf{D} \approx V_s^2 \tau \langle (\mathbf{p} - \langle \mathbf{p} \rangle) (\mathbf{p} - \langle \mathbf{p} \rangle) \rangle. \quad (1.22)$$

The p.d.f.,  $f(\theta, \phi)$ , satisfies a conservation equation

$$\frac{\partial f}{\partial t} + \nabla \cdot (\dot{\mathbf{p}}f) = D_r \nabla^2 f, \quad (1.23)$$

where  $D_r$  is the rotational diffusivity constant. Equations (1.18) and (1.23) are called the forward Kolmogorov or Fokker-Planck equations (see Risken 1989 [96]; Schienbein & Gruler 1993 [100]). Fluid flow is modelled with the Navier-Stokes equations for an incompressible fluid that includes a term for the negatively buoyant cells. The Boussinesq approximation is employed such that this is the only way in which the cells affect the fluid motion. Hence,

$$\nabla \cdot \mathbf{u} = 0 \quad (1.24)$$

and

$$\rho \frac{D\mathbf{u}}{Dt} = -\nabla p_e + nv\Delta\rho\mathbf{g} + \nabla \cdot \boldsymbol{\Sigma}. \quad (1.25)$$

The total number of cells is conserved and the cells can be modelled using a conservation equation of the form

$$\frac{\partial n}{\partial t} = -\nabla \cdot [n(\mathbf{u} + V_s \langle \mathbf{p} \rangle) - \mathbf{D} \cdot \nabla n], \quad (1.26)$$

where  $\mathbf{u}(\mathbf{x})$  is the fluid velocity,  $\langle \mathbf{p}(\mathbf{x}) \rangle$  is the mean cell direction,  $V_s$  is the mean cell swimming speed,  $\boldsymbol{\Sigma}(\mathbf{x})$  and  $\mathbf{D}(\mathbf{x})$  are the fluid stress and cell diffusion tensors respectively,  $n(\mathbf{x})$  is the local cell concentration,  $p_e(\mathbf{x})$  is the excess pressure,  $v$  is the mean volume of a cell, and  $\Delta\rho$  is the the difference between the cell and fluid density. The boundary conditions for a suspension trapped between two solid boundaries are the no flow condition

$$\mathbf{u} = \mathbf{0} \quad \text{at} \quad z = 0, -H, \quad (1.27)$$

and zero cell flux perpendicular to the boundaries

$$\mathbf{k} \cdot (n(\mathbf{u} + V_s \langle \mathbf{p} \rangle) - \mathbf{D} \cdot \nabla n) = 0 \quad \text{at} \quad z = 0, -H. \quad (1.28)$$

We shall assume throughout this thesis that the horizontal boundaries are solid for the following reasons. Although the suspension is typically open to the atmosphere at the upper boundary and a stress free boundary condition may appear to be the most reasonable, there is some evidence to suggest that the upper boundary quickly becomes “rigid” ([61, 60, 84, 42]). Cells swim up to the upper surface and form close-packed

two-dimensional structures that float on the surface. These structures form quickly and appear to be very stable. At subsequent times, when cells encounter the upper boundary, they behave as if it were solid. Perhaps it would be more reasonable to assume a mixed type of boundary condition but at the present time, evidence suggests ([19, 42]), that this would alter the general behaviour of the system very little.

## 1.7 What this thesis is about

This thesis describes a combination of experimental and theoretical techniques that have been used to study the mechanics involved in bioconvection in a suspension of gyrotactic swimming algae called *Chlamydomonas nivalis*.

Chapter 2 describes experiments on bioconvection to obtain quantitative data on the pattern wavelengths and how they vary with suspension concentration, depth and time. Other observations are discussed, such as mode interactions and the formation and breakup of annular patterns. A general measure of pattern is examined whereby images are associated with a rippled surface in Euclidean three space and its Gaussian and mean curvatures.

Chapter 3 investigates the linear analysis, both analytical and numerical, of the recent continuum model proposed by [85] in a container of finite depth. A further extension that the cell swimming speed is taken to be a random variable, and the effect of this on the linear analysis is examined. The value of the variance of the cell swimming speed is found to have a critical nature.

Chapter 4 details a computer aided, analytical expansion of the gyrotactic Fokker-Planck equation for  $f(\theta, \phi)$  in terms of surface spherical harmonics. It is found that algebraic approximations for the diffusion tensor and mean cell swimming velocity can be obtained and convergence is rapid for a range of realistic parameters. These expressions can be applied directly to the fully non-linear equations for cell concentration and fluid flow.

Chapter 5 considers the fully non-linear problem of bioconvection in a “deep” suspension. Models of purely upswimming micro-organisms ([19]) do not possess an instability in deep bioconvection in the absence of an upper boundary but models incorporating gyrotaxis do. For the physically realisable situation of small vertical

variation, a weakly non-linear analysis is constructed to give an amplitude equation for the non-linear saturation of an initial disturbance and steady state solutions are explicitly calculated. The possibility of horizontally travelling vertical plume solutions is also investigated. By introducing a background vorticity, a Hopf bifurcation is generated and the ensuing limit cycle produces a travelling front of horizontally travelling, vertical plumes. The analysis of a small vertical variation to the steady state solutions introduces the possibility of vertically travelling pulses, or blips, down a plume, which are also seen in experiments.

## Chapter 2

# An Experimental Investigation of Bioconvection

### 2.1 Introduction

The purpose of this investigation is to attempt to quantify observations of pattern formation by swimming micro-organisms in a rational and reproducible manner. In this chapter, methods will be described that we have developed for measuring the attributes of these patterns in suspensions of a particular micro-organism, the algae *Chlamydomonas nivalis*. Observations of pattern formation have been recorded before by such authors as Wager (1911) [119], Loeffler & Mefferd (1952) [77], Wille & Ehret (1968) [122], [74] and recently Kessler (1984) [60] but the results have tended to be of a qualitative nature. This is one of the first, controlled experiments aimed at quantitatively cataloguing aspects of the bioconvection patterns. It is hoped that the large data set of 39 experiments will be used in future analysis. Methods will be described to Fourier analyse the images, with emphasis on the dominant unstable wavenumber and how this changes with time. It will be shown that this wavenumber increases with time, not continuously, but discretely as new modes become unstable on top of already developed modes. Observations of pattern development and mode interactions will be discussed and a general measure of the patterns based on curvatures of an associated landscape will be proposed. Finally some experiments that were performed to investigate the mechanisms for gyrotaxis, by increasing the density of the medium with respect to the algae, will be described.

## 2.2 Culturing and concentrating the algae

Before measuring bioconvection patterns, it is necessary to breed a “homogeneous” culture of cells that are in a fully motile stage of development. This is essential as there are numerous forms of these organisms depending on their environmental conditions. For example, when bad times of limited nutrients arise the algae metamorphose into dormant cysts. There are a number of media that could be used, such as the slightly cloudy “Soil Water Medium” or media based on Fish Meal as in James (1978) [52]. “Bolds Basal Medium” was used because it is relatively clear, mimics the natural conditions of the cells and is reasonably easy to make whilst being easily adaptable (Bold & Wynne 1978 [8]). This medium allowed normal, moderate growth and was used in large flasks to reduce the glare of the light source and facilitate mutual shading. Alternatively, the medium plus vitamin B12 (often recommended to increase the percentage of swimming cells) in smaller flasks allowed faster growth plus an assurance of motility. However, the vitamin B12 produced some abnormal development when used continuously over many months. The cells were subcultured every four to six weeks and, ideally, experiments were only performed on fresh green cultures of about three to four weeks old. There is some evidence to suggest (Kessler, personal communication 1995) that the cells are not gyrotactic within the first week after subculturing. The cells are left to breed under two, cool white, fluorescent tubes which give a maximum light intensity of 500 lx. A cycle of twelve hours of darkness followed by twelve hours of light is used. It is important to realise that the cells have their own diurnal cycles of breeding, dividing and feeding, and it is essential to carry out experiments during the correct motile phase. The cells’ cycle was set to coincide with my own daily cycle so that full advantage of their motility could be taken. Like many of us *Chlamydomonas* do not perform well within the first few hours of daylight! Half way through their day they appear to perform best and produce the most robust patterns. Tomson & Demets (1989) [108] have studied the daily cycle of *Chlamydomonas eugametos* in detail and suggest that they are most motile in the middle of their day. In the first few hours of light the cells are concerned with dividing and in their evening they begin to stick together in preparation for mating. Tomson & Demets (1989) [108] also suggest that the cells breed best when the suspension is not agitated, and that they do not divide at all if the suspension is regularly well-mixed. The cells also tend to stop swimming with

a sudden change of temperature, and hence, all steps of the breeding and experimental processes took place at a constant temperature ( $25 \pm 2^\circ$  C) within the laboratory, at a set time in the day. All the equipment required in culturing was washed and rinsed in distilled water and then carefully sterilized (autoclaved at 15 pounds per square inch of pressure for 15 minutes) to avoid contamination by bacteria and fungi. Cleanliness is crucial as if cultures become infected then it is very difficult to remove the infection.

Because *Chlamydomonas* are geotactic, it is easy to concentrate them (see Kessler [58, 59]). By using a long-necked flask with a small piece of absorbent cotton wool placed within the suspension, half way down the neck, the cells can be harvested from the top. This is because the cells' average swimming direction is upwards and they will swim through the cotton wool but will not be convected back down, as in the absence of the cotton wool. After 24 hours or more, clear liquid is left at the bottom of the flask and concentrated suspension at the top. If left too long, the cells will quickly run out of nutrients and metamorphose into a non-motile state. Alternatively, by floating a piece of absorbent cotton wool in a suspension, the cells will swim to the highest point and get stuck in the cotton wool. Again, if this is left too long it will dry out and kill the cells (Figure 2.1). The concentrated suspension can be transferred by pipette to a petri

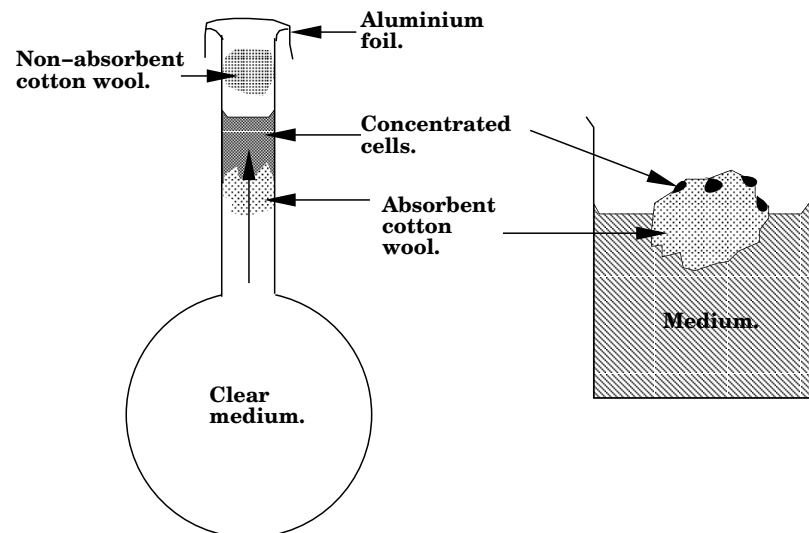


Figure 2.1: Two methods of concentrating the cells: a) cells swim up through absorbent cotton wool in a thin necked flask and remain in the suspension above the cotton wool; b) cells swim up through a floating raft of absorbent cotton wool and become trapped within it at the surface.

dish. It was found that plastic petri dishes were the most regularly shaped and so the 5cm diameter, circular, sterile variety were generally used. One of the first reactions of the cells is to stick to the petri dish walls. To avoid this problem, a small amount of clear medium from the culture flask was put into the petri dish. It was cleaned and polished with a lens tissue before filling with the concentrated suspension. If the cells still stuck then the dish and suspension were left in darkness for twenty four hours. This usually gave the cells sufficient time to get used to their new environment and reproducible patterns were generally observed.

### 2.3 Parameter measurement and control

As well as being geotactic and gyrotactic, *Chlamydomonas* are also sensitive to light (i.e. phototactic). (Foster & Smyth 1980 [33]). It was therefore necessary to limit this effect as much as possible. One way that was considered is to let the patterns form in darkness and then to flash a light on for the purpose of recording visual images. The cells, however, exhibit a photophobic response to a sharp increase in light intensity and they stop swimming for a short period before eventually adjusting their swimming stroke, such that their flagella are both aligned, and swimming in the reverse direction (Witman 1993 [123]; Ruffer & Nultsch 1985 [99]). Instead, a very low, red light source at wavelengths of about 622 – 780nm was used, to which *Chlamydomonas* do not appear to respond significantly ([33]). Heating the suspension with the light source was undesirable and so an infra-red filter was placed between the light source and the cells. Finally, a milk glass filter was used directly under the suspension to create an even, non-directional light source. The light intensity at the final stage did not exceed 5 lx, measured using a standard light meter.

After concentrating the suspensions of algae, it is necessary to measure their concentration. This was achieved after experimentation by first killing the cells, using iodine or heating them, and then sampling from the well mixed suspension using a microslide. A typical microslide is a hollow tube of rectangular cross-section, with dimensions of 0.2mm deep by approximately 1mm wide and 40mm long and thus, the volume per unit area, when the slide is flat on the table, is easily calculated. When the cells are dead, they sink to the bottom of the slide. Using a microscope linked to

an image processing system the number of cells in the picture were counted automatically and, after calibration with a graticule, the concentration was calculated. The microscope was set up with a light source directly below the microslide. The light was adjusted so that it was focused through the spheroidal cells onto the video lense and hence pinpoints of bright light in the centres of the cells were obtained. This allowed touching cells to be counted independently. This is good for counting purposes but not good for calculating cross-sectional areas. The counting process was set up to reject items that are too small or too large. Counting was repeated ten times on the same microslide and up to three microslides were used to calculate an average concentration for the suspension. To check the accuracy of this process a standard haemo-cytometer was used to count cells by eye. The calculations of concentration compared well, with the automated method giving a value of 84% of the manual method after counting 1039 cells by eye. This was within the error ranges of both methods and so it was not necessary to scale the concentrations from the automated method. To measure the depth of the suspensions, a calibrated microscope was used that was first focused on the bottom of the petri dish and then on the surface of the suspension. The microscope was calibrated by using glass slides of known thickness (measured using a micrometer). To ease the focusing the surfaces of the slides were smeared. A combination of the slides and fine focus was used to measure the depth to within  $\pm 0.03\text{mm}$  of the surface of the suspension. The surface is easily identifiable as cells group together and form rafts of unit thickness at the surface. Realistically, however, this error bound should be doubled to allow for small errors in calibrating the microscope and focusing on the scratches on the bottom of the petri dish.

It was found that plastic petri dishes were the flattest and the depth did not vary significantly over the dish (maximum error  $\approx 0.03\text{mm}$ ). It is assumed that the depth is constant over the majority of the central region of the suspension. In situations where the suspension was very concentrated the bottom could not be focused on and, hence, this had to be done prior to filling the dish with suspension.

## 2.4 Experimental arrangement

All experimental work was completed on a minimal budget and use was made of whatever, often old, equipment was available. By far the most up to date unit was the Leitz stereo micro/macroscope which was connected to a Z80 based Seescan image processor. The image processor can in no way be described as state of the the art technology but was sufficient for our purposes and was used primarily to implement the cell counting

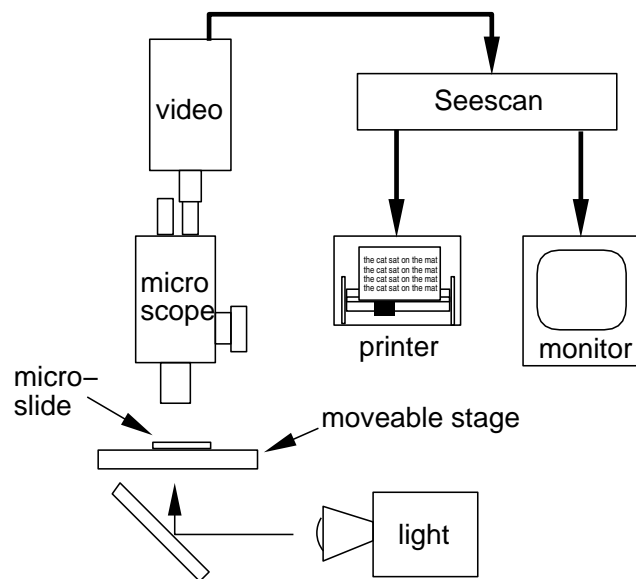


Figure 2.2: Experimental setup for cell concentration measurements.

algorithm. For the bioconvection experiments, the videocamera was focused directly onto the petri dish. In general the suspensions were mixed well, and then pictures were captured every ten seconds. Mixing correctly is very important since if unwanted fluid motion is initiated then the initial pattern that forms may be affected. For instance, spin-up will result in higher concentrations in the centre, whereas secondary circulations in the horizontal plane could influence the generation of a sheet instability as opposed to point instabilities. For each of the experiments a total of nine pictures were captured and saved on  $3\frac{1}{2}$  inch magnetic disks. These pictures were then transferred to a PC 286, via a serial port, where they were then transferred across the network to a Unix system. A graphics package, IDL (Research Systems Inc., Colorado), was utilized to analyse the data on the Unix workstation.

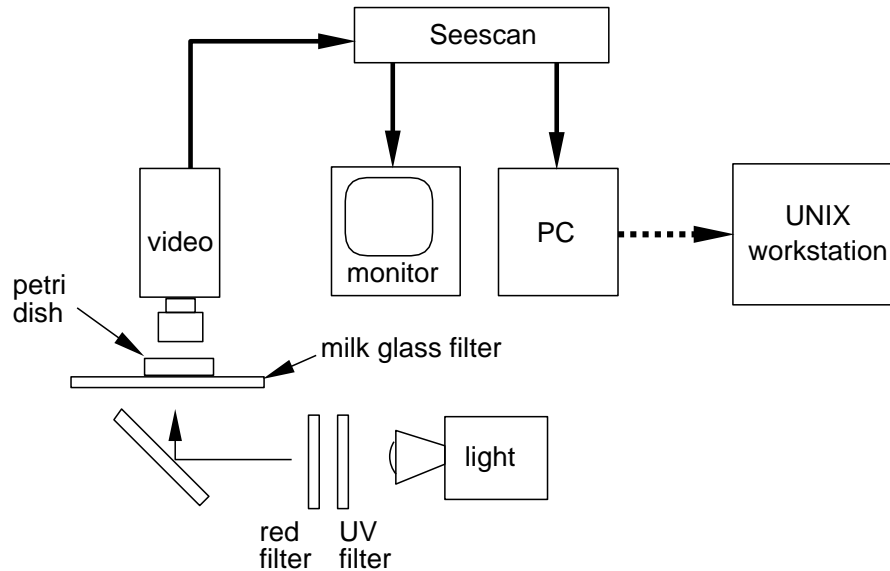


Figure 2.3: Experimental setup for recording images of bioconvection in a petri dish.

## 2.5 Image processing and characterization

The images consist of  $256 \times 256$  pixels of 128 grey shades plus an unused bit (Figure 2.4). This gives a total picture size of 64 kbytes. Thus, each experiment takes up a total of 0.6 Mbytes. This can be greatly reduced after compression. It can be clearly seen that the horizontal and vertical scales differ. This was due to the camera that was used and it was necessary to rescale the images accordingly. The graphics package IDL was selected to analyse the images due to its ease of use and adaptability.

The set of nine pictures each contain unwanted information such as:

- the walls of the dish,
- reflections and scratches on the dish,
- localized or irregular light sources, and
- the boundary of the picture.

The first three can be eliminated by subtracting the first image, when there is no convection, from the next eight images. The last item becomes important when Fourier analysing the images. Suitable use of windowing functions can solve this problem. By Fourier transforming the images, it is possible to extract a measure of the most dominant wavelength at a given instance and investigate how it changes with time.

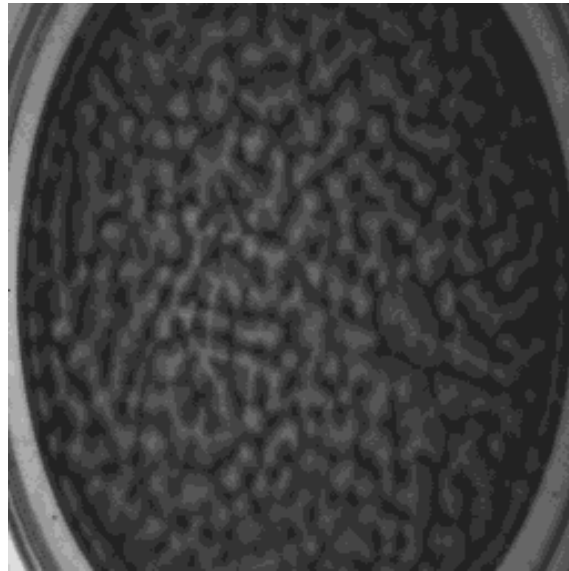


Figure 2.4: Example of a bioconvection image as initially recorded.

### 2.5.1 Discrete Fourier transforms

The images are composed of a two-dimensional, discrete, real data set and one would expect there to be a corresponding two dimensional discrete complex Fourier space. One of the best ways to obtain this is to use the Fast Fourier Transform (or FFT) algorithm developed by Cooley & Tukey (1965) [23] (see Bingham 1974 [7] for a history of the method). Press *et al.* in Numerical Recipes [89] (Chapters 12 and 13) describe the workings of the FFT succinctly, and it is only necessary here to consider the approximation errors involved in the process in more detail. Firstly, we may dispel any concern about the resolution of the picture as it contains  $256 \times 256$  pixels and we will only be considering up to a maximum of 60 wave lengths per picture. This gives a minimum of four pixels per oscillation and satisfies the Nyquist condition of at least two pixels per oscillation. However we should be aware of the problems linked with transforming discrete data, such as aliasing. Aliasing occurs as a result of the information “lost” when enforcing an upper bound on frequency in Fourier space. The “energy” misplaced due to the higher frequencies is reflected back onto lower frequencies in Fourier space. This is summed up in Figure (2.6). The reader is again referred to the relevant section in Numerical Recipes [89] (page 496). The discrete Fourier transform of an image  $h(x, y)$

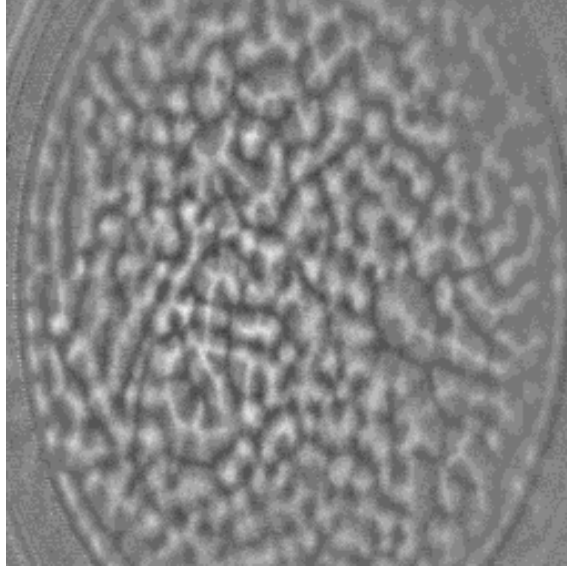


Figure 2.5: The same image as before but after the first image, where bioconvection does not occur, has been subtracted.

of size  $N^2$  in two dimensions is given by

$$H(k_x, k_y) = \sum_{y=0}^{N-1} \sum_{x=0}^{N-1} e^{\frac{2\pi i x}{N}} e^{\frac{2\pi i y}{N}} h(x, y), \quad (2.1)$$

where  $H$  is in general complex, and contains phase information as well as the power spectrum. A procedure in the graphics package IDL was used to perform the FFT on the real, two dimensional image array. The procedure returns a complex array of the same size. The structures of the two arrays are given in Figure (2.7) with an example of a hexagonal pattern shown schematically. The distance in Fourier space of the dots from the origin indicates the wavenumber (wavenumber is used here as the number of waves in 256 pixels) and its position indicates its direction. Phase information is also contained in the argument of each complex number in  $H$ .

### 2.5.2 Fourier spectrum estimation and analysis

The aim here is to extract the most dominant wavenumber contained in the image. The Fourier spectrum is a measure of the spectral components of an image at varying wavenumbers. The discrete Fourier spectrum,  $\mathcal{P}_n$ , is defined on  $\frac{N}{2}$  intervals (called

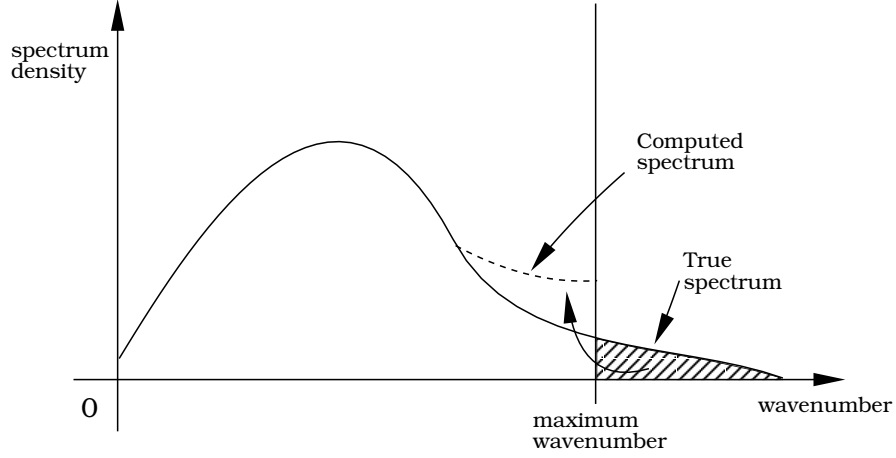


Figure 2.6: Aliasing and how it affects the Fourier spectrum. The energy from higher wavenumbers beyond the cutoff wavenumber is reflected back onto the discrete Fourier spectrum.

bins),  $I_n = [n, n + 1)$  where  $n = 0, \dots, \frac{N}{2} - 1$ , as

$$\mathcal{P}_n = \sum_{d(k_x, k_y) \in I_n} |H(k_x, k_y)|^2 \quad (2.2)$$

where  $d(k_x, k_y)$  is the distance in Fourier space of  $(k_x, k_y)$  from the origin. As the scales in  $h$  space for  $x$  and  $y$  are different (depending on the construction of the video camera), it is necessary to scale the distance in the transform space,  $H$ , accordingly. How does this Fourier spectrum compare with the continuous Fourier spectrum? As the two dimensional FFT is essentially two FFT performed in the  $x$  and  $y$  directions consecutively we may consider the errors involved in just one dimension. The image has an edge and, hence, we are in effect multiplying the original infinite image by a square windowing function. This is equivalent to finding the convolution of the image Fourier space with that of the square window Fourier space. There is a certain amount of “leakage” from one bin to the next due to the windowing function, and it can be shown that it has a typical fall off rate of  $(\pi s)^{-2}$ , where  $s$  is the frequency offset in bins (Numerical Recipes [89], pages 545 – 551). The square of the transformation of the window function determines the leakage,  $\mathcal{L}$ , where

$$\mathcal{L}(s) = \frac{1}{\mathcal{W}_{ss}} \left| \sum_{x=0}^{N-1} e^{\frac{2\pi i s x}{N}} \mathcal{W}(x) \right|^2, \quad (2.3)$$

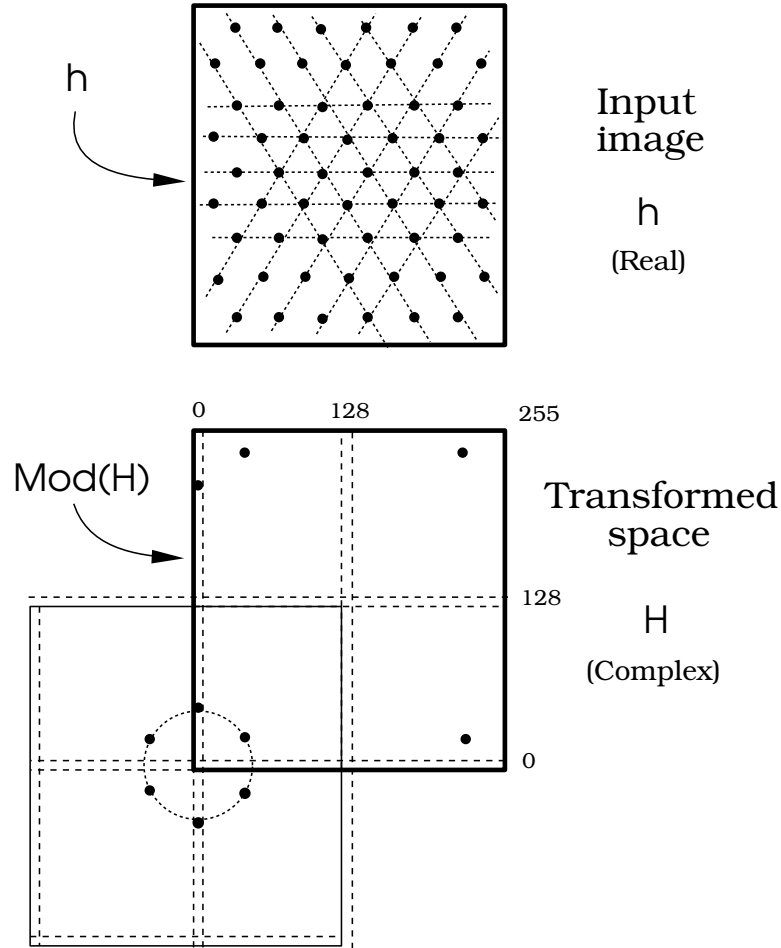


Figure 2.7: Discrete image and Fourier transformed space: an example of a hexagonal pattern. The upper square indicates the input image and the lower square (with a thick boundary) indicates the form of the fast Fourier transformed output space and how it is to be interpreted (the square with a thin boundary).

where  $\mathcal{W}(k)$  is the windowing function and  $\mathcal{W}_{ss} = N \sum_{k=0}^{N-1} \mathcal{W}^2(k)$ . For a square windowing function

$$\mathcal{L}(s) = \frac{1}{N^2} \left[ \frac{\sin \pi s}{\sin \frac{\pi s}{N}} \right]^2. \quad (2.4)$$

For Fourier spectrum analyses it is the oscillatory nature of the leakage which is undesirable (a manifestation of the Gibbs phenomenon whereby sharp edges introduce oscillatory errors). A solution is to use a different windowing function that does not have the sharp edges of the square windowing function. The Hann window was chosen (Numerical Recipes [89], pages 545 – 549) as it removes the oscillatory nature of the leakage and the error rapidly decreases to zero outside a small range in the Fourier

spectrum space. The Hann window is essentially a cosine (plus a constant) about the center of the image and reaches a minimum of zero at the edges. This has the additional benefit of favourably weighting the information in the centre of the picture. The Hann window in two dimensions is defined as

$$\mathcal{W}_H(x, y) = \frac{1}{4} \left[ 1 - \cos \frac{2\pi x}{N} \right] \left[ 1 - \cos \frac{2\pi y}{N} \right] \quad (2.5)$$

and is multiplied with the image before application of the FFT algorithm.

### 2.5.3 Dominant wavenumber analysis

In general the discrete Fourier spectrum can be graphed as a rather noisy bar chart with one or more dominant wavenumbers. But how do we extract this wavenumber and produce an estimate of the variance of this value? Figure (2.11) shows a typical time series of nine images taken one every 10 seconds and Figure (2.12) the corresponding Fourier spectra. As the first frame is subtracted from each subsequent frame the background “noise” will increase with time as the differences between the two frames become greater. Also, a range of wavenumbers become unstable with maybe one most unstable wavenumber. An unnormalised double Gaussian distribution is fitted to the “noise” and “not so unstable wavenumbers” and the other is fitted to the dominant most unstable wavenumber. The unnormalized double Gaussian distribution,  $\bar{?}(X = n)$ , is defined as

$$\bar{?}(X = n) = A_1?( \lambda_1; X = x + \mu_1) + A_2?( \lambda_2; X = x + \mu_2), \quad (2.6)$$

where

$$?( \lambda_i; X = x) = e^{-\left(\frac{x}{\lambda_i}\right)^2}. \quad (2.7)$$

Figure (2.8) shows a close up of this curve fitting. The trial curve is fit using a least squares algorithm. It was found that this method could be used on large sets of Fourier spectra where the curve fitting was effectively implemented on a computer. However, it was necessary to investigate some measures of the errors involved so that we could be warned if the curve fitting was inappropriate (for example if there exists two or more dominant peaks).

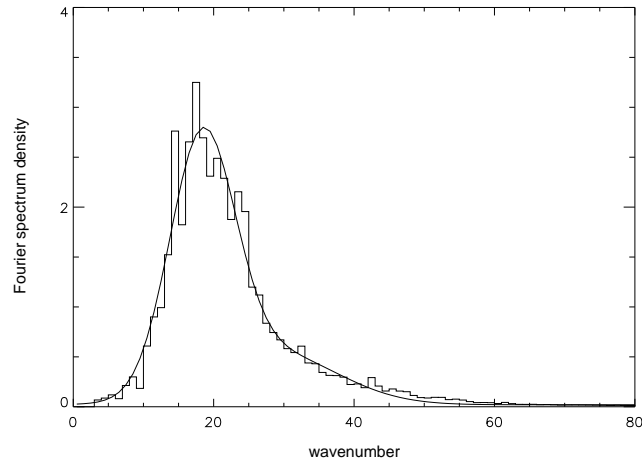


Figure 2.8: An example of curve fitting using the unnormalised double Gaussian distribution to an image's Fourier spectrum. The horizontal axis measures wavenumber and the vertical axis is the Fourier density.

#### 2.5.4 Error analysis

Due to the nature of the bar graph, standard confidence tests are not particularly relevant here. That is to say that the Fourier spectrum contains information on the harmonics of the patterns and it would be unreasonable to assume the spectrum has a particular shape. What we are interested in achieving is to fit a curve to the general outline of the spectrum. Moreover we wish to ignore the possible large fluctuations of the spectrum. This could be achieved by first smoothing the data, but this has the disadvantage of losing some important information on the harmonics. Alternatively, two statistics are chosen that describe how well the unnormalized double Gaussian distribution fits the data. A small value ( $< 0.1$ ) of both of the statistics indicates that the curve fitting is successful, whereas a large value of any one statistic does not necessarily imply that the curve fitting is inappropriate but does indicate that greater attention should be paid. If both statistics are large then this is a strong indication that the curve fitting is ineffectual. In only a small number of cases it is necessary to estimate the most unstable wavenumber by eye (for example, experiment x120h, Figures 2.11 and 2.12, in which there are two dominant wavenumbers in the initial pattern). The sum modulus error, normalised with respect to the area under the bar graph, is a good measure of the absolute roughness of the bar graph and the Kolmogorov-Smirnov statistic describes variations in the trends of cumulative data (e.g. von Mises, 1964

[118]). The sum modulus error has a different character to the chi-squared statistic in that it represents the small errors as much as the large. It is defined as

$$\mathcal{E}_M = \frac{1}{\sum_{n=0}^{N-1} \mathcal{P}_n} \sum_{n=0}^{N-1} |\mathcal{P}_n - \bar{?}(X = n)|, \quad (2.8)$$

where  $\mathcal{P}_n$  is the Fourier spectrum at wavenumber  $n$  and  $\bar{?}(X = n)$  is the unnormalized double Gaussian distribution. The normalised Kolmogorov-Smirnov statistic is defined as

$$\mathcal{E}_{KS} = \frac{1}{\sum_{n=0}^{N-1} \mathcal{P}_n} \max_{n=0..N-1} \sum_{j=0}^n (\mathcal{P}_n - \bar{?}(X = n)) \quad (2.9)$$

and measures the maximum cumulative error rather than the total sum error. A calculation of the significance of  $\mathcal{E}_{KS}$  (e.g. Stephens 1970 [105]) is not strictly relevant in this context as the spikes found in the Fourier spectrums are very real entities and represent unstable modes or harmonics and not random events.

If  $\mathcal{E}_M$  is large then this indicates that the data is not very smooth and many harmonics exist. If  $\mathcal{E}_{KS}$  is large then this indicates that the general trend of the unnormalised double Gaussian distribution deviates significantly from the data.

Regardless of the form of the error estimates, the  $\bar{?}$  appears to be the natural choice of function to fit for the majority of experiments. In this way a most unstable wavenumber can be extracted as a function of time. In particular the first unstable wavenumber and the final (or near final wavenumber as the pattern may take hours to fully evolve) most unstable wavenumber can be examined as a function of concentration and suspension depth.

## 2.6 Experimental examples

Below we present experimental data for each experiment and display a number of examples of the differing patterns that one might expect with *Chlamydomonas nivalis*. Dark regions indicate a high local cell concentration. There are nine frames per experiment taken consecutively every ten seconds unless otherwise stated. The very last picture in each experiment was recorded after a sufficiently long time such that the pattern appeared stationary (typically 5 to 10 minutes).

### **2.6.1 Tables**

Below, all of the experiments vital statistics are recorded detailing measurements of initial and well developed dominant pattern wavelengths.

Experimental data							
Expt. Name	Conc. $M/cm^3$	Depth $cm$	$k_0$ /dish	$k_\infty$ /dish	$\lambda_0$ $cm$	$\lambda_\infty$ $cm$	Notes
x108a	2.75	0.333	14.09	n/a	0.369	n/a	
x108b	2.07	0.396	10.71	n/a	0.486	n/a	
x108c	6.31	0.365	19.47	22.57	0.267	0.230	
x108d	3.06	0.444	11.10	17.30	0.468	0.301	
x114a	0.808	0.522	10.80	n/a	0.481	n/a	mixed modes
x114b	1.02	0.729	7.50	n/a	0.693	n/a	mixed modes
x114c	0.886	0.399	12.48	n/a	0.417	n/a	mixed modes
x117e	1.64	0.381	15.76	n/a	0.330	n/a	slow to develop
x117f	2.30	0.456	15.10	n/a	0.344	n/a	slow to develop
x117g	1.88	0.690	10.00	n/a	0.520	n/a	slow to develop
x120a	2.81	0.282	15.40	n/a	0.338	n/a	mixed modes
x120h	2.47	0.528	8.87	19.10	0.586	0.272	2 mixed modes, starts in centre
x120i	2.15	0.645	10.08	18.61	0.516	0.279	mixed modes, starts in centre
x208b	1.89	0.384	14.96	16.73	0.348	0.311	every 30 seconds
x208c	1.89	0.318	14.20	10.64	0.366	0.489	every 20 seconds
x208d	3.62	0.310	17.15	14.54	0.303	0.358	
x208j	1.89	0.469	07.34	17.18	0.708	0.303	2 peaks, L dominant
x208k	1.89	0.469	14.70	14.79	0.354	0.352	2 peaks, L dominant
x208l	1.89	0.469	08.63	15.62	0.603	0.333	2 peaks, R dominant
x208m	1.89	0.723	09.97	15.11	0.522	0.344	
x208n	1.89	0.384	15.12	15.67	0.344	0.332	
x209e	2.09	0.355	14.25	16.66	0.365	0.312	
continued.....							

Table 2.1: Table of experimental measurements where the subscript 0 means the first unstable mode to be measured and  $\infty$  means the final pattern mode. Wavenumbers (waves per width of dish) are indicated by  $k$  and the dimensional wavelength by  $\lambda$ . For the final pattern, n/a indicates that the images are not available.

### 2.6.2 Images

Here a selection of the experiments are displayed which have been chosen for their variety. Figure 2.9 describes the order in which the images appear.

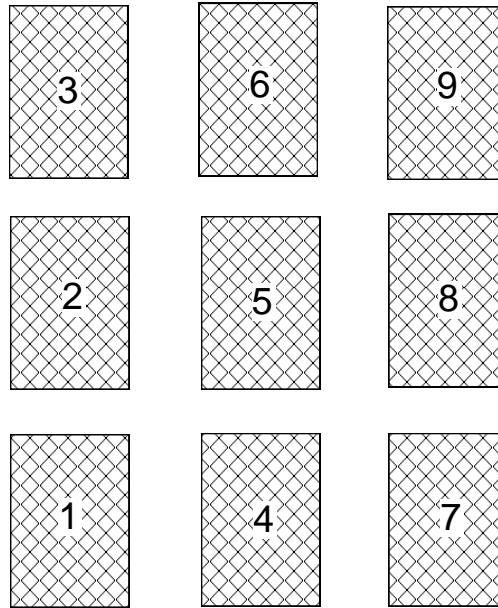


Figure 2.9: Key. Order in which images are recorded. Pictures taken one every 10 seconds unless otherwise stated.

## 2.7 Dominant wavenumber results

### 2.7.1 The initial disturbance

The suspension is initially well-mixed such that there is a uniform concentration profile. In general, an initial instability is apparent after 20 to 30 seconds and if the cells swim at  $50\mu\text{ms}^{-1}$  then they have only travelled 1 to  $1.5\text{mm}$  in this time. This may not be sufficient for the majority of cells to be involved in an overturning instability and they will not have had sufficient time to swim to the equilibrium solution, as assumed in the linear analysis of Chapter 3, in which vertical cell diffusion is balanced by the up swimming cells and there is no horizontal variation (the depths in the experiments generally being of the order of  $5\text{mm}$ ). A proportion of the cells may, however, have had enough time to aggregate at the top and initiate the overturning. In which case, the Rayleigh-Taylor instability is due to a reduced density gradient than that determined

Experimental data continued.....							
Name	Conc. $M/cm^3$	Depth $cm$	$k_0$ /dish	$k_\infty$ /dish	$\lambda_0$ $cm$	$\lambda_\infty$ $cm$	Notes
x215f	4.19	0.468	13.87	22.20	0.375	0.234	
x215g	4.19	0.291	17.26	20.62	0.301	0.252	
x215h	4.19	0.186	27.67	17.48	0.188	0.297	
y11i	4.30	0.282	19.66	22.52	0.264	0.231	
y11j	4.30	0.282	17.76	21.89	0.293	0.238	
y11k	4.30	0.282	15.75	24.19	0.330	0.215	
y11l	4.30	0.282	17.45	23.52	0.298	0.221	every 30 seconds
y12b	11.8	0.342	18.08	36.84	0.288	0.141	
y12c	4.00	0.297	16.71	28.03	0.311	0.186	
y12d	15.0	0.195	28.24	28.02	0.184	0.186	
y12e	11.8	0.118	34.84	32.95	0.149	0.158	
y12f	11.8	0.168	30.59	32.72	0.170	0.159	
y12m	3.60	0.324	15.71	17.30	0.331	0.301	
y12n	11.8	0.342	15.70	25.58	0.331	0.203	
y02i	4.30	0.228	23.09	34.15	0.225	0.152	
y02j	4.30	0.300	28.73	45.19	0.181	0.115	
y02k	4.30	0.300	29.86	43.05	0.174	0.121	every 30 seconds

Table 2.2: Table of experimental measurements (continued) where the subscript 0 means the first unstable mode to be measured and  $\infty$  means the final pattern mode. Wavenumbers are indicated by  $k$  and the dimensional wavelength by  $\lambda$ . For the final pattern, n/a indicates that the images are not available.

name	initial pattern	final pattern
x108a	$D$	$D_H$
x108b	$X$	$D/L$
x108c	$X$	$D$
x108d	$L$	$D$
x114a	$D$	$D$
x114b	$L$	$D$
x114c	$D$	$D$
x117e	$D$	$L/D$
x117f	$X$	$D$
x117g	$X$	$X$
x120a	$D$	$D$
x120h	$M$	$D$
x120i	$M$	$D$
x208b	$D_T$	$D$
x208c	$D_T$	$D$
x208d	$D$	$M$
x208j	$X$	$D$
x208k	$D/L$	$D$
x208l	$L$	$D$
x208m	$X$	$D_H$
x208n	$D_T$	$D$
x209e	$X$	$D_H$

Table 2.3: Experimental initial and final patterns observed. The types of patterns are indicated by  $D$  = dots,  $L$  = lines,  $X$  =dots joined by lines in  $X$  or  $Y$  shapes and  $M$  = mixed. The subscript  $T$  means that the pattern evolves through a torus stage and the subscripts  $H$  and  $S$  mean clear evidence of hexagonal or square arrays respectively.

name	initial pattern	final pattern
x215f	$L$	$D/L$
x215g	$X_T$	$D/L$
x215h	$D_T$	$D+$ empty
y02i	$X$	$D_H$
y02j	$X$	$D_H$
y02k	$X$	$D_H$
y11i	$X$	$D_H$
y11j	$X$	$D_H$
y11k	$X$	$D_H$
y11l	$X$	$D_H$
y12b	$M$	$D_S$
y12c	$M$	$D_H$
y12d	$M$	$D$
y12e	$M_T$	$D$
y12f	$M_T$	$D$
y12m	$X$	$D_H$
y12n	$M$	$D$

Table 2.4: Experimental initial and final patterns observed. Continued....

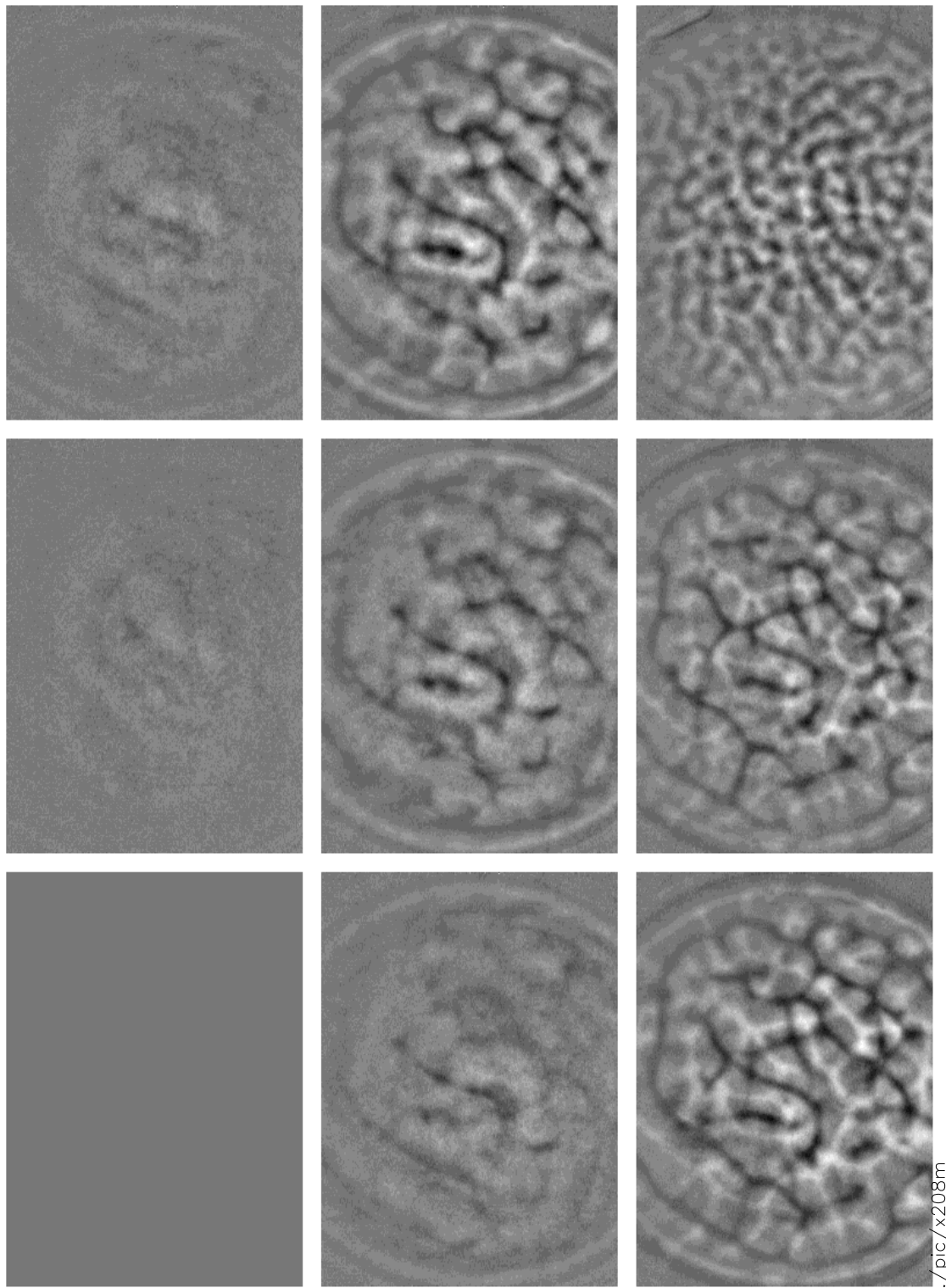


Figure 2.10: Experiment number x208m. Concentration =  $1.89 \times 10^6 \text{ cm}^{-3}$ , depth =  $7.23 \text{ mm}$ . Pictures taken one every 10 seconds.

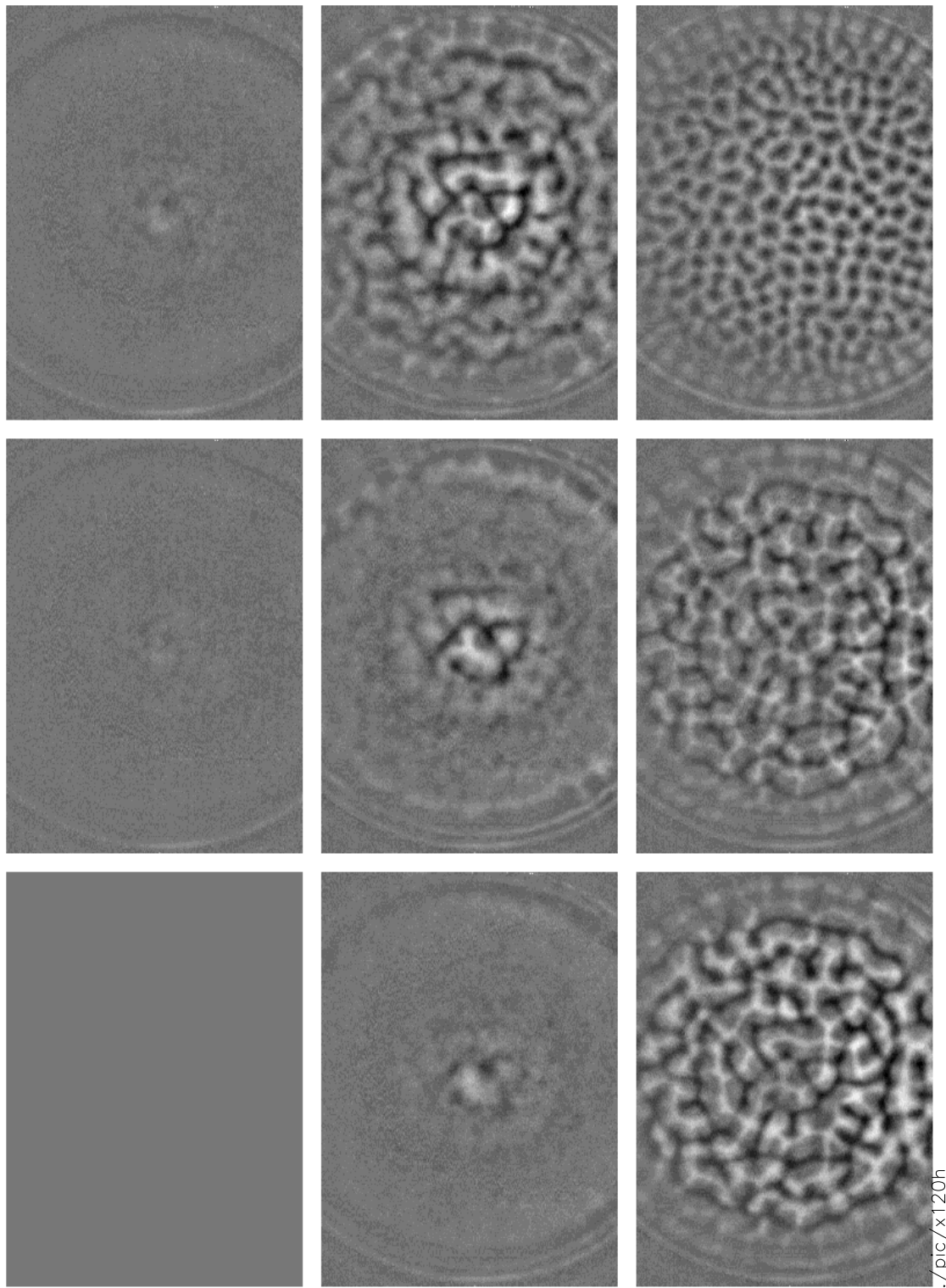


Figure 2.11: Experiment number x120h. Concentration =  $2.47 \times 10^6 \text{ cm}^{-3}$ , depth =  $5.28 \text{ mm}$ . Pictures taken one every 10 seconds.

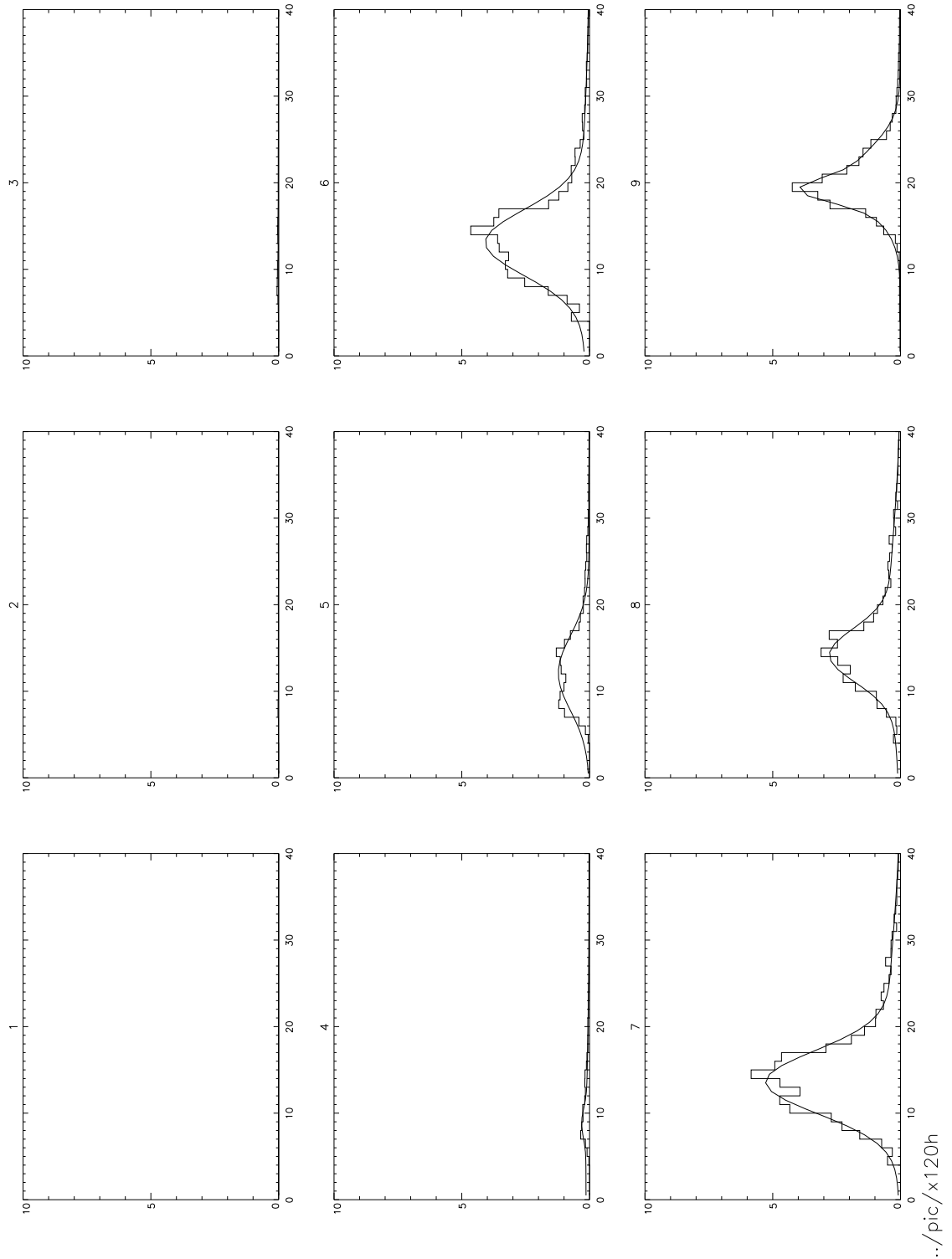


Figure 2.12: Experiment number x120h. Fourier spectra of images. Horizontal axis is wavenumber and vertical axis is Fourier density. Concentration =  $2.47 \times 10^6 \text{ cm}^{-3}$ , depth =  $5.28 \text{ mm}$ . Pictures taken one every 10 seconds.

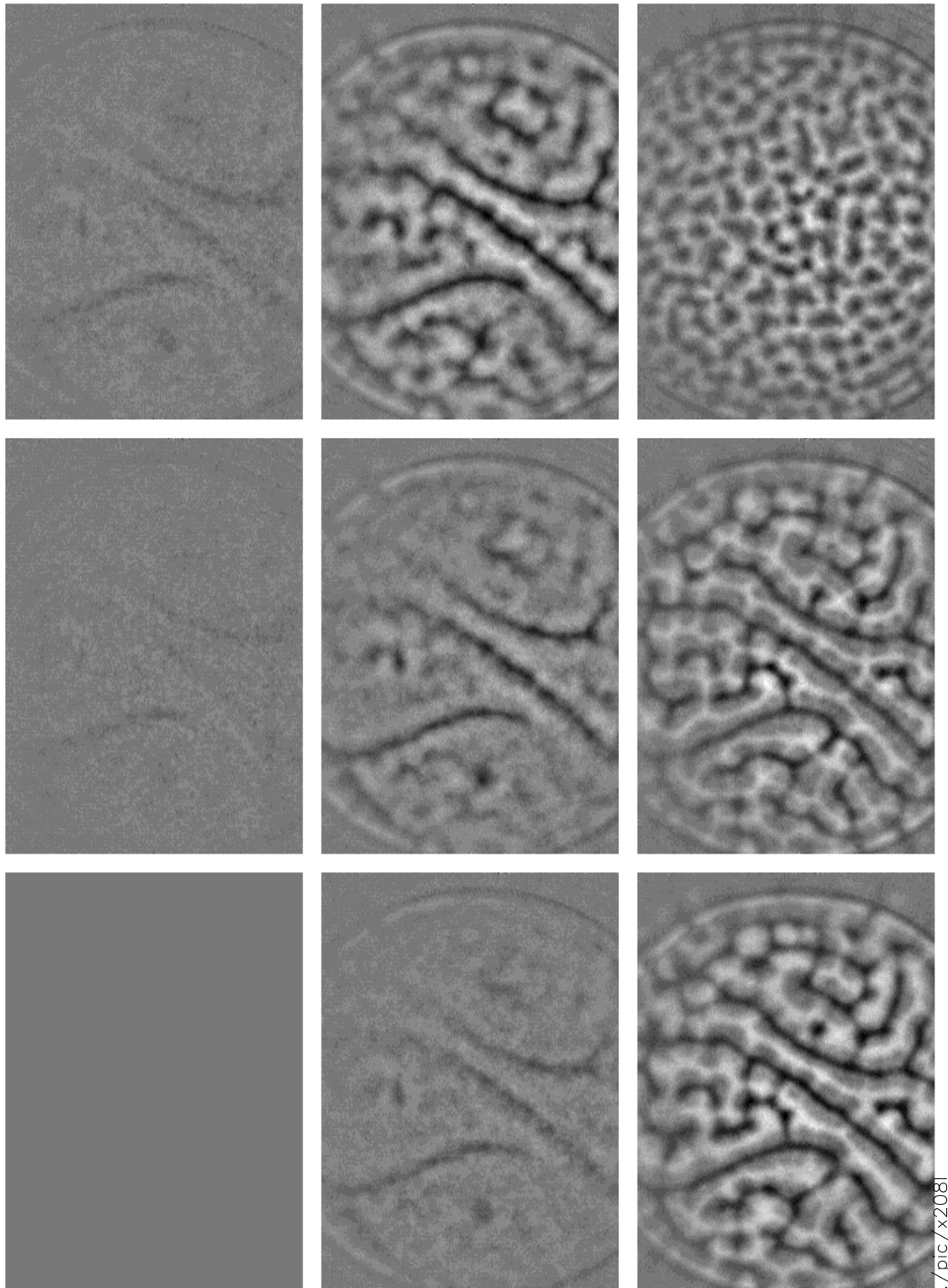


Figure 2.13: Experiment number x208l. Concentration =  $1.89 \times 10^6 \text{cm}^{-3}$ , depth =  $4.69 \text{mm}$ . Pictures taken one every 10 seconds.

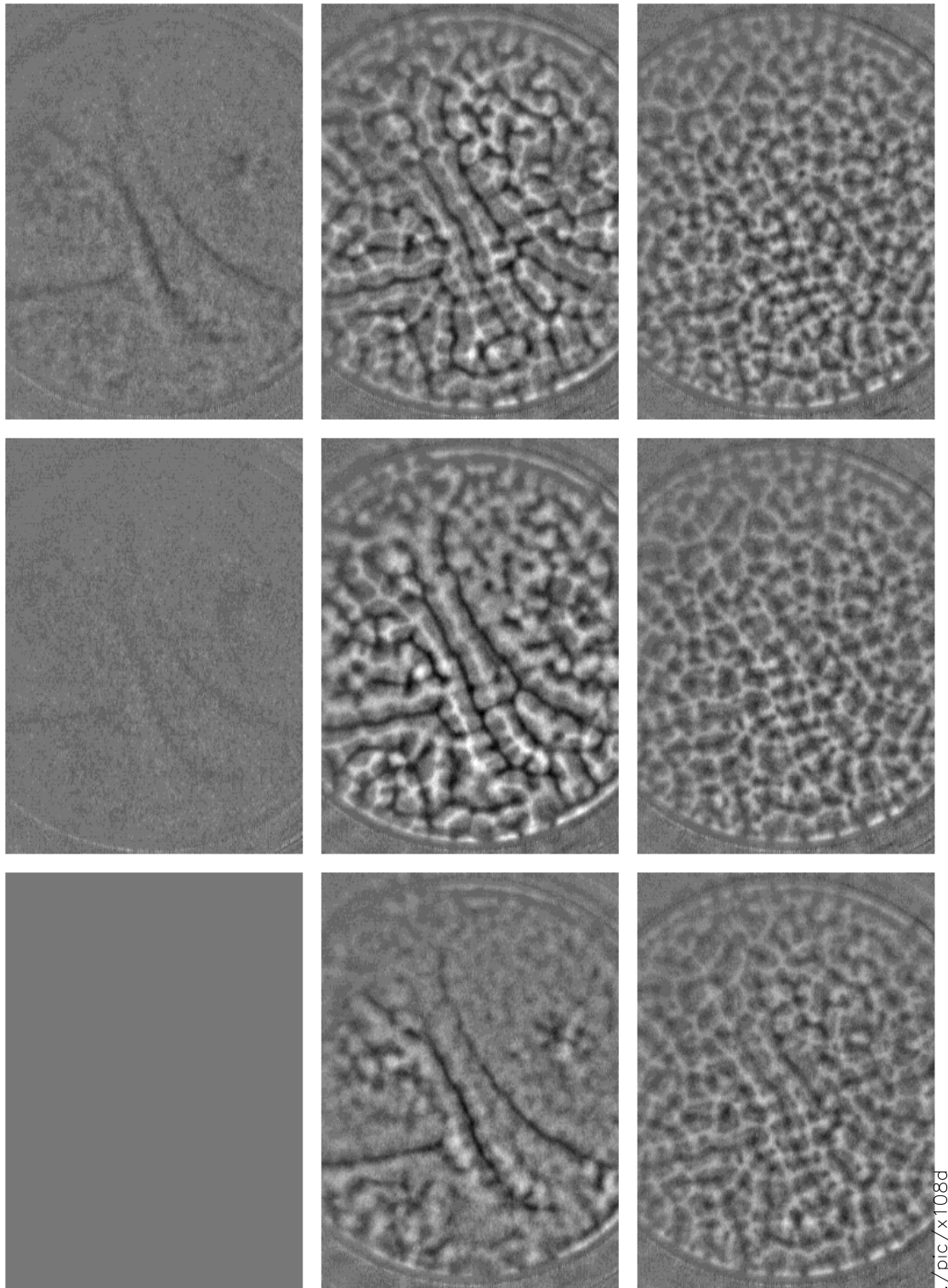


Figure 2.14: Experiment number x108d. Concentration =  $3.06 \times 10^6 \text{ cm}^{-3}$ , depth =  $4.44 \text{ mm}$ . Pictures taken one every 10 seconds.

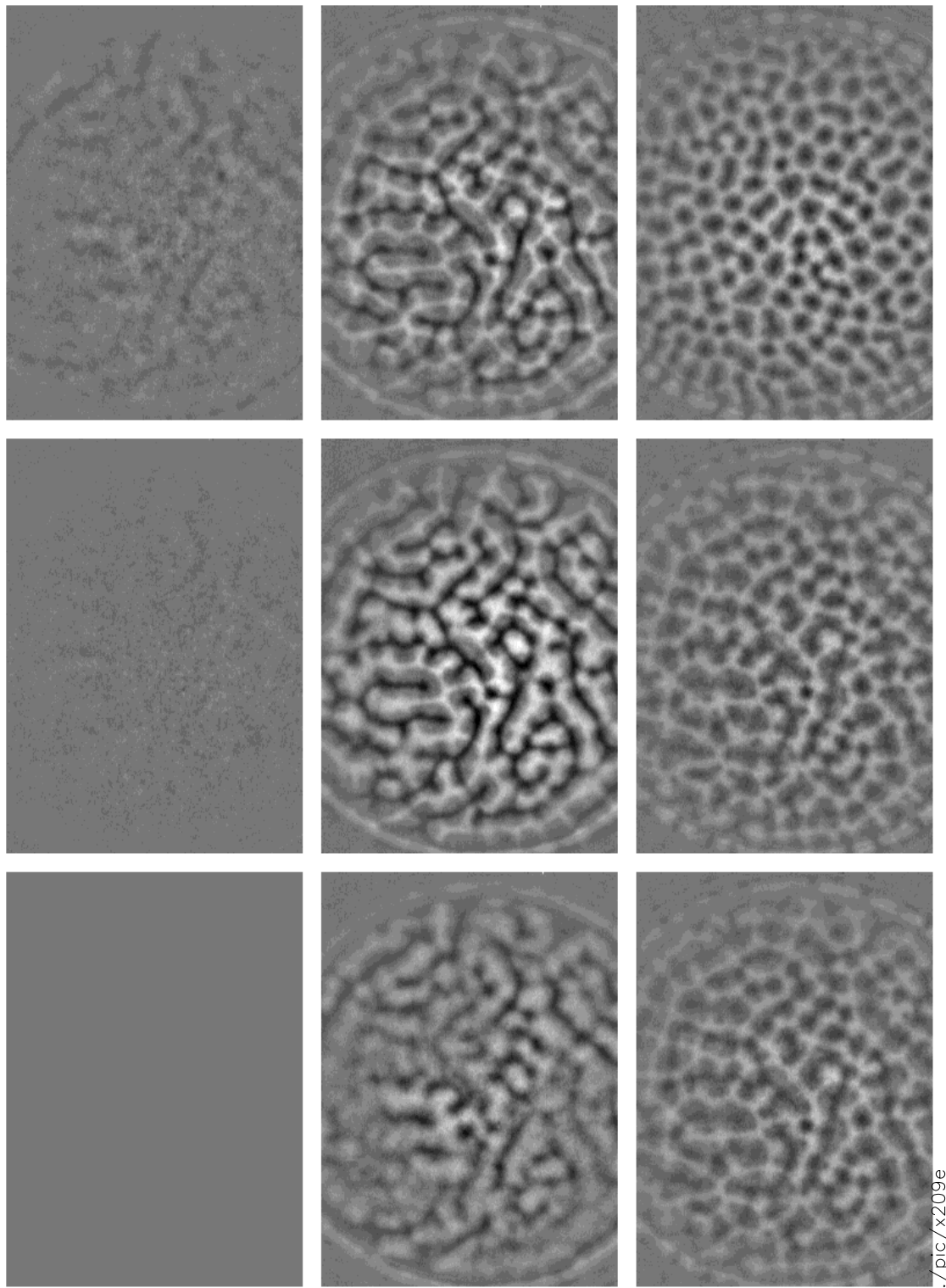


Figure 2.15: Experiment number x209e. Concentration =  $2.09 \times 10^6 \text{ cm}^{-3}$ , depth =  $3.55 \text{ mm}$ . Pictures taken one every 10 seconds.

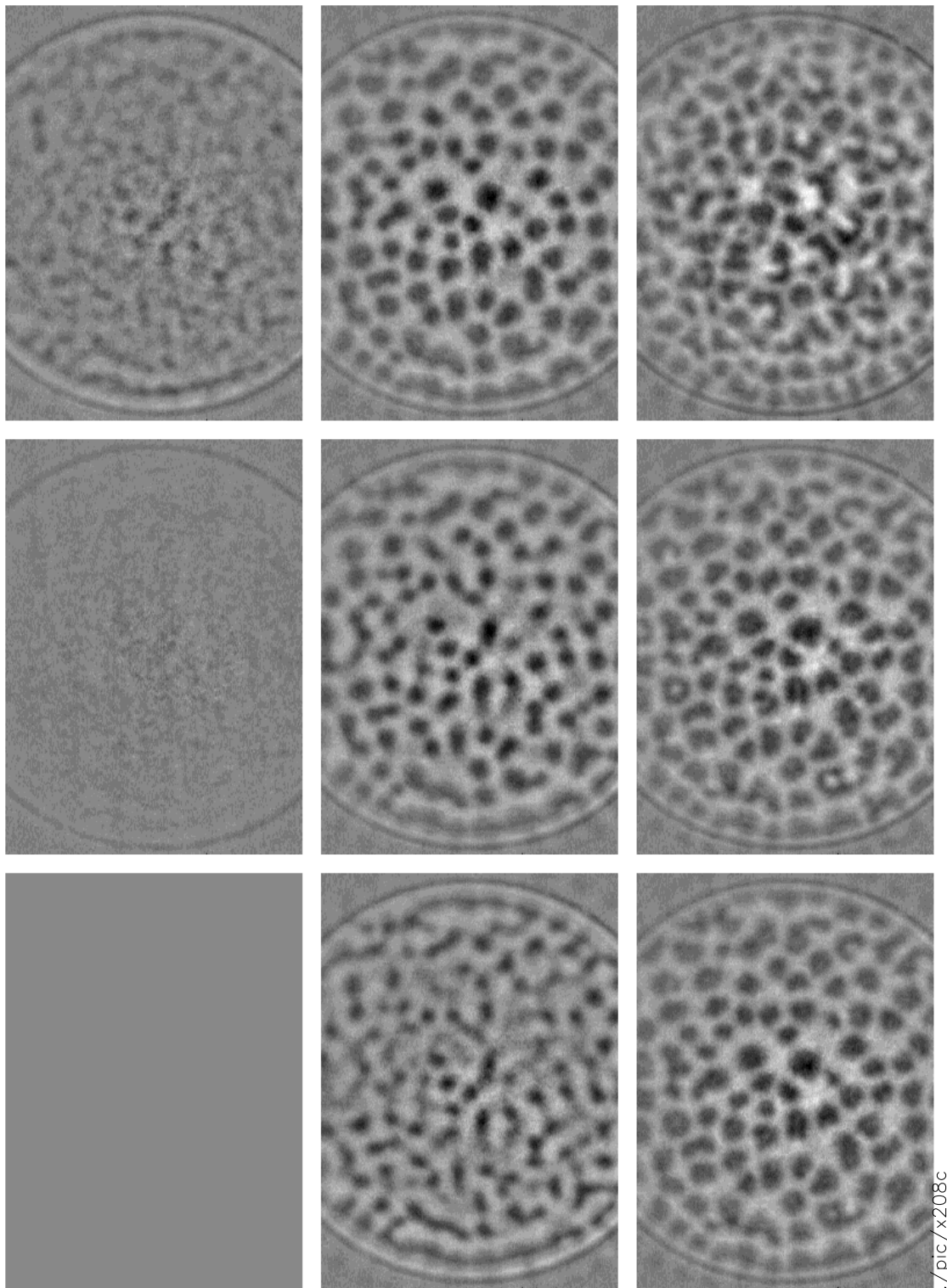


Figure 2.16: Experiment number x208c. Concentration =  $1.89 \times 10^6 \text{ cm}^{-3}$ , depth =  $3.18 \text{ mm}$ . Pictures taken one every 20 seconds.

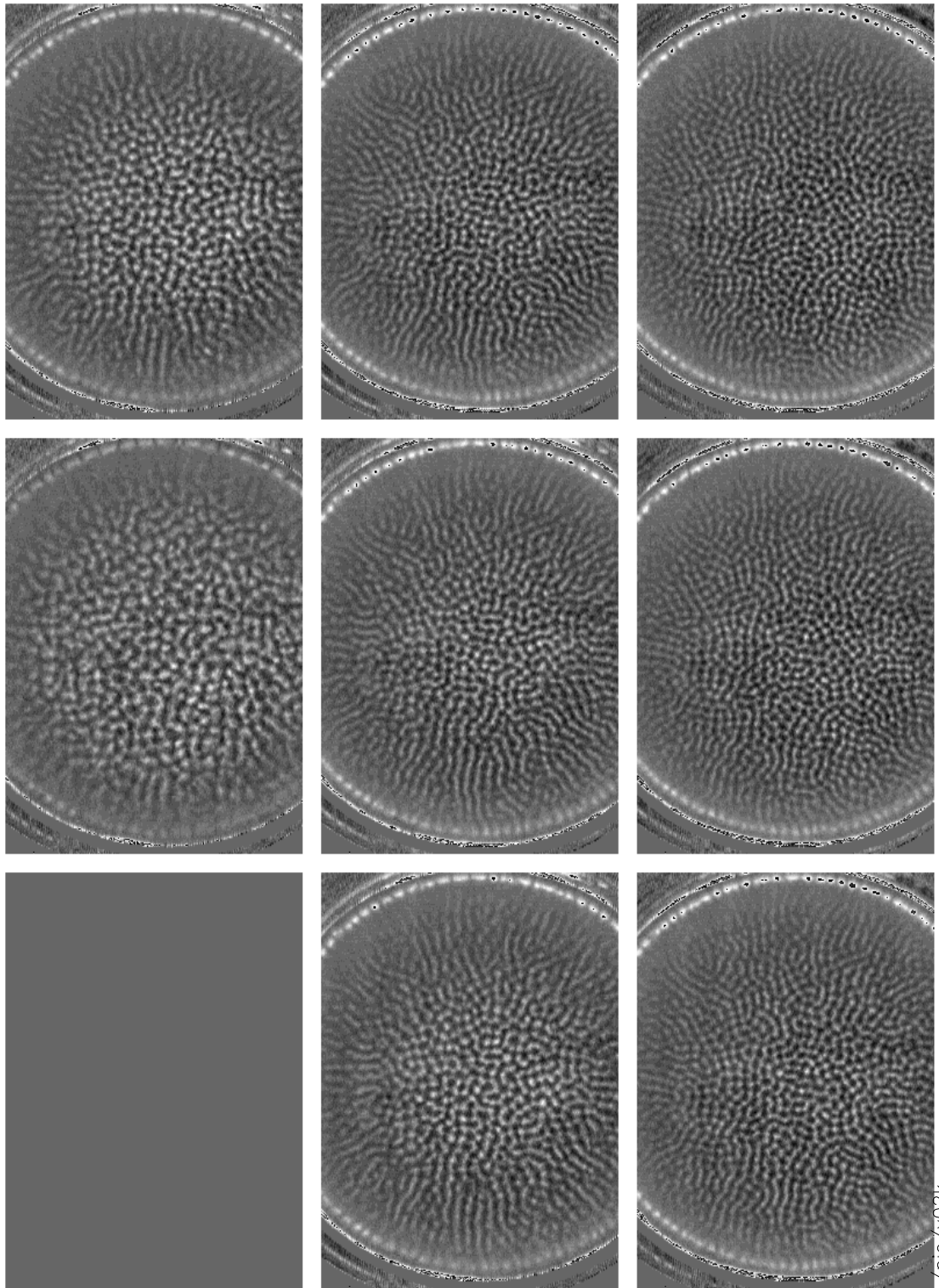


Figure 2.17: Experiment number y02k. Concentration =  $12.2 \times 10^6 \text{ cm}^{-3}$ , depth =  $3.00 \text{ mm}$ . Pictures taken one every 30 seconds.

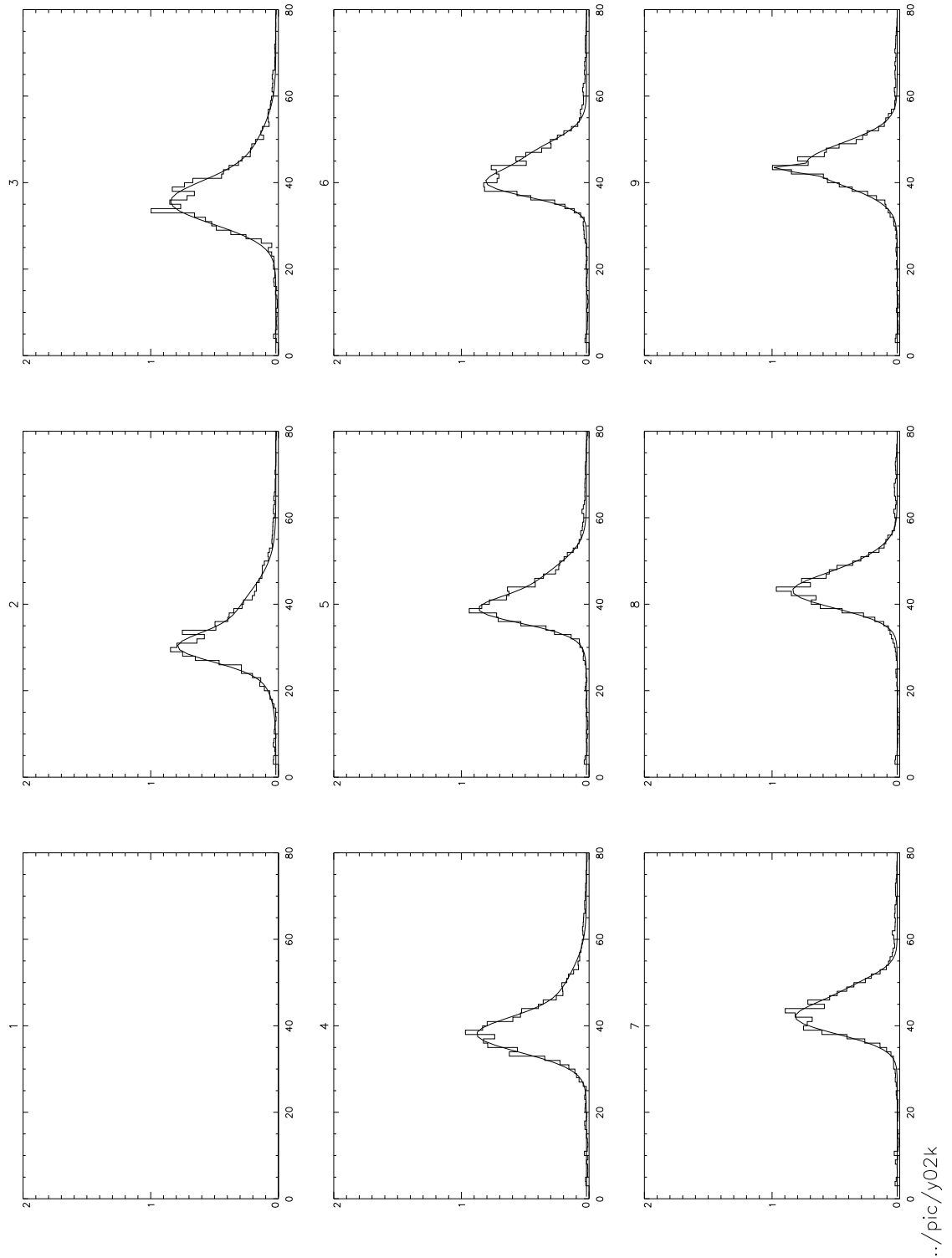


Figure 2.18: Experiment number y02k. Fourier spectra of images. Horizontal axis is wavenumber and vertical axis is Fourier density. Concentration =  $12.2 \times 10^6 \text{ cm}^{-3}$ , depth =  $3.00 \text{ mm}$ . Pictures taken one every 10 seconds.

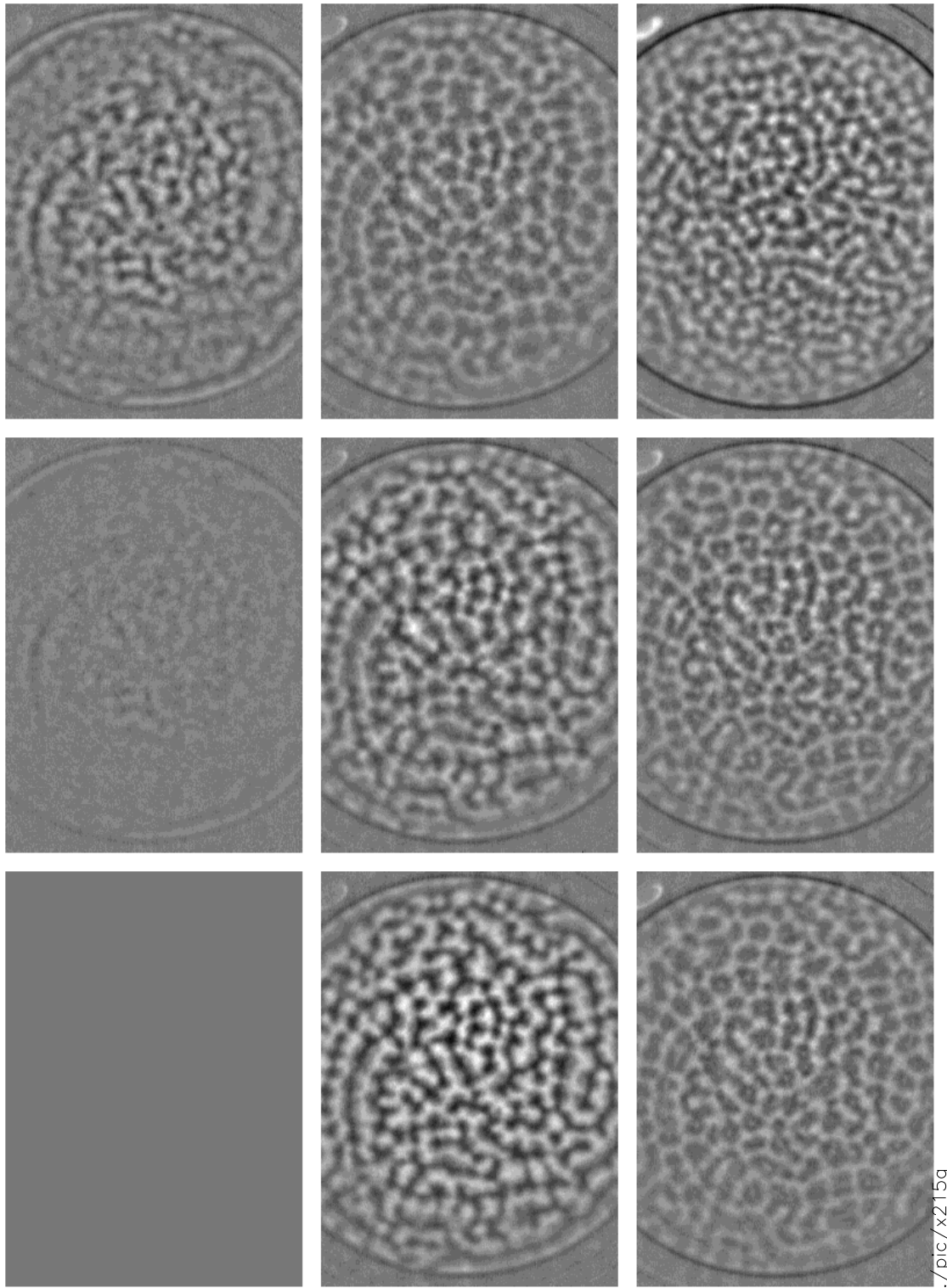


Figure 2.19: Experiment number x215g. Concentration =  $4.19 \times 10^6 \text{cm}^{-3}$ , depth =  $2.91 \text{mm}$ . Pictures taken one every 10 seconds.

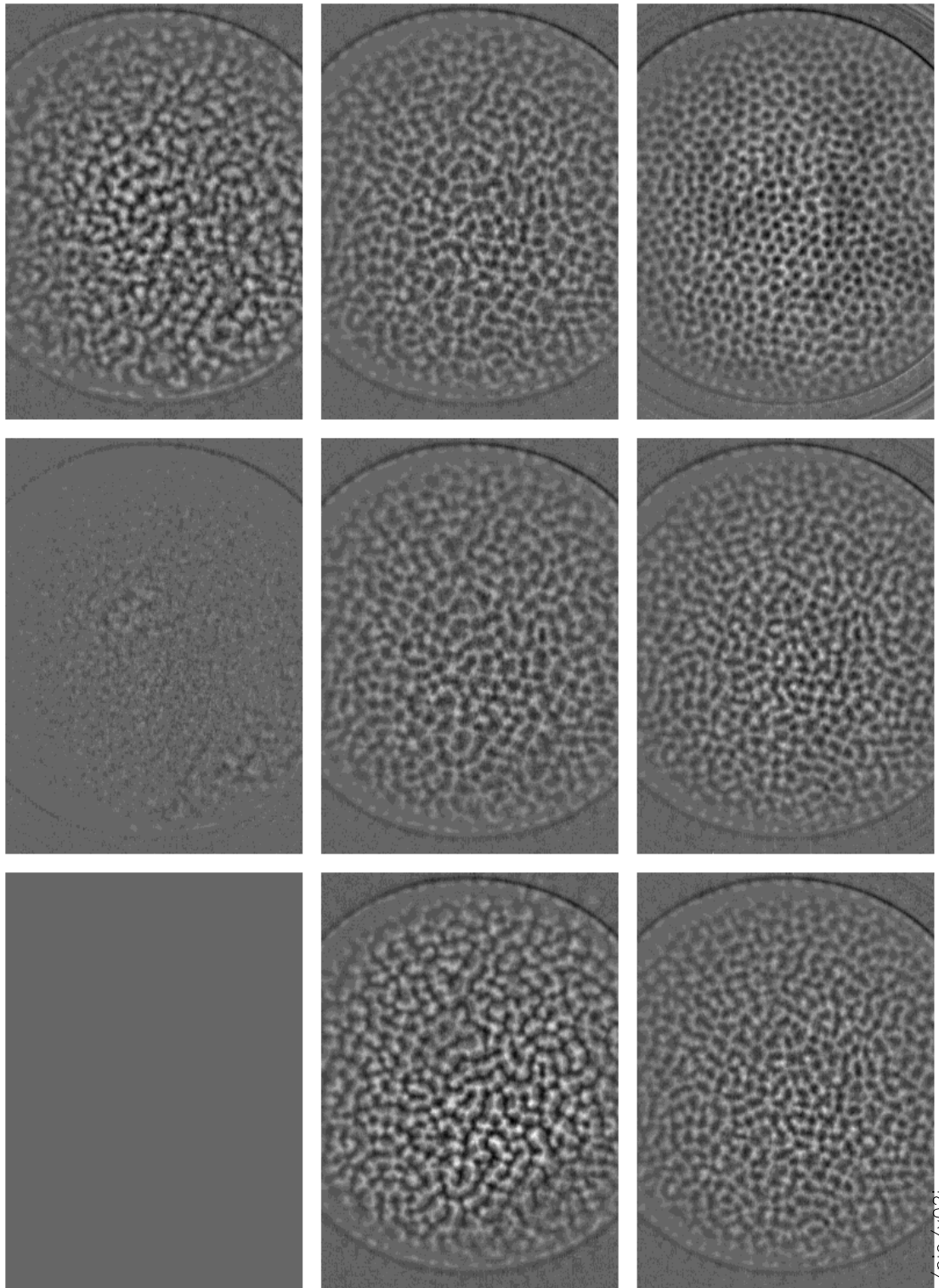


Figure 2.20: Experiment number y02i. Concentration =  $4.6 \times 10^6 \text{ cm}^{-3}$ , depth =  $2.28 \text{ mm}$ . Pictures taken one every 10 seconds.



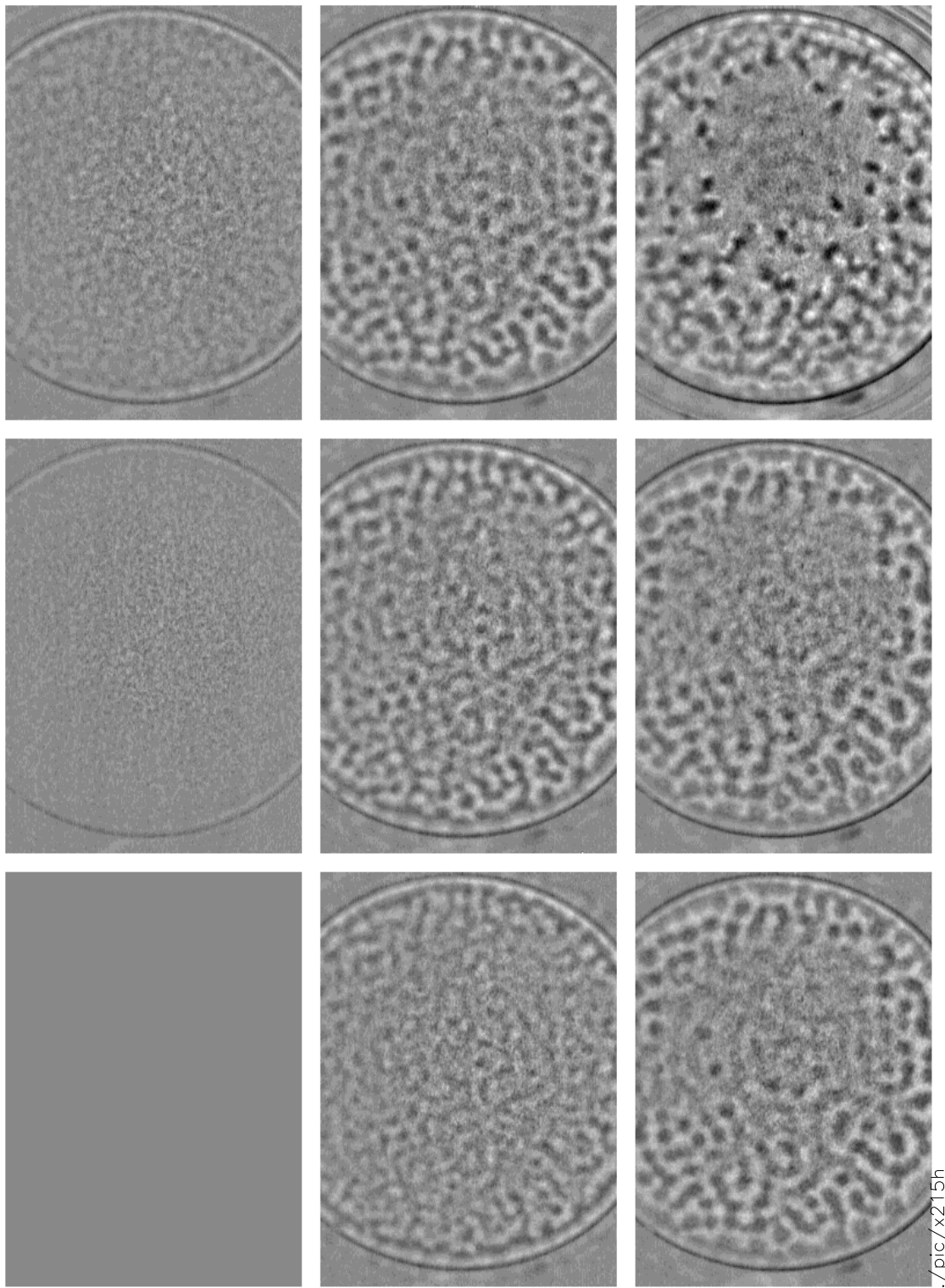


Figure 2.22: Experiment number x215h. Concentration =  $4.19 \times 10^6 \text{ cm}^{-3}$ , depth =  $1.86 \text{ mm}$ . Pictures taken one every 10 seconds.

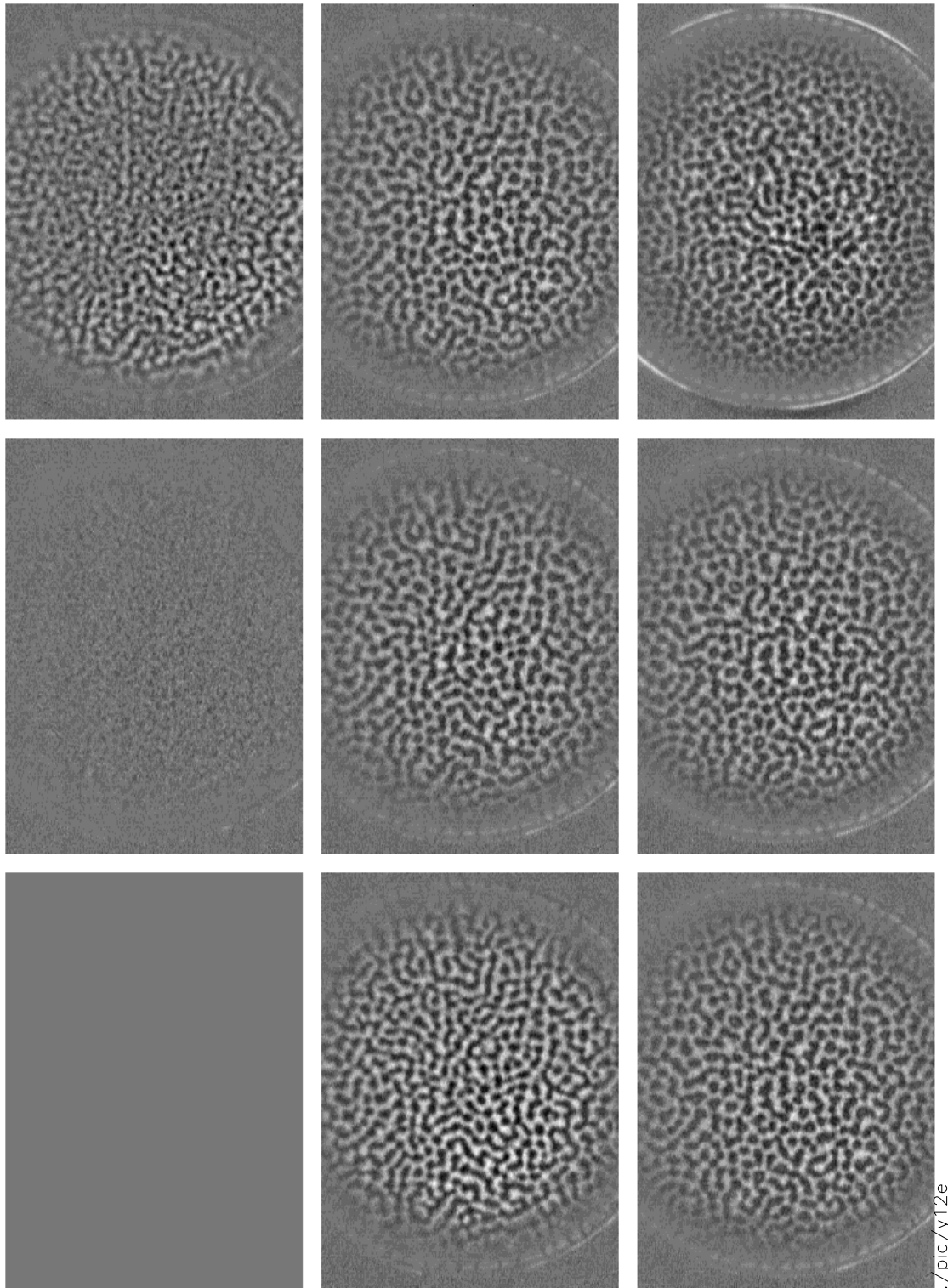


Figure 2.23: Experiment number y12e. Concentration =  $11.8 \times 10^6 \text{ cm}^{-3}$ , depth =  $1.18 \text{ mm}$ . Pictures taken one every 10 seconds.

from the exponential distribution of Chapter 3. Alternatively, the observed initial instability may be a gyrotactic instability (or perhaps a combination of both). Thus, it is difficult to isolate the mechanisms involved in the initial disturbance.

The wavenumber,  $k$ , is related to a physical wavelength by

$$\lambda = \frac{I_w}{k}, \quad (2.10)$$

where  $I_w$  is the image width and equals  $5.2\text{cm}$ . Figure (2.24) describes how the first observation of a most unstable wavelength varies with concentration and suspension. The diameter of the circle is proportional to the wavelength and the centre of the circle indicates its position in parameter space. In general the wavelength increases with

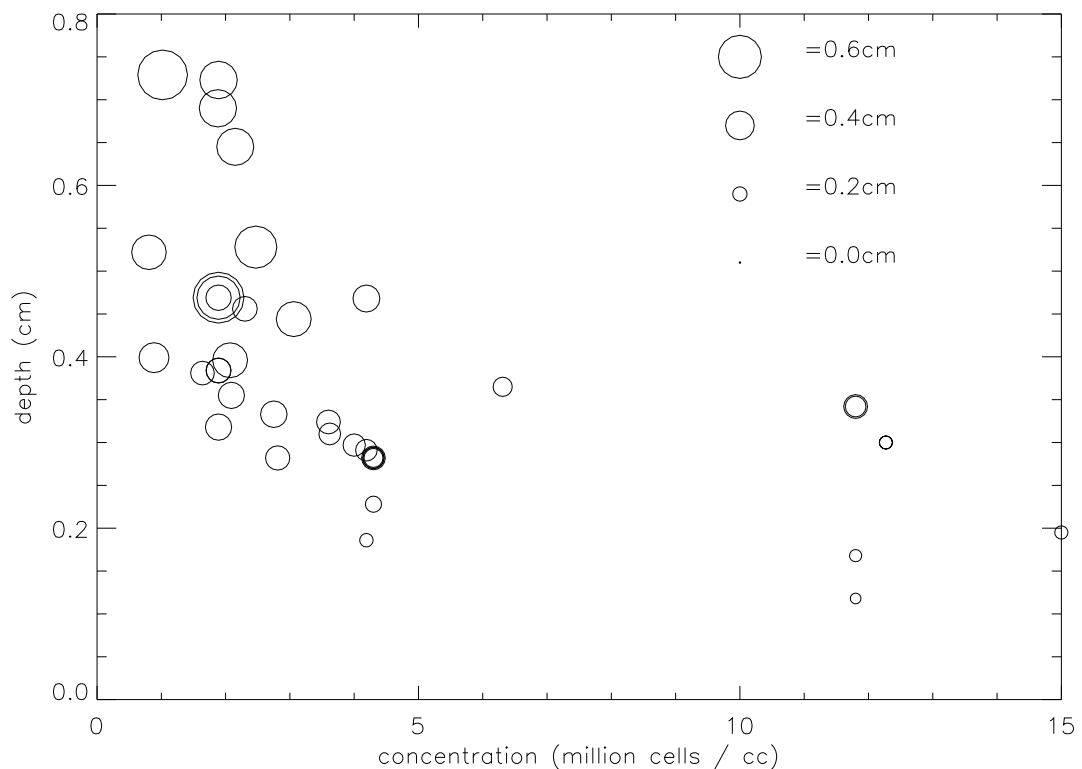


Figure 2.24: Dominant wavelengths of the initial disturbance from a fully mixed suspension of *Chlamydomonas nivalis* against concentration and suspension depth. The diameter of the circles represent the most unstable wavelength measured on a continuous scale in  $cm$ .

depth and decreases very slowly with concentration. The patterns have been grouped into four groups and Figure (2.25) shows how the pattern varies with concentration and depth. There are a number of regions in the concentration/depth parameter space

that require further explanation. The region  $M$  described in Figure (2.25) displays acute sensitivity to the initial conditions. However carefully the suspension is mixed there will always be some coherent fluid motion. Depending on the nature of this motion the initial pattern will either develop as dots or lines. In terms of the Fourier spectrum, there is a range of equally unstable wavelengths and, depending on the initial conditions, any can dominate the pattern. However, the well developed pattern appears to be free of any such degeneracy.

### 2.7.2 The well developed pattern

It is difficult to decide when in fact the well developed pattern occurs. In many cases the pattern tends towards a regular array of dots but in other cases either no regular pattern exists or no long term pattern is visible at all! Indeed, after 24 hours either an exceedingly regular pattern emerges or the cells are stuck together at the bottom. It is not always necessary to wait 24 hours and the impatient investigator need only wait 5 to 10 minutes before the pattern reaches a stage where there is very little or no further variation. As mentioned previously 8 images were recorded at 10 second intervals and a long term image recorded after about 5 minutes. The dominant wavenumber analysis was performed and the results are displayed in Figure (2.26) where the dominant wavenumber is plotted against depth and concentration. The results vary significantly from the initial disturbance in that the wavelength decreases with concentration and there is no significant change with depth. Certainly the well developed pattern is independent of the initial conditions and Figure (2.26) is much smoother than Figure (2.24). A clear difference occurs in the shape of the Fourier spectra of the initial and well developed patterns. The initial patterns' Fourier spectra contain harmonics and competing unstable wavenumbers whereas the final patterns Fourier spectra contain just one unstable wavenumber as the patterns are generally characterised by a regular array of dots. This can clearly be seen in Figure (2.11), where it is also obvious that the pattern wavenumber has increased with time. In some situations of very low concentration and small depth it was observed (but not recorded) that although an initial instability occurred, long time patterns were not visible. At the time these patterns were not sufficiently repeatable to warrant recording and the cells appeared to stick to the walls of the dish soon after. There are a number of possible explanations. One is that the cells

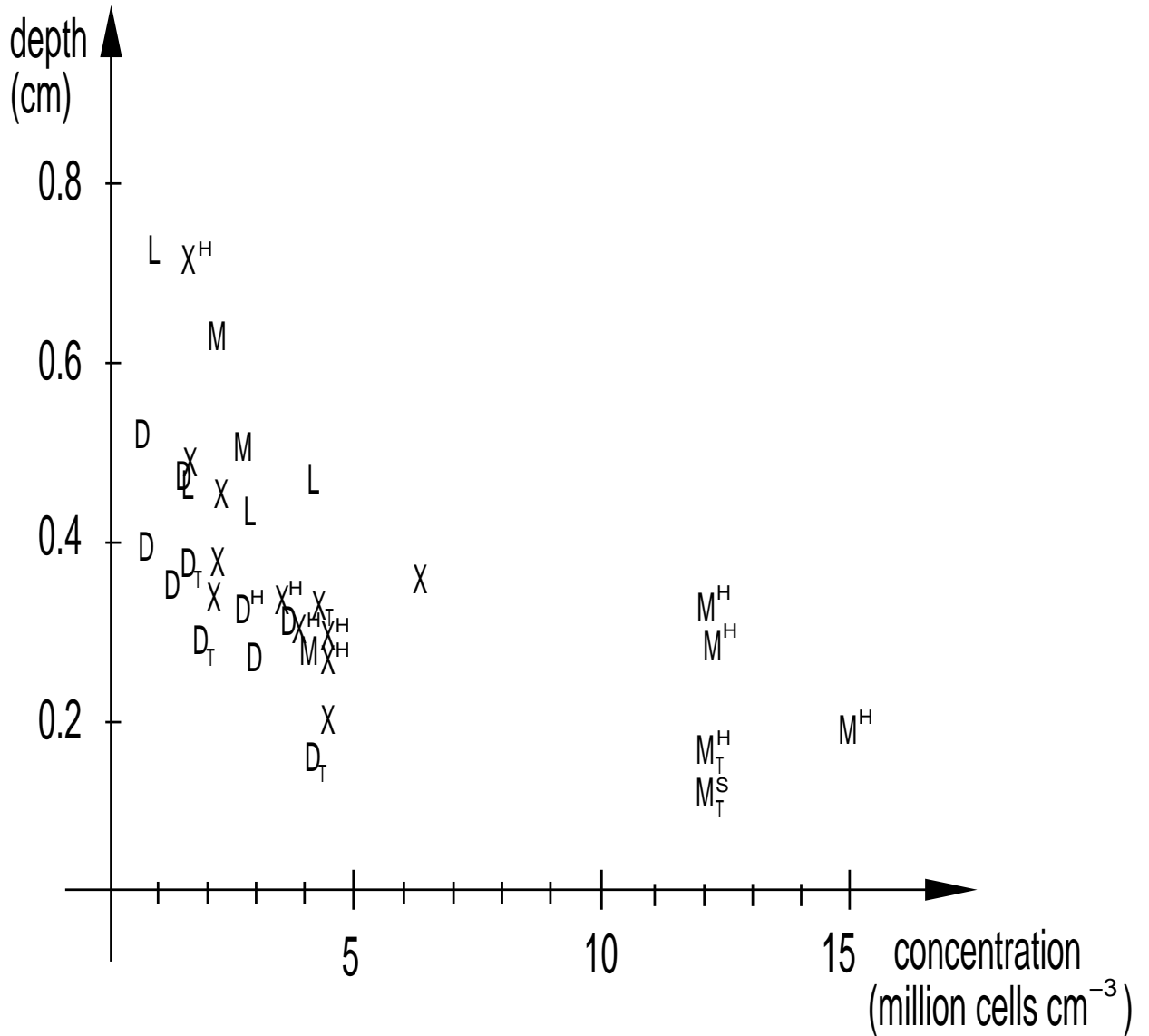


Figure 2.25: Pattern type of the initial disturbance from a fully mixed suspension of *Chlamydomonas nivalis* against concentration and suspension depth. The regions correspond to the dominant pattern present where  $D$  = dots,  $L$  = lines,  $X$  = dots joined by lines in  $X$  or  $Y$  shapes and  $M$  = mixed. The subscript  $T$  means that the pattern evolves through a torus stage and the subscripts  $H$  and  $S$  mean clear evidence of hexagonal or square arrays respectively.

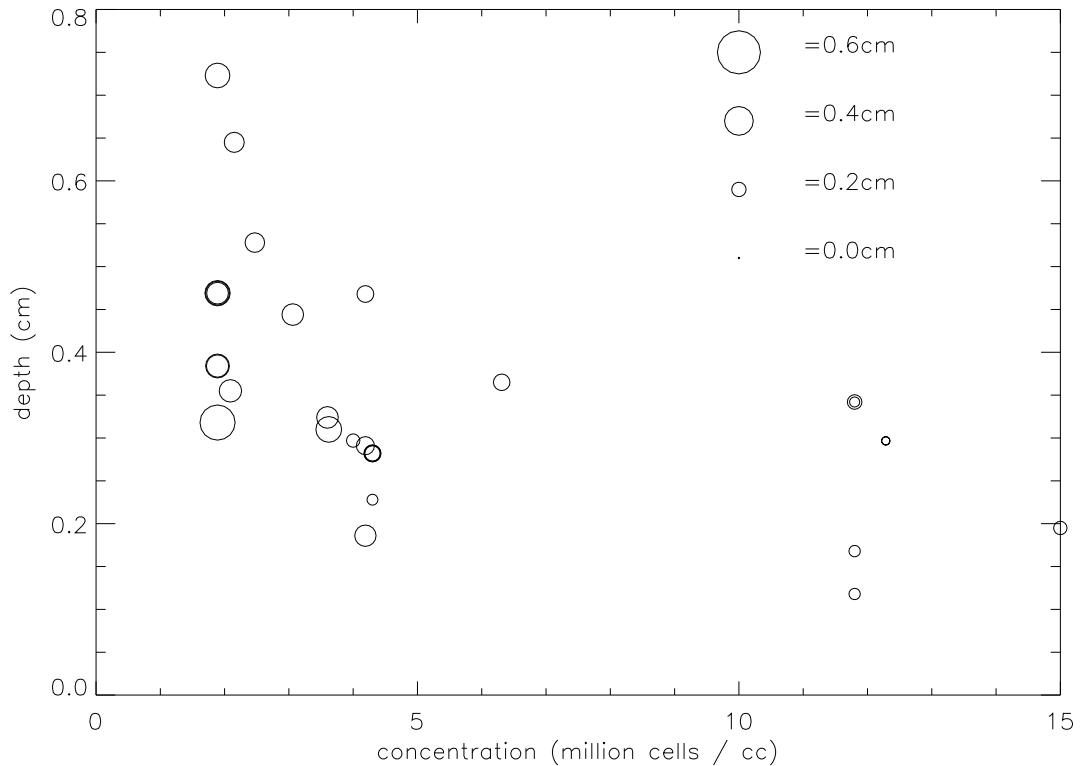


Figure 2.26: Dominant wavelengths of the final observed pattern in a suspension of *Chlamydomonas nivalis* against concentration and suspension depth. The diameter of the circles represent the most unstable wavelength measured on a continuous scale in *cm*. The dots represent experiments performed where a final pattern was not recorded.

were separated during mixing, swam to the top and promptly stuck together and sank. Alternatively the cells could have been fully independently motile but of insufficient concentration to set up long term bioconvection patterns but may instead have set up a stable vertical concentration gradient. Irregular long time patterns are also hard to interpret but, by considering the Fourier spectra, appear to be time dependent mode interactions of two or more modes.

### 2.7.3 Transitional mode interaction

Although we have seen that the wavenumber,  $k$ , increases from the initial instability to the final steady state, it does not always do so monotonically. Figure (2.27) shows three identical experiments performed within ten minutes of each other in a region of parameter space where the patterns are sensitive to the initial conditions. Exper-

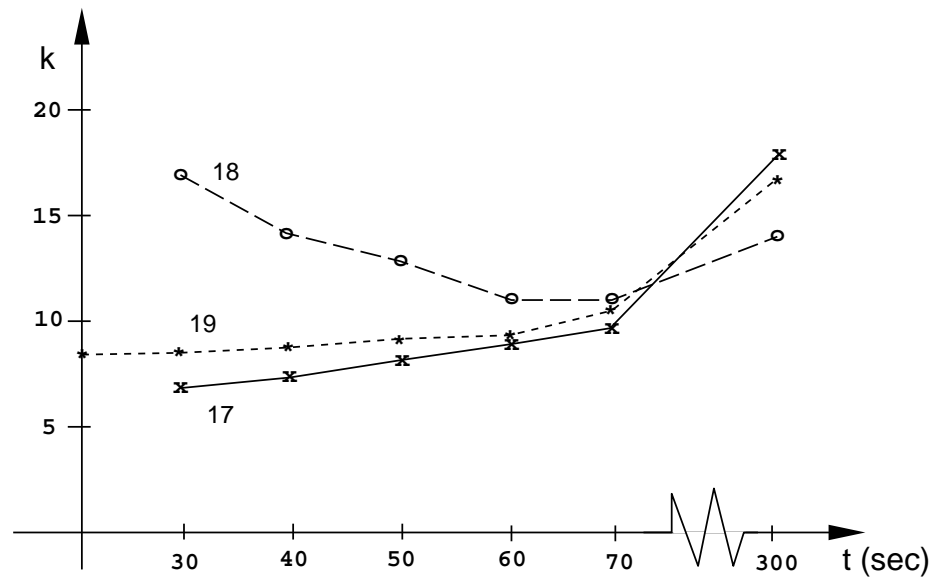


Figure 2.27: How the dominant pattern wavenumber varies with time. Three identical experiments where the initial instability is highly dependent on the initial conditions.

iment x208j was performed between the other two. It was observed that the initial instability was dependent on the type of mixing that was used beforehand even though care was taken not to set up any bulk fluid motion and whatever motion was present died away in under a couple of seconds. Whatever the initial instability the patterns evolved towards the same long term state. Figure (2.28) is a typical example of how a pattern's Fourier spectrum evolves with time. One of the first observations to be made concerns the oscillatory nature of the amplitude of the Fourier spectrum. The initial instability quickly increases in size until it hits the bottom of the dish and the cells then have to swim back up to the surface. During this period the amplitude of the unstable mode decreases. Any new instability that occurs must exist on top of the recently set up fluid motion and, in this respect, the patterns that occur have a discrete set of wavelengths. The overall amplitude of the Fourier spectrum is seen to increase when this new instability occurs. It can clearly be seen that the initial instability is composed of distinct competing wavenumbers and as time progresses shorter and shorter wavelengths become unstable. It is also apparent when viewing the bargraphs in Figure (2.12) that each new shorter wavelength that becomes unstable does so at the expense of the the previous most unstable wavelength. Figure (2.29a) shows how the wavenumber increases as opposed to a continuous increase in Figure (2.29b). These

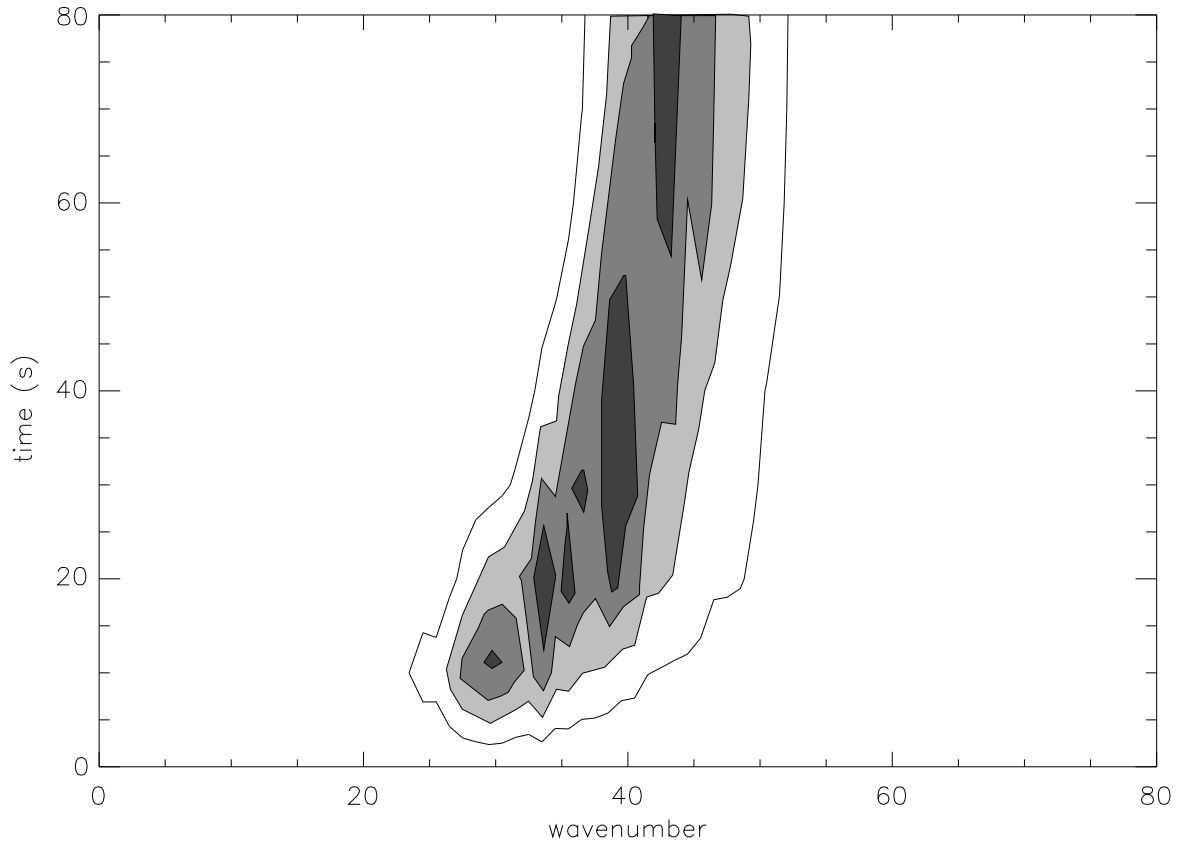


Figure 2.28: A contour plot of the Fourier spectrum of experiment y02k varying with time. Different modes generally become unstable to modes of larger wavenumber.

Fourier spectra become clearer when they are contrasted with the images. In general, the first instability to occur tends to be sheets or lines when viewed from above. (Although dots are also quite common.) The sheet instability generally becomes unstable to a dot type instability or sometimes to something resembling a lattice of nodes joined by lines. These patterns further break down into smaller dots or other connected patterns. So, in general, two dimensional patterns become unstable to three dimensional patterns. But what occurs between the initial instability and the long time pattern is a complicated set of mode interactions. For example, tori can be formed as seen in Figure (2.30). Initially the suspension is well mixed and the cells are able to swim to the top (before any instability forms) thus initiating a Rayleigh-Bénard type instability. The initial disturbance is generally two dimensional and in the form of descending sheets of concentrated suspension (bioconvection rolls). This quickly breaks down to a three dimensional instability of descending plumes. As a plume hits the bottom of the

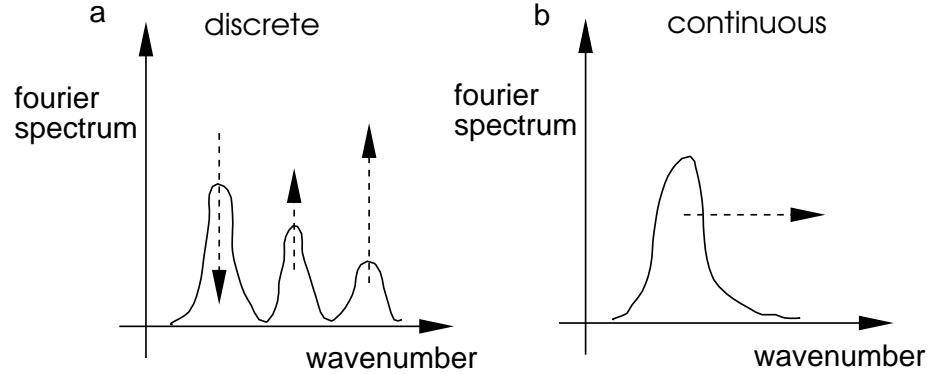


Figure 2.29: Unstable wavenumbers varying with time. a) a discretely varying dominant wavenumber. b) a continuously varying dominant wavenumber.

dish it spreads out entraining clear fluid in its wake at the upper surface. It is when the clear fluid reaches the bottom of the dish that the ring vortex can be clearly seen as an annulus when view from above. The annulus increases its diameter and forms a *closed* bioconvection roll. Eventually this two dimensional rotationally invariant roll becomes unstable to three dimensional plumes. Figure (2.31) illustrates this possible process as a cartoon viewed from above. This is only one possibility and the final pattern could be produced by different mechanisms. Nonetheless, this possibility has been seen to occur and annuli can be observed in Figure (2.20) eventually breaking up into dots. Another mechanism that has been noticed is where a dot becomes elongated and breaks up into two smaller dots. By comparing the three pictures for each independent experiment given in Section (2.6) it is possible to track the unstable wavelengths and see how they vary with time in relation to the type of pattern present.

## 2.8 A measure of pattern

Here a measure of pattern will be proposed that distinguishes between a dot pattern and a line pattern. First, we associate the image intensity,  $z(x, y)$ , with the smooth surface

$$\mathbf{r}(x, y) = (x, y, z(x, y)) \quad (2.11)$$

embedded in Euclidean three-space. The key to the following argument is that by using bending alone one can recreate the line (or ridge in our new geometry) pattern from a plane. This is not so with the dot (or hill) pattern which requires some stretching of

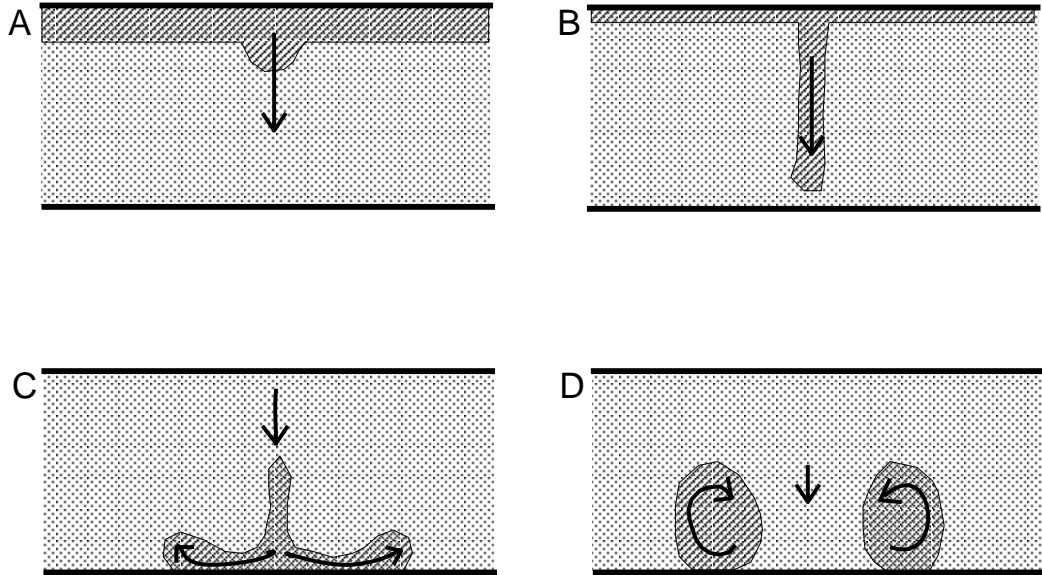


Figure 2.30: A sketch to illustrate how clear fluid can be entrained in a plume and an annulus pattern can be formed when viewed from above. a) cells swim up to the top and overturn due to a Rayleigh-Taylor instability. b) gyrotaxis produces thin plumes. c) the plumes hit the bottom of the dish and spread out forming a ring vortex. d) clear fluid is entrained in the wake of the plume and an annulus is set up.

the plane as well as bending (see Figure 2.32). It is this combination of bending and stretching that we shall measure. Consider the tangent space at a point on the surface that is spanned by the vectors

$$\mathbf{r}_x = (1, 0, z_x) \quad (2.12)$$

and

$$\mathbf{r}_y = (0, 1, z_y). \quad (2.13)$$

The “first fundamental form” describes length and area (do Carmo 1976 [29]) and is defined as

$$ds^2 = E dx^2 + 2F dx dy + G dy^2 \quad (2.14)$$

where

$$E = \mathbf{r}_x \cdot \mathbf{r}_x, \quad (2.15)$$

$$F = \mathbf{r}_x \cdot \mathbf{r}_y \quad (2.16)$$

and

$$G = \mathbf{r}_y \cdot \mathbf{r}_y. \quad (2.17)$$

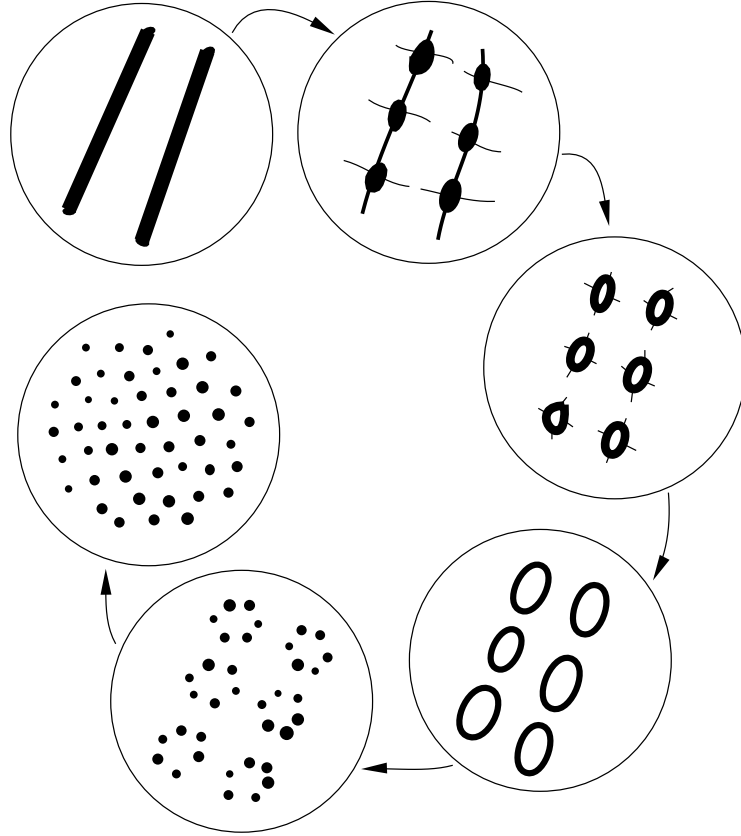


Figure 2.31: Possible mode interactions. Patterns can become unstable to other new modes. In particular, two dimensional patterns can become unstable to three dimensional patterns. These dot patterns can form annuli. When large enough, the annuli are essentially two dimensional patterns and can again become unstable to three dimensional patterns. Eventually the pattern settles down to a regular array of dots. In general the pattern wavelength decreases with time.

Let the unit normal to the surface be defined as

$$\mathbf{n} = \frac{\mathbf{r}_x \wedge \mathbf{r}_y}{|\mathbf{r}_x \wedge \mathbf{r}_y|} \equiv \frac{1}{\sqrt{1 + z_x^2 + z_y^2}}(-z_x, -z_y, 1). \quad (2.18)$$

Now consider the “second fundamental form”, which represents the way in which the tangent plane diverges from the surface, and is defined as

$$Ldx^2 + Mdx dy + Ndy^2 \quad (2.19)$$

where

$$L = \mathbf{r}_{xx} \cdot \mathbf{n}, \quad (2.20)$$

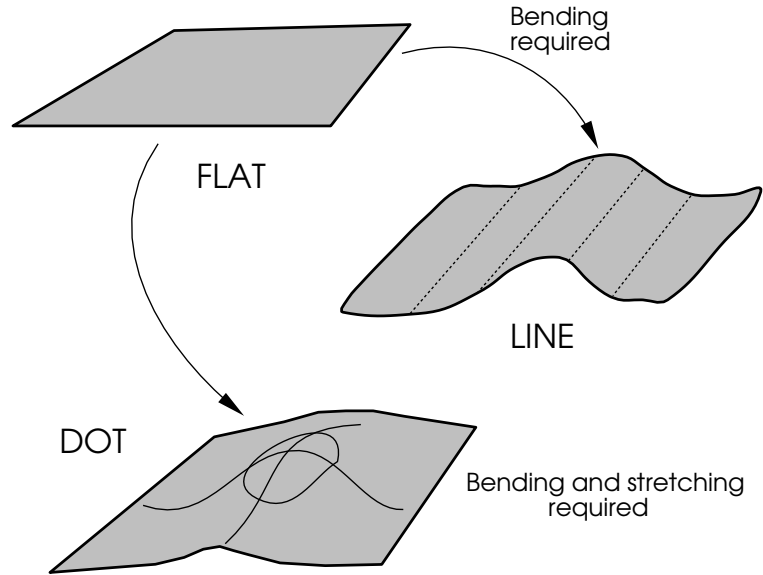


Figure 2.32: Bending and stretching a plane to produce a line pattern or a dot pattern.

$$M = \mathbf{r}_{xy} \cdot \mathbf{n} \quad (2.21)$$

and

$$N = \mathbf{r}_{yy} \cdot \mathbf{n}. \quad (2.22)$$

For the surface  $\mathbf{r}(x, y) = (x, y, z(x, y))$  the coefficients are  $E = 1 + z_x^2$ ,  $F = z_x z_y$ ,  $G = 1 + z_y^2$ ,  $L = \frac{z_{xx}}{H}$ ,  $M = \frac{z_{xy}}{H}$  and  $N = \frac{z_{yy}}{H}$  where  $H = \sqrt{1 + z_x^2 + z_y^2}$ .

The two principal surface curvatures are determined from the eigenvalue problem

$$\det \left\{ \begin{pmatrix} L & M \\ M & N \end{pmatrix} - \kappa \begin{pmatrix} E & F \\ F & G \end{pmatrix} \right\} = 0. \quad (2.23)$$

It can be shown that the Gaussian curvature (or the product of the two principal curvatures) on a surface embedded in Euclidean three-space, can be written as (see do Carmo 1976 [29])

$$\kappa_g = \frac{LN - M^2}{EG - F^2}, \quad (2.24)$$

and the mean curvature (i.e. the mean of the two principal curvatures) is

$$\kappa_m = \frac{1}{2} \frac{LG - 2MF + NE}{EG - F^2}. \quad (2.25)$$

Once evaluated with the surface  $\mathbf{r}(x, y)$ , these expressions can be written as

$$\kappa_g = \frac{z_{xx}z_{yy} - z_{xy}^2}{H^4} \quad (2.26)$$

and

$$\kappa_m = \frac{1}{2} \frac{z_{xx}(1 + z_y^2) + z_{yy}(1 + z_x^2) - 2z_{xy}z_xz_y}{H^3}. \quad (2.27)$$

$\kappa_g(x, y)$  is a measure of the local bending and stretching required to produce the surface from a plane. If no stretching is required then  $\kappa_g \equiv 0$  and the surface is said to be isomorphic to the plane. The only such surfaces are “ruled surfaces” which are defined as the surface swept out by a straight line. A subset of these surfaces are “developable surfaces” such as cylinders and corrugated roofs. A version of the Gauss-Bonnet theorem states that for a smooth closed bounded surface,  $S$ , with  $n$  sides and internal angles  $\alpha_i$

$$\sum_{i=1}^n \alpha_i = (n - 2)\pi + \int_{dS} \kappa_n ds + \int_S \kappa_g dS \quad (2.28)$$

where  $\kappa_n$  is the “normal curvature” of the bounding curve. This formula is related to the Euler formula  $2 - \text{holes} = \text{faces} - \text{edges} + \text{vertices}$  for partitions of a closed bounded surface in Euclidean three-space. For a surface such as ours,  $\sum \alpha_i = 2\pi$  and if we preprocess our images such that the boundary curves are geodesics (i.e. normal curvature is zero) then  $\int_S \kappa_g dS = 0$ . Geodesic boundaries are easy to enforce by requiring that the surface is “flat” at the edges.

In this study we are interested in the local behaviour of the surface and in particular the signs of the Gaussian and mean curvatures and the image area these regions occupy. This information will provide us with a characterization of the image and how this changes with time.

### 2.8.1 Preprocessing

Contained within the pictures is a small amount of noise and also some small scale structures. For example, debris, dust, scratches on the petri dish or lenses and, of course, sampling inaccuracies. For the purposes of curvature calculations, these structures can prove troublesome and must be eliminated beforehand. There are a number of methods for filtering out noise. Initially, we chose to use a band-pass filter of the fifth order Butterworth type to remove high and low wavenumbers. Unfortunately, this filter had the effect of introducing a low level, oscillatory signal to the image which, unless its wavelength matched that of the image, was sufficient to corrupt the curvature calculation. We opted instead for a more sophisticated method of moving averages (Tukey

1977 [110]; Cressie 1993 [26]). We found that by using a combination of a median moving average (Justusson 1981 [57]; Tyan 1981 [112]), which preserves edges and ignores outliers, and a mean moving average, which smooths sharp edges but is sensitive to outliers, we were able to construct a smooth surface that had all of the bioconvection structures intact. The median moving average is defined as the median of a points neighbours within a suitable distance. If this neighbourhood is too large, the filter has the undesirable effect of rounding corners. The mean moving average is defined as the mean of a point's neighbours and smooths the image. We found that a neighbourhood width of five was best for both filters, with the mean following the median, in that the image appeared uncorrupted. A couple of applications of this combined filter removed the undesirable noise and created a smooth surface with similar characteristics to the original image.

### 2.8.2 Numerical gradients

To calculate the surface curvatures for a surface  $z(x_i, y_j) \equiv z_{ij}$  it is first necessary to approximate the surface gradients  $z_x, z_y, z_{xx}, z_{yy}$  and  $z_{xy}$ . Fourth order accurate expressions for these gradients are

$$z_x = \frac{-z_{i+2,j} + 8z_{i+1,j} - 8z_{i-1,j} + z_{i-2,j}}{12h_x} + O(h_x^4), \quad (2.29)$$

$$z_{yy} = \frac{-z_{i,j+2} + 16z_{i,j+1} - 30z_{i,j} + 16z_{i,j-1} - z_{i,j-2}}{12h_y^2} + O(h_y^4) \quad (2.30)$$

and similarly for  $z_y, z_{xx}$  and  $z_{xy}$  where  $h_x$  and  $h_y$  are the horizontal and vertical lengths between pixels. A choice of 0.1 for  $h_x$  is sufficient for an accuracy of  $10^{-3}$  for the gradient calculation. Equations (2.26) and (2.27) are used to calculate the Gaussian and mean curvatures. These expressions are not valid at the edges of the image however, but the curvatures there are not relevant and are left unevaluated.

### 2.8.3 Interpretation

As mentioned before, if  $\kappa_g$  is zero at a point then it is locally isomorphic to a plane and is in a class of surfaces called "ruled" surfaces. We can gain even more information on the shape of the surface, and hence the type of image pattern, by considering what the combinations of signs of  $\kappa_m$  and  $\kappa_g$  refer to. Figure (2.33) explains how combinations of  $\kappa_m$  and  $\kappa_g$  determine the local form of the surface. To allow for small errors,  $\kappa_g$  is

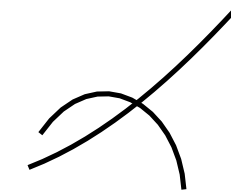
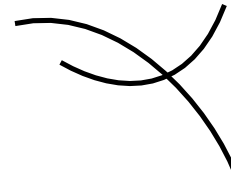
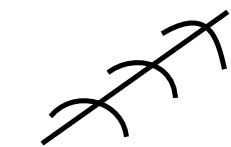
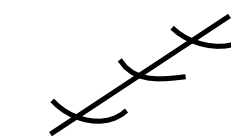
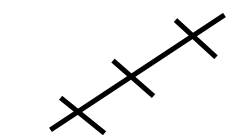
	White dot	$\kappa_g > 0$ $\kappa_m < 0$
	White line	$\kappa_g < 0$ $\kappa_m < 0$
	Black line	$\kappa_g < 0$ $\kappa_m > 0$
	Black dot	$\kappa_g > 0$ $\kappa_m > 0$
	White ridge	$\kappa_g = 0$ $\kappa_m < 0$
	Black ridge	$\kappa_g = 0$ $\kappa_m > 0$
	Flat	$\kappa_g = 0$ $\kappa_m = 0$

Figure 2.33: Different combinations of  $\kappa_m$  and  $\kappa_g$  imply different local surface structures. In particular, if  $\kappa_g < 0$  then the principal curvatures have different signs and we have a saddle point. If  $\kappa_g > 0$  then the principal curvatures have the same sign and we have a local minimum or maximum. The sum of the principal curvatures,  $\kappa_m$ , provides the extra information required to determine the form of the local surface structure.

considered as equal to zero if and only if  $-\kappa_{gx} < \kappa_g < \kappa_{gx}$  where  $\kappa_g = \frac{\max(\text{abs}(\kappa_g))}{100}$  and likewise for  $\kappa_m$ . Figure (2.34) shows a typical example where the different colours represent regions of qualitatively different local surface structures. We can sum the areas of the image for different shapes in a window within the image to get measures of how the pattern changes with time. If  $A_{bd}$ ,  $A_{bl}$ ,  $A_{wd}$ ,  $A_{wl}$  and  $A_f$  are image areas which are black (b), white (w), dots (d), lines (l) or flat (f) then the normalised coefficients  $C_{bd}$ ,  $C_{bl}$ ,  $C_{wd}$  and  $C_{wl}$  can be defined as

$$C_{bd} = \frac{A_{bd}}{A_w - A_f} \quad (2.31)$$

etc., where  $A_w$  is the area of the sample window, and represent the proportion of the whole pattern taken up by a particular type of pattern. These pattern coefficients are shown in Figure (2.35) for experiment x120h (Figure 2.11) and it is clear that the proportion of black dots increases with time and black lines initially increase but then decrease. We do not consider the cases where the surface is locally isomorphic to a plane as it is hard to distinguish these structures from local fluctuations caused by “noise” and the choice of filter. Hence, we can conclude that this method is effective at isolating particular image structures and differentiating between them.

Figure (2.37) is another example of the coefficients for experiment x208l where the curvatures are displayed in Figure (2.36). There are general characteristics for both example images.

- The percentage of white dots decreases with time.
- The percentage of white lines increases with time.
- The percentage of black dots decreases and then increases with time.
- The percentage of black lines increases and then decreases with time.
- Striped linear patterns are observed, indicating that line patterns almost immediately become unstable along their length.
- Well developed patterns are well defined with an overall increase in black dots and white lines and a decrease in white dots and black lines, indicating a change from line patterns to dot patterns.

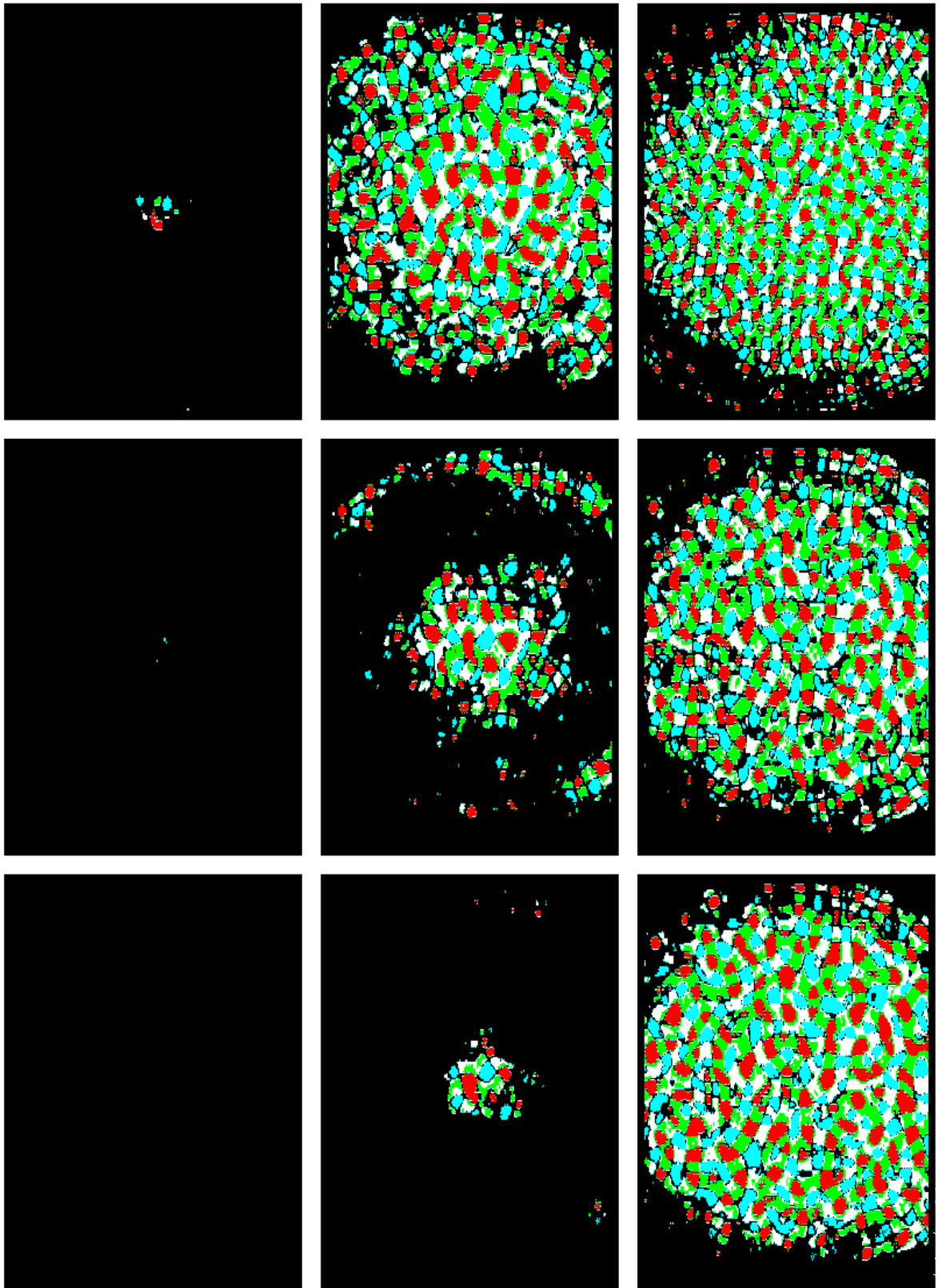


Figure 2.34: An example (experiment x120h) of image characteristic curvatures varying with time. Key: Blue = cell concentration maximums or black dots; Red = cell concentration minimums or white dots; White = high cell concentration saddles or black dots.

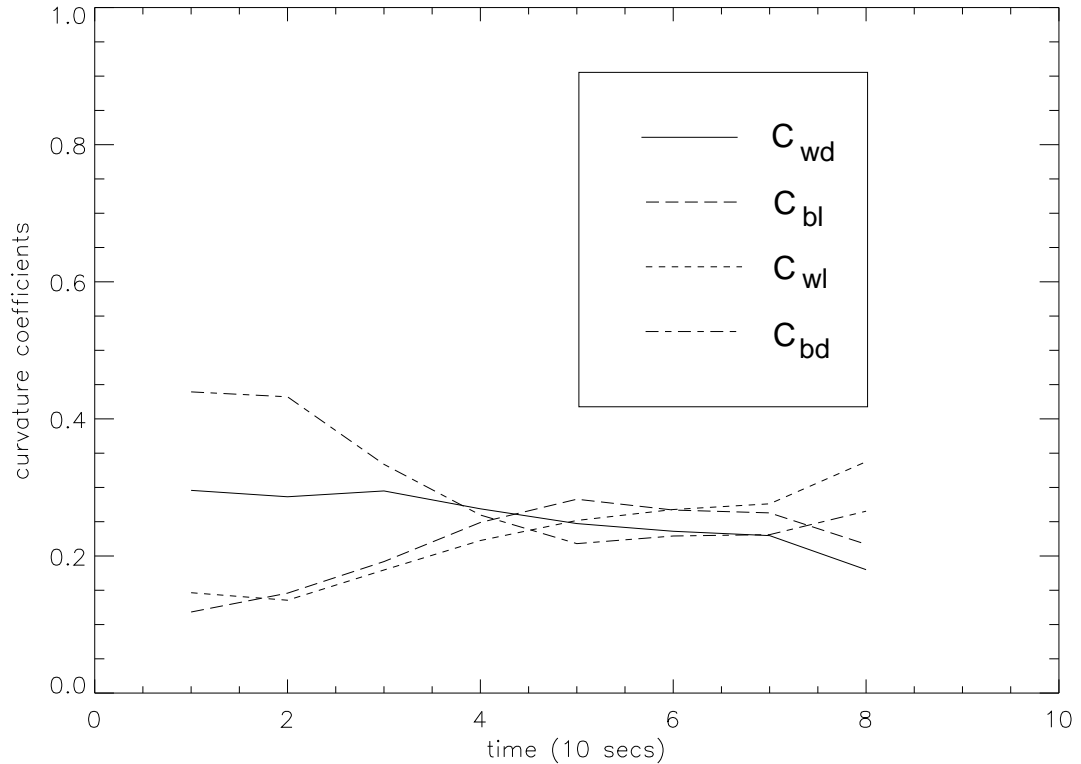


Figure 2.35: x120h. Image pattern coefficients varying with time. Dash-dotted line:  $C_{bd}$ , black dot coefficient; Dashed line:  $C_{bl}$ , black line coefficient; Solid line:  $C_{wd}$ , white dot coefficient; Dotted line:  $C_{wl}$ , white line coefficient.

In particular Figure (2.36) displays background large scale structures that could either be generic or a result of the pre-mixing.

Further investigations could focus on the possible connections between these coefficients and the dimension of the pattern that they represent. For example, a pattern of a regular array of dots is essentially a three dimensional pattern whereas an array of bioconvection rolls is a two dimensional pattern. In the same manner a pattern consisting of large tori could be classed as being closer to a two dimensional pattern and many other patterns would be somewhere between two and three dimensional. The analysis of the curvature coefficients could provide some means of determining this average dimension. In particular, the coefficients  $C_{bl}$  and  $C_{bd}$  indicate the levels of two and three dimensional structures of concentrated cells. Defining the pattern dimension,  $\mathcal{D}_p$ , as

$$\mathcal{D}_p = 2 + \frac{C_{bd}}{C_{bl} + C_{bd}} \quad (2.32)$$

provides a basic measure of the pattern dimension.

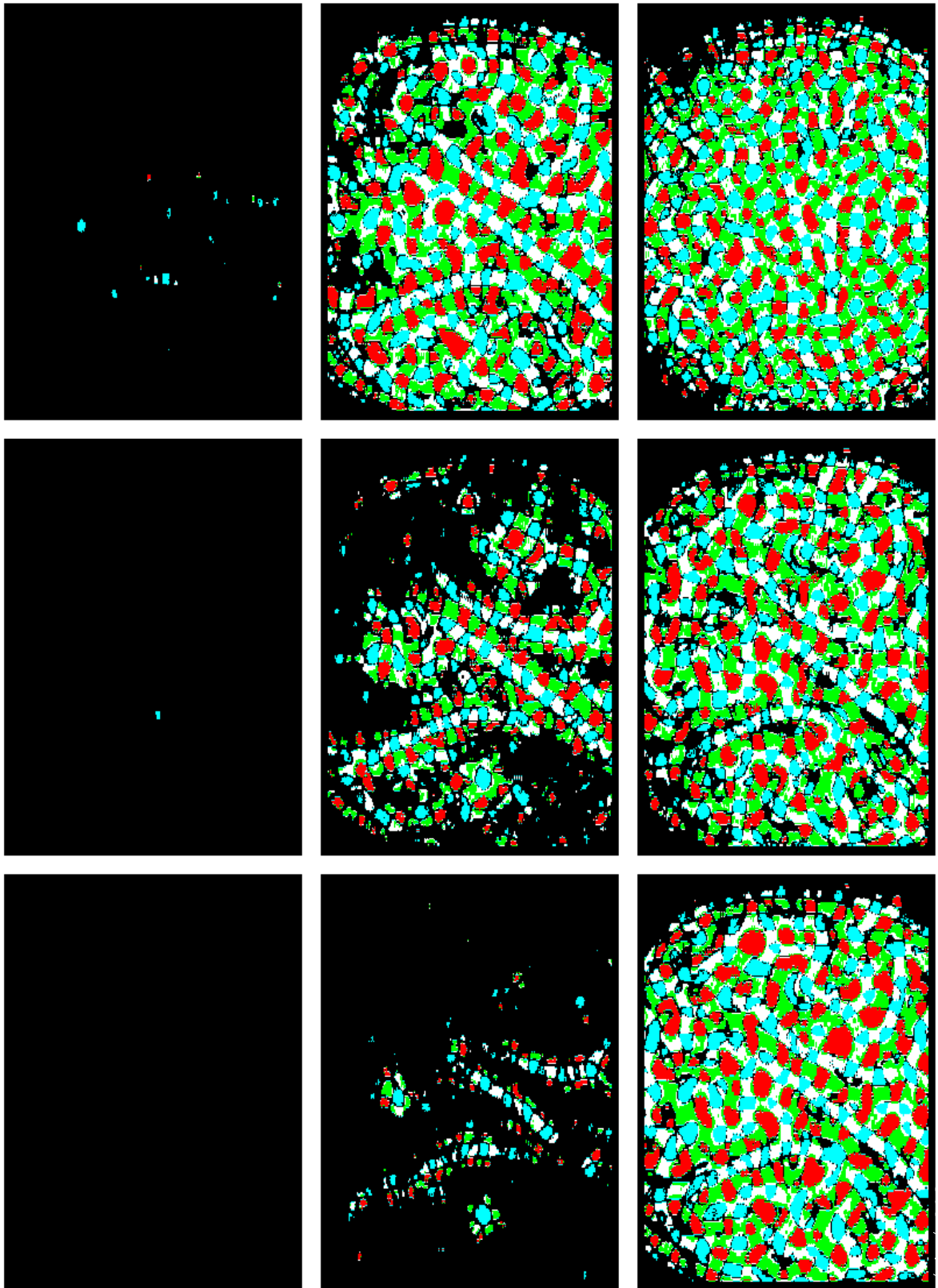


Figure 2.36: An example (experiment x2081) of image characteristic curvatures varying with time. Key: Blue = cell concentration maximums or black dots; Red = cell concentration minimums or white dots; White = high cell concentration saddles or black dots.

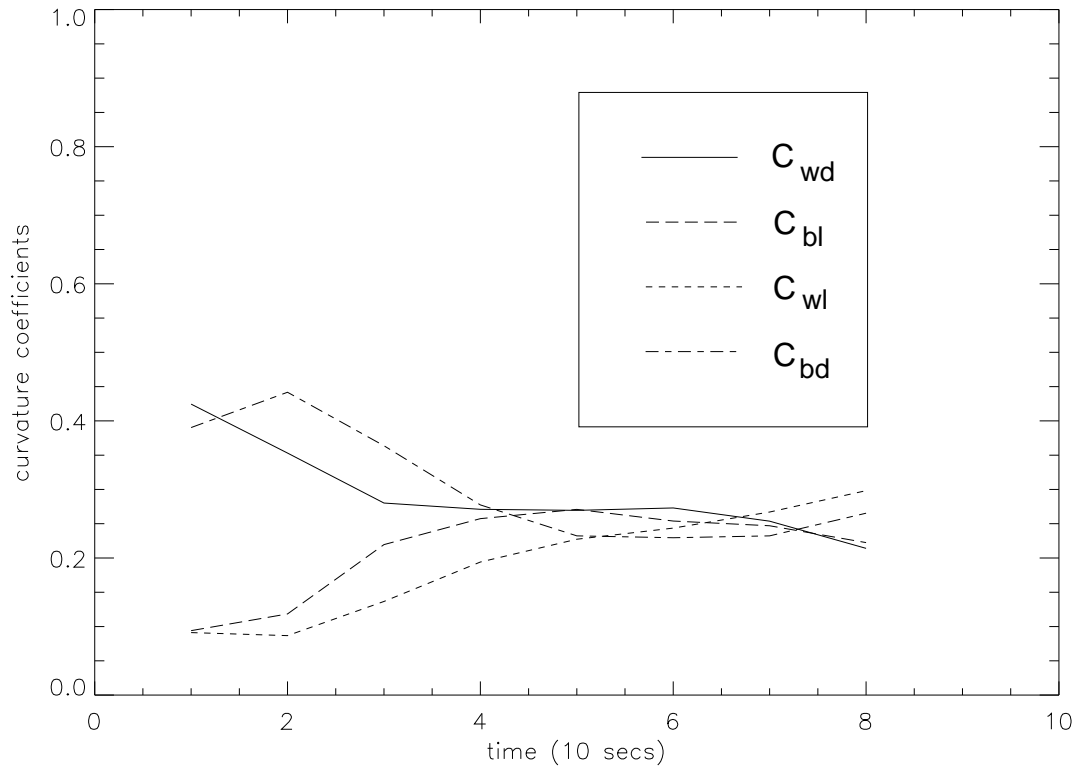


Figure 2.37: x2081. Image pattern coefficients varying with time. Dash-dotted line:  $C_{bd}$ , black dot coefficient; Dashed line:  $C_{bl}$ , black line coefficient; Solid line:  $C_{wd}$ , white dot coefficient; Dotted line:  $C_{wl}$ , white line coefficient.

## 2.9 Varying the density of the suspending fluid

An experimental attempt was made to alter the strength of the cells' negative bouyancy and gyrotaxis and, hence, to measure the strength of the alternative sedimentary mechanism proposed by Alun M. Roberts (1995, personal communication) that has been neglected in our model to date (see Section 1.3). Theoretically, Hill, Jones and Pedley (1995, personal communication) have independently estimated the orienting forces due to sedimentation (which we shall call the taxis due to sedimentation) to be an order of magnitude less than for gyrotaxis. Experimentally our results were inconclusive. The unreactive chemical Percoll<sup>1</sup>, which has a higher density than water, was added to suspensions of swimming micro organisms in different proportions and observations were made of the behaviour of the organisms. Percoll (registered trademark of Pharmacia,

<sup>1</sup>Recently Lebert & Häder (1996) [72] have reported their findings on experiments with a similar chemical called Ficoll to vary geotaxis in *Euglena gracilis*.

Inc.) is a colloidal Polyvinylpyrrolidone (PVP) coated silica and is normally used to set up gradients in suspension density for cell separation. It has a higher density than water (density of Percoll equals  $1.13 \pm 0.005 \text{gcm}^{-3}$ ) which is desirable but also a higher viscosity ( $0.1 \pm 0.05 \text{gcm}^{-1} \text{s}^{-1}$  at  $20^\circ \text{C}$ , equal to ten times that of water) and higher pH ( $8.9 \pm 0.3$  at  $20^\circ \text{C}$ ) which are not.

### 2.9.1 Theoretical predictions

#### Case I:-

In their standard medium (of density  $1.0 \text{gcm}^{-3}$ ) *Chlamydomonas nivalis* are bottom heavy and will, on average, swim upwards. They are, however, denser than the surrounding fluid (cells are of density  $1.05 \text{gcm}^{-3}$ ) and will cause a Rayleigh-Taylor instability when they accumulate at the upper boundary. Gyrotaxis acts such that the cells swim towards downflowing fluid. The taxis due to sedimentation results from the high relative drag of the cell's flagella to the cell body, when the cell experiences the otherwise negligible sedimentation force (relative to the cell swimming speed), and acts in the same manner as gyrotaxis.

#### Case II:-

If enough Percoll is added (approximately 38.5 % from previous measurements of density) such that the cells are neutrally bouyant then

1. There are no torques due to sedimentation.
2. The cells are bottom heavy and swim upwards.
3. The cells accumulate at the upper boundary but cannot cause a Rayleigh-Taylor instability.
4. Cells swim towards regions of downflowing fluid (gyrotaxis) but a gyrotactic instability cannot occur.

#### Case III:-

If the cells are slightly positively bouyant then

1. The taxes due to sedimentation acts to point the cell downwards but is smaller than

2. the torque due to the bottom heaviness of the cell acting to point the cell upwards. The cells swim upwards on average.
3. The cells accumulate at the upper boundary but cannot cause a Rayleigh-Taylor instability.
4. Cells swim towards regions of downflowing fluid (gyrotaxis) but a gyrotactic instability cannot occur.

**Case IV:-**

If the cells are positively bouyant such that the torques due to sedimentation and the bottom heaviness of the cell cancel each other out then

1. The cells have no preferred swimming direction and accumulate neither at the top nor bottom boundaries in the short term.
2. In the long term, the cells accumulate at the upper boundary due to sedimentation.
3. The cells are neither attracted to upflowing nor downflowing fluid.

**Case V:-**

If we increase the suspension density with Percoll such that the torques due to sedimentation are greater than bottom heaviness but in the opposite sense then

1. The cells preferred swimming direction is downwards.
2. The cells accumulate at the lower boundary.
3. A Rayleigh-Taylor instability is possible with heavier, cell free suspension above lighter concentrated suspension.
4. Cells swim towards regions of upflowing fluid - *negative gyrotaxis*.

This last case would result in upwards tending plumes and is the opposite of the normal situation.

### 2.9.2 Experimental observations

Five experiments were performed with Percoll using suspension ratios of 0:1 (0% Percoll), 1:4 (20%), 1:2 (33%), 2:1 (67%) and 3:1 (75%). This provided overall suspension densities of  $1.000\text{ cm}^{-3}$ ,  $1.026\text{ cm}^{-3}$ ,  $1.043\text{ cm}^{-3}$ ,  $1.087\text{ cm}^{-3}$  and  $1.098\text{ cm}^{-3}$ , respectively. The suspensions were well mixed in small test tubes, left to settle over a couple of days and then observed through a microscope set up to view from the side. Table 2.5 illustrates the results which were largely inconclusive. The major problem with

Percoll culture ratio	bouyancy	mean swimming direction	R-T instability ?	gyrotactic instability ?	% cells alive	notes
0:1	negative	upwards	yes	yes	90	normal
1:4	neg-neut	upwards	little	little	40	less focused
1:2	neutral	none	no	no	1	many stuck to sides swimmers in middle
2:1	positive	-	no	no	0	floating at top
3:1	positive	-	no	no	0	floating at top

Table 2.5: Observations of suspensions of *Chlamydomonas nivalis* and Percoll in different ratios.

the experiments being the unwanted increase in viscosity with higher ratios of Percoll. This interferes with the cells locomotion and agglutinability and many cells seem to be clumped together. Also there is not just one cell density but a whole range of densities and some cells can be positively bouyant at the same time as others being negatively bouyant.

There are two balances that could be measured in theory, represented by Cases II and IV. Case II, neutral bouyancy, can be measured as approximately corresponding to a Percoll-culture ratio of 1:2 and leads to a cell density calculation of  $1.04 \pm 0.02\text{ gcm}^{-3}$  (this has been independently estimated as  $1.05\text{ gcm}^{-3}$ ). Case IV represents a suspension where micro-organisms have no preferred swimming direction and this situation may have been seen in the Percoll-culture ratio of 1:2, but it is difficult to say due to the

very small levels of operational (alive?) cells. Case V was never observed. The only thing that we can conclude from these results is that our value for the cell density is approximately correct. Perhaps we can conjecture, however, that the torque due to sedimentation is small compared with that due to bottom heaviness and we are justified in neglecting the sedimentation altogether. More experiments with Percoll (or other agents) may produce clearer results, especially if it is possible to observe individual micro-organisms as the Percoll concentration is increased (or Ficoll concentration, as in Lebert & Häder 1996 [72]).

## 2.10 Discussion

In this chapter we have developed techniques for recording bioconvection patterns in a shallow dish as functions of suspension concentration, depth and time. In doing so it was necessary to construct a methodology for measuring the cell concentration (which was achieved using computer processing techniques) and depth, and for culturing the cells such that they were always healthy and fully motile. All the experiments were performed on a limited budget but this did not adversely affect the results. We have refined techniques to process the images and extract the dominant pattern wavenumber using Fourier analysis. The initial pattern wavenumber and the well developed pattern wavenumber were analysed in detail and it was found that the initial wavenumber decreased with increasing depth but hardly varied at all with concentration. Conversely, the well developed wavenumber increased with concentration and slightly increased with depth. Each of the patterns were categorized and the interaction of unstable modes as the pattern evolved with time was explored. In particular, mechanisms for the existence of annular patterns were proposed. Also, a new method of analysing the pattern structure has been investigated that adopts the methods of surface geometry. Each image is associated with a surface in Euclidean three-space where the images intensity relates to the surface elevation. The corresponding local surface curvatures are used to identify the local surface structure and, hence, the local image structure. A critical feature of this work's success was the construction of a median/mean moving average filter to remove unwanted noise and create a smooth surface. The filter is not ideal but was found to be better than using Fourier analysis. Perhaps we require

higher level statistical modelling of the surface. For example, approximating a local quadratic surface using least squares fit and applying diagnostics in a similar manner to regression analysis (see for example Cressie, 1993 [26]). Regardless of the benefits of such extra complications the four telltale pattern statistics defined, plus the graphical images of surface curvature themselves provide a basis for future investigation and allow the exploration of local pattern structures, and how they fit in globally, that are not immediately obvious to the naked eye. In particular the existence of larger scale patterns on the scale of the dish and the fact that line patterns *immediately* become unstable to dotted patterns. The reorganisation necessary for the qualitative pattern change is also more clearly observed.

The neutral substance Percoll was used to increase the density of suspensions of micro-organisms in an attempt to isolate a hypothetical mechanism for cell orientation due to sedimentation. However, the presence of Percoll interfered with the cells and rendered them immobile (or perhaps dead). Experiments with Percoll on individual micro-organisms may produce clearer results or perhaps we could repeat the experiments using Ficoll instead of Percoll (see Lebert & Häder 1996 [72]).

Figure (2.22) shows a sequence of images where the suspension is very shallow ( $1.86\text{mm}$ ) and the concentration is reasonably high. Bioconvection is initiated but the plumes that develop do not fully fill the dish. As time progresses, the plumes emigrate towards the edge of the dish and, in particular, towards one side leaving an off-centre, clear patch with no patterns. Close inspection of these plumes reveals a significant elevation of the upper fluid surface directly above them and this may affect their stability. Concentrated plumes exist for long periods of time on the edge of the clear patch but tend to wander and appear to be repelled by any close neighbours. It is possible that the upper surface tension may affect the stability of these dense plumes in very shallow layers and this needs to be investigated further.

Future research should also try to discover the effect of horizontal boundaries on the pattern. This could be investigated by observing patterns in large annular dishes of varying aspect to establish the effect of two side walls.

Recently, some cursory experiments have been performed on a long horizontal tube of diameter  $1.5\text{cm}$ , filled with a suspension of *Chamydomonas nivalis* of concentration 1 million cells per  $\text{cm}^3$  and rotating about a horizontal axis. Initial results indicate that

for no rotation “disorderly” bioconvection occurs with plumes descending throughout the tube’s cross-section. If the rotation rate is slowly increased from zero the patterns become more orderly and for a range of rotation rates (1 rev / min to 2 rev / min) form dense rings perpendicular to the cylinder axis. As the rotation rate increases, these rings move closer together and inevitably some collide. Ultimately, the whole system collapses and for a rotation rate of 5 rev / min there is no discernable pattern. If the rotation rate is decreased from this value no patterns are observed well into the region of rotation rates for which patterns were previously observed. Patterns spontaneously occur if the rotation rate is decreased sufficiently. It is hypothesised that by slowly rotating the cylinder we are driving the fluid in a linear bioconvection roll and that as it becomes stronger it becomes unstable to patterns along the cylinder axis. The possibility of multiple patterns for a given rotation rate raises some important questions about mode interaction, such as splitting and annihilation, and it will be a goal of future research to repeat the experiments quantitatively and to understand the mechanisms behind them.

## Chapter 3

# Finite Depth Stochastic Gyrotactic Bioconvection - Linear Analysis

### 3.1 Introduction

The aim of this chapter is to predict a particular most unstable mode (i.e. one that grows most rapidly) from the initial equilibrium solution. This can be compared, in principle, with the experiments of Chapter 2. In practice, however, it may be difficult to realise the very first unstable mode before the non-linear effects become significant and form finite amplitude convection cells.

Here, an equilibrium solution, of the full equations for finite depth and zero flow, is found and a small perturbation allowing weak ambient flow is made. Initially the Fokker-Planck equation described in the previous chapter has to be solved. Brenner & Weissmann (1972) [12] describe the use of asymptotic expansions in their analysis of dipolar spheres subject to external couples and rotational Brownian motion and this has been extended by Pedley & Kessler (1990) [85] for their infinite depth model. This work initially follows that of [85] but with minor corrections. In the [85] infinite depth model, the first order correction to the diffusion tensor did not appear in the full linear equations. However, in the finite depth case, the first order diffusion tensor is of paramount importance and can determine the range of unstable wavenumbers.

When the full linear equations are solved using asymptotic and numerical techniques with finite depth, the analysis is similar to that of Hill *et al.* (1989) [42], with the added complications of the non-constant diffusion and mean cell swimming velocity being modelled using the Fokker-Planck equation. The [42] model is itself an extension of the older Childress *et al.* (1975) [19] model with the inclusion of a deterministic gyrotactic mechanism.

Hillesdon *et al.* (1995) [45] and [44] investigate patterns formed by chemotactic (or more specifically aerotactic) bacteria and some of their analytic and numerical techniques stem from the same sources as those contained in this chapter. In their models the analysis is further complicated by discontinuities in the bacterial concentration gradient and ideas from the theory of penetrative convection (Veronis 1963 [115]) need to be employed to understand the non-linear behaviour of the system. However, their model does not include coupling of fluid flow and cell orientation in a Fokker-Planck equation.

Finally, we investigate the effect of modelling the swimming speed as a random variable and compare our predictions with the experiments of Chapter 2.

## 3.2 Linear Solution of the Fokker-Planck Equation

### 3.2.1 The Fokker-Planck equation on a sphere

Equations (1.18) and (1.23) give the steady gyrotactic Fokker-Planck equation as

$$\nabla \cdot (\dot{\mathbf{p}}f) = D_r \nabla^2 f \quad (3.1)$$

where

$$\dot{\mathbf{p}} = \frac{1}{2B} [\mathbf{k} - (\mathbf{k} \cdot \mathbf{p})\mathbf{p}] + \frac{1}{2}\boldsymbol{\Omega} \wedge \mathbf{p} + \alpha_0 \mathbf{p} \cdot \mathbf{E} \cdot (\mathbf{I} - \mathbf{p}\mathbf{p}), \quad (3.2)$$

which gives

$$\frac{1}{2B} \nabla \cdot [(\mathbf{k} - (\mathbf{k} \cdot \mathbf{p})\mathbf{p})f] + \frac{1}{2} \nabla \cdot [(\boldsymbol{\Omega} \wedge \mathbf{p})f] + \alpha_0 \nabla \cdot [(\mathbf{p} \cdot \mathbf{E} \cdot (\mathbf{I} - \mathbf{p}\mathbf{p}))f] = D_r \nabla^2 f. \quad (3.3)$$

Here  $\mathbf{k}$ ,  $\boldsymbol{\Omega}$  and  $\mathbf{E}$  are constants, and  $tr(\mathbf{E}) \equiv \nabla \cdot \mathbf{u} = 0$ .  $\mathbf{p}$  is a unit vector perpendicular to the unit sphere and so, for any function  $g = g(\mathbf{p})$ , it follows that  $\nabla g$  is perpendicular

to  $\mathbf{p}$ . Thus  $(\mathbf{p} \cdot \nabla)g = 0$ . We also know that  $\nabla \cdot \mathbf{p} = 2$ , by direct calculation,  $\nabla \mathbf{p} = \mathbf{I} - \mathbf{p}\mathbf{p}$ , and  $(\nabla \wedge \mathbf{p})_i \equiv \epsilon_{ijk} p_{j,k} = \frac{1}{2} \epsilon_{ijk} (p_{j,k} + p_{k,j}) = 0$  since  $\nabla \mathbf{p} = (\nabla \mathbf{p})^T$ . Consider Equation (3.3) term by term:

- $\nabla \cdot f \mathbf{k} \equiv \mathbf{k} \cdot \nabla f$
- $\nabla \cdot [(\mathbf{k} \cdot \mathbf{p})\mathbf{p}f] \equiv (\mathbf{k} \cdot \mathbf{p})f \nabla \cdot \mathbf{p} + \mathbf{p} \cdot \nabla [(\mathbf{k} \cdot \mathbf{p})f] \equiv 2(\mathbf{k} \cdot \mathbf{p})f$
- $\nabla \cdot [(\boldsymbol{\Omega} \wedge \mathbf{p})f] \equiv (\boldsymbol{\Omega} \wedge \mathbf{p}) \cdot \nabla f + f \nabla \cdot (\boldsymbol{\Omega} \wedge \mathbf{p}) \equiv \boldsymbol{\Omega} \cdot (\mathbf{p} \wedge \nabla f) - f \boldsymbol{\Omega} \cdot \nabla \wedge \mathbf{p} \equiv \boldsymbol{\Omega} \cdot (\mathbf{p} \wedge \nabla f)$
- $\nabla \cdot (f \mathbf{p} \cdot \mathbf{E}) \equiv \mathbf{p} \cdot \mathbf{E} \cdot \nabla f + \mathbf{E} : (\mathbf{I} - \mathbf{p}\mathbf{p}) \equiv \mathbf{p} \cdot \mathbf{E} \cdot \nabla f - f \mathbf{p} \cdot \mathbf{E} \cdot \mathbf{p}$
- $\nabla \cdot [f(\mathbf{p} \cdot \mathbf{E} \cdot \mathbf{p})\mathbf{p}] \equiv f(\mathbf{p} \cdot \mathbf{E} \cdot \mathbf{p}) \nabla \cdot \mathbf{p} + \mathbf{p} \cdot \nabla (f(\mathbf{p} \cdot \mathbf{E} \cdot \mathbf{p})) \equiv 2f(\mathbf{p} \cdot \mathbf{E} \cdot \mathbf{p})$ .

Substituting back into Equation (3.3) gives

$$\frac{1}{2B} (\mathbf{k} \cdot \nabla f - 2\mathbf{k} \cdot \mathbf{p}f) + \frac{1}{2} \boldsymbol{\Omega} \cdot (\mathbf{p} \wedge \nabla f) + \alpha_0 [\mathbf{p} \cdot \mathbf{E} \cdot \nabla f - 3f(\mathbf{p} \cdot \mathbf{E} \cdot \mathbf{p})] = D_r \nabla^2 f. \quad (3.4)$$

Now if we non-dimensionalize (the explanation for this particular scaling will be given in Section 3.3) by putting

$$\boldsymbol{\Omega} = \frac{V_s^2 \tau}{H^2} \boldsymbol{\omega} \quad (3.5)$$

and

$$\mathbf{E} = \frac{V_s^2 \tau}{H^2} \mathbf{e} \quad (3.6)$$

where  $V_s^2 \tau$  can be thought of as a typical diffusion scale (see Equation 1.22) and  $H$  is the depth of the suspension, then

$$\mathbf{k} \cdot \nabla f - 2(\mathbf{k} \cdot \mathbf{p})f + \eta \boldsymbol{\omega} \cdot (\mathbf{p} \wedge \nabla f) + 2\eta \alpha_0 [\mathbf{p} \cdot \mathbf{e} \cdot \nabla f - 3\mathbf{p} \cdot \mathbf{e} \cdot \mathbf{p}f] = \lambda^{-1} \nabla^2 f \quad (3.7)$$

where<sup>1</sup>

$$\lambda = \frac{1}{2D_r B} \quad (3.8)$$

and

$$\eta = \frac{B V_s^2 \tau}{H^2}. \quad (3.9)$$

$\eta$  is the dimensionless gyrotaxis parameter. Using our best estimates (from Table 3.2, later)  $\lambda = 2.2$  and  $\eta = 1.8 \times 10^{-4} \times H^{-2}$  where  $H$  is depth of layer in *cm* (or  $\eta = 33d^{-2}$ , see later).

---

<sup>1</sup>Note:  $\lambda$  differs by a factor of  $\frac{1}{2}$  omitted in error in [85] but corrected in [86] review.

### 3.2.2 Solution for zero flow

Consider the equilibrium state of no flow where  $\mathbf{u} = \boldsymbol{\omega} = \mathbf{e} = \mathbf{0}$  and  $f = f^0$ . Writing  $\mathbf{p} = (\sin \theta \cos \phi, \sin \theta \sin \phi, \cos \theta)$  and  $\mathbf{k} = (0, 0, 1)$ , gives

$$\left( \frac{\partial f^0}{\partial \theta} \hat{\boldsymbol{\theta}} + \frac{\partial f^0}{\partial \phi} \frac{1}{\sin \theta} \hat{\boldsymbol{\phi}} \right) \cdot \mathbf{k} - 2f^0 \cos \theta = \lambda^{-1} \frac{1}{\sin \theta} \frac{\partial}{\partial \theta} \left( \sin \theta \frac{\partial f^0}{\partial \theta} \right) + \lambda^{-1} \frac{1}{\sin^2 \theta} \frac{\partial^2 f^0}{\partial \phi^2} \quad (3.10)$$

which implies that

$$\frac{1}{\sin \theta} \frac{\partial}{\partial \theta} \left( \sin \theta \frac{\partial f^0}{\partial \theta} \right) + \frac{1}{\sin^2 \theta} \frac{\partial^2 f^0}{\partial \phi^2} = -\lambda \left( \sin \theta \frac{\partial f^0}{\partial \theta} + 2f^0 \cos \theta \right). \quad (3.11)$$

For zero flow, we can assume axial symmetry and thus  $f^0$  is independent of  $\phi$  and  $f^0 = f^0(\theta)$  only. Substituting  $x = \cos \theta$  into Equation (3.11) yields

$$f^{0''} (1 - x^2) - 2 - 2xf^{0'} - (1 - x^2)\lambda f^{0'} + 2\lambda x f^0 = 0, \quad (3.12)$$

where the prime indicates differentiation with respect to  $x$ . Integrating gives

$$(1 - x^2) (f^{0'} - \lambda f^0) = A \quad (3.13)$$

where  $A$  is a constant, which is found to be zero by noting that  $f^0$  and  $f^{0'}$  are both finite at  $x = 1$ . Hence

$$f^0 = \mu_\lambda e^{\lambda \cos \theta}. \quad (3.14)$$

Applying the normalization condition that the integral of  $f^0$  over the unit sphere is 1, gives

$$\mu_\lambda \left[ -\lambda^{-1} e^{\lambda \cos \theta} \right]_0^\pi = \frac{1}{2\pi} \quad (3.15)$$

which implies that

$$\mu_\lambda = \frac{\lambda}{4\pi \sinh \lambda}. \quad (3.16)$$

This is a special case of the Fisher distribution on a sphere (see Mardia, 1972; [79]).

Since the mean of  $\mathbf{p}$  is

$$\langle \mathbf{p} \rangle = \int_S \mathbf{p} f(\mathbf{p}) d\mathbf{p}, \quad (3.17)$$

we can write

$$\langle \mathbf{p} \rangle^0 = \int_0^{2\pi} \int_0^\pi \begin{pmatrix} \sin \theta \cos \phi \\ \sin \theta \sin \phi \\ \cos \theta \end{pmatrix} \mu_\lambda e^{\lambda \cos \theta} \sin \theta d\theta d\phi. \quad (3.18)$$

Integrating first with respect to  $\phi$  gives zero components in the  $\mathbf{i}$  and  $\mathbf{j}$  directions. Then, integrating by parts with respect to  $\theta$  yields

$$\langle \mathbf{p} \rangle^0 = \begin{pmatrix} 0 \\ 0 \\ K_1 \end{pmatrix} \quad (3.19)$$

where

$$K_1 = \coth \lambda - \lambda^{-1}. \quad (3.20)$$

Similarly,

$$\langle \mathbf{pp} \rangle^0 = \int_0^{2\pi} \int_0^\pi \begin{pmatrix} \sin \theta \cos \phi \\ \sin \theta \sin \phi \\ \cos \theta \end{pmatrix} \begin{pmatrix} \sin \theta \cos \phi \\ \sin \theta \sin \phi \\ \cos \theta \end{pmatrix} \mu_\lambda e^{\lambda \cos \theta} \sin \theta \, d\theta \, d\phi. \quad (3.21)$$

On integrating the matrix  $\mathbf{pp}$  with respect to  $\phi$ , only the diagonal terms survive because their  $\phi$  components are  $\cos^2 \phi$ ,  $\sin^2 \phi$  and 1 respectively. Hence

$$\langle \mathbf{pp} \rangle^0 = \mu_\lambda \pi \int_0^\pi \begin{pmatrix} \sin^2 \theta & & 0 \\ & \sin^2 \theta & \\ 0 & & 2 \cos^2 \theta \end{pmatrix} e^{\lambda \cos \theta} \sin \theta \, d\theta. \quad (3.22)$$

Integrating by parts twice gives

$$\langle \mathbf{pp} \rangle_{11}^0 = \langle \mathbf{pp} \rangle_{22}^0 = \frac{K_1}{\lambda} \quad (3.23)$$

and

$$\langle \mathbf{pp} \rangle_{33}^0 = 1 - \frac{2K_1}{\lambda}. \quad (3.24)$$

Hence, from the definition of  $\mathbf{D}$  in Chapter 1,

$$\mathbf{D}^0 = V_s^2 \tau [\langle \mathbf{pp} \rangle^0 - \langle \mathbf{p} \rangle^0 \langle \mathbf{p} \rangle^0] \quad (3.25)$$

so that

$$\mathbf{D}_{11}^0 = \mathbf{D}_{22}^0 = V_s^2 \tau \frac{K_1}{\lambda} \quad (3.26)$$

and

$$\mathbf{D}_{33}^0 = V_s^2 \tau \left( 1 - 2 \frac{2K_1}{\lambda} - K_1^2 \right) = V_s^2 \tau K_2, \quad (3.27)$$

on defining

$$K_2 = 1 - \coth^2 \lambda + \frac{1}{\lambda^2}. \quad (3.28)$$

### 3.2.3 First order perturbation

From the equilibrium state of no flow ( $\mathbf{u} = \boldsymbol{\omega} = \mathbf{e} = \mathbf{0}$ ), we perturb to

$$\begin{aligned}\mathbf{u} &= \epsilon \mathbf{u}^1, \\ \boldsymbol{\omega} &= \epsilon \boldsymbol{\omega}^1, \\ \mathbf{e} &= \epsilon \mathbf{e}^1, \\ f &= f^0 + \epsilon f^1,\end{aligned}\tag{3.29}$$

where  $0 < \epsilon \ll 1$ . At  $O(\epsilon)$ , Equation (3.7) gives

$$\mathbf{k} \cdot \nabla f^1 - 2\mathbf{k} \cdot \mathbf{p} f^1 + \eta \boldsymbol{\omega}^1 \cdot (\mathbf{p} \wedge \nabla f^0) + 2\eta \alpha_0 [\mathbf{p} \cdot \mathbf{e}^1 \cdot \nabla f^0 - 3\mathbf{p} \cdot \mathbf{e}^1 \cdot \mathbf{p} f^0] = \lambda^{-1} \nabla^2 f^1,\tag{3.30}$$

which in spherical polar coordinates  $(\theta, \phi)$  becomes

$$\begin{aligned}& \frac{\lambda^{-1}}{\sin \theta} \frac{\partial}{\partial \theta} \left( \sin \theta \frac{\partial f^1}{\partial \theta} \right) + \frac{\lambda^{-1}}{\sin^2 \theta} \frac{\partial^2 f^1}{\partial \phi^2} - \mathbf{k} \cdot \hat{\boldsymbol{\theta}} \frac{\partial f^1}{\partial \theta} + 2 \cos \theta f^1 \\ &= \eta \left( \boldsymbol{\omega}^1 \cdot \mathbf{p} \wedge \hat{\boldsymbol{\theta}} \frac{\partial f^0}{\partial \theta} + 2\alpha_0 \mathbf{p} \cdot \mathbf{e}^1 \cdot \hat{\boldsymbol{\theta}} \frac{\partial f^0}{\partial \theta} - 6\alpha_0 \mathbf{p} \cdot \mathbf{e}^1 \cdot \mathbf{p} f^0 \right),\end{aligned}\tag{3.31}$$

where

$$\begin{aligned}\frac{\partial f^0}{\partial \theta} &= -\mu_\lambda \lambda \sin \theta e^{\lambda \cos \theta}, \\ \hat{\boldsymbol{\theta}} &= (\cos \theta \sin \phi, \cos \theta \cos \phi, -\sin \theta)^T, \\ \mathbf{p} \wedge \hat{\boldsymbol{\theta}} &= (-\sin \theta, \cos \theta, 0)^T, \\ \mathbf{p} \cdot \mathbf{e}^1 \cdot \hat{\boldsymbol{\theta}} &= -\frac{3}{4} e_{33} \sin 2\theta + \left[ \frac{1}{4} (e_{11} - e_{22}) \cos 2\phi + \frac{1}{2} e_{12} \sin 2\phi \right] \sin 2\theta \\ &\quad + [e_{13} \cos \phi + e_{23} \sin 2\phi] \cos 2\theta\end{aligned}$$

and

$$\begin{aligned}\mathbf{p} \cdot \mathbf{e}^1 \cdot \mathbf{p} &= \frac{1}{2} e_{33} (3 \cos^2 \theta - 1) + \left[ \frac{1}{2} (e_{11} - e_{22}) \cos 2\phi + e_{12} \sin 2\phi \right] \sin^2 \theta \\ &\quad + [e_{13} \cos \phi + e_{23} \sin 2\phi] \sin 2\theta.\end{aligned}\tag{3.32}$$

### 3.2.4 First order perturbation for spherical cells: $\alpha_0 = 0$

Firstly we consider purely spherical cells, i.e.  $\alpha_0 = 0$ , and then extend this result for arbitrary values of  $\alpha_0$ . For spherical cells, Equation (3.31) simplifies to

$$\frac{\lambda^{-1}}{\sin \theta} \frac{\partial}{\partial \theta} \left( \sin \theta \frac{\partial f^1}{\partial \theta} \right) + \frac{\lambda^{-1}}{\sin^2 \theta} \frac{\partial^2 f^1}{\partial \phi^2} - \mathbf{k} \cdot \hat{\boldsymbol{\theta}} \frac{\partial f^1}{\partial \theta} + 2 \cos \theta f^1$$

$$= -\eta (\omega_2^1 \cos \phi - \omega_1^1 \sin \phi) \mu_\lambda \lambda \sin \theta e^{\lambda \cos \theta}. \quad (3.33)$$

Suppose that

$$f^1 = \lambda \mu_\lambda \eta (\omega_2^1 \cos \phi - \omega_1^1 \sin \phi) g(\theta), \quad (3.34)$$

for some function  $g(\theta)$ . On substituting  $x = \cos \theta$ , it follows that

$$((1-x^2)g')' - \frac{g}{(1-x^2)} - \lambda ((1-x^2)g)' = -\lambda (1-x^2)^{\frac{1}{2}} e^{\lambda x}. \quad (3.35)$$

Expanding the exponential term as

$$\lambda e^{\lambda x} = \sum_{n=1}^{\infty} \frac{\lambda^n x^{n-1}}{(n-1)!}, \quad (3.36)$$

and writing  $g(x)$  as a power series in  $\lambda$

$$g(x) = \sum_{n=1}^{\infty} \lambda^n G_n(x), \quad (3.37)$$

(assuming convergence at this stage), we find by comparing the coefficients of  $\lambda^n$  in (3.35) that

$$((1-x^2)G'_n)' - \frac{G_n}{(1-x^2)} - \lambda ((1-x^2)G_{n-1})' = -\frac{(1-x^2)^{\frac{1}{2}} x^{n-1}}{(n-1)!}. \quad (3.38)$$

The first two terms suggest using an expansion in terms of associated Legendre polynomials of order one (see Appendix A.1). Suppose that

$$G_n(x) = \sum_{r=1}^n a_{nr} P_r^1(x) \quad (3.39)$$

where  $a_{nr} = 0$  for  $n < r$  or  $n, r < 1$ , and apply Legendre's associated equation (A.1).

This gives

$$-\sum_{r=1}^n a_{nr} r(r+1) P_r^1 - \sum_{r=1}^{n-1} a_{n-1,r} \frac{d}{dx} ((1-x^2) P_r^1) = -(1-x^2)^{\frac{1}{2}} \frac{x^{n-1}}{(n-1)!}. \quad (3.40)$$

If  $m = 1$  in Equation (A.7), then

$$(2n+1)xP_n^1 = (n+1)P_{n-1}^1 + nP_{n+1}^1. \quad (3.41)$$

Also, substituting (A.6) and (A.9) into (A.10) gives

$$(1-x^2)P_n^{1'} = xP_n^1 - \frac{n(n+1)}{(2n+1)} (P_{n+1}^1 - P_{n-1}^1). \quad (3.42)$$

Using (3.42) in (3.40) gives

$$\begin{aligned} \sum_{r=1}^n a_{nr} r(r+1) P_r^1 + \sum_{r=1}^{n-1} -a_{n-1,r} \left[ x P_r^1 - \frac{r(r+1)}{2r+1} (P_{r+1}^1 - P_{r-1}^1) \right] \\ = (1-x^2)^{\frac{1}{2}} \frac{x^{n-1}}{(n-1)!}, \end{aligned} \quad (3.43)$$

and applying (3.41) implies

$$\begin{aligned} \sum_{r=1}^n a_{nr} r(r+1) P_r^1 - \sum_{r=1}^{n-1} a_{n-1,r} \left[ \frac{r+1}{2r+1} P_{r-1}^1 + \frac{r}{2r+1} P_{r+1}^1 + \frac{r(r+1)}{2r+1} (P_{r+1}^1 - P_{r-1}^1) \right] \\ = (1-x^2)^{\frac{1}{2}} \frac{x^{n-1}}{(n-1)!}. \end{aligned} \quad (3.44)$$

Multiplying by  $P_m^1$  and integrating from  $x = -1$  to  $1$ , using (A.4), gives

$$a_{nm} = -\frac{m+2}{(m+1)(2m+3)} a_{n-1,m+1} + \frac{m-1}{(2m-1)m} a_{n-1,m-1} + \frac{b_{nm}}{m(m+1)} \quad (3.45)$$

where

$$b_{nm} = \frac{2m+1}{2(n-1)!m(m+1)} \int_{-1}^1 (1-x^2)^{\frac{1}{2}} x^{n-1} P_m^1(x) dx. \quad (3.46)$$

Then from Gradshteyn & Ryzhik (1980) [38]

$$b_{n+1,m} = \begin{cases} 0 & \forall (n+m) \text{ even,} \\ \frac{(2m+1)\Gamma(\frac{n+1}{2})\Gamma(\frac{n+2}{2})}{4\Gamma(n+1)\Gamma(\frac{n-m+3}{2})\Gamma(\frac{n+m+4}{2})} & \forall (n+m) \text{ odd,} \end{cases} \quad (3.47)$$

where  $n+1 \geq m$  (see Appendix A.2). This implies that  $a_{n+1,m} = 0$  for  $n+m$  even.

We require the  $a_{ij}$  for  $i \geq j \geq 1$ . Substituting the values of  $b_{ij}$  into the expression for the coefficients  $a_{ij}$  above, gives  $a_{11} = \frac{1}{2}$ ,  $a_{22} = \frac{5}{36}$ ,  $a_{31} = \frac{1}{120}$ ,  $a_{33} = \frac{13}{540}$ ,  $a_{42} = \frac{1}{1296}$  and  $a_{51} = \frac{47}{30240}$ .

We can now calculate what effect the weak ambient flow (with  $\alpha_0 = 0$ ) has on  $\mathbf{p}$  and  $\mathbf{D}$ . The mean value of the perturbation to the orientation is

$$\begin{aligned} \langle \mathbf{p} \rangle^1 &= \int_S \mathbf{p} f^1(\mathbf{p}) d\mathbf{p} \\ &= \mu_\lambda \lambda \eta \int_0^{2\pi} \int_0^\pi (\omega_2 \cos \phi - \omega_1 \sin \phi) \begin{pmatrix} \sin \theta \cos \phi \\ \sin \theta \sin \phi \\ \cos \theta \end{pmatrix} \\ &\quad \times \left[ \sum_{n=1}^{\infty} \lambda^n \sum_{r=1}^n a_{nr} P_r^1(\cos \theta) \right] \sin \theta d\theta d\phi. \end{aligned} \quad (3.48)$$

Integrating with respect to  $\phi$

$$\langle \mathbf{p} \rangle^1 = \begin{pmatrix} \omega_2 \\ -\omega_1 \\ 0 \end{pmatrix} \eta J_1 \quad (3.49)$$

where

$$J_1 = \mu_\lambda \lambda \pi \int_0^\pi \sum_{n=1}^{\infty} \lambda^n \sum_{r=1}^n a_{nr} P_r^1(\cos(\theta)) \sin^2(\theta) d\theta \quad (3.50)$$

Integrating term-by-term, assuming the series to be uniformly convergent, we can use Equation (A.4) with  $k$  set to 1 to get

$$J_1 = \frac{4}{3} \pi \lambda \mu_\lambda \sum_{l=0}^{\infty} \lambda^{2l+1} a_{2l+1,1}. \quad (3.51)$$

In a similar way, we can calculate the second moments

$$\langle \mathbf{p}\mathbf{p} \rangle^1 = \int_S \mathbf{p}\mathbf{p} f^1(\mathbf{p}) d\mathbf{p} \quad (3.52)$$

from which we find that the diagonal terms are zero and that  $\langle \mathbf{p}\mathbf{p} \rangle$  is symmetric. Also,

$$\begin{aligned} \langle \mathbf{p}\mathbf{p} \rangle_{13}^1 &= \langle \mathbf{p}\mathbf{p} \rangle_{31}^1 = \omega_2 \eta J_2, \\ \langle \mathbf{p}\mathbf{p} \rangle_{23}^1 &= \langle \mathbf{p}\mathbf{p} \rangle_{32}^1 = -\omega_1 \eta J_2 \end{aligned} \quad (3.53)$$

where

$$J_2 = \frac{4}{5} \pi \lambda \mu_\lambda \sum_{l=1}^{\infty} \lambda^{2l} a_{2l,2}. \quad (3.54)$$

In both cases, for  $J_1$  and  $J_2$ , it can be seen that the  $a_{ij}$ 's decrease rapidly with increasing values of  $i$  and  $j$ , and the series converge rather quickly even though  $\lambda = 2.2$ . Only three or four terms in the sum are required in each case for an accuracy of two significant figures.

### 3.2.5 First order perturbation for aspherical cells: $\alpha_0 \neq 0$

By considering the form of  $\mathbf{p} \cdot \mathbf{e}^1 \cdot \hat{\boldsymbol{\theta}}$  and  $\mathbf{p} \cdot \mathbf{e}^1 \cdot \mathbf{p}$  in Equations (3.32) we can clearly write the additional contribution from terms in  $\alpha_0$  in Equation (3.34) as

$$\begin{aligned} f^{1*}(x) &= -2\alpha_0 \lambda \mu_\lambda \eta \left\{ \frac{3}{4} e_{33} g_2(x) + \left[ \frac{1}{2} (e_{11} - e_{22}) \cos 2\phi + e_{12} \sin 2\phi \right] g_4(x) \right. \\ &\quad \left. + [e_{13} \cos \phi + e_{23} \sin \phi] g_3(x) \right\} \end{aligned} \quad (3.55)$$

for some functions  $g_2(x)$ ,  $g_3(x)$  and  $g_4(x)$  where  $x = \cos \theta$ . If  $L$  is the operator

$$L\bullet = \frac{\partial}{\partial x} \left( (1-x^2) \frac{\partial}{\partial x} \bullet \right) - \lambda \frac{\partial}{\partial x} ((1-x^2)\bullet), \quad (3.56)$$

then

$$Lg_2 = 2e^{\lambda x} [-\lambda x(1-x^2) + 3x^2 - 1], \quad (3.57)$$

$$Lg_3 - \frac{g_3}{1-x^2} = e^{\lambda x} (1-x^2)^{\frac{1}{2}} [2x^2\lambda - \lambda + 6x], \quad (3.58)$$

$$Lg_4 - \frac{4g_4}{1-x^2} = e^{\lambda x} (1-x^2) [\lambda x + 3]. \quad (3.59)$$

Equation (3.58) can be treated as in Section 3.2.4 but for a different right hand side. Equation (3.59) is similar to the above but requires expansions in terms of  $P_n^2(x)$  instead of  $P_n^1(x)$ . For more details the reader is referred to [85, Appendix A]. Equation (3.57) requires particular mention so as to correct an error in the [85] analysis.

Substituting  $g_2 = G(x)e^{\lambda x}$  into Equation (3.57) gives

$$G'(1-x^2)e^{\lambda x} = -2x(1-x^2)e^{\lambda x} + \text{const.} \quad (3.60)$$

To avoid a singularity at  $x = 1$ , put  $\text{const} = 0$ . Integrating Equation (3.60) gives

$$g_2 = e^{\lambda x} (B - x^2). \quad (3.61)$$

The normalization condition  $\int_{-1}^1 g_2 dx = 0$  (from the normalization condition on f) implies

$$g_2 = e^{\lambda x} \left( 1 - 2\frac{K_1}{\lambda} - x^2 \right) \quad (3.62)$$

We shall now calculate the contributions to  $\langle \mathbf{p} \rangle^1$  which will be indicated by the index (2). First note that

$$f^{1(2)}(\mathbf{p}) = -\frac{3}{2}\alpha_0 \lambda \mu_\lambda \eta e_{33} g_2(x). \quad (3.63)$$

The  $i$  and  $j$  components of  $\langle \mathbf{p} \rangle^{1(2)}$  are zero, as they have  $\sin \phi$  and  $\cos \phi$  terms, and so

$$\langle \mathbf{p} \rangle^{1(2)} = -\frac{3}{2}\alpha_0 \lambda \mu_\lambda \eta e_{33} \mathbf{k} \int_0^\pi \int_0^{2\pi} e^{\lambda \cos \theta} \left( 1 - \frac{2K_1}{\lambda} - \cos^2 \theta \right) \cos \theta \sin \theta d\phi d\theta. \quad (3.64)$$

On substituting  $x = \cos \theta$  and integrating by parts, we get

$$\langle \mathbf{p} \rangle^{1(2)} = -12\alpha_0 \eta \mu_\lambda \pi e_{33} \mathbf{k} \left[ -\frac{K_1}{\lambda} \cosh \lambda + \left( 1 + \frac{K_1}{\lambda} \right) \frac{\sinh \lambda}{\lambda} - \frac{3}{\lambda^2} \cosh \lambda = \frac{3}{\lambda^3} \sinh \lambda \right] \quad (3.65)$$

where  $\mu_\lambda = \lambda/4\pi \sinh \lambda$  and  $K_1 = \coth \lambda - 1/\lambda$ . Hence

$$\langle \mathbf{p} \rangle^{1(2)} = -3\alpha_0 \eta e_{33} K_4 \mathbf{k} \quad (3.66)$$

where<sup>2</sup>

$$K_4 = 1 - \coth^2 \lambda - \frac{2K_1}{\lambda} + \frac{\coth \lambda}{\lambda}. \quad (3.67)$$

### 3.2.6 Summary

There are nine constants defined (to allow comparison with [85]) by

$$\begin{aligned} \mu_\lambda &= \frac{\lambda}{4\pi \sinh \lambda} \\ K_1 &= \coth \lambda - \frac{1}{\lambda} \\ K_2 &= 1 - \coth^2 \lambda + \frac{1}{\lambda^2} \\ K_4 &= 1 - \coth^2 \lambda - \frac{2K_1}{\lambda} + \frac{\coth \lambda}{\lambda} \\ &= K_2 - \frac{K_1}{\lambda} \\ K_5 &= -\frac{2}{\lambda} \left[ 2 + \frac{5}{\lambda^2} - \frac{4 \coth \lambda}{\lambda} - \coth^2 \lambda \right] \\ &= -\frac{2}{\lambda} \left[ 1 + K_2 - \frac{4K_1}{\lambda} \right] \end{aligned} \quad (3.68)$$

$$\begin{aligned} J_1 &= \frac{4}{3} \pi \lambda \mu_\lambda \sum_{l=0}^{\infty} \lambda^{2l+1} a_{2l+1,1} \\ J_2 &= \frac{4}{5} \pi \lambda \mu_\lambda \sum_{l=1}^{\infty} \lambda^{2l} a_{2l,2} \\ J_4 &= \frac{4}{3} \pi \lambda \mu_\lambda \sum_{l=0}^{\infty} \lambda^{2l+1} \tilde{a}_{2l+1,1} \\ J_5 &= \frac{4}{5} \pi \lambda \mu_\lambda \sum_{l=0}^{\infty} \lambda^{2l} \tilde{a}_{2l,2} \\ J_6 &= \frac{16}{5} \pi \lambda \mu_\lambda \sum_{l=0}^{\infty} \lambda^{2l} \bar{a}_{2l,2}, \end{aligned} \quad (3.69)$$

where  $a$ ,  $\tilde{a}$  and  $\bar{a}$  are defined by:-

---

<sup>2</sup>This is not in agreement with [85]. The definition of  $K_4$  here is the corrected version of that appearing in [85].

•

$$a_{nm} = -\frac{m+2}{(m+1)(2m+3)}a_{n-1,m+1} + \frac{m-1}{(2m-1)m}a_{n-1,m-1} + \frac{b_{nm}}{m(m+1)} \quad (3.70)$$

where

$$b_{n+1,m} = \begin{cases} 0 & \forall (n+m) \text{ even,} \\ \frac{(2m+1)\Gamma(\frac{n+1}{2})\Gamma(\frac{n+2}{2})}{4\Gamma(n+1)\Gamma(\frac{n-m+3}{2})\Gamma(\frac{n+m+4}{2})} & \forall (n+m) \text{ odd.} \end{cases} \quad (3.71)$$

•

$$\tilde{a}_{nm} = -\frac{m+2}{(m+1)(2m+3)}\tilde{a}_{n-1,m+1} + \frac{m-1}{(2m-1)m}\tilde{a}_{n-1,m-1} + \frac{\tilde{b}_{nm}}{m(m+1)} \quad (3.72)$$

where

$$\tilde{b}_{n+1,m} = \begin{cases} 0 & \forall (n+m) \text{ even,} \\ -\frac{(2m+1)\Gamma(\frac{n+1}{2})\Gamma(\frac{n+2}{2})(n^2+5n+4+m+m^2)}{16\Gamma(n+1)\Gamma(\frac{n-m+5}{2})\Gamma(\frac{n+m+6}{2})} & \forall (n+m) \text{ odd.} \end{cases} \quad (3.73)$$

•

$$\bar{a}_{nm} = -\frac{m+3}{(m+1)(2m+3)}\bar{a}_{n-1,m+1} + \frac{m-2}{(2m-1)m}\bar{a}_{n-1,m-1} + \frac{\bar{b}_{nm}}{m(m+1)} \quad (3.74)$$

where

$$\bar{b}_{n+1,m} = \begin{cases} 0 & \forall (n+m) \text{ even,} \\ -\frac{(2m+1)\Gamma(\frac{n+2}{2})\Gamma(\frac{n+3}{2})(n+4)}{8\Gamma(n+2)\Gamma(\frac{n-m+5}{2})\Gamma(\frac{n+m+6}{2})} & \forall (n+m) \text{ odd.} \end{cases} \quad (3.75)$$

Hence  $J_i \propto \lambda\mu_\lambda\eta \quad \forall i$ . The mean cell swimming direction is given by

$$\langle \mathbf{p} \rangle = \begin{pmatrix} 0 \\ 0 \\ K_1 \end{pmatrix} + \epsilon \left[ \eta J_1 \begin{pmatrix} \omega_2 \\ -\omega_1 \\ 0 \end{pmatrix} - 2\alpha_0 \eta \begin{pmatrix} e_{13}J_4 \\ e_{23}J_4 \\ \frac{3}{2}e_{33}K_4 \end{pmatrix} \right] + O(\epsilon^2) \quad (3.76)$$

and the expected value of  $\mathbf{pp}$  is

$$\begin{aligned} \langle \mathbf{pp} \rangle &= \begin{pmatrix} \frac{K_1}{\lambda} & 0 & 0 \\ 0 & \frac{K_1}{\lambda} & 0 \\ 0 & 0 & 1 - 2\frac{K_1}{\lambda} \end{pmatrix} + \epsilon \left[ \eta J_2 \begin{pmatrix} 0 & 0 & \omega_2 \\ 0 & 0 & -\omega_1 \\ \omega_2 & -\omega_1 & 0 \end{pmatrix} \right. \\ &\quad \left. - 2\alpha_0 \eta \begin{pmatrix} -\frac{3}{4}e_{33}K_5 + \frac{1}{4}(e_{11} - e_{22})J_6 & \frac{1}{2}e_{12}J_6 & e_{13}J_5 \\ \frac{1}{2}e_{12}J_6 & -\frac{3}{4}e_{33}K_5 - \frac{1}{4}(e_{11} - e_{22})J_6 & e_{23}J_5 \\ e_{13}J_5 & e_{23}J_5 & \frac{3}{2}e_{33}K_5 \end{pmatrix} \right] \\ &\quad + O(\epsilon^2). \end{aligned} \quad (3.77)$$

$\lambda$	$K_1$	$K_2$	$K_4$	$K_5$	
0.3	0.099	0.33	-0.0039	-0.013	
1.0	0.31	0.28	-0.037	-0.048	
2.2	0.57	0.16	-0.10	-0.11	
3.0	0.67	0.10	-0.12	-0.14	
$\lambda$	$J_1$	$J_2$	$J_4$	$J_5$	$J_6$
0.3	0.015	$7.4 \times 10^{-4}$	$-4.6 \times 10^{-3}$	-0.02	-0.040
1.0	0.14	0.024	-0.064	-0.064	-0.12
2.2	0.45	0.16	-0.26	-0.13	-0.20
3.0	0.60	0.27	-0.41	-0.18	-0.22

Table 3.1: Values of the  $K$  and  $J$  constants, for varying values of  $\lambda$ , from Pedley & Kessler (1990) with corrections for  $K_4$ .

The diffusion is then approximated by Equation (1.22) given in the previous chapter. Up to  $O(\epsilon)$ , this is

$$\mathbf{D} = V_s^2 \tau [\langle \mathbf{p} \mathbf{p} \rangle^0 - \langle \mathbf{p} \rangle^0 \langle \mathbf{p} \rangle^0] + \epsilon V_s^2 \tau [\langle \mathbf{p} \mathbf{p} \rangle^1 - (\langle \mathbf{p} \rangle^0 \langle \mathbf{p} \rangle^1 + \langle \mathbf{p} \rangle^1 \langle \mathbf{p} \rangle^0)]. \quad (3.78)$$

On substitution this yields

$$\begin{aligned} \frac{1}{V_s^2 \tau} \mathbf{D} = & \begin{pmatrix} \frac{K_1}{\lambda} & 0 & 0 \\ 0 & \frac{K_1}{\lambda} & 0 \\ 0 & 0 & K_2 \end{pmatrix} + \epsilon \left[ \eta (J_2 - J_1 K_1) \begin{pmatrix} 0 & 0 & \omega_2 \\ 0 & 0 & -\omega_1 \\ \omega_2 & -\omega_1 & 0 \end{pmatrix} \right. \\ & \left. - 2\alpha_0 \eta \begin{pmatrix} -\frac{3}{4} e_{33} K_5 + \frac{1}{4} (e_{11} - e_{22}) J_6 & \frac{1}{2} e_{12} J_6 & e_{13} (J_5 - K_1 J_4) \\ \frac{1}{2} e_{12} J_6 & -\frac{3}{4} e_{33} K_5 - \frac{1}{4} (e_{11} - e_{22}) J_6 & e_{23} (J_5 - K_1 J_4) \\ e_{13} (J_5 - K_1 J_4) & e_{23} (J_5 - K_1 J_4) & \frac{3}{2} e_{33} (K_5 - 2K_1 K_4) \end{pmatrix} \right] \\ & + O(\epsilon^2). \end{aligned} \quad (3.79)$$

### 3.3 Linearizing the main model equations

We start this section by reviewing the main equations of the model which are the incompressibility condition

$$\nabla \cdot \mathbf{u} = 0, \quad (3.80)$$

momentum balance

$$\rho \frac{D\mathbf{u}}{Dt} = -\nabla p_e + nv\Delta\rho\mathbf{g} + \nabla \cdot \boldsymbol{\Sigma}, \quad (3.81)$$

and the cell conservation equation

$$\frac{\partial n}{\partial t} = -\nabla \cdot [n(\mathbf{u} + V_s \langle \mathbf{p} \rangle) - \mathbf{D} \cdot \nabla n]. \quad (3.82)$$

The boundary conditions are of no flow

$$\mathbf{u} = \mathbf{0} \quad \text{at} \quad z = 0, -H, \quad (3.83)$$

and no cell flux perpendicular to the boundaries

$$\mathbf{k} \cdot (n(\mathbf{u} + V_s \langle \mathbf{p} \rangle) - \mathbf{D} \cdot \nabla n) = 0 \quad \text{at} \quad z = 0, -H. \quad (3.84)$$

Here  $\mathbf{u}(\mathbf{x})$  is the fluid velocity,  $\langle \mathbf{p}(\mathbf{x}) \rangle$  is the mean cell direction,  $V_s$  is the mean cell swimming speed,  $\boldsymbol{\Sigma}(\mathbf{x})$  and  $\mathbf{D}(\mathbf{x})$  are the fluid stress and cell diffusion tensors respectively,  $n(\mathbf{x})$  is the local cell concentration,  $p_e(\mathbf{x})$  is the excess pressure,  $v$  is the mean volume of a cell, and  $\Delta\rho$  is the the difference between the cell and fluid density. It has been assumed that the upper and lower surfaces are rigid, which is reasonable because the cells appear to quickly form a ‘solid’ boundary on the fluid surface. A possible improvement could be to have a more general combination of both a rigid and a stress free condition at the upper surface. However, there is some experimental evidence to suggest that the exact form of this boundary condition does not significantly change the general pattern formation. We shall also assume Newtonian stress as the volume

fraction of the cells is much less than one (but see Section 3.4 where the effect of non-Newtonian stress terms is investigated). Hence, for now,

$$\boldsymbol{\Sigma} = 2\mu\mathbf{E}. \tag{3.85}$$

Name	Description	Typical Value	Units
length scale	average cell diameter	10	$\mu m$
length scale	cell spacing	100	$\mu m$
length scale	convection patterns	0.2 – 2.0	$cm$
$D$	diffusivity	$5 \times 10^{-5} - 5 \times 10^{-4}$	$cm^2/s$
$\rho$	fluid density	1	$gm/cm^3$
$\rho + \Delta\rho$	cell density	1.05	$gm/cm^3$
$v$	cell volume	$5 \times 10^{-10}$	$cm^3$
$h$	centre of gravity offset	0 – 0.5	$\mu m$
$\alpha_0$	cell eccentricity	0.20 – 0.31	
$\alpha_0$	including flagella	0.40	
$\alpha_-$	viscous torque parameter	6.8	
$V_s$	cell swimming speed	63	$\mu m/s$
$\mu$	dynamic viscosity	$10^{-2}$	$gm/cm s$
$g$	acceleration due to gravity	$10^3$	$cm/s^2$
$\lambda$	small $\Rightarrow$ random behaviour	2.2	
	large $\Rightarrow$ deterministic		
$\tau$	direction correlation time	1.3	$s$
$B$	gyrotaxis parameter	3.4	$s$
$B$	including flagella	6.3	$s$
$D_r$	cells' rotational diffusivity	0.067	$s^{-1}$
$S_c$	Schmidt number	19	

Table 3.2: Parameter estimates and measurements (from [42, 85, 53, 41]).

An equilibrium solution to the above equations is

$$\mathbf{u} = \mathbf{0}, \quad n = Ne^{\kappa z}, \quad \langle \mathbf{p} \rangle = \langle \mathbf{p} \rangle^0 \quad \text{and} \quad \mathbf{D} = \mathbf{D}^0 \tag{3.86}$$

where  $\kappa$  and  $N$  are unknown constants.  $\kappa^{-1}$  represents a local scale height and is determined by substituting this equilibrium solution into the cell conservation equation,

$$\nabla \cdot [N e^{\kappa z} V_s \langle \mathbf{p} \rangle^0 - \mathbf{D}^0 \cdot \mathbf{k} N \kappa e^{\kappa z}] = 0, \quad (3.87)$$

which implies that

$$\kappa = \frac{V_s \langle \mathbf{p} \rangle_3^0}{D_{33}^0}. \quad (3.88)$$

From Equations (3.76) and (3.79),

$$\kappa = \frac{K_1}{K_2 V_s \tau}. \quad (3.89)$$

On applying the normalisation condition

$$\int_{-H}^0 n dz = H \bar{n}, \quad (3.90)$$

where  $\bar{n}$  is the mean cell concentration and  $n = N e^{\kappa z}$  it follows that

$$N = \frac{H \bar{n} \kappa}{1 - e^{-\kappa H}}. \quad (3.91)$$

Lengths are scaled on  $H$ , the depth of the suspension, cell concentration on  $N$ , and diffusivity on  $V_s^2 \tau$ , where  $V_s$  is the cell swimming speed and  $\tau$  is the direction correlation time, or the time taken for a cell to orientate itself. Hence, the remaining scalings follow:

$$\begin{aligned} \tilde{\mathbf{x}} &= \frac{\mathbf{x}}{H}, & \tilde{n} &= \frac{n}{N}, \\ \tilde{\mathbf{D}} &= \frac{\mathbf{D}}{V_s^2 \tau}, & \tilde{t} &= \frac{t V_s^2 \tau}{H^2}, \\ \tilde{\mathbf{u}} &= \frac{\mathbf{u} H}{V_s^2 \tau}, & \tilde{\Sigma} &= \frac{\Sigma H^2}{V_s^2 \tau \mu} \end{aligned}$$

and

$$\tilde{p}_e = \frac{p_e H^2}{\mu V_s^2 \tau}. \quad (3.92)$$

Dropping tildes, the governing equations become

$$\nabla \cdot \mathbf{u} = 0, \quad (3.93)$$

$$S_c^{-1} \frac{D\mathbf{u}}{Dt} = -\nabla p_e - \gamma n \mathbf{k} + \nabla \cdot \Sigma \quad (3.94)$$

and

$$\frac{\partial n}{\partial t} = -\nabla \cdot \left[ n \mathbf{u} + d \frac{K_2}{K_1} n \langle \mathbf{p} \rangle - \mathbf{D} \cdot \nabla n \right], \quad (3.95)$$

where

$$d = H\kappa = \frac{K_1 H}{K_2 V_s \tau} \quad (3.96)$$

is the ratio of layer depth,  $H$ , to sublayer depth,  $\kappa^{-1}$ . For  $d \gg 1$  we say we have a “deep suspension”, and for  $d \ll 1$  we have a “shallow suspension”. The Schmidt and Rayleigh numbers are defined as

$$S_c = \frac{\nu}{V_s^2 \tau} \quad (3.97)$$

and

$$R = \gamma d = \frac{Nvg\Delta\rho H^4 K_1}{\nu\rho V_s^3 \tau^2 K_2}. \quad (3.98)$$

$R$  is based not on the sub-layer depth as in [19] but on the depth of the whole layer, following [42]. The equilibrium state is  $\mathbf{u} = \mathbf{0}$ ,  $\langle \mathbf{p} \rangle = \langle \mathbf{p} \rangle^0$ ,  $n = e^{dz}$ ,  $\mathbf{D} = \mathbf{D}^0$ ,  $\mathbf{\Sigma} = \mathbf{0}$  and  $\boldsymbol{\omega} = \mathbf{0}$ . Consider a perturbation from this equilibrium solution by setting

$$\begin{aligned} \mathbf{u} &= \epsilon \mathbf{u}^1, \\ \langle \mathbf{p} \rangle &= \langle \mathbf{p} \rangle^0 + \epsilon \langle \mathbf{p} \rangle^1, \\ n &= e^{dz} + \epsilon n^1, \\ p_e &= p_e^0 + \epsilon p_e^1, \\ \mathbf{\Sigma} &= \epsilon \mathbf{\Sigma}^1, \\ \mathbf{D} &= \mathbf{D}^0 + \epsilon \mathbf{D}^1. \end{aligned} \quad (3.99)$$

To  $O(\epsilon)$ , the governing equations become

$$\nabla \cdot \mathbf{u}^1 = 0, \quad (3.100)$$

$$S_c^{-1} \frac{\partial \mathbf{u}^1}{\partial t} = -\nabla p_e^1 - \gamma n^1 \mathbf{k} + \nabla \cdot \mathbf{\Sigma}^1 \quad (3.101)$$

and

$$\frac{\partial n^1}{\partial t} = -\nabla \cdot \left[ e^{dz} \mathbf{u}^1 + d \frac{K_2}{K_1} e^{dz} \langle \mathbf{p} \rangle^1 + d \frac{K_2}{K_1} n^1 \langle \mathbf{p} \rangle^0 - \mathbf{D}^0 \cdot \nabla n^1 - d e^{dz} \mathbf{D}^1 \cdot \mathbf{k} \right]. \quad (3.102)$$

These five p.d.e.’s in five unknowns are reduced to two p.d.e.’s in two unknowns as follows. Expanding the third equation we obtain

$$\begin{aligned} \frac{\partial n^1}{\partial t} &= -d e^{dz} u_3^1 - d \frac{K_2}{K_1} e^{dz} \partial_i \langle \mathbf{p} \rangle_i^1 - d^2 \frac{K_2}{K_1} e^{dz} \langle \mathbf{p} \rangle_3^1 \\ &\quad - d \frac{K_2}{K_1} \langle \mathbf{p} \rangle_i^0 \partial_i n^1 + D_{ij}^0 \partial_i \partial_j n^1 + D_{33}^1 d^2 e^{dz} + d e^{dz} \partial_i D_{i3}^1, \end{aligned} \quad (3.103)$$

where  $\partial_i \equiv \partial/\partial x_i$ . Consider the components in the terms of  $\partial_i \langle \mathbf{p} \rangle_i^1$  and  $\partial_i D_{i3}^1$  (Equations 3.76 and 3.79). We know

$$\begin{aligned}\partial_1 \omega_2 &= \partial_3 \partial_1 u_1^1 - \partial_1 \partial_1 u_3^1 \\ \partial_2 \omega_1 &= \partial_2 \partial_2 u_3^1 - \partial_3 \partial_2 u_2^1.\end{aligned}$$

Since  $\partial_3 (\partial_i u_i^1) = 0$ , we get

$$\partial_1 \omega_2 - \partial_2 \omega_1 = -\partial_i \partial_i u_3^1 \quad (3.104)$$

and similarly

$$\begin{aligned}\partial_1 e_{13} + \partial_2 e_{23} &= \frac{1}{2} (\partial_3 \partial_1 u_1^1 + \partial_1 \partial_1 u_3^1 + \partial_3 \partial_2 u_2^1 + \partial_2 \partial_2 u_3^1) \\ &= \frac{1}{2} (-\partial_3 \partial_3 u_3^1 + \partial_1 \partial_1 u_3^1 + \partial_2 \partial_2 u_3^1) \\ &= \frac{1}{2} \nabla^2 u_3^1 - \partial_3 \partial_3 u_3^1.\end{aligned} \quad (3.105)$$

Hence from Equation (3.76) we obtain

$$\partial_i \langle \mathbf{p} \rangle_i^1 = -\eta J_1 \nabla^2 u_3^1 - 2\alpha_0 \eta \left[ J_4 \left( \frac{1}{2} \nabla^2 u_3^1 - \partial_3 \partial_3 u_3^1 \right) + \frac{3}{2} K_4 \partial_3 \partial_3 u_3^1 \right] \quad (3.106)$$

or

$$\partial_i \langle \mathbf{p} \rangle_i^1 = -\eta (J_1 + \alpha_0 J_4) \nabla^2 u_3^1 + \eta \alpha_0 (2J_4 - 3K_4) \partial_3 \partial_3 u_3^1. \quad (3.107)$$

Similarly, from equation (3.79) we obtain

$$\begin{aligned}\partial_i D_{i3}^1 &= -\eta \nabla^2 u_3^1 (J_2 - J_1 K_1) - 2\alpha_0 \eta \left[ (J_5 - K_1 J_4) \left( \frac{1}{2} \nabla^2 u_3^1 - \partial_3 \partial_3 u_3^1 \right) \right. \\ &\quad \left. + \frac{3}{2} (K_5 - 2K_1 K_4) \right] \partial_3 \partial_3 u_3^1,\end{aligned} \quad (3.108)$$

which gives

$$\begin{aligned}\partial_i D_{i3}^1 &= -\eta (J_2 - J_1 K_1 + \alpha_0 (J_5 - K_1 J_4)) \nabla^2 u_3^1 \\ &\quad + \eta \alpha_0 (2(J_5 - K_1 J_4) - 3(K_5 - 2K_1 K_4)) \partial_3 \partial_3 u_3^1.\end{aligned} \quad (3.109)$$

On defining the following functions,

$$\begin{aligned}H_1 &= -\eta (J_1 + \alpha_0 J_4), \\ H_2 &= \eta \alpha_0 (2J_4 - 3K_4), \\ H_3 &= -\eta (J_2 - J_1 K_1 + \alpha_0 (J_5 - K_1 J_4)), \\ H_4 &= \eta \alpha_0 (2(J_5 - K_1 J_4) - 3(K_5 - 2K_1 K_4))\end{aligned} \quad (3.110)$$

we have

$$\partial_i \langle \mathbf{p} \rangle_i^1 = H_1 \nabla^2 u_3^1 + H_2 \partial_3 \partial_3 u_3^1$$

and

$$\partial_i D_{i3}^1 = H_3 \nabla^2 u_3^1 + H_4 \partial_3 \partial_3 u_3^1. \quad (3.111)$$

Substituting Equations (3.111) into Equation (3.103) yields

$$\begin{aligned} \frac{\partial n^1}{\partial t} = & de^{dz} \left\{ -1 + \left[ H_3 - \frac{K_2}{K_1} H_1 \right] \nabla^2 \right. \\ & + \left[ H_4 - \frac{K_2}{K_1} H_2 \right] \partial_3 \partial_3 + 3\alpha_0 \eta \left[ d \frac{K_2}{K_1} K_4 - d(K_5 - 2K_1 K_4) \right] \partial_3 \left. \right\} u_3^1 \\ & + \left\{ \frac{K_1}{\lambda} (\partial_1 \partial_1 + \partial_2 \partial_2) + dK_2 \partial_3 \partial_3 - K_2 \partial_3 \right\} n^1. \end{aligned} \quad (3.112)$$

Now consider Equation (3.101) and rewrite  $\nabla \cdot \boldsymbol{\Sigma}^1$  as  $\nabla^2 \mathbf{u}^1$ . If we take the divergence of Equation (3.101), and take the Laplacian of the third component of Equation (3.101) we get the system of equations

$$0 = -\nabla^2 p_e^1 - \gamma \partial_3 n^1 \quad (3.113)$$

and

$$S_c^{-1} \frac{\partial}{\partial t} (\nabla^2 u_3^1) = -\partial_3 \nabla^2 p_e^1 + \nabla^2 \nabla^2 u_3^1 - \gamma \nabla^2 n^1. \quad (3.114)$$

Substituting the former into the latter gives

$$S_c^{-1} \frac{\partial}{\partial t} (\nabla^2 u_3^1) = \nabla^4 u_3^1 - \gamma \nabla^2 n^1 + \gamma \partial_3 \partial_3 n^1. \quad (3.115)$$

We now have two equations, (3.112) and (3.115), in terms of the independent variables  $n^1$  and  $u_3^1$  only.

The next step involves introducing a horizontal planform and an exponential component in  $t$ . The particular choices of normal modes are

$$u_3^1 = W(z) e^{i(lx+my)+\sigma t} \quad (3.116)$$

and

$$n^1 = \Phi(z) e^{i(lx+my)+\sigma t}. \quad (3.117)$$

On substituting (3.117) into Equations (3.115) and (3.112), we get

$$\left(\frac{\sigma}{S_c} + k^2 - \frac{d^2}{dz^2}\right) \left(k^2 - \frac{d^2}{dz^2}\right) W = -Rd^{-1}k^2\Phi \quad (3.118)$$

and

$$\begin{aligned} \left(K_2 \frac{d^2}{dz^2} - K_2 d \frac{d}{dz} - \frac{K_1}{\lambda} k^2 - \sigma\right) \Phi = de^{dz} \left[ 1 - \left(H_3 + H_4 - (H_2 + H_1) \frac{K_2}{K_1}\right) \frac{d^2}{dz^2} \right. \\ \left. - 3d\alpha_0 \eta \left(\frac{K_2}{K_1} K_4 - (K_5 - 2K_1 K_4)\right) \frac{d}{dz} + \left(H_3 - \frac{K_2}{K_1} H_1\right) k^2 \right] W \end{aligned} \quad (3.119)$$

where  $k = \sqrt{l^2 + m^2}$ .

Using the definitions, (3.110), for the  $H_i$ , we define

$$\begin{aligned} P_1 &= J_1 \left(K_1 + \frac{K_2}{K_1}\right) - J_2, \\ P_2 &= -J_5 + K_1 J_4 + 2(J_5 - K_1 J_4) - 3(K_5 - 2K_1 K_4) - \frac{K_2}{K_1} (J_4 - 3K_4), \\ P_3 &= 3 \left(K_4 \left(2K_1 + \frac{K_2}{K_1}\right) - K_5\right), \\ P_4 &= J_4 \left(K_1 + \frac{K_2}{K_1}\right) - J_5 \end{aligned} \quad (3.120)$$

from which we see that  $P_2 = P_3 - P_4$ . We can thus rewrite Equation (3.119) as

$$\begin{aligned} \left(K_2 \frac{d^2}{dz^2} - K_2 d \frac{d}{dz} - \frac{K_1}{\lambda} k^2 - \sigma\right) \Phi \\ = de^{dz} \left[ 1 - \eta(P_1 + P_2 \alpha_0) \frac{d^2}{dz^2} - \eta \alpha_0 d P_3 \frac{d}{dz} + \eta(P_1 + P_4 \alpha_0) k^2 \right] W. \end{aligned} \quad (3.121)$$

Finally, if we define

$$\begin{aligned} P_V &= K_2, \\ P_H &= \frac{K_1}{\lambda}, \\ P_5 &= P_1 - P_4 \alpha_0 + P_3 \alpha_0, \\ P_6 &= P_3 \alpha_0, \\ P_7 &= P_1 + P_4 \alpha_0, \end{aligned} \quad (3.122)$$

then we can write the last equation as

$$\begin{aligned} \left(P_V \frac{d^2}{dz^2} - P_V d \frac{d}{dz} - P_H k^2 - \sigma\right) \Phi \\ = de^{dz} \left[ 1 - \eta P_5 \frac{d^2}{dz^2} - \eta P_6 d \frac{d}{dz} + \eta P_7 k^2 \right] W, \end{aligned} \quad (3.123)$$

where the  $P_i$  are functions of the parameter  $\lambda = (2D_r B)^{-1}$  and the shape parameter  $\alpha_0$  only. Pedley & Kessler (1990) [85] use the data of Hill & Häder (1996) [41] to calculate  $\lambda$  as lying between 1.85 and 2.63. They choose to take an average value, as we shall, of 2.2. As we know  $B$  from Table (3.2), we can calculate  $D_r$  to be  $0.067 s^{-1}$ . The cell eccentricity,  $\alpha_0$ , is in the range 0.2 – 0.31 but Jones (1995) has calculated an effective  $\alpha_0$  of 0.40 to allow for the cells' flagella and swimming characteristics. The direction correlation time,  $\tau$ , can be calculated from observations of the horizontal diffusion to be 1.3 s ([85]), but see Section 3.8 where we use a direct observational estimate of 5 s.

$\alpha_0$	$\lambda$	$P_5$	$P_6$	$P_7$	$P_H$	$P_V$
0.0	2.2	0.22	0.0	0.22	0.26	0.16
0.2	0.3	0.050	-0.00017	0.050	0.33	0.33
0.2	1.0	0.14	-0.0050	0.14	0.31	0.28
0.2	2.2	0.22	-0.022	0.20	0.26	0.16
0.2	3.0	0.23	-0.028	0.19	0.22	0.10
0.31	2.2	0.21	-0.035	0.19	0.26	0.16
0.40	2.2	0.21	-0.044	0.18	0.26	0.16
1.00	2.2	0.20	-0.11	0.13	0.26	0.16

Table 3.3: The values of the constants  $P$  for typical values of  $\lambda$  and  $\alpha_0$ .

The boundary conditions (3.83) become

$$W = 0 \quad \text{on } z = 0, -1 \tag{3.124}$$

and

$$\frac{dW}{dz} = 0 \quad \text{on } z = 0, -1. \tag{3.125}$$

By taking the  $z$  component of the flux and applying the above conditions, Equation (3.84) becomes

$$\Phi d - \frac{d\Phi}{dz} = 0 \quad \text{on } z = 0, -1. \tag{3.126}$$

The exponential appearing in Equation (3.123) prevents an explicit solution from being found and we must resort to finding numerical or asymptotic solutions.

### 3.4 The effect of leading order non-Newtonian stress terms

Pedley & Kessler (1990) [85] have considered a number of additional effects that the micro-organisms can have on the fluid through the variation in fluid stresses.

Three specific effects were investigated each of which are discussed in more detail in [85].

- $\Sigma^p$ . Rigid cells do not let fluid deform as it would in the absence of cells (Batchelor, 1970 [3]). The resulting stresses are termed Batchelor stresses. The stress system for a suspension of spheroids was analysed by Batchelor (1970) [3].
- $\Sigma^d$ . Stresses associated with the effective particle rotation caused by rotary diffusion of the cells axis of symmetry. This is explained by Brenner (1972) [10] and also by Hinch & Leal (1972) [46].
- $\Sigma^s$ . The stresslets (see [3]) caused by the swimming actions of the individual micro-organisms.

Pedley & Kessler (1990) [85] report that,

“It fortunately turns out that, for the parameter values appropriate to *Chlamydomonas nivalis*, the quantities  $\Sigma^p$  and  $\Sigma^d$  are negligibly small so errors in computing them are unimportant.”

In fact, they show that these terms have no qualitative effect and no significant quantitative effect ( $\Sigma^d < 1\%$  of  $\Sigma^s$ ) and are dropped. We choose to drop the Batchelor stresses from the outset. This just leaves terms for the intrinsic swimming stresslets and rotational diffusion which can be combined and are calculated to be (from [85])

$$\Sigma^{sd} = nS' \left( \langle \mathbf{pp} \rangle - \frac{1}{3} \mathbf{I} \right) \quad (3.127)$$

where

$$S' = S + 2\mu v D_r \alpha_5 \quad (3.128)$$

$$S = 6\pi b \mu V_s \alpha_F l \cos(\gamma_f), \quad (3.129)$$

$$\gamma_f = \frac{\cosh^{-1} r}{r(r^2 - 1)^{\frac{1}{2}}} \quad (3.130)$$

and

$$r = \frac{a}{b} = \sqrt{\frac{1 + \alpha_0}{1 - \alpha_0}}. \quad (3.131)$$

$a$  is half of the cell length,  $b$  is half of the cell breadth and  $l$  is the length of the thrust points from the cell's centre of gravity, which are on average inclined at an angle  $\gamma_f$  from  $\mathbf{p}$  (see [85]).  $\alpha_5 = 3.15$  ([85]) and  $\alpha_F \approx 1.08$  as calculated by Happel & Brenner (1965) [39]. In the definition of  $S'$ ,  $S$  is the term due to the intrinsic stresslets and the other term is due to rotational diffusion. Hence, we can use Equation (3.77) to calculate  $\boldsymbol{\Sigma}^{sd}$  to leading order. (Or we can use the constants  $A$  to  $G$  given in Pedley & Kessler, 1990 [85], correcting the first term for  $C$  by changing the misprinted  $J_4$  to a  $J_6$ .) The non-zero stress at zero flow does no more than alter the first order excess pressure term. Non-dimensionalising  $\boldsymbol{\Sigma}^{sd}$ , we obtain the equation for fluid flow at  $O(\epsilon)$ , as

$$S_c^{-1} \frac{\partial \mathbf{u}^1}{\partial t} = -\nabla p_e^1 - \gamma n^1 \mathbf{k} + \nabla^2 \mathbf{u}^1 + \nabla \cdot \boldsymbol{\Sigma}^{sd}, \quad (3.132)$$

where

$$\boldsymbol{\Sigma}^{sd} = \chi^{sd} n \left( \langle \mathbf{p}\mathbf{p} \rangle - \frac{1}{3} \mathbf{I} \right) \quad (3.133)$$

and

$$\chi^{sd} = \frac{\mu V_s^2 \tau S N}{H^2}. \quad (3.134)$$

$\nabla \cdot \boldsymbol{\Sigma}^{sd}$  can be rewritten as

$$\begin{aligned} \nabla \cdot \boldsymbol{\Sigma}^{sd} &= K_3 \frac{\chi^{sd}}{3} \begin{pmatrix} 0 \\ 0 \\ 2 \end{pmatrix} \partial_3 n^0 + \epsilon K_3 \frac{\chi^{sd}}{3} \begin{pmatrix} -\partial_1 n^1 \\ -\partial_2 n^1 \\ 2\partial_3 n^1 \end{pmatrix} \\ &+ \epsilon \chi^{sd} \begin{pmatrix} \partial_1 \langle \mathbf{p}\mathbf{p} \rangle_{11} n^0 + \partial_2 \langle \mathbf{p}\mathbf{p} \rangle_{21} n^0 + \partial_3 (\langle \mathbf{p}\mathbf{p} \rangle_{31} n^0) \\ \partial_1 \langle \mathbf{p}\mathbf{p} \rangle_{21} n^0 + \partial_2 \langle \mathbf{p}\mathbf{p} \rangle_{22} n^0 + \partial_3 (\langle \mathbf{p}\mathbf{p} \rangle_{32} n^0) \\ \partial_1 \langle \mathbf{p}\mathbf{p} \rangle_{31} n^0 + \partial_2 \langle \mathbf{p}\mathbf{p} \rangle_{32} n^0 + \partial_3 (\langle \mathbf{p}\mathbf{p} \rangle_{33} n^0) \end{pmatrix} \\ &+ O(\epsilon^2). \end{aligned} \quad (3.135)$$

Utilizing Equations (3.77), (3.104) and (3.105) we find that the Laplacian of the third component of  $\nabla \cdot \boldsymbol{\Sigma}^{sd}$  at  $O(\epsilon)$  is

$$\begin{aligned} \nabla^2 \left( \nabla \cdot \boldsymbol{\Sigma}^{sd1} \right)_3 &= \chi^{sd} \nabla^2 \left[ \frac{2K_3}{3} \partial_3 n^1 - (\alpha_0 J_5 + J_2) n^0 \nabla^2 u_3^1 \right. \\ &\quad \left. + \alpha_0 (2J_5 - 3K_5) n^0 \partial_3^2 n_3^1 - 3\alpha_0 K_5 \partial_3 n^0 \partial_3 u_3^1 \right] \end{aligned} \quad (3.136)$$

and the divergence of  $\nabla \cdot \boldsymbol{\Sigma}^{sd}$  at  $O(\epsilon)$  becomes

$$\nabla \cdot \left( \nabla \cdot \boldsymbol{\Sigma}^{sd1} \right) = \frac{K_3}{3} \chi^{sd} [3\partial_3^2 n^1 - \nabla^2 n^1]$$

$$\begin{aligned}
& + n^0 \chi^{sd} \partial_3 \left[ \left( \frac{3}{2} \alpha_0 K_5 - \frac{\alpha_0}{2} J_6 - 2\alpha_0 J_5 - 2J_2 \right) \nabla^2 u_3^1 \right. \\
& \quad \left. + \alpha_0 \left( -\frac{9}{2} K_5 + \frac{1}{2} J_6 + 4J_5 \right) \partial_3^2 u_3^1 \right] \\
& + \partial_3 n^0 \chi^{sd} \left[ (-2\alpha_0 J_5 - 2J_2) \nabla^2 u_3^1 + \alpha_0 (4J_5 - 3K_5) \partial_3^2 u_3^1 \right] \\
& + \partial_3^2 n^0 \chi^{sd} \left[ -3\alpha_0 K_5 \partial_3 u_3^1 \right]. \tag{3.137}
\end{aligned}$$

Both of these expressions are in terms of the dependent variables  $n^1$  and  $u_3^1$  and their derivatives. Hence we can use the same method as before to reduce the system of five equations in five unknowns to two equations in two unknowns.

Taking the divergence of Equation (3.132), and the Laplacian of the third component of Equation (3.132) we obtain the following system of equations at  $O(\epsilon)$ :

$$0 = -\nabla^2 p_e^1 - \gamma \partial_3 n^1 + \nabla \cdot (\nabla \cdot \boldsymbol{\Sigma}^{sd1}) \tag{3.138}$$

and

$$S_c^{-1} \frac{\partial}{\partial t} (\nabla^2 u_3^1) = -\partial_3 \nabla^2 p_e^1 + \nabla^2 \nabla^2 u_3^1 - \gamma \nabla^2 n^1 + \nabla^2 (\nabla \cdot \boldsymbol{\Sigma}^{sd1})_3. \tag{3.139}$$

Substituting the first equation into the second gives

$$S_c^{-1} \frac{\partial}{\partial t} (\nabla^2 u_3^1) = \nabla^4 u_3^1 - \gamma \nabla^2 n^1 + \gamma \partial_3 \partial_3 n^1 - \partial_3 \nabla \cdot (\nabla \cdot \boldsymbol{\Sigma}^{sd1}) + \nabla^2 (\nabla \cdot \boldsymbol{\Sigma}^{sd1})_3. \tag{3.140}$$

This equation was derived to highlight the additional leading order terms due to a non-Newtonian stress. In particular, odd ordered derivatives are introduced that affect the qualitative form of the equations. In general, if  $V_s$ , the cell size and the cell concentration are sufficiently large then the additional terms could be significant. However, for *Chlamydomonas nivalis* the terms are negligibly small.  $S$  can be estimated from the values in Table 3.2 to be  $S \approx 4 \times 10^{-10}$  and the other term in the definition of  $S'$  is estimated as  $2\mu v D_r \alpha_5 \approx 2 \times 10^{-12}$  and, hence, using Equation (3.91) and (3.129),

$$\chi^{sd} = \frac{\mu V_s^2 \tau S' N}{H^2} \approx (6\pi b \mu^2 \alpha_{Fl} \cos(\gamma_f)) \frac{K_1}{K_2} V_s^2 \frac{\bar{n}}{H} \approx 10^{-13} \times \frac{\bar{n}}{H} \tag{3.141}$$

where  $\bar{n}$  is concentration in cells per  $cm^3$  and  $H$  is suspension depth in  $cm$ . Hence,  $\chi^{sd}$ , is negligibly small compared with the Newtonian term which is  $O(1)$ . Also, Equation (3.140) is far more complicated than Equation (3.115). In the following sections, we shall ignore the additional stress terms and concentrate on the effects of including

non-deterministic swimming cells. Future work could consider the above equations, as the non-Newtonian stress terms may become significant in the non-linear regime where local variations in concentration are large.

### 3.5 Asymptotic analysis

The work in this section uses similar techniques to those in [42]. (See Van Dyke, 1964 [114], for a description of the ideas involved.) We shall consider Equations (3.118) and (3.123) plus the boundary conditions (3.124), (3.125) and (3.126) above. If we assume that *Chlamydomonas nivalis* is a self propelled spheroid and use the corresponding values  $\lambda = 2.2$  and  $\alpha_0 = 0.31$  (but see Sections 3.6, 3.7, 3.8 and 3.9 for recent estimates) then

$$P_V \approx 0.16$$

$$P_H \approx 0.26$$

$$P_5 \approx 0.21$$

$$P_6 \approx -0.035$$

$$P_7 \approx 0.19.$$

$P_6$  appears to be too small to be classed as order one but by noting that  $P_5$ ,  $P_6$  and  $P_7$  always appear in Equation (3.123) multiplied by  $\eta$  (and  $\eta \approx 33d^{-2}$ ) then it simplifies matters to consider  $P_i$  order one and  $\eta$  order  $d^n$  for some  $n$  and  $i = 5, 6, 7$ . Henceforth, we shall assume that all of the  $P$ 's are of the same order and all approximately of order one. This assumption is justified asymptotically provided we either assume that  $d$  is much smaller than (for shallow layers) or much larger than (for deep layers)  $P_i$  for all  $i$ . Using the definition of  $d$  and Equation (3.9) we can write

$$\eta = \frac{BK_1^2}{\tau K_2^2} d^{-2} \approx 33d^{-2} \tag{3.142}$$

where we have used  $B = 3.4$  and  $\tau = 1.3$ .

There are two natural asymptotic expansions which could be considered here; one for small  $d$  and one for large  $d$ . Firstly it is important to understand what we mean by small  $d$ . By Equation (3.96)

$$H = \frac{K_2 V_s \tau d}{K_1} \tag{3.143}$$

then, from Tables 3.1 and 3.2,  $H = 23d \mu m$ . If  $d = 0.1$ , then the depth of the fluid is equal to  $2.3 \mu m$ , which is very small for a fluid layer! A typical experimental depth of  $5mm$  gives  $d = 220$  (2 s.f.), which is well within the validity for the large  $d$  expansion. The small  $d$  expansion, however, is important for comparison with the numerical solutions in the next section.

### 3.5.1 Shallow layer analysis ( $0 < d \ll 1$ )

For the shallow layer, suppose that the pattern wavelength is comparable with the sublayer depth and set  $\tilde{k} = k/d$  where  $\tilde{k} \sim 1$ . There are six boundary conditions which imply that we need to keep the highest order derivatives. The leading order balance in Equation (3.118) must be

$$\left(D^2 - \frac{\sigma}{S_c}\right) D^2 W = -d\tilde{k}^2 R\Phi. \quad (3.144)$$

Otherwise we obtain the trivial solution. Here and henceforth  $D \equiv d/dz$ . Without loss of generality, we shall always assume  $\Phi \sim 1$  and hence  $W \sim dR$ . Close to neutrally stable solutions we can neglect  $\sigma$  and there are then four non-trivial leading order balances of Equation (3.123) to be considered.

- **CASE I**

$$D^2 \Phi = 0 \quad (3.145)$$

which implies  $R \ll O(d^{-2})$  and  $\eta R \ll O(d^{-2})$ .

- **CASE II**

$$P_V D^2 \Phi = dW \quad (3.146)$$

which implies  $R \sim d^{-2}$  and  $\eta R \ll O(d^{-2})$ .

- **CASE III**

$$P_V D^2 \Phi = d [W - \eta P_5 D^2 W] \quad (3.147)$$

which implies  $R \sim d^{-2}$  and  $\eta R \sim d^{-2}$ .

- **CASE IV**

$$P_V D^2 \Phi = -d\eta P_5 D^2 W \quad (3.148)$$

which implies  $R \ll O(d^{-2})$  and  $\eta R \sim d^{-2}$ .

This is summed up in Figure (3.1). Case III leads to lengthy numerical analysis and so this case has not been considered further.

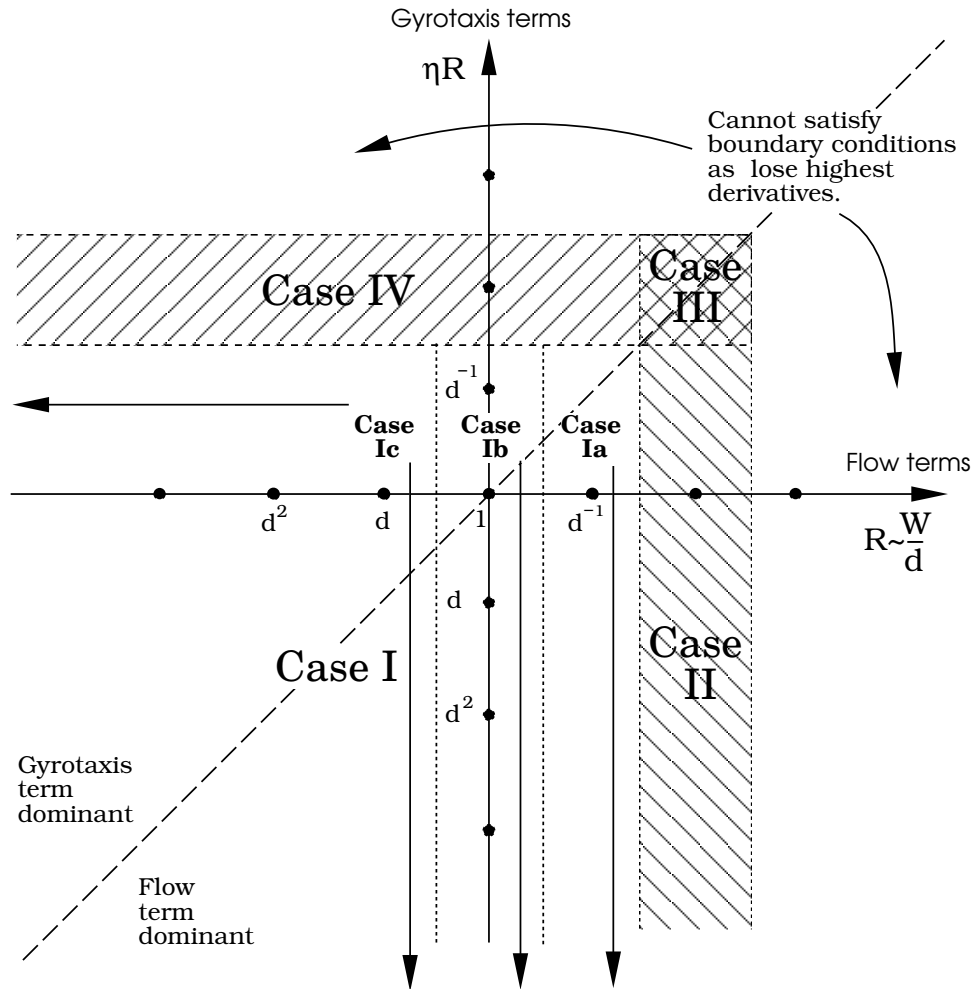


Figure 3.1: Regions of the parameter space covered by the leading order balances of the linear equations for bioconvection in a shallow layer ( $d \ll 1$ ). There are four major balances.

- **CASE I** No terms appear on the right hand side at leading order. We divide case I into three regions (see Figure 3.1) with similar behaviour, which covers every possibility within the region in just three calculations.

**CASE Ia:**

Firstly consider the scaling

$$\eta \sim 1, \quad R \sim d^{-1}, \quad W \sim 1, \quad (3.149)$$

and try a solution of the form

$$R = \sum_{n=-1}^{\infty} d^n R_n, \quad W = \sum_{n=0}^{\infty} d^n W_n, \quad \Phi = \sum_{n=0}^{\infty} d^n \Phi_n. \quad (3.150)$$

At this stage we shall also assume that  $\sigma$  is of the form

$$\sigma = \sum_{n=0}^{\infty} d^n \sigma_n \quad (3.151)$$

so that it appears at leading order. Later it will be shown that  $\sigma \sim d$  and that, for the whole of case Ia,  $\sigma$  is positive and hence the solution is always unstable. The leading order gives

$$\begin{aligned} -\frac{\sigma_0}{S_c} D^2 W_0 + D^4 W_0 + R_{-1} \tilde{k}^2 \Phi_0 &= 0 \\ -\sigma_0 \Phi_0 + P_V D^2 \Phi_0 &= 0 \end{aligned} \quad (3.152)$$

with boundary conditions  $D\Phi_0 = W_0 = DW_0 = 0$  on  $z = 0, -1$ . This implies that  $\Phi_0 = A e^{i \frac{\sigma_0}{P_V} z} + B e^{-i \frac{\sigma_0}{P_V} z}$ . The boundary conditions imply that either  $\sigma_0 = 0$  or  $\Phi \neq 1$ . Hence  $\sigma \leq O(d)$  and the leading order solution is

$$\Phi_0 = 1, \quad W_0 = -\frac{R_{-1} \tilde{k}^2}{24} (z^4 + 2z^3 + z^2). \quad (3.153)$$

The second order gives

$$\begin{aligned} D^4 W_1 + R_{-1} \tilde{k}^2 \Phi_1 &= -\tilde{k}^2 R_0 \Phi_0 + \frac{\sigma_1}{S_c} D^2 W_0 \\ P_V D^2 \Phi_1 &= P_V D \Phi_0 - \eta P_5 D^2 W_0 + W_0 + \sigma_1 \Phi_0 \end{aligned} \quad (3.154)$$

with boundary conditions  $D\Phi_1 - \Phi_0 = DW_1 = W_1 = 0$  at  $z = 0, -1$ . A solvability condition for this set of equations is that the integral of the second equation over  $z = 0, -1$  must equal zero. This gives

$$\sigma_1 = \frac{R_{-1} \tilde{k}^2}{720}. \quad (3.155)$$

Hence  $\sigma$  is always positive.  $\eta$  plays no part here and we can reduce it arbitrarily and hence cover the whole of case Ia.

**CASE Ic:**

Now consider the scaling

$$\eta \sim d^{-2}, \quad R \sim d, \quad W \sim d^2, \quad (3.156)$$

at the top of the region for case Ic and hence consider a solution of the form

$$R = \sum_{n=1}^{\infty} d^n R_n, \quad W = \sum_{n=2}^{\infty} d^n W_n, \quad \Phi = \sum_{n=0}^{\infty} d^n \Phi_n, \quad \eta = d^{-2} \eta_{-2}. \quad (3.157)$$

At this stage assume  $\sigma$  to be of the form

$$\sigma = \sum_{n=1}^{\infty} d^n \sigma_n \quad (3.158)$$

as we know  $\sigma_0 = 0$  from above. The leading order gives

$$\begin{aligned} D^4 W_2 + R_1 \tilde{k}^2 \Phi_0 &= 0 \\ P_V D^2 \Phi_0 &= 0 \end{aligned} \quad (3.159)$$

with boundary conditions  $D\Phi_0 = W_2 = DW_2 = 0$  on  $z = 0, -1$ . This has solution

$$\Phi_0 = 1, \quad W_2 = -\frac{R_1 \tilde{k}^2}{24} (z^4 + 2z^3 + z^2). \quad (3.160)$$

The second order gives

$$\begin{aligned} D^4 W_3 + R_1 \tilde{k}^2 \Phi_1 &= -\tilde{k}^2 R_2 \Phi_0 + \frac{\sigma_1}{S_c} D^2 W_2 \\ P_V D^2 \Phi_1 &= P_V D \Phi_0 - \eta_{-2} P_5 D^2 W_2 + \sigma_1 \Phi_0 \end{aligned} \quad (3.161)$$

with boundary conditions  $D\Phi_1 - \Phi_0 = DW_3 = W_3 = 0$  at  $z = 0, -1$ . The solvability condition, on the second equation as before, now implies  $\sigma_1 = 0$ . Considering the second equation at third order and integrating we get the solvability condition  $\sigma_2 = -P_H \tilde{k}^2$ . Hence all modes are stable for this choice of scaling for  $R$ .

**CASE Ib:**

So now consider the scaling

$$\eta \sim d^{-1}, \quad R \sim 1, \quad W \sim d \quad (3.162)$$

for case Ib, and expand the variables as

$$R = \sum_{n=0}^{\infty} d^n R_n, \quad W = \sum_{n=1}^{\infty} d^n W_n, \quad \Phi = \sum_{n=0}^{\infty} d^n \Phi_n, \quad \eta = d^{-1} \eta_{-1}. \quad (3.163)$$

As before, assume  $\sigma$  to be of the form

$$\sigma = \sum_{n=1}^{\infty} d^n \sigma_n \quad (3.164)$$

as  $\sigma_0 = 0$  from above. The leading order gives

$$\begin{aligned} D^4 W_1 + R_0 \tilde{k}^2 \Phi_0 &= 0 \\ P_V D^2 \Phi_0 &= 0 \end{aligned} \quad (3.165)$$

with boundary conditions  $D\Phi_0 = W_1 = DW_1 = 0$  on  $z = 0, -1$ . This has the solution

$$\Phi_0 = 1, \quad W_1 = -\frac{R_0 \tilde{k}^2}{24} (z^4 + 2z^3 + z^2). \quad (3.166)$$

The second order gives

$$\begin{aligned} D^4 W_2 + R_0 \tilde{k}^2 \Phi_1 &= -\tilde{k}^2 R_1 \Phi_0 + \frac{\sigma_1}{S_c} D^2 W_1, \\ P_V D^2 \Phi_1 &= P_V D\Phi_0 - \eta_{-1} P_5 D^2 W_1 + \sigma_1 \Phi_0 \end{aligned} \quad (3.167)$$

with boundary conditions  $D\Phi_1 - \Phi_0 = DW_2 = W_2 = 0$  at  $z = 0, -1$ . The solvability condition again implies  $\sigma_1 = 0$ . The third order gives

$$\begin{aligned} D^4 W_3 + R_0 \tilde{k}^2 \Phi_2 &= 2\tilde{k}^2 D^2 W_1 - \tilde{k}^2 R_2 \Phi_0 - \tilde{k}^2 R_1 \Phi_1 + \frac{\sigma_2}{S_c} D^2 W_1, \\ P_V D^2 \Phi_2 &= P_V D\Phi_1 + P_H \tilde{k}^2 \Phi_0 + W_1 - \eta_{-1} P_5 D^2 W_2 \\ &\quad - \eta_{-1} P_6 DW_1 - z\eta_{-1} P_5 D^2 W_1 + \sigma_2 \Phi_0 \end{aligned} \quad (3.168)$$

and the second equation at fourth order is

$$\begin{aligned} P_V D^2 \Phi_3 &= P_V D\Phi_2 + P_H \tilde{k}^2 \Phi_1 + W_2 + zW_1 - \eta_{-1} P_5 D^2 W_3 - \eta_{-1} z P_5 D^2 W_2 \\ &\quad - \frac{\eta_{-1}}{2} P_5 z^2 D^2 W_1 - \eta_{-1} P_6 DW_1 - \eta_{-1} z P_6 DW_1 - \eta_{-1} P_7 \tilde{k}^2 W_1 \\ &\quad + \sigma_3 \Phi_0 + \sigma_2 \Phi_1. \end{aligned} \quad (3.169)$$

The solution at second order is

$$\begin{aligned} \Phi_1 &= -\eta_{-1} \frac{P_5}{P_V} W_1 + z \\ W_2 &= -\tilde{k}^2 \left[ R_0 \left( \eta_{-1} \frac{P_5 R_0 \tilde{k}^2}{720 P_V} \left( \frac{z^8}{56} + \frac{z^7}{14} + \frac{z^6}{12} \right) + \frac{z^5}{120} \right) + \frac{R_1}{24} z^4 \right] \\ &\quad + A_2 z^3 + B_2 z^2 \end{aligned} \quad (3.170)$$

where

$$\begin{aligned} A_2 &= \frac{\tilde{k}^2 R_0}{40} - \frac{\tilde{k}^2 R_1}{12} - \frac{\tilde{k}^4 R_0^2 P_5 \eta_{-1}}{12 \times 720 P_V} \\ B_2 &= \frac{\tilde{k}^2 R_0}{60} - \frac{\tilde{k}^2 R_1}{24} - \frac{3\tilde{k}^4 R_0^2 P_5 \eta_{-1}}{56 \times 720 P_V}. \end{aligned} \quad (3.171)$$

Applying solvability at third order implies

$$\sigma_2 = \tilde{k}^2 \left( \frac{R_0}{720} - P_H \right). \quad (3.172)$$

It is not necessary to obtain a solution for  $\Phi_2$  before applying solvability at fourth order, which gives

$$\sigma_3 = \frac{\tilde{k}^2 R_1}{720} - \frac{\tilde{k}^2 R_0}{720} \left[ \frac{1}{2} + \eta_{-1}(P_5 - P_6) \right] + \frac{\tilde{k}^4 R_0 \eta_{-1}}{720} \left[ P_7 + \frac{3R_0 P_5}{7 \times 720 P_V} \right]. \quad (3.173)$$

Therefore, when  $\sigma = 0$  we have

$$R = 720 P_H \left\{ 1 + d \left[ \frac{1}{2} + \eta_{-1}(P_5 - P_6) - \tilde{k}^2 \eta_{-1} \left( P_7 + \frac{3P_5 P_H}{7P_V} \right) \right] \right\} + O(d^2). \quad (3.174)$$

Now for the purpose of calculating the next order in the absence of gyrotaxis consider fourth order with  $\eta = 0$ . The solvability condition, after solving the third order equation and looking for neutral curves, gives

$$R = 720 P_H \left\{ 1 + \frac{1}{2} d + d^2 \left( \frac{13}{105} + \tilde{k}^2 \left[ \frac{1}{21} - \frac{5P_H}{462P_V} \right] \right) \right\} + O(d^3). \quad (3.175)$$

Linearity shows that when  $\eta \sim 1$ ,

$$R = 720 P_H \left\{ 1 + \frac{1}{2} d + d^2 \left( \frac{13}{105} + \eta(P_5 - P_6) + \tilde{k}^2 \left[ \frac{1}{21} - \frac{5P_H}{462P_V} - \eta \left( P_7 + \frac{3P_5 P_H}{7P_V} \right) \right] \right) \right\} + O(d^3). \quad (3.176)$$

The curve of  $R(\tilde{k})$  changes behaviour at a critical value of  $\eta$  given by

$$\eta_c = \frac{\left( \frac{1}{21} - \frac{5P_H}{462P_V} \right)}{\left( P_7 + \frac{3P_5 P_H}{7P_V} \right)}, \quad (3.177)$$

and leads us to the conclusion that, to first order for values of  $\eta$  smaller than this critical value, the most unstable mode has zero wavenumber but above it the most unstable wavenumber is non-zero.

## • CASE II

Consider the scaling

$$\eta \sim d, \quad R \sim d^{-2}, \quad W \sim d^{-1}, \quad (3.178)$$

which is consistent with case II, and propose a solution of the form

$$R = \sum_{n=-2}^{\infty} d^n R_n, \quad W = \sum_{n=-1}^{\infty} d^n W_n, \quad \Phi = \sum_{n=0}^{\infty} d^n \Phi_n, \quad \eta = d\eta_1. \quad (3.179)$$

We are interested in neutral curves so we will consider  $\sigma = 0$  ab initio. The leading order equations are

$$\begin{aligned} D^4 W_{-1} + R_{-2} \tilde{k}^2 \Phi_0 &= 0 \\ P_V D^2 \Phi_0 - W_{-1} &= 0 \end{aligned} \quad (3.180)$$

with boundary conditions  $D\Phi_0 = W_{-1} = DW_{-1} = 0$  at  $z = 0, -1$ . Eliminating  $\Phi_0$  gives

$$P_V D^6 W_{-1} + R_{-2} \tilde{k}^2 W_{-1} = 0 \quad (3.181)$$

and  $W_{-1} = DW_{-1} = D^5 W_{-1} = 0$  at  $z = 0, -1$ . The auxiliary equation has roots  $w e^{\frac{i\pi n}{3}}$  where  $n = 1, 2, 3, 4, 5, 6$  and  $w^6 = R_{-2} \tilde{k}^2 / P_V$ . Hence

$$\begin{aligned} W_{-1} &= A_1 \cos wz + A_2 \sin wz + e^{\frac{wz\sqrt{3}}{2}} \left[ A_3 \cos \frac{wz}{2} + A_4 \sin \frac{wz}{2} \right] \\ &+ e^{-\frac{wz\sqrt{3}}{2}} \left[ A_5 \cos \frac{wz}{2} + A_6 \sin \frac{wz}{2} \right]. \end{aligned} \quad (3.182)$$

Applying the boundary conditions gives the set of linear equations

$$\mathbf{M}\mathbf{A} = 0 \quad (3.183)$$

to solve where  $\mathbf{A}$  is a column vector of constants  $A_1$  to  $A_6$  and  $\mathbf{M}$  is a matrix of coefficients. For a non-zero solution we require

$$\det \mathbf{M} = 0. \quad (3.184)$$

This implies that either

$$\sin \frac{w}{2} = 0 \quad (3.185)$$

or

$$\cos \frac{w}{2} \cosh^2 \frac{w\sqrt{3}}{2} - 2 \cosh \frac{w\sqrt{3}}{2} + 2 \cos \frac{w}{2} - \cos^3 \frac{w}{2} = 0. \quad (3.186)$$

Different solutions for  $w$  correspond to different branches of the neutral curve and different modes of instability in  $W$ . The order of the solution mode is defined as the number of regions of different sign. So a mode two solution changes sign once. Equation (3.185) implies  $w = 2m\pi$  where  $m = 1, 2, 3, \dots$ . For large  $w$

Equation (3.186) becomes  $\cos \frac{w}{2} \cosh^2 \frac{w\sqrt{3}}{2} \approx 0$  which implies  $\cos \frac{w}{2} \approx 0$  and hence  $w = w_{2n+1} \approx (2n + 1)\pi$  for  $n = 0, 1, 2, 3, \dots$ . By plotting the curve

$$y = \cos \frac{w}{2} \cosh^2 \frac{w\sqrt{3}}{2} - 2 \cosh \frac{w\sqrt{3}}{2} + 2 \cos \frac{w}{2} - \cos^3 \frac{w}{2} \quad (3.187)$$

it is easily seen that the root at  $n = 0$  does not exist but the root at approximately  $n = 1$  does (Figure 3.2).

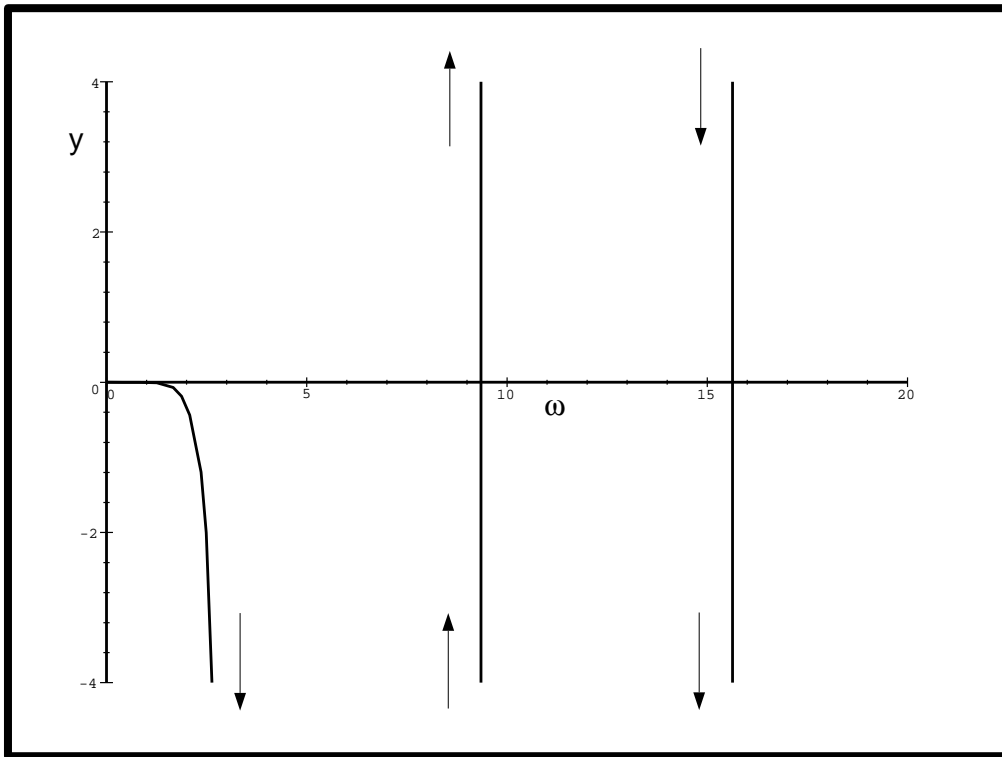


Figure 3.2: Graph of Equation (3.187) against  $w$  indicating its roots.

Hence, we have the infinite set of roots  $w_2 = 2\pi, w_3 \approx 3\pi, w_4 = 4\pi, w_5 \approx 5\pi, \dots$

It seems reasonable to consider the smallest value of  $w$  first. We find that

$$R^{(2)} = \frac{(2\pi)^6 P_V}{\tilde{k}^2} d^{-2} + O(d^{-1}) \approx 6.15 \times 10^4 \frac{P_V}{\tilde{k}^2} d^{-2} + O(d^{-1}) \quad (3.188)$$

Calculating  $W_{-1}$  for this case we get <sup>3</sup>

$$W_{-1} \propto \sin \pi z \left[ \sinh \pi \sqrt{3} \cos \pi z - 2 \sinh \left( \pi \left[ z + \frac{1}{2} \right] \sqrt{3} \right) \cosh \frac{\pi \sqrt{3}}{2} \right]. \quad (3.189)$$

<sup>3</sup>Note: missing 2 in [42].

As  $W_{-1}(-\frac{1}{2}) = 0$  we find that for this case the first unstable mode (for lowest  $R$ ) has order two. That is to say that there are two convection cells stacked one on the other.  $\eta$  does not appear in this analysis and we may decrease the magnitude of  $\eta$  (and complete case II) without changing the leading orders.

• **CASE IV**

The scalings here are of the form

$$\eta \sim d^{-m}, \quad R \sim d^{m-2}, \quad W \sim d^{m-1}, \quad (3.190)$$

where  $m = 1, 2, 3, 4, \dots$ . Beginning with  $m = 2$ , we look for a solution of the form

$$R = \sum_{n=0}^{\infty} d^n R_n, \quad W = \sum_{n=1}^{\infty} d^n W_n, \quad \Phi = \sum_{n=0}^{\infty} d^n \Phi_n, \quad \eta = d\eta_2. \quad (3.191)$$

where  $\sigma = 0$  ab initio. The leading order implies

$$\begin{aligned} D^4 W_1 + \tilde{k}^2 R_0 \Phi_0 &= 0 \\ D^2 (P_V \Phi_0 + P_5 \eta_{-2} W_1) &= 0 \end{aligned} \quad (3.192)$$

with boundary conditions  $D\Phi_0 = W_1 = DW_1 = 0$  at  $z = 0, -1$ . Hence

$$\begin{aligned} \Phi_0 &= \eta_{-2} \frac{P_5}{P_V} (K - W_1), \\ W_1 &= A \cos wz + B \sin wz - (A + K) \cosh wz - B \sinh wz + K \end{aligned} \quad (3.193)$$

where  $A, B$  and  $K$  are constants and

$$w^4 = \frac{\tilde{k}^2 R_0 \eta_{-2} P_5}{P_V}. \quad (3.194)$$

They are related by the equations

$$\begin{pmatrix} \cos w - \cosh w & \sinh w - \sin w \\ \sinh w + \sin w & \cos w - \cosh w \end{pmatrix} \begin{pmatrix} A \\ B \end{pmatrix} = K \begin{pmatrix} \cosh w - 1 \\ -\sinh w \end{pmatrix}. \quad (3.195)$$

Proceeding to the second and third orders, the cell conservation equation gives

$$P_V D^2 \Phi_1 + \eta_{-2} P_5 D^2 W_2 = P_V D\Phi_0 - \eta_{-2} P_5 z D^2 W_1 - \eta_{-2} P_6 DW_1 \quad (3.196)$$

with boundary conditions  $D\Phi_1 - \Phi_0 = W_2 = DW_2 = 0$  at  $z = 0, -1$ . The solvability condition is satisfied identically. The third order yields

$$\begin{aligned} P_V D^2 \Phi_2 + \eta_{-2} P_5 D^2 W_3 &= P_V D\Phi_1 + P_H \tilde{k}^2 \Phi_0 + W_1 \\ -\eta_{-2} P_5 z D^2 W_2 - \eta_{-2} P_5 \frac{z^2}{2} D^2 W_1 &- \eta_{-2} P_6 DW_2 - \eta_{-2} P_6 z DW_1 \\ + P_7 \tilde{k}^2 W_1 \eta_{-2} & \end{aligned} \quad (3.197)$$

Applying the solvability condition gives

$$\int_{-1}^0 W_1 dz = -FK, \tag{3.198}$$

where

$$F = \frac{\frac{P_H P_5}{P_V} \eta_{-2} \tilde{k}^2}{1 + \eta_{-2} P_7 \tilde{k}^2 - \eta_{-2} P_5 \left( \frac{P_H}{P_V} \tilde{k}^2 + 1 \right) + \eta_{-2} P_6}. \tag{3.199}$$

Evaluating Equation (3.198), we obtain

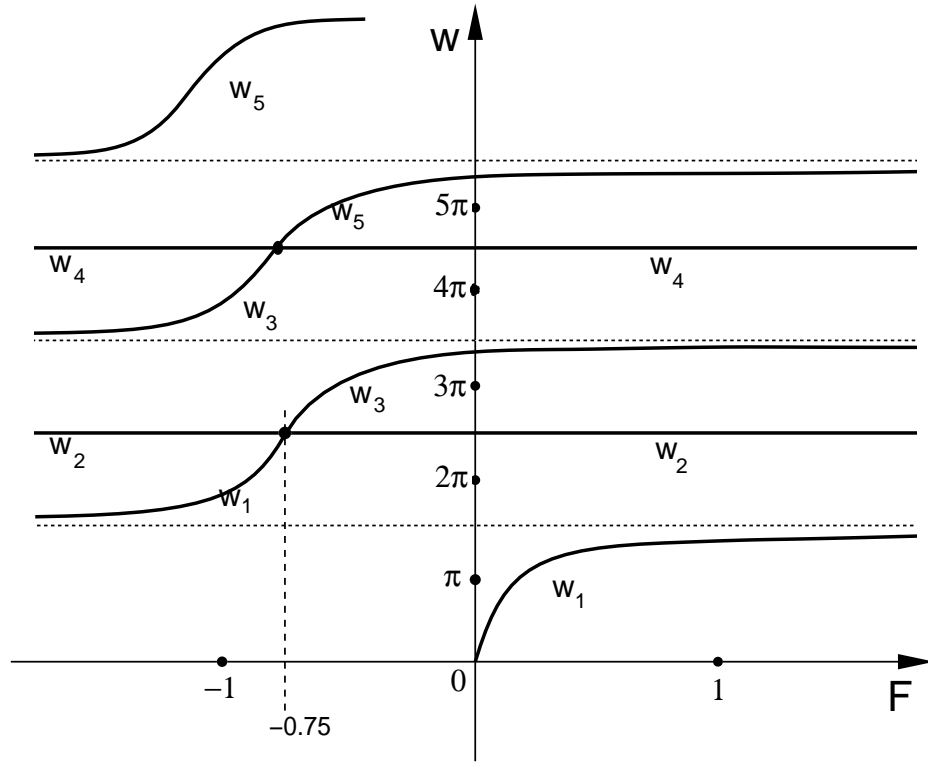


Figure 3.3: Graph of  $F$  against  $w$  from Equation (3.202).

$$A \sin w - A \sinh w + B \cos w + B \cosh w - 2B = K(\sinh w - w - Fw). \tag{3.200}$$

Combining this with Equations (3.195) gives

$$\begin{pmatrix} \cos w - \cosh w & \sinh w - \sin w & 1 - \cosh w \\ \sinh w + \sin w & \cos w - \cosh w & \sinh w \\ \sin w - \sinh w & \cos w + \cosh w - 2 & w - \sinh w + Fw \end{pmatrix} \begin{pmatrix} A \\ B \\ K \end{pmatrix} = 0. \tag{3.201}$$

Hence if  $M$  is the above matrix then we require  $\det M = 0$  for there to be a solution. This implies

$$w(1 + F)(1 - \cos w \cosh w) = 2 [\sinh w(1 - \cos w) + \sin w(1 - \cosh w)]. \quad (3.202)$$

Consider the left hand side vanishing. This implies the roots are independent of  $F$ . Hence,  $1 - \cos w \cosh w = 0$  or  $w = 0$ . As  $w$  increases  $\cosh w$  is exponentially steep. Therefore we require  $\cos w \approx 0$  for  $w$  quite large. Hence  $w \approx (2m + 1)\frac{\pi}{2}$  for  $m = 0, 1, 2, 3, \dots$ . By considering the graph of  $y = 1 - \cos w \cosh w$ , we can see that  $m = 0$  is not a solution (as  $w$  is insufficiently large for the argument to hold). Consider the right hand side

$$\sinh w(1 - \cos w) + \sin w(1 - \cosh w) = 0. \quad (3.203)$$

For large  $w$  we get  $e^w(1 - \cos w - \sin w) = 0$ . The roots common with above are  $w \approx (4n + 1)\frac{\pi}{2}$  for  $n = 1, 2, 3, \dots$ . Then from Equation (3.201) we get  $K = 0$  and

$$W_1 = A \left\{ \cos wz - \cosh wz + \left( \frac{\cos w - \cosh w}{\sin w - \sinh w} \right) (\sin wz - \sinh wz) \right\}. \quad (3.204)$$

$W_1$  is antisymmetric and this implies even modes.

Now consider other solutions, dependent on  $F$ . By considering large  $F$  we can establish the asymptotes for the curves but it is easier just to plot  $F$  as a function of  $w$  (see Figure 3.3). Expanding around  $w = 0$  as  $\tilde{k} \rightarrow 0$  and  $F \rightarrow 0$  implies

$$w_1^4 \rightarrow \frac{720 \frac{P_H}{P_V} P_5 \eta_{-2} \tilde{k}^2}{1 - (P_5 - P_6) \eta_{-2}}. \quad (3.205)$$

Hence from Equation (3.194)

$$R_0^{(1)} \rightarrow \frac{720 P_H}{1 - (P_5 - P_6) \eta_{-2}} \quad (3.206)$$

as  $\tilde{k} \rightarrow 0$ .

### 3.5.2 Deep layer analysis ( $d \gg 1$ )

Consider the case where  $\sigma = 0$  and  $k \sim 1$  where  $d^{-1}$  is small.

$$(D^2 - k^2)^2 W = -k^2 d^{-1} R \Phi \quad (3.207)$$

and

$$(P_V D^2 - P_V dD - P_H k^2) \Phi = d e^{dz} [1 - \eta P_5 D^2 - \eta d P_6 D + \eta P_7 k^2] W. \quad (3.208)$$

If we expand for large  $d$  then the leading order equations do not contain the highest order derivatives and hence the solutions cannot satisfy all of the boundary conditions. Therefore we require a solution within the boundary layer at the top which can be matched to a solution for the outer region. Consider the outer solution where the cell concentration is exponentially small. Then

$$(P_V D^2 - P_V dD - P_H k^2) \Phi = 0 \quad (3.209)$$

which, when expanding  $\Phi$  in powers of  $d^{-1}$  and applying the boundary conditions at  $z = -1$ , implies  $\Phi = 0$ . We also have

$$(D^2 - k^2)^2 W = 0 \quad (3.210)$$

with  $W = DW = 0$  on  $z = -1$  which implies

$$W = -kA(z+1) \cosh k(z+1) + (A + B(z+1)) \sinh k(z+1) \quad (3.211)$$

where  $A$  and  $B$  are constants and can be formally expanded in terms of  $d^{-1}$ .

Now consider the inner region. We have

$$(D_I^2 - d^{-2} k^2)^2 W = -d^{-5} R k^2 \Phi \quad (3.212)$$

and

$$(P_V D_I^2 - P_V D_I - P_H k^2 d^{-2}) \Phi = e^{z_I} d [d^{-2} - \eta P_5 D_I^2 - \eta P_6 D_I + \eta P_7 k^2 d^{-2}] W \quad (3.213)$$

where the scalings for the inner region are  $z_I = dz$  and  $D_I = d^{-1}D$ . The boundary conditions become  $(D_I - 1)\Phi = W = D_I W = 0$  on  $z_I = 0$ . The first equation implies that for a non-trivial solution  $R \sim d^5 W$ . The second equation is complicated by the exponential term  $e^{z_I} \sim 1$  and hence we examine the parameter ranges where the right hand side does not appear at leading order. Assuming  $\Phi \sim 1$ , we require  $W \leq O(1)$  and  $\eta W \leq O(d^{-2})$  for the exponential term not to appear at leading order. We are investigating the equations for the case when  $\sigma = 0$  (on the neutral curve) so we expect there to be only a limited region of parameter space where the equations remain self

consistent. This region is given in Figure (3.4). We are restricted to this region because of the balance of terms in Equation (3.213) at third order, where the term  $-P_H k^2 \Phi_0$  first appears. If there are no terms on the right hand side, then we are led to the solvability condition  $P_H k^2 = 0$  which is unhelpful. If there are terms on the right hand side before third order, then the solvability condition yields  $R = 0$  or  $\eta = 0$  at leading orders which is again unhelpful. Thus we are restricted to the L-shaped region shown. We immediately see from Figure (3.4) that, as  $\eta$  increases (allowing  $W$  and  $R$  to vary),  $R$  initially remains constant but at some value of  $\eta$  the gyrotactic terms become important and  $R(k = 0)$  starts decreasing. So, consider  $W \sim d^{-n}$  where  $n = 1, 2, 3, \dots$

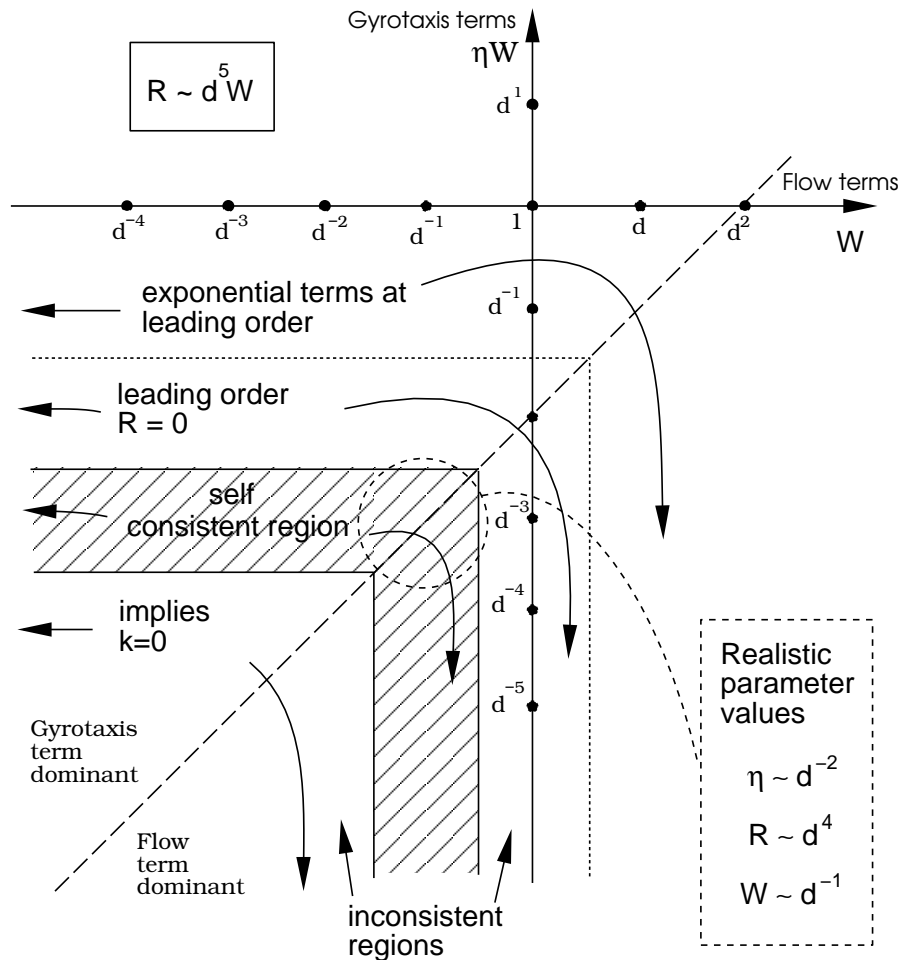


Figure 3.4: Regions of parameter space corresponding to leading order balances of the linear equations for bioconvection in a deep layer ( $d \gg 1$ ). The shading indicates the self consistent region of parameter space where a neutral curve can exist.

and we write

$$W = \sum_{m=n}^{\infty} W_{-m} d^{-m}, \quad (3.214)$$

$$\Phi = \sum_{m=0}^{\infty} \Phi_{-m} d^{-m} \quad (3.215)$$

and

$$R = d^{5-n} R_{5-n} + d^{5-n-1} R_{5-n-1} + \dots \quad (3.216)$$

To first order

$$D_I^4 W_{-n} + R_{5-n} k^2 \Phi_0 = 0 \quad (3.217)$$

and

$$P_V D_I (D_I - 1) \Phi_0 = 0 \quad (3.218)$$

with appropriate boundary conditions. This has solutions

$$W_{-n} = a_{-n} z_I^3 + b_{-n} z_I^2 + R_{5-n} k^2 (z_I + 1 - e^{z_I}) \quad (3.219)$$

and

$$\Phi_0 = e^{z_I} \quad (3.220)$$

where the  $a$ 's and  $b$ 's are constants. At second order

$$D_I^4 W_{-n-1} + R_{5-n} k^2 \Phi_{-1} = -R_{5-n-1} k^2 \Phi_0 \quad (3.221)$$

and

$$P_V D_I (D_I - 1) \Phi_{-1} = 0 \quad (3.222)$$

and boundary conditions at  $z = 0$  which has a solution

$$W_{-n-1} = a_{-n-1} z_I^3 + b_{-n-1} z_I^2 + R_{5-n-1} k^2 (z_I + 1 - e^{z_I}) \quad (3.223)$$

and

$$\Phi_{-1} = 0. \quad (3.224)$$

To match the inner and outer solutions up to second order, consider the intermediate region such that  $z_\zeta \sim 1$  as  $d^{-1} \rightarrow 0$  where

$$z_\zeta = \frac{z}{\zeta(d^{-1})} \quad (3.225)$$

and  $\zeta(d^{-1}) \rightarrow 0$  as  $d^{-1} \rightarrow 0$  and satisfies  $0 < d^{-1} \ll \zeta \ll 1 \ll d$ . Expanding the inner solution by writing  $z_\zeta = z_I \frac{d^{-1}}{\zeta}$  gives (where terms on the right hand side are in order of size)

$$\begin{aligned} W &= d^{-n+2} [\zeta^3 da_{-n} z_\zeta^3 + \zeta^2 b_{-n} z_\zeta^2 + \zeta^3 a_{-n-1} z_\zeta^3 + d^{-1} z_\zeta \zeta k^2 R_{5-n} + d^{-1} \zeta^2 b_{-n-1} z_\zeta^2] \\ &\quad + O(d^{-n}, \zeta^4 d^{-n}). \end{aligned} \quad (3.226)$$

Expanding the outer solution by writing  $z = \zeta z_\zeta$  gives (in order of size)

$$\begin{aligned} W &= d^\xi [(-k \cosh k A_{-\xi} + \sinh k A_{-\xi} + \sinh k B_{-\xi}) \\ &\quad + (-k^2 \sinh k A_{-\xi} + \sinh k B_{-\xi} + k \cosh k B_{-\xi}) \zeta z_\zeta \\ &\quad + \left( -k^3 \frac{\cosh k}{2} A_{-\xi} - k^2 \frac{\sinh k}{2} A_{-\xi} + k^2 \frac{\sinh k}{2} B_{-\xi} + k \cosh k B_{-\xi} \right) \zeta^2 z_\zeta^2 \Big] \\ &\quad + h.o.t. \end{aligned} \quad (3.227)$$

The process now involves matching terms in  $z_\zeta$ . If we attempt to match any of the first three terms in Equation (3.226) than we get that at least the first two terms (linearly independent in  $A_\zeta$  and  $B_\zeta$ ) in Equation (3.227) must be zero. This leads to the trivial solution. Hence  $a_{-n} = a_{-n-1} = b_{-n} = 0$  and we must match the fourth term in Equation (3.226). This implies  $\xi = n - 1$ ,

$$(A_{n+1} + B_{-n+1}) \sinh k - k A_{-n+1} \cosh k = 0, \quad (3.228)$$

$$B_{-n+1} \sinh k + B_{-n+1} k \cosh k - k^2 A_{-n+1} \sinh k = k^2 R_{5-n} \quad (3.229)$$

and

$$-k^3 \frac{\cosh k}{2} A_{-n+1} - k^2 \frac{\sinh k}{2} A_{-n+1} + k^2 \frac{\sinh k}{2} B_{-n+1} + k \cosh k B_{-n+1} = b_{-n-1}. \quad (3.230)$$

First consider the most general solution in the upper right corner of the L-shaped region in parameter space such that two terms appear at third order on the right hand side of Equation (3.213). Here we have  $\eta \sim d^{-2}$  and  $n = 1$ . Third order gives (cell conservation equation only)

$$P_V D_I (D_I - 1) \Phi_{-2} - P_H k^2 \Phi_0 = e^{z_I} [W_{-1} - \eta_{-2} (P_5 D_I^2 + P_6 D_I) W_{-1}]. \quad (3.231)$$

Then, the solvability condition is obtained by integrating from  $-\infty$  to 0. At third order this gives

$$R_4 = \frac{2P_H}{1 - (P_5 - P_6)\eta_{-2}}, \quad (3.232)$$

where  $P_6$  is negative. Therefore, as  $P_5 > P_6$ ,  $R_4$  can be negative for sufficiently large  $(P_5 - P_6)\eta_{-2}$  and the asymptotics break down. This is similar to the analysis of Hill *et al.* (1989) [42] in which, for particular values of the gyrotaxis number, the leading order in the Rayleigh number became singular or negative.

Solving for the constants<sup>4</sup> we get

$$A_0 = \frac{k^2 \sinh k R_4}{k^2 - \sinh^2 k}, \quad (3.233)$$

$$B_0 = \frac{(k \cosh k - \sinh k)k^2 R_4}{k^2 - \sinh^2 k} \quad (3.234)$$

and

$$b_{-2} = \frac{(k - \cosh k \sinh k)k^3 R_4}{k^2 - \sinh^2 k}. \quad (3.235)$$

To find the  $k$  dependence, we consider the solvability condition at fourth order and obtain

$$R_3 = \frac{4b_{-2}}{k^2}. \quad (3.236)$$

Hence

$$R = \frac{2P_H d^4}{1 - (P_5 - P_6)\eta_{-2}} \left[ 1 + 4d^{-1}k \frac{(k - \sinh k \cosh k)}{k^2 - \sinh^2 k} + O(d^{-2}) \right]. \quad (3.237)$$

This is a monotonically increasing function of  $k$  (as in [42]) and implies that, for  $k \leq O(1)$ , the most unstable wavenumber is zero. (See Figure 3.5 where  $4k(k - \sinh k \cosh k)/(k^2 - \sinh^2 k)$  is plotted with  $k$ ). The expression does not say anything about the global most unstable wavenumber for general  $k$ .

It is easy to show that we can cover the whole region in parameter space by reducing the importance of certain terms. Going left in parameter space where  $\eta \sim d^{-2}$  and  $W \sim d^{-1}$  we get that the solvability condition at third order gives

$$R_3 = -\frac{2P_H}{(P_5 - P_6)\eta_{-1}} \quad (3.238)$$

which implies that the asymptotics are not valid for small values of  $k$ . We clearly need to balance the advection and gyrotaxis terms, and not let the gyrotaxis terms dominate, to keep the Rayleigh number finite for small  $k$ . Going down in the L-shaped region ( $\eta \sim d^{-3}$  and  $W \sim d^{-1}$ ) the solvability conditions give

$$R = 2P_H d^4 \left[ 1 + d^{-1} \left( \eta_{-3}(P_5 - P_6) + \frac{4k(k - \sinh k \cosh k)}{k^2 - \sinh^2 k} \right) + O(d^{-2}) \right]. \quad (3.239)$$

---

<sup>4</sup>corrected from [42]

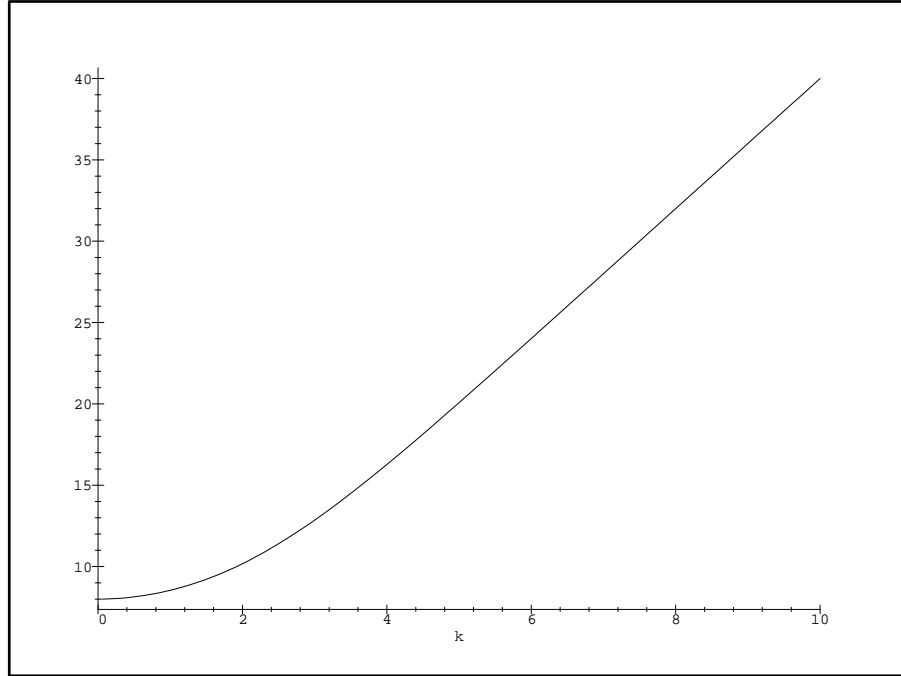


Figure 3.5: A monotonically increasing function,  $4k(k - \sinh k \cosh k)/(k^2 - \sinh^2 k)$ , of  $k$ .

This function is a monotonically increasing function of  $k$  and gives a most unstable wavenumber of zero (for small  $k \leq O(1)$ ).

### 3.5.3 A summary of the asymptotic results

Shallow layer,  $d \ll 1$

- $\eta \leq O(1)$  Mode one solutions belong to Case Ib, Equation (3.175), where  $R \sim 1$  and

$$R^{(1)} = 720P_H \left\{ 1 + \frac{1}{2}d + d^2 \left( \frac{13}{105} + \tilde{k}^2 \left[ \frac{1}{21} - \frac{5P_H}{462P_V} \right] \right) \right\} + O(d^3). \quad (3.240)$$

Modes of order greater than two belong to Case II and imply that  $R \sim d^{-2}$ . Equation (3.188) gives  $R$  for a mode two solution with similar expressions for other modes,

$$R^{(n)} = \frac{w_n^6 P_V}{\tilde{k}^2} d^{-2} + O(d^{-1}) \quad (3.241)$$

where  $n = 2, 3, \dots$ ,  $w_n = n\pi$  if  $n$  is even and  $w_n \approx n\pi$  if  $n$  is odd.

- $\eta \sim 1$  Modes of order one again come from Case Ib and  $R$  is given by (Equation 3.176)

$$R^{(1)} = 720P_H \left\{ 1 + \frac{1}{2}d + d^2 \left( \frac{13}{105} + \eta(P_5 - P_6) + \tilde{k}^2 \left[ \frac{1}{21} - \frac{5P_H}{462P_V} - \eta \left( P_7 + \frac{3P_5P_H}{7P_V} \right) \right] \right) \right\} + O(d^3). \quad (3.242)$$

modes of higher order belong to Case III and it can be seen that

$$R^{(n)} \sim d^{-2} \quad (3.243)$$

where  $n = 2, 3, \dots$

- $\eta \sim d^{-1}$  Mode one is from Case Ib, Equation (3.174),

$$R^{(1)} = 720P_H \left\{ 1 + d \left[ \frac{1}{2} + \eta_{-1}(P_5 - P_6) - \tilde{k}^2 \eta_{-1} \left( P_7 + \frac{3P_5P_H}{7P_V} \right) \right] \right\} + O(d^2). \quad (3.244)$$

Modes of higher orders are from Case IV (where  $m = 1$ ), Equation (3.194),

$$R^{(n)} = \frac{w_n^4 P_V}{\tilde{k}^2 \eta_{-1} P_5} d^{-1} + O(1) \quad (3.245)$$

where  $n = 2, 3, \dots$ ,  $w_2 = \frac{5\pi}{2}$  and  $\frac{5\pi}{2} \leq w_3 \leq \frac{9\pi}{2}$  (see Figure 3.3 for the values of  $w$  as functions of  $F$ ).

- $\eta \sim d^{-2}$  All modes are determined in Case IV, Equation (3.194), and give

$$R^{(n)} = \frac{w_n^4 P_V}{\tilde{k}^2 \eta_{-2} P_5} + O(d) \quad (3.246)$$

where  $n = 1, 2, 3, \dots$ . Even modes have a constant  $w_n$  with  $\tilde{k}$ , but odd modes have  $w_n = w_n(F(\tilde{k}^2))$ , where  $\frac{(2n-1)\pi}{2} \leq w_n \leq \frac{(2n+3)\pi}{2}$ . This is outlined in Figure 3.3. For  $\eta_{-2} < \frac{1}{P_5}$  where  $w \rightarrow 0$  and  $\tilde{k} \in \mathbb{R}$  then

$$R^{(1)} \rightarrow \frac{720P_H}{1 - (P_5 - P_6)\eta_{-2}} \quad (3.247)$$

as  $\tilde{k} \rightarrow 0$ .

- $\eta \geq O(d^{-m})$  where  $m \geq 3$  All modes are covered by Case IV,

$$R^{(n)} = \frac{w_n^4 P_V}{\tilde{k}^2 \eta_{-m} P_5} d^{m-2} + O(d^{m-1}) \quad (3.248)$$

where the  $w_n$  are given in Figure 3.3.

Deep layer,  $d \gg 1$

- $\eta \leq O(d^{-4})$

$$R^{(1)} = 2P_H d^4 \left[ 1 + d^{-1} \left( \frac{4k}{k^2 - \sinh^2 k} (k - \sinh k \cosh k) \right) + O(d^{-2}) \right]. \quad (3.249)$$

- $\eta \sim d^{-3}$  (Equation 3.239)

$$R^{(1)} = 2P_H d^4 \left[ 1 + d^{-1} \left( \frac{4k}{k^2 - \sinh^2 k} (k - \sinh k \cosh k) + \eta_{-3}(P_5 - P_6) \right) + O(d^{-2}) \right]. \quad (3.250)$$

- $\eta \sim d^{-2}$  (Equation 3.237)

$$R^{(1)} = \frac{2P_H d^4}{1 - (P_5 - P_6)\eta_{-2}} \left[ 1 + d^{-1} \frac{4k(k - \sinh k \cosh k)}{k^2 - \sinh^2 k} + O(d^{-2}) \right]. \quad (3.251)$$

- $\eta \geq O(d^{-1})$  (Equation 3.238)

$$R^{(1)} = -\frac{2P_H d^3}{P_5 - P_6 \eta_{-1}} + O(d^2), \quad (3.252)$$

and asymptotics break down for small  $k$ .

### 3.6 Numerical analysis

In this section we pursue solutions to the full linear equations in a similar manner to that of [42]. A numerical scheme implemented by Cash & Moore (1980) [14] and supplied by Dr. D. R. Moore, called “NRK”, was used. The scheme is a fourth-order finite difference scheme that iterates using the Newton-Raphson-Kantorovich algorithm. The program was supplied in FORTRAN and routines were written to search for the neutral curves of the equations given initial guesses for the concentration and velocity fields,  $\Phi$  and  $W$ , and the Rayleigh number,  $R$ . An initial value of the wavenumber,  $k$ , was provided and trial solutions were guessed until a solution was found. This solution formed the basis of the next solution estimate for a higher value of  $k$ . In this way, provided the steps in  $k$  were sufficiently small the neutral curve could be traced with an efficient number of iterations. Guessing a good initial value of  $R$  was highly important and this was where the asymptotic solutions in the previous section proved useful. The form of the mesh used in the  $z$  direction was also highly important. This was especially true for the deep layer and large  $k$  solutions where most of the activity

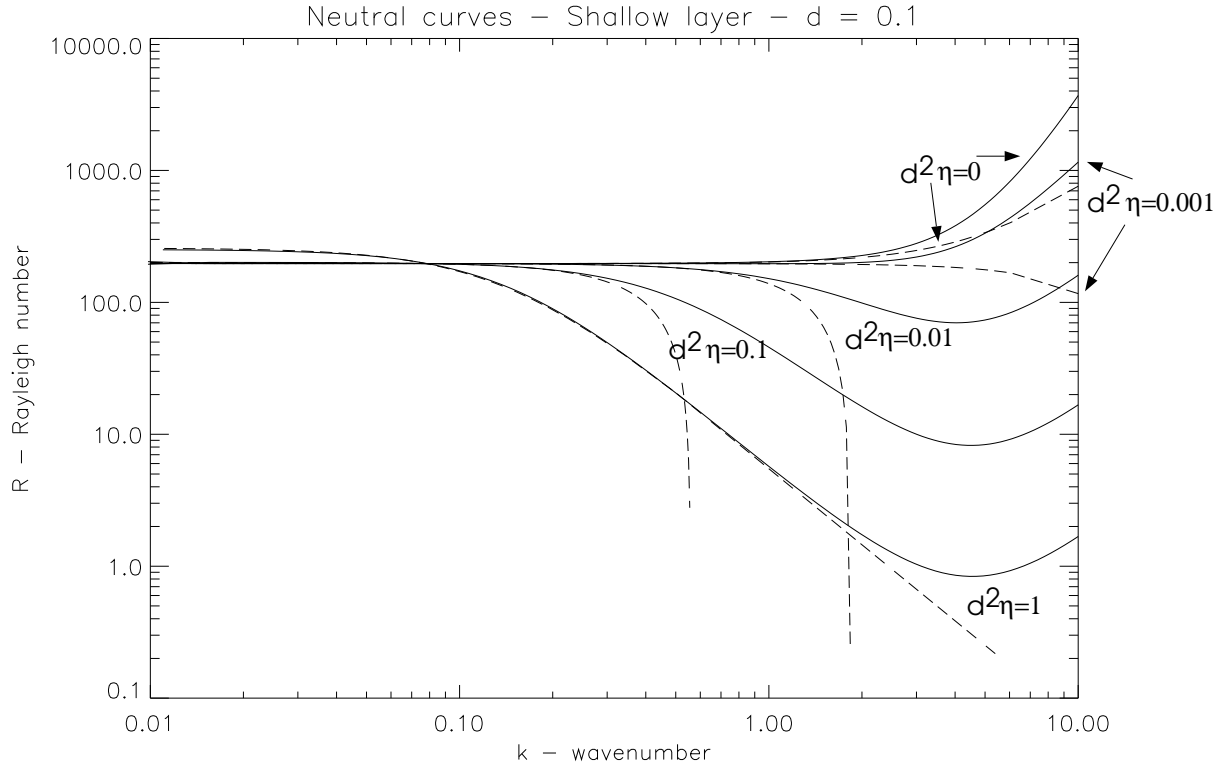


Figure 3.6: Curves of neutral linear stability for a shallow layer ( $d = 0.1$  and  $\alpha_0 = 0.2$ ) and varying  $d^2\eta$ . Dotted lines are curves from the asymptotic results and solid lines are from the numerical results.

in  $\Phi$  occurs in a small fraction of the layer depth at the top. Hence, a variety of continuously varying meshes were used to both gain a solution and check its validity. A grid point doubling algorithm was also used so that a rough solution could be found (such as with six grid points) and then a number of refinements could be made to improve the solution accuracy by doubling the number of grid points and interpolating the previous solution. Up to eighty-one grid points were used to obtain convergent solutions but this was not always necessary. An accuracy of six significant figures was always achieved for convergence. The convergence of some numerical solutions was *slow* if a) extreme parameter values were used, b) the trial solution curve was dissimilar to the actual solution, c) the trial Rayleigh number was not a good estimate or d) the numerical grid did not contain enough nodes in significant areas. There are a number of parameters that can be varied.  $P_V$  and  $P_H$  are functions of the parameter  $\lambda$  alone but  $P_5$ ,  $P_6$  and  $P_7$  are functions of  $\lambda$  and  $\alpha_0$ .  $d$  is the non-dimensional layer depth,  $\eta(d)$  is the gyrotactic orientation parameter,  $k$  is the wavenumber and  $R(d, k, \eta, \lambda, \alpha_0)$

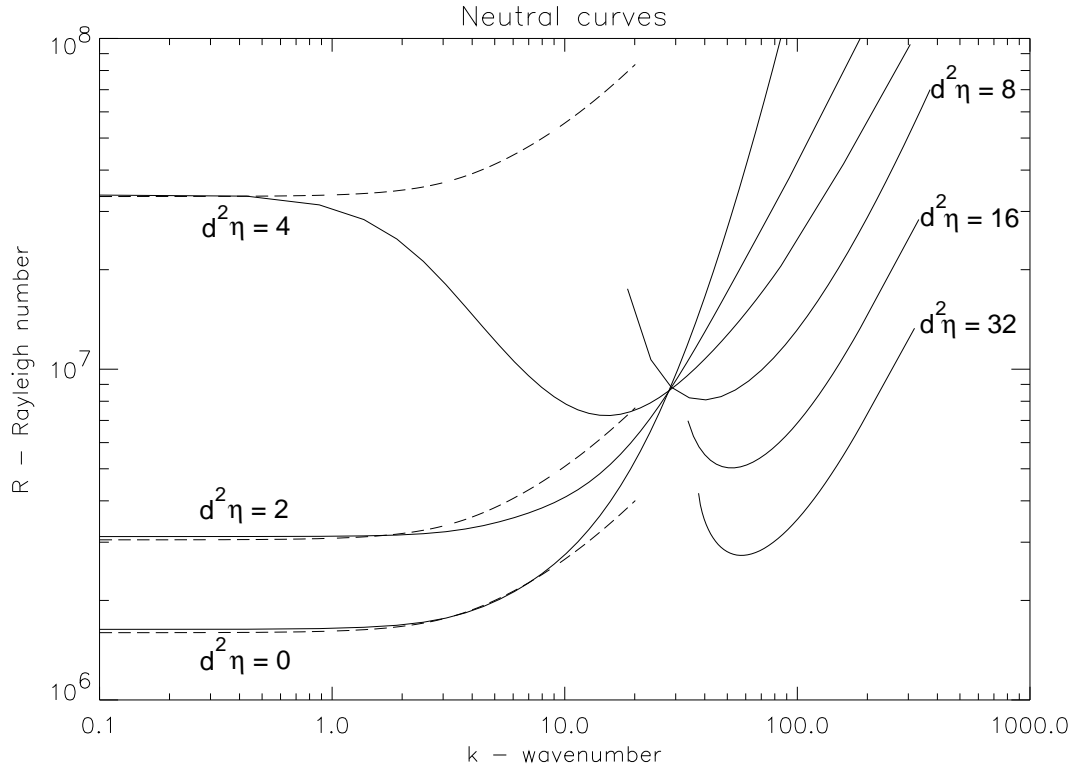


Figure 3.7: Curves of neutral linear stability for a deep layer ( $d = 40$  and  $\alpha_0 = 0.2$ ) and varying  $d^2\eta$ . Dotted lines are curves from the asymptotic results and solid lines are from the numerical results.

is the Rayleigh number based on the whole suspension depth and is the eigenvalue to be determined. We choose to fix  $\lambda = 2.2$  (following Pedley & Kessler 1990 [85]) thus leaving four parameters to vary. Figures (3.6) to (3.8) show comparisons between the numerical and asymptotic solutions. The values of the parameters have been chosen so that comparisons with [42] and [19] can be made. Good agreement was always obtained between asymptotic and numerical solutions, for  $k \leq O(1)$ , provided either  $d \ll 1$ , for shallow layers, or  $d^{-1} \ll 1$  and  $P_i$ , for deep layers. In fact, many of the asymptotic results hold true for orders of  $k$  larger than one, especially for very deep layers. Clearly, the new terms due to gyrotaxis also affect the diffusion tensor and, hence, we no longer have a simple balance of identifiable terms.

For shallow layers ( $d \ll 1$ ) non-zero wavenumbers are destabilized with increasing  $\eta$  and zero wavenumbers are very slightly stabilized (Figure 3.6). The most unstable wavenumber is non-zero for sufficiently large  $d^2\eta$ . Figure (3.11) shows the flow and concentration profiles for a mode one solution, where it can be seen that the perturba-

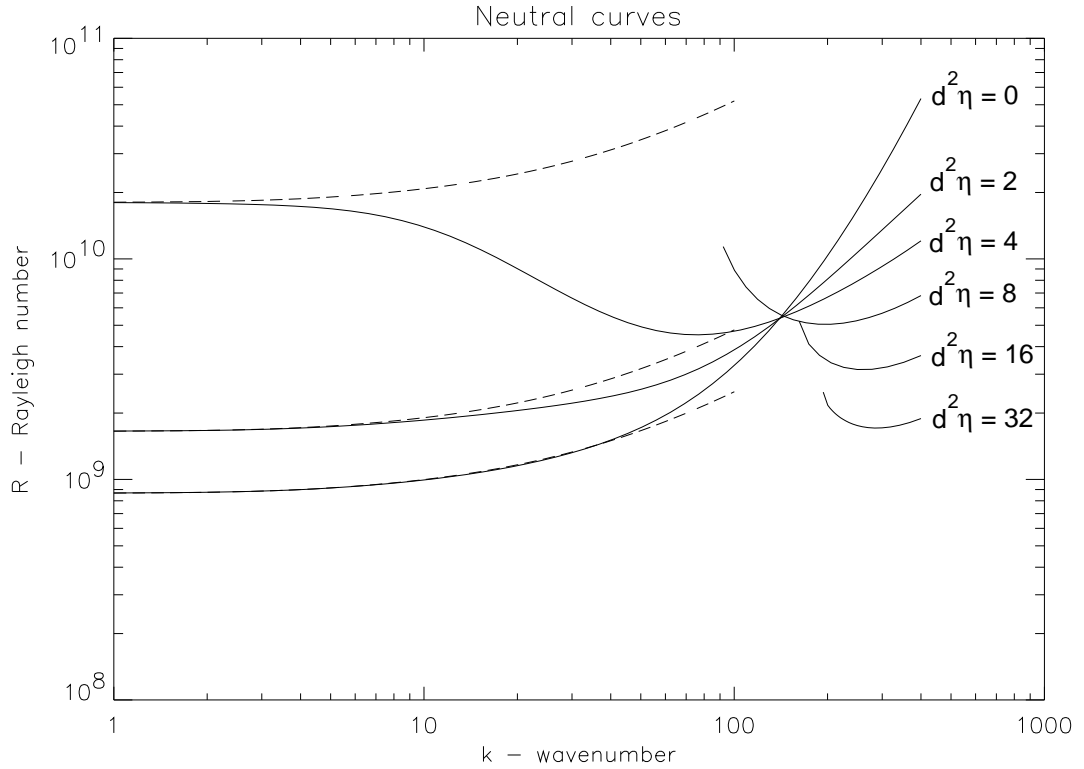


Figure 3.8: Curves of neutral linear stability for a deep layer ( $d = 200$  and  $\alpha_0 = 0.2$ ) and varying  $d^2 \eta$ . Dotted lines are curves from the asymptotic results and solid lines are from the numerical results.

tions act over the whole suspension layer and are almost symmetrical. For deep layers ( $d \gg 1$ ) the perturbations are greatest towards the upper surface (see Figures 3.12 and 3.13). For deep layers, large wavenumbers are destabilized and small wavenumbers are stabilized with increasing  $\eta$ . In particular, we find that for  $\eta = 0$ , the most unstable wavenumber is zero but as  $\eta$  increases and exceeds some critical value the most unstable wavenumber jumps to a non-zero value. The asymptotics presented here can not predict the critical value or the non-zero most unstable wavenumber as the dynamics occur for  $k \geq O(1)$ . Figure (3.10) shows a curve where it is clear that minimums of the neutral curve occur at a zero and a non-zero wavenumber. As  $\eta$  increases still further  $R(k = 0) \rightarrow \infty$ . The value of  $\eta$  for which  $R(k) \rightarrow \infty$  first as  $k \rightarrow 0$  can be calculated from the asymptotics (Equation 3.237) to be

$$\eta_c = \frac{d^{-2}}{P_5 - P_6}. \tag{3.253}$$

If  $\lambda = 2.2$  and  $\alpha_0 = 0.2$  then  $d^2 \eta_c \approx 4.2$ . The asymptotics also suggest that in all cases

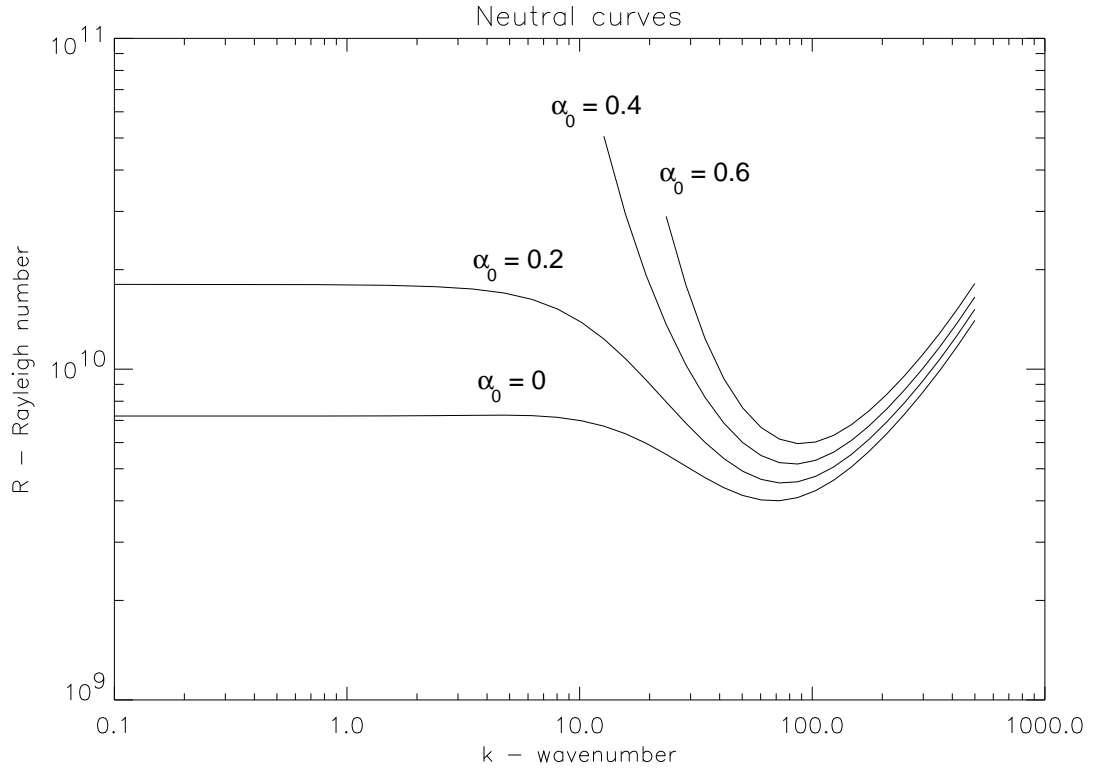


Figure 3.9: Numerical curves of neutral linear stability for a deep layer ( $d = 200$ ), with  $d^2\eta = 4$  and varying  $\alpha_0$ . Increasing  $\alpha_0$  stabilizes modes with long horizontal wavelengths.

where  $\eta < \eta_c$  the neutral curve increases slightly with  $k$  for  $k \leq O(1)$  before increasing or decreasing when  $k > O(1)$ . Figure (3.9) describes the dependence of the neutral curve on  $\alpha_0$ . The value of  $\alpha_0$  does not affect the neutral curve significantly for large  $k$  but increasing  $\alpha_0$  stabilizes modes with long length scales. This is due to the decrease in  $P_5$  and  $P_6$  when  $\alpha_0$  increases. If the cells become less rod-like ( $\alpha_0 \rightarrow 0$ ), then the cells will be less constrained to swim along streamlines and diffusive processes could lead to long wavelength instabilities.

The Rayleigh number,  $R$ , based on the suspension depth,  $H$  (following [42]), is related to the Rayleigh number of [19],  $\hat{R}$ , based on the sublayer depth,  $\kappa^{-1}$ , by the equation

$$R = d^3 \hat{R}. \quad (3.254)$$

Childress *et al.* (1975) [19] found that, in their model for two rigid boundaries (for isotropic diffusion), the critical value of their Rayleigh number,  $\hat{R}_c$ , behaved like  $720/d^4$

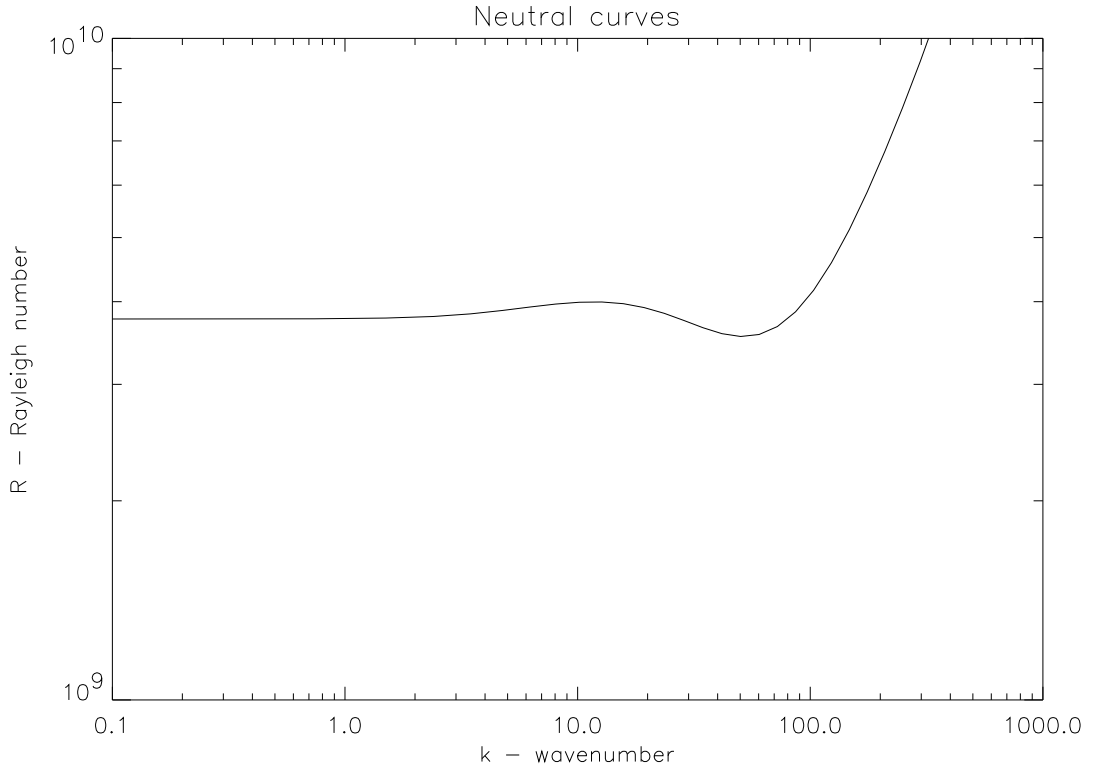


Figure 3.10: Numerical curve of neutral linear stability for a deep layer ( $d = 200$ ), with  $d^2\eta = 3.3$ ,  $\alpha_0 = 0$ . Here we see a combination of both zero and non-zero dominant unstable wavenumbers. For every  $d$  we find that there is a critical  $\eta$  that determines the bifurcation between there being a zero and a non-zero most unstable wavenumber.

for small  $d$  and  $\hat{R}_c$  decreased to 2 as  $d \rightarrow \infty$ . For free-rigid boundary conditions they found that  $\hat{R}_c \sim 320/d^4$  for small  $d$  and  $\hat{R}_c \sim 4/d$  for large  $d$ . Hill *et al.* (1989) [42] derive an equation in their asymptotic analysis similar to Equation (3.237) which describes the behaviour of the neutral curve close to  $k = 0$ . Hence, for small  $k$ ,

$$R \approx \frac{2P_H d^4}{1 - (P_5 - P_6)\hat{\eta}} \quad (3.255)$$

where the depth independent gyrotaxis number is defined as (following Hill *et al.* 1989 [42])

$$\hat{\eta} = d^2\eta. \quad (3.256)$$

Equation (3.255) is only valid for small enough  $\hat{\eta}$ , but we find from Figures (3.7) and (3.8) that if  $d$  is large and  $\hat{\eta} = 32$  then the minimum of the neutral curve is a factor of 2 larger than this value when  $\hat{\eta} = 0$ . Hence, the critical Rayleigh number is given by  $R_c \sim 4P_H d^4$ . Therefore, we find (as the qualitative results of Hill *et al.* 1989 [42] also

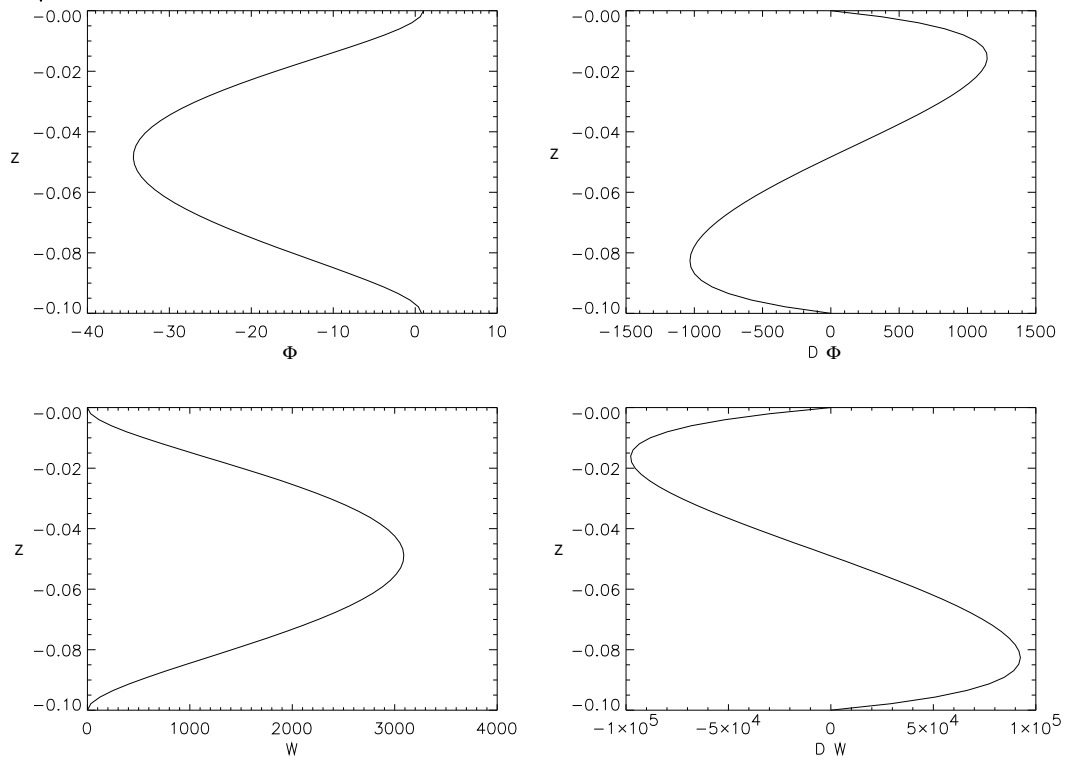


Figure 3.11: Profiles of neutrally stable numerical solutions for a shallow layer ( $d = 0.1$ ) with  $\eta = 0.1$ ,  $\alpha_0 = 0.2$  and  $k = 10$ , for which it is found that  $R \approx 1155$ . This is a mode one solution.

suggest) that  $\hat{R}_c/d$  is initially large and decreases to a constant value as  $d \rightarrow \infty$ . From Figures (3.6) to (3.8) we find that if  $\hat{\eta} = 33$  then  $\hat{R}_c/d = 300$  for  $d = 0.1$ ,  $\hat{R}_c/d = 1.17$  for  $d = 40$  and  $\hat{R}_c/d = 1.12$  for  $d = 200$ . The approximate limit of  $\hat{R}_c/d$ , from above, of  $4P_H$  is equal to 1.04.

The experimental results of Chapter 2 indicate that the wavenumber of the initial pattern depends only on the suspension depth, whereby the wavenumber decreases with increasing depth. The theoretically determined dimensional pattern wavelength, after scaling with  $H \approx 2.3 \times 10^{-3}d$ , is seen from Figures (3.6) to (3.8) to increase with increasing depth, thus agreeing with the measurements of Chapter 2.

Thus, the present model appears to agree, at least qualitatively, with experimental observations. In contrast, a most unstable wavenumber of zero, as in the model of Childress *et al.* (1975) [19], appears to contradict that seen in experiments. However, [19] show that, in their model, the growth rate is zero at zero wavenumber but increases with the wavenumber until a maximum is reached. They argue that, immediately

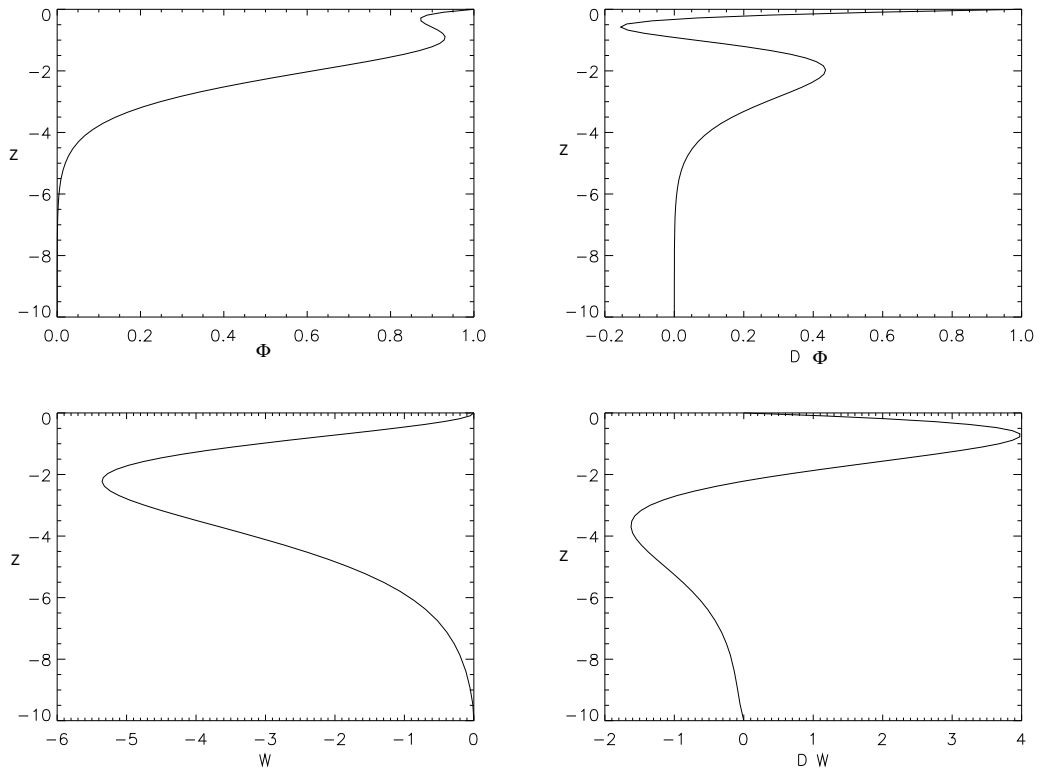


Figure 3.12: Profiles of neutrally stable numerical solutions for a deep layer ( $d = 10$ ) with  $\eta = 0.1$ ,  $\alpha_0 = 0.2$  and  $k = 10$ , for which it is found that  $R \approx 22024$ . This is a mode one solution.

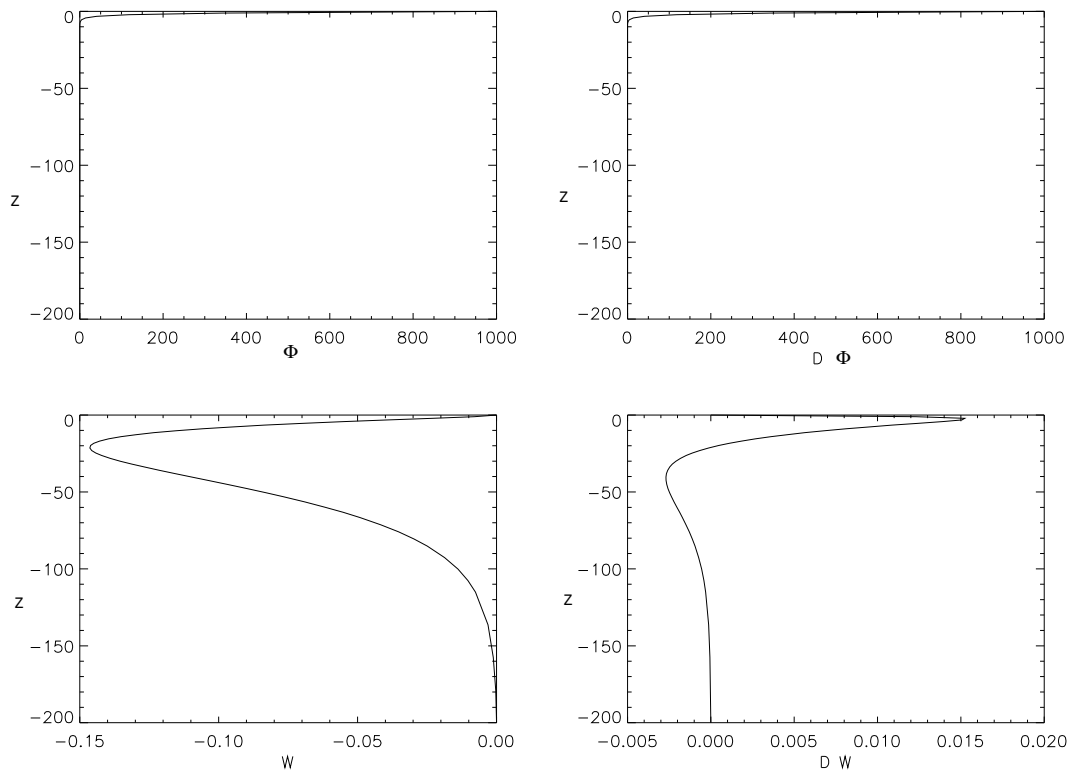


Figure 3.13: Profiles of neutrally stable numerical solutions for a deep layer ( $d = 200$ ) with  $d^2\eta = 8$ ,  $\alpha_0 = 0.2$  and  $k = 100$ , for which it is found that  $R \approx 8.5 \times 10^9$ . This is a mode one solution.

above the neutral curve, the wavelength with the greatest linear growth rate is the one observed in experiments. However, Childress & Spiegel (1978) [21] show that the bifurcation to instability is subcritical and, hence, linear analysis cannot predict the observed initial pattern wavelength. Hill *et al.* (1989) [42] find that, in their model of deterministic gyrotactic bioconvection, a non-zero most unstable wavenumber exists for a sufficiently large gyrotactic orientation parameter. They also prove, for the case of free-free boundary conditions, that the bifurcation to instability is stationary, using the method of the exchange of stability ([42], Appendix A). However, they find that the method does not work with rigid-rigid or rigid-free boundary conditions. We can use the same method with our model and obtain exactly the same conclusions. Hill *et al.* (1989) [42] were then able to demonstrate the existence of oscillatory solutions numerically for a range of extreme parameter values. We were unable to find oscillatory solutions for our model.

Recently Jones *et al.* (1994) [55, 54] show that it is sufficient to assume that *Chlamydomonas nivalis* is a self-propelled spheroid, provided certain parameters are adjusted, without involving explicit details of the cells' locomotory machinery. Thus supporting the model used in the present analysis. They show that  $\alpha_0$ ,  $\alpha_-$  and  $B$  should be adjusted to 0.40, 12.6 and 6.3, respectively, to allow for the effects of the flagella of *Chlamydomonas nivalis* and its swimming characteristics (see Section 3.8 for more numerical analysis on the adjusted parameter ranges and Section 3.9 for a comparison with experiments).

### 3.7 The effect of swimming speed as a random variable

It is clear from the discussion given in Pedley & Kessler (1990) [85] that randomness in the cell swimming direction is important for a number of reasons. Most importantly it alters the mean cell response to the external torques and changes the form of the diffusion tensor. It is necessary to include these factors in the model for the sake of consistency. From the previous section, it is also apparent that the linear behaviour of the diffusion tensor, and hence the existence of a non-zero most unstable wavenumber, is dependent on the balance between deterministic processes and randomness in the cell swimming direction. But how else does the cell swim in a random manner? A feature

that has been overlooked so far is that the individual cells swim at vastly different speeds. In this section we shall investigate the effect of modelling the cell swimming speed as an independent random variable and discuss how it affects the diffusion tensor and linear analysis. In the real world, with inhomogeneous cultures of *Chlamydomonas nivalis*, it should be expected that there will be a large variance in cell swimming speed corresponding to different stages in the cells' life. Unfortunately it is rather difficult to get data on such things. Hill & Häder (1996) [41] investigated cell swimming speed with cell orientation. They found that experimental calculations of swimming speed were dependent on the choice of time step size between measurements of position. The cells swim in a smooth fashion and their mean swimming direction is affected by the various taxes. In two experiments Hill & Häder (1996) [41] tracked swimming micro-organisms, firstly in a vertical plane and then in a horizontal plane. Both planes were of small focal depths. Using new techniques of data analysis they were able to calculate mean cell swimming velocities and standard deviations as functions of the time step size and orientation. The data were extrapolated back to a time step size of zero to give the actual swimming velocities. For the vertical plane  $\langle V \rangle = 52 \pm 5 \mu\text{ms}^{-1}$  with a standard deviation of  $30 \pm 5 \mu\text{ms}^{-1}$  and for the horizontal plane  $\langle V \rangle = 65 \pm 5 \mu\text{ms}^{-1}$  with a standard deviation of  $30 \pm 5 \mu\text{ms}^{-1}$ . The first experiment means that the standard deviation is 0.58 of the mean and the second 0.46 of the mean.

Theoretically we begin by considering again the calculation for the diffusion tensor  $\mathbf{D}$  given in Chapter 1 (Equation 1.21) and assume that it takes a cell  $\tau$  seconds to settle to a preferred direction (the direction correlation time). Hence,

$$\mathbf{D} = \tau (\langle \mathbf{V}\mathbf{V} \rangle - \langle \mathbf{V} \rangle^2), \quad (3.257)$$

where  $\mathbf{V}$  is a random variable. Assuming that the swimming speed,  $V$ , and swimming direction,  $\mathbf{p}$ , are independent, we can write  $\mathbf{V} = V\mathbf{p}$ . We know that  $\langle V \rangle = V_s$  and, hence, we have

$$\mathbf{D} = V_s^2 \tau \left( \frac{\langle V^2 \rangle}{V_s^2} \langle \mathbf{p}\mathbf{p} \rangle - \langle \mathbf{p} \rangle^2 \right). \quad (3.258)$$

By varying the ratio

$$\mathcal{N} = \frac{\langle V^2 \rangle}{V_s^2} \quad (3.259)$$

we can change the nature of the diffusion tensor. The data of Hill & Häder (1996) [41] gives  $\mathcal{N}$  as bounded by 1.15 and 1.45. From Equation (3.79) we can calculate the

modified diffusion tensor to be

$$\begin{aligned} \frac{1}{V_s^2 \tau} \mathbf{D} = & \begin{pmatrix} \frac{K_1}{\lambda} \mathcal{N} & 0 & 0 \\ 0 & \frac{K_1}{\lambda} \mathcal{N} & 0 \\ 0 & 0 & (1 - \frac{2K_1}{\lambda}) \mathcal{N} - K_1^2 \end{pmatrix} + \epsilon \left[ \eta (J_2 \mathcal{N} - J_1 K_1) \begin{pmatrix} 0 & 0 & \omega_2 \\ 0 & 0 & -\omega_1 \\ \omega_2 & -\omega_1 & 0 \end{pmatrix} \right. \\ & - 2\alpha_0 \eta \begin{pmatrix} (\frac{3}{4} e_{33} K_5 + \frac{1}{4} (e_{11} - e_{22}) J_6) \mathcal{N} & \frac{1}{2} e_{12} J_6 \mathcal{N} & e_{13} (J_5 \mathcal{N} - K_1 J_4) \\ \frac{1}{2} e_{12} J_6 \mathcal{N} & (-\frac{3}{4} e_{33} K_5 - \frac{1}{4} (e_{11} - e_{22}) J_6) \mathcal{N} & e_{23} (J_5 \mathcal{N} - K_1 J_4) \\ e_{13} (J_5 \mathcal{N} - K_1 J_4) & e_{23} (J_5 \mathcal{N} - K_1 J_4) & \frac{3}{2} e_{33} (K_5 \mathcal{N} - 2K_1 K_4) \end{pmatrix} \\ & \left. + O(\epsilon^2) \right] \end{aligned} \quad (3.260)$$

Substituting the diffusion tensor into the governing equations we find that it only alters the definitions of the  $P_i$ . If we assume that  $\lambda = 2.2$  then they become

$$\begin{aligned} P_H &= 0.26\mathcal{N} \\ P_V &= 0.48\mathcal{N} - 0.33 \\ P_5 &= 0.38 - 0.21\alpha_0 - \mathcal{N}(0.16 - 0.20\alpha_0) \\ P_6 &= \alpha_0(-0.43 + 0.33\mathcal{N}) \\ P_7 &= 0.38 - 0.22\alpha_0 - \mathcal{N}(0.16 - 0.13\alpha_0). \end{aligned} \quad (3.261)$$

$P_6$  is the only term which can change sign for  $\mathcal{N} < 2$  and it does so if  $\mathcal{N} > 1.3$ . This is the average of the bounds determined above from the experiments of Hill & Häder (1996) [41]. If  $\alpha_0 = 0.4$  and  $\mathcal{N} > 3.75$  then all of the parameters will have changed sign and this will have a major effect on the linear analysis. It is, however, unlikely that  $\mathcal{N}$  could be so large. Figure (3.14) describes how the neutral curve varies as a function of  $\mathcal{N}$  given  $\eta$  and  $\alpha_0$ . The ratio of the leading order horizontal and vertical diffusions,

$$P_H/P_V \approx \frac{0.26\mathcal{N}}{0.48\mathcal{N} - 0.33}, \quad (3.262)$$

also has some significance. Clearly, if  $\mathcal{N} = 1$  then the ratio is greater than one (as discussed in Pedley *et al.* 1990 [83]), but if  $\mathcal{N} > 1.5$  then the ratio is less than one (as proposed in Childress *et al.* 1975 [19]). The true nature of the diffusion tensor and, hence, the value of  $\mathcal{N}$  should be established by independent experiments. Thus, the evidence is inconclusive for a negative or a positive value of  $P_6$ . Perhaps the best that we can do is to assume that  $P_6$  is small, even when  $d$  is large, and therefore we may assume  $P_6 = 0$ . This is not altogether convincing and more accurate experiments may

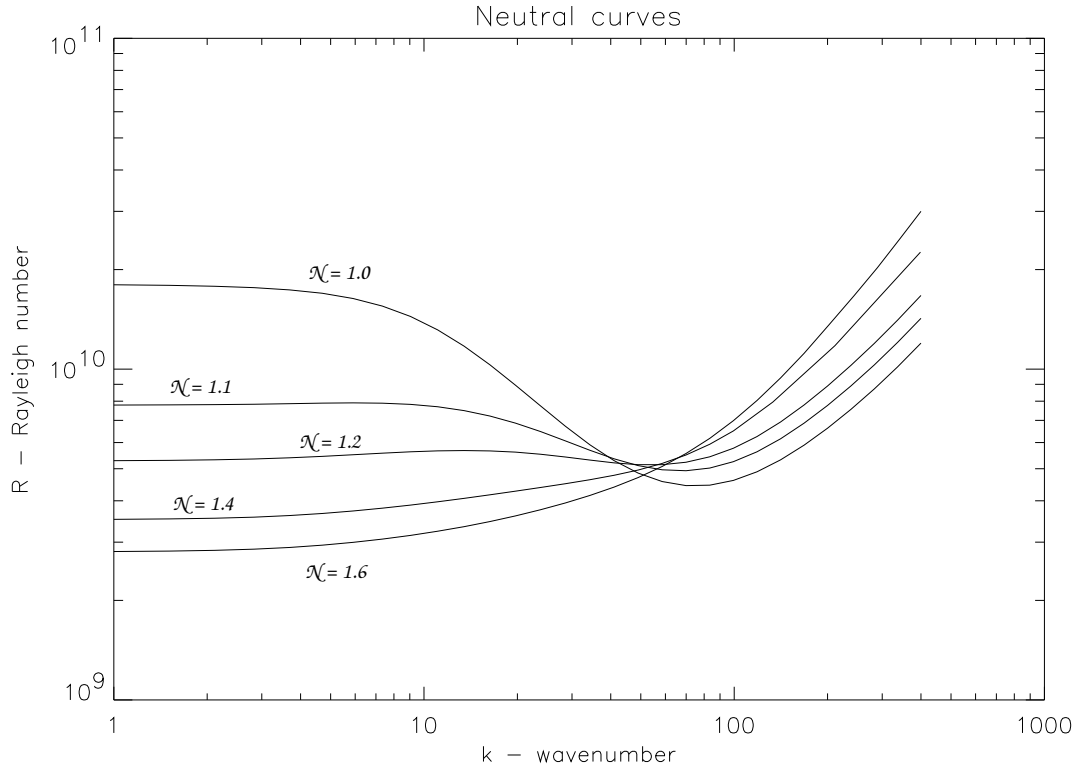


Figure 3.14: Neutral curves for a deep layer ( $d = 200$ ) where  $d^2\eta = 4$ ,  $\alpha_0 = 0.2$  and  $\mathcal{N}$  varies.

need to be performed to elucidate the problem. Alternatively, a better approximation to the diffusion tensor might improve the situation.

As a further example of modelling swimming speed as a random variable, consider the Gamma distribution which has a realistic behaviour (see Figure 3.15) where  $P(V = 0) = 0$  and  $P(V = x) \rightarrow 0$  quickly as  $x \rightarrow \infty$ .

$$P(V = x) = \frac{1}{\Gamma(\xi)} \lambda^\xi x^{\xi-1} e^{-\lambda x} \tag{3.263}$$

where  $x \in [0, \infty)$  and  $\xi$  and  $\lambda$  are variables. Kessler (1995, personal communication) has been using this distribution to fit data obtained on the swimming speed of bacteria. We find that

$$\mathbf{D} = V_s^2 \tau \left( \frac{\xi + 1}{\xi} \langle \mathbf{p}\mathbf{p} \rangle - \langle \mathbf{p} \rangle^2 \right) \tag{3.264}$$

and, hence, we require  $\xi < 3.3$  for  $P_6$  to change sign.

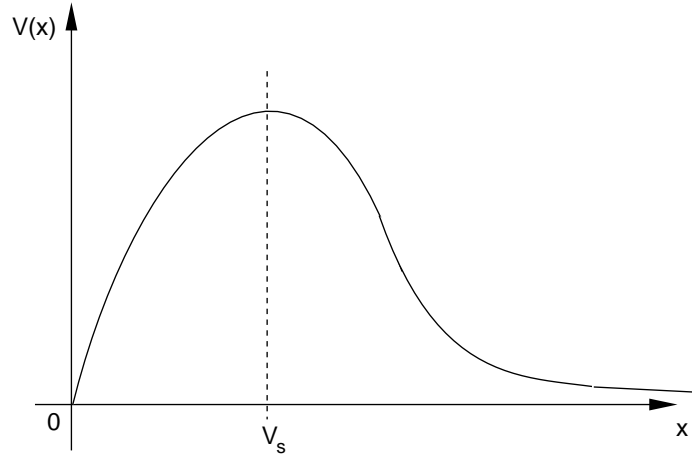


Figure 3.15: The Gamma distribution  $P(V = x)$  where  $V_s$  is its mean.

### 3.8 Numerical analysis for our best parameter measurements

As mentioned in Section 3.6, Jones *et al.* (1995) [54] suggest that allowances may be made for the swimming behaviour of *Chlamydomonas nivalis* and its flagella by increasing  $\alpha_0$  to 0.40 and  $B$  to 6.3 s. Also, it has been suggested ([85]) that the value of 1.3 used above of the direction correlation time,  $\tau$ , is “significantly shorter than the observational estimate of 5 s”. In this section, we will take  $\tau = 5$  s. We also choose to take  $\mathcal{N} = 1.3$ , for the reasons given in Section 3.7, such that  $P_6 = 0$ . Neutral curves for the updated parameter ranges are displayed in Figure (3.16) where it can be seen that, for the realistic parameter value of  $\eta = 16d^{-2}$ , there is most definitely a non-zero most unstable wavenumber and a reduction in this value dramatically alters the neutral curve such that zero becomes the most unstable wavenumber for  $\eta \approx 4d^{-2}$ . Given a large enough value of  $d^2\eta$ , a non-zero most unstable wavenumber will always exist for all  $d$ . Figure (3.16) has the same general characteristics of the previous curves but has a diminished response to an increase in  $\eta$  due to the reduction in  $(P_5 - P_6)$ .

### 3.9 Comparison with experiments

Although we have no way of drawing a neutral curve from the experiments, because we have no reliable data for the non-existence of pattern, (especially as  $d$  changes with each experiment) the data points from Chapter 2 should lie above the neutral curve

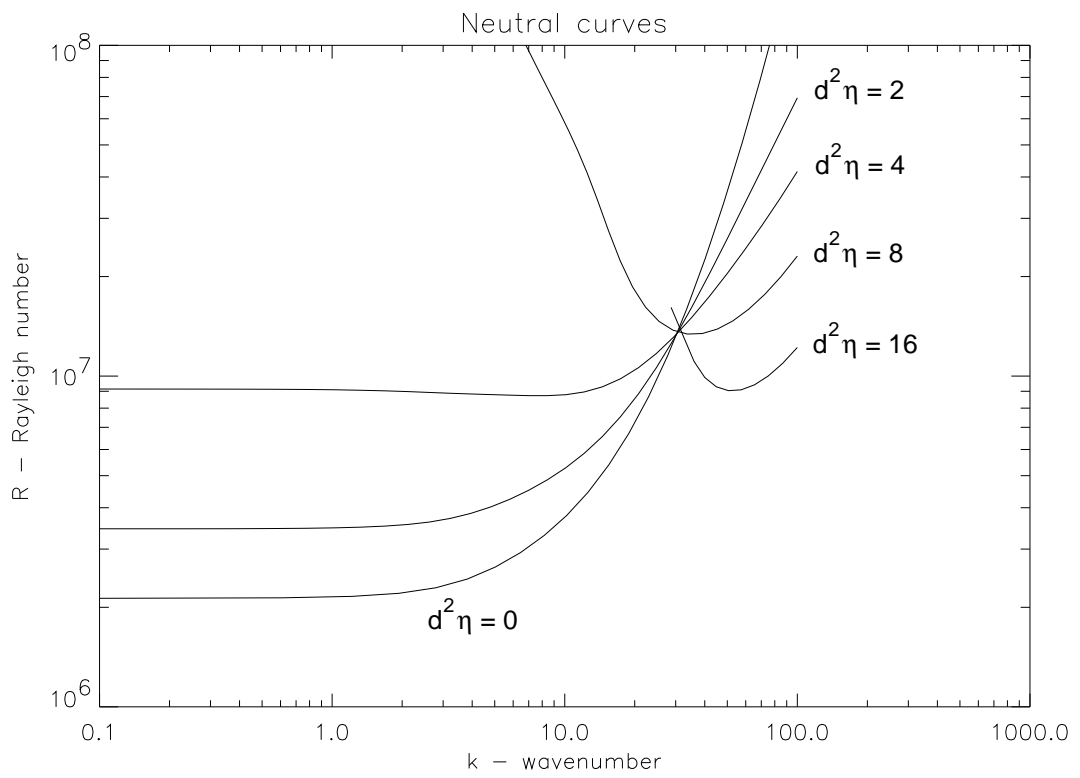


Figure 3.16: Neutral curves for  $d = 40$  using parameter estimates and measurements of  $\alpha_0 = 0.4$  and  $\mathcal{N} = 1.34$ .

for a given measured value of  $d$ . Here, we are assuming that the initially observed pattern consists of rolls (as we can reasonably assume from Chapter 2). Before direct comparisons are made between the theoretical predictions and the experimental data, it is necessary to investigate some important timescales. Firstly, we must establish whether the flows caused by the initial mixing have diminished and secondly, we must consider whether the cells have had sufficient time to form the exponential equilibrium solution as assumed in this linear analysis. Similar arguments were presented in the papers by Hill *et al.* (1989) [42] and Pedley *et al.* (1988) [83]. We assume that the petri dish and suspension are in solid body rotation with angular velocity  $\mathbf{\Omega}$  until the container is instantaneously brought to rest (as in Hill *et al.* (1989) [42]). Hence, the time for spin-down of the suspension is  $O(E^{\frac{1}{2}}\mathbf{\Omega}^{-1})$  where  $E$  is the Ekman number. Hill *et al.* (1989) [42] show that if  $\mathbf{\Omega} \sim 1 s^{-1}$  then the decay time is approximately 10 s, which is larger than the estimate of Pedley *et al.* (1988) [83]. If we take the cell swimming speed to be  $63 \mu m s^{-1}$  upwards (Table 3.2) then the cells would require 100 seconds to swim a typical depth of 6 mm from bottom to top. The cells typically form patterns 30 seconds after the initial mixing. Hence, we can assume that the majority of the fluid motion due to mixing has decayed away before the onset of instability but that the cells do not always have sufficient time to swim and form the exponential equilibrium profile assumed in the linear analysis of this chapter. In some situations in which the suspension is deep it may be more appropriate to use the linear analysis of Pedley & Kessler (1990) [85] (see Chapter 5).

Seven experiments share a similar depth of approximately 0.4 cm, and these will be considered as this depth implies that  $d \approx 200$  for  $\tau = 1.3$  and  $d \approx 40$  for  $\tau = 5$ , as can be seen from Table 3.4. These results can be compared directly with existing results from the linear analysis. In computing Table 3.4, the following expressions for  $d$ ,  $R$  and  $\kappa$  were used in conjunction with Table 3.2.

$$d = \kappa H, \tag{3.265}$$

$$R = \frac{vg\Delta\rho\kappa^2}{\nu\rho V_s^2\tau} \left( \frac{H^5\bar{n}}{1 - e^{-\kappa H}} \right) \tag{3.266}$$

and

$$\kappa = \frac{K_1}{K_2 V_s \tau}. \tag{3.267}$$

As

$$\eta = \frac{BV_s^2\tau}{H^2} = \frac{BV_s^2\tau\kappa^2}{d^2}, \tag{3.268}$$

and if  $\tau = 1.3s$  and  $B = 3.4s$  (the original estimates), then  $\eta \approx 33d^{-2}$ . For the new estimates of  $\tau = 5$  and  $B = 6.3$  (see Jones 1995 [54]),  $\eta = 16d^{-2}$ .

$\tau$	$B$	$\kappa$	$d$	$R$	$\eta$
1.3	3.4	435	$435H$	$9170H^5\bar{n}$	$33d^{-2}$
5	6.3	113	$113H$	$161H^5\bar{n}$	$16d^{-2}$

Table 3.4: Calculations of parameters from original and more recent measurements and estimates of  $B$  and  $\tau$ .

Experiment Name	$\lambda_0$ ( <i>cm</i> )	$\tilde{\lambda}_0$	$\tilde{k}_0$	$d$	$R (\times 10^6)$	$d$	$R (\times 10^6)$
				$\tau = 1.3$		$\tau = 5$	
x108b	0.486	1.23	5.11	172	185	44.7	3.25
x108d	0.468	1.05	5.98	193	484	50.2	8.50
x114c	0.417	1.05	5.98	174	82.2	45.2	1.44
x208j	0.708	1.51	4.16	204	393	53.07	6.90
x208k	0.354	0.755	8.32	204	393	53.0	6.90
x208l	0.603	1.29	4.87	204	393	53.0	6.90
x215f	0.375	0.801	7.84	204	863	53.0	15.2

Table 3.5: Experimental measurements of wavenumbers and corresponding calculations of  $d$  and  $R$  depending on the value of  $\tau$ . Seven experiments have been chosen with similar depths so that they can be compared with the theoretical predictions.

Comparing the data from the  $\tau = 1.3$  and  $\tilde{k}_0$  columns of Table 3.5 with Figure (3.8) (for  $\eta = 32d^{-2}$  we find that the measured Rayleigh numbers are all less than the minimum value,  $2 \times 10^9$ , of the neutral curve. Also, the wavenumbers are 20 to 40 times smaller than the predicted values. Comparing the data from the  $\tau = 5$  and  $\tilde{k}_0$  columns of Table 3.5 with Figure (3.16) reveals that the measured Rayleigh numbers are now of comparable order to the neutral curve but the measured wavenumbers are 5 to 10 times

smaller than those predicted. Reducing  $\eta$  to  $4d^{-2}$  would have the desirable effect of making the predicted most unstable wavenumber to be similar to the measured value. In general, increasing  $\tau$  and decreasing  $B$  improves the agreement between experiments and theoretical predictions. It is also possible to adjust other parameters in the Rayleigh number such that the neutral curve coincides more precisely with the measured data points but the choice of values would be somewhat arbitrary and it should be the priority of experimental work to establish more precise independent measurements of these parameters. The stochastic and deterministic models of gyrotactic bioconvection ([42]) differ in their quantitative predictions of initial pattern wavelengths. Typically Hill *et al.* (1989) [42] predict a wavelength of 2 to 3 *cm* in a suspension of depth 1 *cm* and we predict a wavelength of approximately 1 *mm*. Experimental measurements give a typical wavelength of between 4 and 7 *mm*, halfway between the two predictions.

### 3.10 Discussion

The asymptotic analysis described in the previous sections is a useful tool as it gives us an initial estimate for the value of the Rayleigh number and provides us with an understanding of the underlying instabilities through the balancing of different terms. In this chapter we have successfully solved the linear equations asymptotically and have demonstrated the accuracy that can be obtained by making quite loose statements about the order of various parameters. Good agreement between numerical and asymptotic solutions was always obtained provided the expansion parameter,  $d$  (or  $d^{-1}$ ), was sufficiently small so as to be able to consider parameters such as  $k$ ,  $P_6$  and  $S_c^{-1}$  to be of order one. No evidence of oscillatory solutions was discovered as in [42].

We have shown that modelling the organisms' swimming in a non-deterministic fashion has important consequences for the shape of the neutral curves. We have also shown that a non-zero most unstable wavenumber will always exist (as in the deterministic model for finite depth by [42] but not in the non-gyrotactic model of [19]) provided the gyrotactic orientation parameter is sufficiently large.

Perhaps we may speculate that through evolution the cells have optimized their swimming strategies so as not to waste energy on random events and such that, for a given depth, colonies will self-organise into patterns with non-zero wavenumber once a

critical concentration of cells is surpassed. This enables the cells to collide more often and hence to mate more efficiently. For suspensions of low cell concentration where bioconvection is not possible, the cells will swim to the two-dimensional fluid surface where there is also a strong likelihood that they will come into contact with another cell and can mate. Improvements to the diffusion approximation may be needed to clarify the situation.

Weakly non-linear analyses have been successfully performed by a number of authors for cellular instabilities in Rayleigh-Bénard convection, where there is a non-zero most unstable wavenumber, such as Fauve (1985) [32], Lennie *et al.* (1988) [73], Malkus & Veronis (1958) [78], Newell & Whitehead (1969) [81] and Schlüter *et al.* (1965) [101] to name but a few. Childress & Spiegel (1978) [21] investigated the weakly non-linear analysis of the Childress *et al.* (1975) [19] model where there is a zero most unstable wavenumber. Using a multiple scale expansion they found that the stationary bifurcation was subcritical. Similar analyses have been performed by Chapman & Proctor (1980) [16] and Proctor (1981) [90] for thermal convection between poorly conducting slabs. For stochastic gyrotactic bioconvection we find from the linear analysis that it is possible to obtain either a zero most unstable wavenumber or a non-zero most unstable wavenumber depending on the values of the gyrotactic orientation parameter,  $\alpha_0$  and variance of the cell swimming speed. It is also possible to obtain a balance between these two instabilities (see Figure 3.10) and future research could investigate the weakly non-linear analysis of this system. Depassier & Spiegel (1981) [28] have completed a similar analysis of a far simpler system where multiple scales were used to balance long wavelength instabilities with the smaller scale instabilities. However, in our system a process of simplification would be required before such analysis could be pursued.

## Chapter 4

# Spherical Harmonic Expansion of the Fokker-Planck Equation

### 4.1 Introduction

The steady form of the Fokker-Planck equation for gyrotaxis (see Section 1.6.3) is

$$\nabla \cdot (\dot{\mathbf{p}}f) = D_r \nabla^2 f, \quad (4.1)$$

where

$$\dot{\mathbf{p}} = \frac{1}{2B} [\mathbf{k} - (\mathbf{k} \cdot \mathbf{p})\mathbf{p}] + \frac{1}{2}\boldsymbol{\Omega} \wedge \mathbf{p} + \alpha_0 \mathbf{p} \cdot \mathbf{E} \cdot (\mathbf{I} - \mathbf{p}\mathbf{p}). \quad (4.2)$$

Brenner & Weissman (1972) [12] also studied this form of equation when  $\alpha_0 = 0$ . For convenience, they used a coordinate system where the vorticity is perpendicular to the plane of  $\theta = \frac{\pi}{2}$  and then expanded the solution  $f(\theta, \phi)$  as a doubly infinite sum of spherical harmonics. Using identities for the associated Legendre polynomials, the Fokker-Planck equation is reduced to an infinite set of linear difference equations with an infinite number of unknowns. Truncating the spherical harmonic expansion to order  $R$ , they then obtain “... $R(R + 3) + 2$  linear algebraic equations in an equal number of unknowns”. Resorting to a numerical method seems to be the only option for  $R > 3$  and [12] report that “...the required computer time increases roughly as  $R^3$ , and rapidly becomes excessive as  $R$  exceeds 15”. For the case in which the external field is perpendicular to the vorticity vector, the number of equations and unknowns can be reduced by a factor of two due to the symmetries of the system (i.e. by expanding only

in terms of  $A_n^m \cos m\phi P_n^m(\cos \theta)$  where the  $A$ 's are constants and the  $P$ 's are associated Legendre polynomials).

Spherical harmonics are the natural choice of eigenfunctions to use in such an expansion. Strand & Kim (1992) [106] have used spherical harmonic expansions for dipolar non-spherical particles in an external field. Previous to that Kim & Lawrence (1987) [68] constructed similarity solutions, valid for small times, for orientation distributions of axisymmetric particles with external couples. Both papers used their solutions to investigate the rheological properties of suspensions of particles.

In this chapter, we shall initially consider a micro-organism in a vertical two-dimensional flow field, independent of  $y$ . Later, this will be extended to a three dimensional flow field in the absence of vertical vorticity. For a two-dimensional flow field, it is still essential to model the cell swimming direction on a full sphere rather than on a circle. A coordinate system in which the vorticity is perpendicular to the plane  $\phi = 0$ , is used together with an expansion in terms of  $\cos m\phi P_n^m(\cos \theta)$ . By applying a set of identities for spherical harmonics recursively, using the computer algebra package Maple (reducing the potential for human error), a set of  $R(R + 3)/2$  equations in as many unknowns was generated, together with a normalisation condition. Maple was then employed to solve this set of equations using exact arithmetic. See Appendix C for the Maple code.

For the case in which  $\alpha_0$  is zero, spherical harmonics of order two are found to capture the essential behaviour of the system and the expansion to order three is almost indistinguishable from higher orders. The second order approximation can therefore be used in any further non-linear analysis of bioconvection (in which  $\alpha_0 = 0$ ) where relatively simple expressions are beneficial.

The case of non-zero  $\alpha_0$  is not so well behaved. Low order expansions represent the solution adequately only in certain ranges of the rate of strain and vorticity components. To calculate  $\langle \mathbf{p} \rangle$  and  $\mathbf{D}$  only the coefficients of the spherical harmonics up to order 2 are required. The implementation of the methods used here is designed to be adaptable (such that other taxes or combinations of taxes, may be investigated) and could potentially be used in other similar problems.

## 4.2 The coordinate system

The spherical polar coordinate system is chosen such that the vorticity, given by  $\boldsymbol{\omega} = \omega \mathbf{j}$ , is perpendicular to the plane where  $\phi = 0$  (see Figure 4.1). The swimming direction,

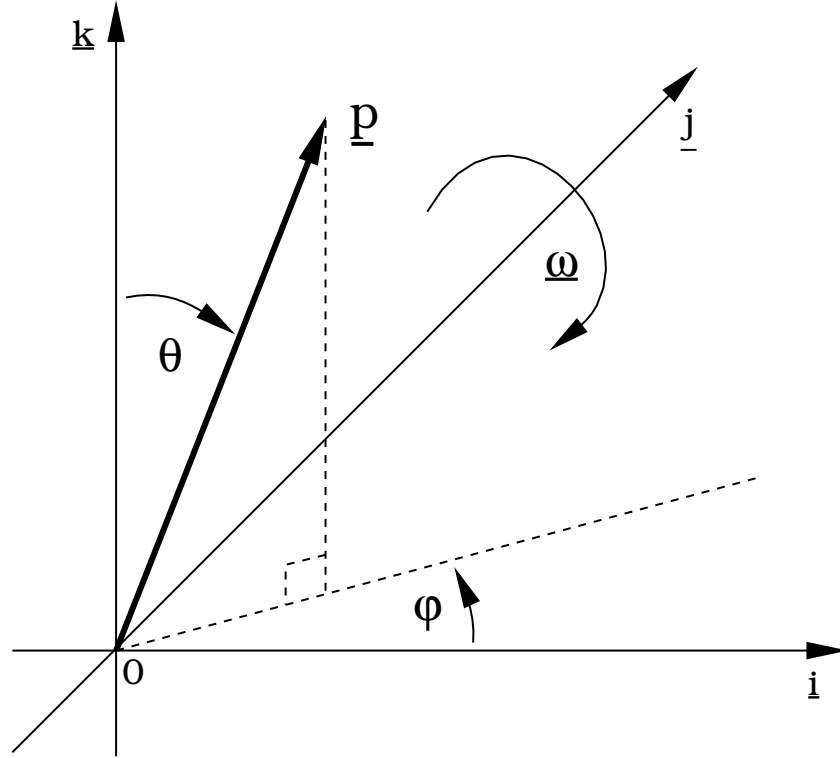


Figure 4.1: The choice of coordinate system on a sphere.

$\mathbf{p}$ , and unit vectors  $\hat{\boldsymbol{\phi}}$  and  $\hat{\boldsymbol{\theta}}$  are given by

$$\mathbf{p} = \begin{pmatrix} \sin \theta \cos \phi \\ \sin \theta \sin \phi \\ \cos \theta \end{pmatrix}, \quad \hat{\boldsymbol{\theta}} = \begin{pmatrix} \cos \theta \cos \phi \\ \cos \theta \sin \phi \\ -\sin \theta \end{pmatrix}, \quad \hat{\boldsymbol{\phi}} = \begin{pmatrix} -\sin \phi \\ \cos \phi \\ 0 \end{pmatrix} \quad (4.3)$$

and also

$$\begin{aligned} \boldsymbol{\omega} \cdot \mathbf{p} \wedge \hat{\boldsymbol{\theta}} &= \omega \cos \phi \\ \boldsymbol{\omega} \cdot \mathbf{p} \wedge \hat{\boldsymbol{\phi}} &= -\omega \cos \theta \sin \phi. \end{aligned} \quad (4.4)$$

The rate-of-strain tensor  $\mathbf{e}$  is

$$\mathbf{e} = \begin{pmatrix} e_{11} & 0 & e_{13} \\ 0 & 0 & 0 \\ e_{13} & 0 & -e_{11} \end{pmatrix} \quad (4.5)$$

and then

$$\begin{aligned}
 \mathbf{p} \cdot \mathbf{e} \cdot \mathbf{p} &= e_{11} \left[ \frac{1}{4} (\cos 2\phi + 3)(1 - \cos 2\theta) - 1 \right] + e_{13} \sin 2\theta \cos \phi \\
 \mathbf{p} \cdot \mathbf{e} \cdot \hat{\theta} &= e_{11} \left[ \frac{1}{4} (\cos 2\phi + 3) \sin 2\theta \right] + e_{13} \cos 2\theta \cos \phi \\
 \mathbf{p} \cdot \mathbf{e} \cdot \hat{\phi} &= e_{11} \left[ -\frac{1}{2} \sin 2\phi \sin \theta \right] - e_{13} \cos \theta \sin \phi.
 \end{aligned} \tag{4.6}$$

Hence the Fokker-Planck equation (4.1) becomes

$$\begin{aligned}
 &\frac{\lambda^{-1}}{\sin \theta} \partial_{\theta} (\sin \theta \partial_{\theta} f) + \frac{\lambda^{-1}}{\sin^2 \theta} \partial_{\phi}^2 f + \sin \theta \partial_{\theta} f + 2 \cos \theta f = \eta \left( \omega \cos \phi \partial_{\theta} f - \omega \frac{\cos \theta}{\sin \theta} \sin \phi \partial_{\phi} f \right) \\
 &+ 2\alpha_0 \eta \left[ (e_{11} (\cos^2 \phi + 1) \sin \theta \cos \theta + e_{13} (\cos^2 \theta - \sin^2 \theta) \cos \phi) \partial_{\theta} f \right. \\
 &- \left. \left( e_{11} \cos \phi \sin \phi + e_{13} \sin \phi \frac{\cos \theta}{\sin \theta} \right) \partial_{\phi} f \right. \\
 &\left. - 3 (e_{11} (\sin^2 \theta \cos^2 \phi - \cos^2 \theta) + 2e_{13} \sin \theta \cos \theta \cos \phi) f \right],
 \end{aligned} \tag{4.7}$$

where  $\lambda = (2D_r B)^{-1}$ ,  $\eta = B\Omega$  and  $\omega$ ,  $e_{11}$  and  $e_{13}$  are scaled with respect to vorticity. For a two dimensional flow, the cell swimming direction distribution will be symmetric about the flow plane and so only even spherical harmonics in  $\phi$  are needed. Hence consider the series

$$f = \sum_{n=0}^{\infty} \sum_{m=0}^n F_n^m \tag{4.8}$$

where we define for ease of writing

$$F_n^m(\theta, \phi) \equiv R_n^m(\phi) P_n^m(\cos \theta) \equiv A_n^m \cos m\phi P_n^m(x) \equiv A_n^m Q_n^m(\theta, \phi). \tag{4.9}$$

Here  $x \equiv \cos \theta$ , the  $A_n^m$  are constants and  $P_n^m$  are associated Legendre polynomials.

Substituting this series into the above equation, making use of the associated Legendre equation (see Appendix A), gives

$$\begin{aligned}
 &\sum_{m,n} \left\{ \lambda^{-1} F_n^m [-n(n+1)] - R_n^m P_n^{m'} \sin^2 \theta + 2 \cos \theta F_n^m \right\} \\
 &= \sum_{m,n} \left\{ -\eta \left( \omega \cos \phi \sin \theta R_n^m P_n^{m'} + \omega \cot \theta \sin \phi R_n^{m'} P_n^m \right) \right. \\
 &- 2\alpha_0 \eta \left[ (e_{11} (\cos^2 \phi + 1) \sin^2 \theta \cos \theta + e_{13} (\cos^2 \theta - \sin^2 \theta) \cos \phi \sin \theta) R_n^m P_n^{m'} \right. \\
 &+ (e_{11} \cos \phi \sin \phi + e_{13} \sin \phi \cot \theta) R_n^{m'} P_n^m \\
 &\left. \left. + 3 (e_{11} (\sin^2 \theta \cos^2 \phi - \cos^2 \theta) + 2e_{13} \sin \theta \cos \theta \cos \phi) R_n^m P_n^m \right] \right\}
 \end{aligned} \tag{4.10}$$

where  $'$  denotes differentiation with respect to the dependent variable.

The normalisation condition that  $f$  integrates to 1 over the surface of the sphere implies that

$$A_0^0 = \frac{1}{4\pi}. \quad (4.11)$$

### 4.3 Calculating the mean quantities

In this section it is shown that only the spherical harmonics up to order two are required to calculate  $\langle \mathbf{p} \rangle$  and  $\mathbf{D}$  and therefore we shall concentrate purely on the convergence of these coefficients.

Firstly, consider  $\langle \mathbf{p} \rangle$  with  $f$  given by spherical harmonics (Equation 4.9). If  $S$  represents the surface of a unit sphere then

$$\langle \mathbf{p} \rangle = \int_S \begin{pmatrix} \sin \theta \cos \phi \\ \sin \theta \sin \phi \\ \cos \theta \end{pmatrix} f(\theta, \phi) dS \equiv \int_S \begin{pmatrix} Q_1^1 \\ 0 \\ Q_1^0 \end{pmatrix} f(\theta, \phi) dS \quad (4.12)$$

and hence we require the integrals of  $\int_S Q_1^1 f dS$  and  $\int_S Q_1^0 f dS$ . Using the identities

$$\int_S Q_n^m Q_{n'}^{m'} dS = \delta_{m'}^m \delta_{n'}^n \frac{2\pi}{2n+1} \frac{(n+m)!}{(n-m)!} \quad (4.13)$$

for  $n, n' \geq m, m' = 1, 2, \dots$  and

$$\int_S Q_n^0 Q_{n'}^{m'} dS = \delta_{m'}^0 \delta_{n'}^n \frac{4\pi}{2n+1}, \quad (4.14)$$

we find that

$$\langle \mathbf{p} \rangle = \frac{4\pi}{3} \begin{pmatrix} A_1^1 \\ 0 \\ A_1^0 \end{pmatrix}. \quad (4.15)$$

Similarly, using the identities

$$\sin^2 \theta \cos^2 \phi = \frac{1}{2} \sin^2 \theta (1 + \cos 2\phi) = \frac{1}{3} Q_0^0 - \frac{1}{3} Q_2^0 + \frac{1}{6} Q_2^2, \quad (4.16)$$

$$\sin \theta \cos \theta \cos \phi = \frac{1}{3} Q_2^1, \quad (4.17)$$

$$\cos^2 \theta = \frac{2}{3} Q_2^0 + \frac{1}{3} Q_0^0 \quad (4.18)$$

and

$$\sin^2 \theta \sin^2 \phi = \frac{1}{2} \sin^2 \theta (1 - \cos 2\phi) = \frac{1}{3} Q_0^0 - \frac{1}{3} Q_2^0 - \frac{1}{6} Q_2^2 \quad (4.19)$$

gives

$$\langle \mathbf{p}\mathbf{p} \rangle = \pi \begin{pmatrix} \frac{4}{3}A_0^0 - \frac{4}{15}A_2^0 + \frac{8}{5}A_2^2 & 0 & \frac{4}{5}A_2^1 \\ 0 & \frac{4}{3}A_0^0 - \frac{4}{15}A_2^0 - \frac{8}{5}A_2^2 & 0 \\ \frac{4}{5}A_2^1 & 0 & \frac{8}{15}A_2^0 + \frac{4}{3}A_0^0 \end{pmatrix}. \quad (4.20)$$

Hence, defining the diffusivity (as in Section 1.6.3) as  $\mathbf{D} = V_s^2 \tau [\langle \mathbf{p}\mathbf{p} \rangle - \langle \mathbf{p} \rangle^2]$ , we obtain

$$\frac{\mathbf{D}}{V_s^2 \tau \pi} = \begin{pmatrix} \frac{4}{3}A_0^0 - \frac{4}{15}A_2^0 + \frac{8}{5}A_2^2 - \frac{16\pi}{9}(A_1^1)^2 & 0 & \frac{4}{5}A_2^1 - \frac{16\pi}{9}A_1^1 A_1^0 \\ 0 & \frac{4}{3}A_0^0 - \frac{4}{15}A_2^0 - \frac{8}{5}A_2^2 & 0 \\ \frac{4}{5}A_2^1 - \frac{16\pi}{9}A_1^1 A_1^0 & 0 & \frac{8}{15}A_2^0 + \frac{4}{3}A_0^0 - \frac{16\pi}{9}(A_1^0)^2 \end{pmatrix}. \quad (4.21)$$

Thus, only the expressions for the five coefficients  $A_1^0$ ,  $A_1^1$ ,  $A_2^0$ ,  $A_2^1$  and  $A_2^2$  in the spherical harmonic expansion are required.

## 4.4 Recursion relations

Below is a summary of the operations or recursion relations that will be used in the following analysis. These relations allow expressions on the LHS to be written in a simpler functional form (RHS). A reference for each relation and the name of the corresponding functional is also given.

- $X_c$  (Equation A.7) :

$$xP_n^m \equiv \frac{n+m}{2n+1}P_{n-1}^m + \frac{n-m+1}{2n+1}P_{n+1}^m \quad (4.22)$$

$$X_c(T_n^m) : T_n^m \mapsto \frac{n+m}{2n+1}T_{n-1}^m + \frac{n-m+1}{2n+1}T_{n+1}^m. \quad (4.23)$$

- $X_{ss}$  :

$$X_{ss}(T_n^m) : T_n^m \mapsto T_n^m - X_c(X_c(T_n^m)). \quad (4.24)$$

- $X_{ssp}$  (substitute Equations A.8 and A.9 in A.10) :

$$(1-x^2)P_n^{m1} \equiv \frac{1}{2n+1}((n+m)(n+1)P_{n-1}^m - n(n-m+1)P_{n+1}^m) \quad (4.25)$$

$$X_{ssp}(T_n^m) : T_n^m \mapsto \frac{1}{2n+1}((n+m)(n+1)T_{n-1}^m - n(n-m+1)T_{n+1}^m). \quad (4.26)$$

- $X_{su}$  (Equation A.8) :

$$(2n+1)\sqrt{1-x^2}P_n^m \equiv P_{n+1}^{m+1} - P_{n-1}^{m+1} \quad (4.27)$$

$$X_{su}(T_n^m) : T_n^m \mapsto T_{n+1}^{m+1} - T_{n-1}^{m+1}. \quad (4.28)$$

- $X_{sd}$  (Equation A.9) :

$$(2n+1)\sqrt{1-x^2}P_n^m \equiv (n+m)(n+m-1)P_{n-1}^{m-1} - (n-m+1)(n-m+2)P_{n+1}^{m-1} \quad (4.29)$$

$$X_{sd}(T_n^m) : T_n^m \mapsto (n+m)(n+m-1)T_{n-1}^{m-1} - (n-m+1)(n-m+2)T_{n+1}^{m-1}. \quad (4.30)$$

- $X_{spu}$  (substitute Equation A.6 in A.10) :

$$\sqrt{1-x^2}P_n^{m'} \equiv P_n^{m+1} - \frac{mx}{\sqrt{1-x^2}}P_n^m \quad (4.31)$$

$$X_{spu}(T_n^m) : T_n^m \mapsto T_n^{m+1} - \frac{mx}{\sqrt{1-x^2}}T_n^m. \quad (4.32)$$

- $X_{spd}$  (substitute Equation A.6 in A.10) :

$$\sqrt{1-x^2}P_n^{m'} \equiv -(n-m+1)(n+m)P_n^{m-1} + \frac{mx}{\sqrt{1-x^2}}P_n^m \quad (4.33)$$

$$X_{spd}(T_n^m) : T_n^m \mapsto -(n-m+1)(n+m)T_n^{m-1} + \frac{mx}{\sqrt{1-x^2}}T_n^m. \quad (4.34)$$

- $X_{sin}$  :

$$S^1 S^m \equiv \frac{1}{2}C^{m-1} - \frac{1}{2}C^{m+1} \quad (4.35)$$

$$X_{sin}(S^1 S^m) : S^1 S^m \mapsto \frac{1}{2}C^{m-1} - \frac{1}{2}C^{m+1}. \quad (4.36)$$

- $X_{cos}$  :

$$C^1 C^m \equiv \frac{1}{2}C^{m-1} + \frac{1}{2}C^{m+1}. \quad (4.37)$$

$$X_{cos}(C^1 C^m) : C^1 C^m \mapsto \frac{1}{2}C^{m-1} + \frac{1}{2}C^{m+1}. \quad (4.38)$$

Here we have made use of the shorthand  $S^m = \sin m\phi$  and  $C^m = \cos m\phi$ .

## 4.5 Simplification

Consider Equation (4.10) a term at a time, trying at each stage to express the whole term as an expression in spherical harmonics with simple non-trigonometric coefficients. Henceforth  $x \equiv \cos \theta$  without mention. The special cases of low and high values of  $m$  and  $n$  are dealt with later.

### 4.5.1 Left hand side

The first term on the left hand side is in the right form. If we apply  $X_{ssp}$  to the second term we will get terms in  $Q_{n\pm 1}^m$ . Similarly applying  $X_c$  to the third term gives us terms in  $Q_{n\pm 1}^m$ .

### 4.5.2 Right hand side - vorticity terms

The first term on the right hand side contains a  $C^1$  so we will make use of the identity  $X_{cos}$  and turn the  $R_n^m$  into  $\frac{A_n^m}{2}(C^{m-1} + C^{m+1})$ . Now we should try and convert the  $P_n^m$  into terms like  $P_n^{m\pm 1}$ . This proves possible with the identities  $X_{spu}$  and  $X_{spd}$ . However, there appears to be an undesirable term,  $\pm \frac{mx}{\sqrt{1-x^2}}P_n^m$ . If this term were to remain in the equation, then it would lead to the problematic integral

$$\int \frac{1}{1-x^2} P_n^m(x) P_p^m(x) dx \quad (4.39)$$

which, on explicit evaluation, gives not one delta function in terms of  $n$  and  $p$ , but an infinite series of delta functions in  $n$  and  $p$  (the integral has a curious behaviour as only  $\min(n, p)$  is relevant and not  $\max(n, p)$ ; see Appendix B), as

$$\int \frac{1}{1-x^2} P_n^m(x) P_p^m(x) dx = \begin{cases} \frac{1}{m} \frac{(\min(p, q) + m)!}{(\min(p, q) - m)!} & p + q \text{ even} \\ 0 & \text{otherwise} \end{cases} \quad (4.40)$$

This would ultimately give an infinite set of infinite-length recursion relations for the  $A_n^m$ . Fortunately, these terms completely cancel out with similar terms produced by the second term on the right hand side, after application of the identity  $X_{sin}$ . Thus, the vorticity terms become

$$\frac{\omega \eta A_n^m}{2} (-Q_n^{m+1} + (n - m + 1)(n + m)Q_n^{m-1}). \quad (4.41)$$

### 4.5.3 Right hand side - rate of strain terms

These terms naturally fall into two groups: the third, fifth and seventh terms multiplied by  $e_{11}$ , and the fourth, sixth and eighth terms multiplied by  $e_{13}$ . Using the operators  $X_{cos}$  and  $X_{sin}$ , the terms in the first group can be written in terms of  $C^{m\pm 2}$  and  $C^m$ , with the “undesirable” terms always cancelling. Except for a factor of  $-2\alpha_0\eta e_{11}$ , these terms are

$$A_n^m C^{m-2} \left( -\frac{1}{4} \cos \theta \sin \theta (n - m + 1)(m + n) P_n^{m-1} + \frac{3 - m}{4} \sin^2 \theta P_n^m \right)$$

$$\begin{aligned}
& + A_n^m C^{m+2} \left( \frac{1}{4} \cos \theta \sin \theta P_n^{m+1} + \frac{3+m}{4} \sin^2 \theta P_n^m \right) \\
& + A_n^m C^m \left( \frac{3}{2} P_n^m \sin^2 \theta - 3 \cos^2 \theta P_n^m \right. \\
& \left. + \frac{3}{2} \cos \theta \frac{1}{2n+1} ((n+m)(n+1)P_{n-1}^m - n(n-m+1)P_{n+1}^m) \right) \quad (4.42)
\end{aligned}$$

and they become

$$\begin{aligned}
& A_n^m \left[ -\frac{1}{4}(n-m+1)(m+n)C^{m-2}X_c(X_{sd}(P_n^{m-1})) + \frac{3-m}{4}C^{m-2}X_{sd}(X_{sd}(P_n^m)) \right. \\
& + \frac{1}{4}C^{m+2}X_c(X_{su}(P_n^{m+1})) + \frac{3+m}{4}C^{m+2}X_{su}(X_{su}(P_n^m)) \\
& + \frac{3}{2}C^mX_{ss}(P_n^m) - 3C^mX_c(X_c(P_n^m)) \\
& \left. + \frac{3}{2} \frac{1}{2n+1} C^m X_c ((n+m)(n+1)P_{n-1}^m - n(n-m+1)P_{n+1}^m) \right] \quad (4.43)
\end{aligned}$$

Hence, we can write

$$\begin{aligned}
& A_n^m \left[ -\frac{1}{4}(n-m+1)(m+n)X_c(X_{sd}(Q_n^{m-1})) + \frac{3-m}{4}X_{sd}(X_{sd}(Q_n^m)) \right. \\
& + \frac{1}{4}X_c(X_{su}(Q_n^{m+1})) + \frac{3+m}{4}X_{su}(X_{su}(Q_n^m)) + \frac{3}{2}X_{ss}(Q_n^m) - 3X_c(X_c(Q_n^m)) \\
& \left. + \frac{3}{2} \frac{1}{2n+1} X_c ((n+m)(n+1)Q_{n-1}^m - n(n-m+1)Q_{n+1}^m) \right]. \quad (4.44)
\end{aligned}$$

The second group of terms multiplied by  $-2\alpha_0\eta e_{13}$  can be expressed in terms of  $C^{m\pm 1}$  using  $X_{cos}$  and  $X_{sin}$ . In a similar manner to the above they become

$$\begin{aligned}
& A_n^m [X_c(X_c(-(n-m+1)(n+m)Q_n^{m-1} + Q_n^{m+1})) \\
& - \frac{1}{2}(-(n-m+1)(n+m)Q_n^{m-1} + Q_n^{m+1}) - mX_c(X_{sd}(Q_n^m) - X_{su}(Q_n^m)) \\
& + \frac{3}{2n+1}X_c((n+m)(n+m-1)Q_{n-1}^{m-1} - (n-m+1)(n-m+2)Q_{n+1}^{m-1} \\
& + Q_{n+1}^{m+1} - Q_{n-1}^{m+1})]. \quad (4.45)
\end{aligned}$$

On summing over  $m$  and  $n$ , but forgetting for the moment about the extreme cases, the whole equation (4.1) becomes

$$\begin{aligned}
0 & = \lambda^{-1}n(n+1)A_n^m Q_n^m + A_n^m X_{ssp}(Q_n^m) - 2A_n^m X_c(Q_n^m) \\
& + \frac{\omega\eta}{2}A_n^m (-Q_n^{m+1} + (n-m+1)(n+m)Q_n^{m-1}) \\
& - 2\alpha_0\eta e_{11}A_n^m \left[ -\frac{1}{4}(n-m+1)(m+n)X_c(X_{sd}(Q_n^{m-1})) + \frac{3-m}{4}X_{sd}(X_{sd}(Q_n^m)) \right. \\
& \left. + \frac{1}{4}X_c(X_{su}(Q_n^{m+1})) + \frac{3+m}{4}X_{su}(X_{su}(Q_n^m)) + \frac{3}{2}X_{ss}(Q_n^m) - 3X_c(X_c(Q_n^m)) \right]
\end{aligned}$$

$$\begin{aligned}
 & + \frac{3}{2} \frac{1}{2n+1} X_c \left( (n+m)(n+1)Q_{n-1}^m - n(n-m+1)Q_{n+1}^m \right) \Big] \\
 & - 2\alpha_0 \eta e_{13} A_n^m \left[ X_c(X_c(-(n-m+1)(n+m)Q_n^{m-1} + Q_n^{m+1})) \right. \\
 & - \frac{1}{2} \left( -(n-m+1)(n+m)Q_n^{m-1} + Q_n^{m+1} \right) - mX_c(X_{sd}(Q_n^m) - X_{su}(Q_n^m)) \\
 & + \frac{3}{2n+1} X_c \left( (n+m)(n+m-1)Q_{n-1}^{m-1} - (n-m+1)(n-m+2)Q_{n+1}^{m-1} \right. \\
 & \left. \left. + Q_{n+1}^{m+1} - Q_{n-1}^{m+1} \right) \right]. \tag{4.46}
 \end{aligned}$$

This equation will be referred to as  $\mathcal{G}_n^m$ .

There are a number of parameters involved here. The search of parameter space has been limited by assuming that  $\lambda$  is given. For the micro-organism *Chlamydomonas nivalis*  $\lambda \approx 2.2$  and, for the purposes of computer algebra, can be written as  $\frac{22}{10}$ . This value will be used throughout the following analysis.

## 4.6 Special cases - extremal terms

There are two cases connected with the finite order of the expansion. One concerns the upper extreme of the expansion and the other concerns special cases around the lower extremity. The first is easily dealt with by just setting all coefficients of order greater than the truncation order to zero. In the second case, note that  $A_n^m = 0$  if  $m, n < 0$  or  $n \geq m$ , and such terms should not appear in Equation (4.46). Consider first the case where  $m = 0$ :

$$S^1 S^0 = \frac{1}{2} C^{-1} - \frac{1}{2} C^1 = 0 \tag{4.47}$$

and

$$C^1 C^0 = \frac{1}{2} C^{-1} + \frac{1}{2} C^1 = C^1, \tag{4.48}$$

in which  $C^m = \cos m\phi$  and  $S^m = \sin m\phi$ . This indicates how the definitions (4.37) and (4.35) for  $X_{cos}$  and  $X_{sin}$  need to be modified. In general, if  $m = 0$  then terms in  $Q_q^p$  where  $p$  is positive are doubled and where  $p$  is negative are set to zero. Terms where  $p = 0$  are unchanged. This gives us the following relations ( $\forall n$ ), which will be summed over  $n$  later:

$$\begin{aligned}
 \mathcal{F}_n^0 := & \lambda^{-1} n(n+1) A_n^0 Q_n^0 + A_n^0 X_{ssp}(Q_n^0) - 2A_n^0 X_c(Q_n^0) - \omega \eta A_n^0 Q_n^1 + \\
 & - 2\alpha_0 \eta e_{11} A_n^m \left[ \frac{1}{2} X_c(X_{su}(Q_n^1)) + \frac{3}{2} X_{su}(X_{su}(Q_n^0)) + \frac{3}{2} X_{ss}(Q_n^0) - 3X_c(X_c(Q_n^0)) \right]
 \end{aligned}$$

$$\begin{aligned}
& + \frac{3}{2} \frac{1}{2n+1} X_c (n(n+1)Q_{n-1}^0 - n(n+1)Q_{n+1}^0) \Big] \\
& - 2\alpha_0 \eta e_{13} A_n^0 \left[ 2X_c(X_c(Q_n^1)) - Q_n^1 + \frac{6}{2n+1} X_c(Q_{n+1}^1 - Q_{n-1}^1) \right]. \quad (4.49)
\end{aligned}$$

The next case to consider is  $m = 1$ . The only terms which may cause concern here are those that involve expressions in  $Q_n^{m-2}$ . These type of terms are restricted to those with the coefficient  $\alpha_0 \eta e_{11}$ . By considering

$$\frac{1}{2}(C^2 + 3)C^1 = \frac{1}{4}C^{-1} + \frac{1}{4}C^3 + \frac{3}{2}C^0 = \frac{1}{4}C^1 + \frac{1}{4}C^3 + \frac{3}{2}C^0 \quad (4.50)$$

we get the equations

$$\begin{aligned}
\mathcal{F}_n^1 & := \lambda^{-1} n(n+1) A_n^1 Q_n^1 + A_n^1 X_{ssp}(Q_n^1) - 2A_n^1 X_c(Q_n^1) \\
& + \frac{\omega \eta}{2} A_n^1 (-Q_n^2 + n(n+1)Q_n^0) \\
& - 2\alpha_0 \eta e_{11} A_n^1 \left[ -\frac{1}{4} n(1+n) X_c(X_{su}(Q_n^0)) + \frac{1}{2} X_{ss}(Q_n^1) \right. \\
& + \frac{1}{4} X_c(X_{su}(Q_n^2)) + X_{su}(X_{su}(Q_n^1)) + \frac{3}{2} X_{ss}(Q_n^1) - 3X_c(X_c(Q_n^1)) \\
& \left. + \frac{3}{2} \frac{1}{2n+1} X_c((n+1)^2 Q_{n-1}^1 - n^2 Q_{n+1}^1) \right] \\
& - 2\alpha_0 \eta e_{13} A_n^1 [X_c(X_c(-n(n+1)Q_n^0 + Q_n^2)) \\
& - \frac{1}{2} (-n(n+1)Q_n^0 + Q_n^2) - X_c(X_{sd}(Q_n^1) - X_{su}(Q_n^1)) \\
& + \frac{3}{2n+1} X_c(n(n+1)Q_{n-1}^0 - n(n+1)Q_{n+1}^0 \\
& + Q_{n+1}^2 - Q_{n-1}^2)]. \quad (4.51)
\end{aligned}$$

## 4.7 Implementation

The complete expansion of Equation (4.1) in spherical harmonics is

$$0 = \sum_{n=0}^R \mathcal{F}_n^0 + \sum_{n=1}^R \mathcal{F}_n^1 + \sum_{n=2}^R \sum_{m=2}^n \mathcal{G}_n^m, \quad (4.52)$$

where  $R$  is the order of the approximation and the spherical harmonic coefficients,  $A_q^p$  (see Equation 4.9), are zero if  $p > q$ ,  $p < 0$ ,  $q > R$  or  $q < 0$ .

As the surface spherical harmonics form an orthonormal basis, we can find the inner product of Equation (4.52) with any other surface spherical harmonic and hence extract a set of  $R(R+3)/2$  simultaneous equations for the  $R(R+3)/2$  unknown coefficients.

The implementation in Maple is straightforward. See Appendix C for the Maple code. Equation (4.52) is calculated and simplified using the recursion functions of Section (4.4). The inner product of this equation with  $Q_q^p$  is then evaluated using Equations (4.13) and (4.14). This is repeated for all allowed values of  $m$  and  $n$ , and eventually this set of equations is solved explicitly using Maple's inbuilt algebraic solver. The most significant cost in computer time and memory is due to solving the equations. The shorthand

$$\zeta = \eta\omega, \quad (4.53)$$

$$\xi = \alpha_0\eta e_{11} \quad (4.54)$$

and

$$\chi = \alpha_0\eta e_{13} \quad (4.55)$$

is used throughout the following analysis.

## 4.8 Results for $\alpha_0 = 0$

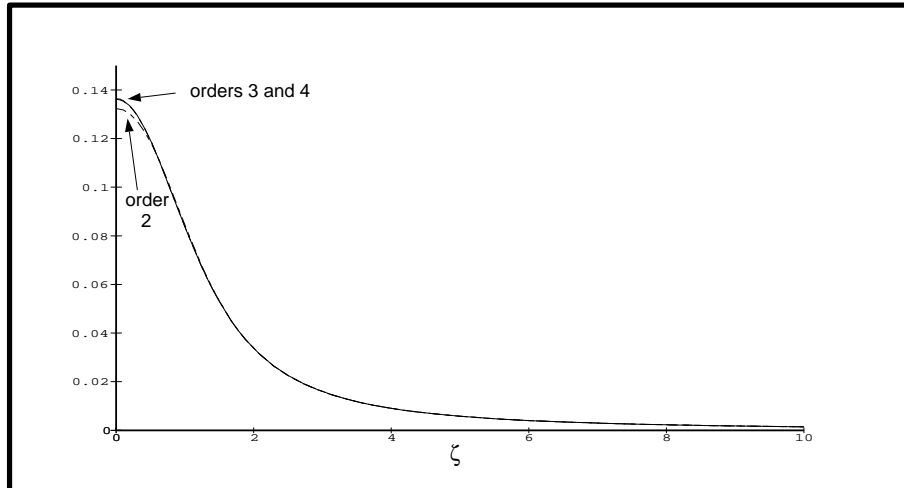


Figure 4.2: Graph of the coefficient  $A_1^0$  with  $\zeta$  for orders of approximation of 2, 3 and 4.

If we set  $\alpha_0 = 0$ , so that the cell is spherical and the effects of rate-of-strain vanish, we look at the case where there is a balance between the gravitational and vorticity driven torques. This case is easy to visualise and one can imagine the deterministic situation in which vorticity increases and the cells' swimming angle to the vertical

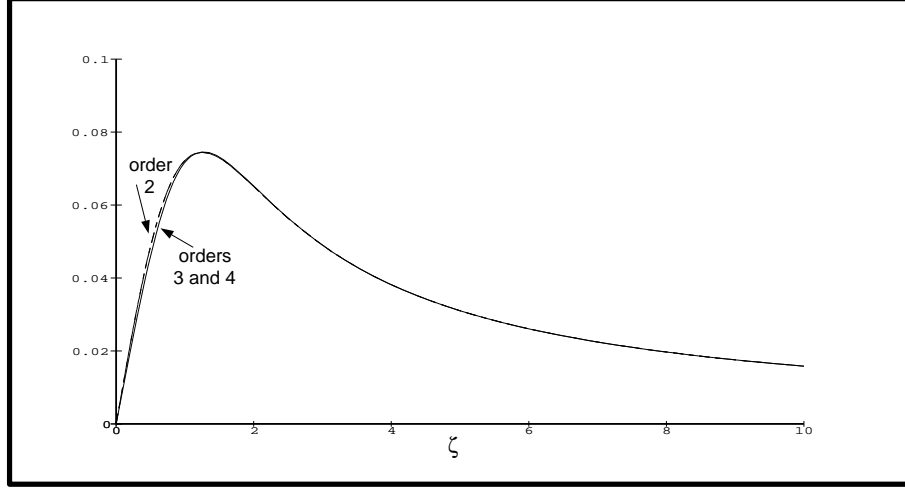


Figure 4.3: Graph of the coefficient  $A_1^1$  with  $\zeta$  for orders of approximation of 2, 3 and 4.

increases with it. If the vorticity increases too much, then the terms no longer balance and the cell tumbles. We expect to see a similar situation with the stochastic model, with the cells' average swimming angle with the vertical increasing with vorticity. For very high values of vorticity, the cell orientation distribution function is no longer sharply peaked but almost uniform.

The five simultaneous equations for the second order approximation are

$$\begin{aligned}
 \frac{20}{33}A_1^0 + \frac{2}{3}\zeta A_1^1 + \frac{4}{15}A_2^0 - \frac{1}{3\pi} &= 0 \\
 -\frac{2}{3}\zeta A_1^0 + \frac{20}{33}A_1^1 + \frac{2}{5}A_2^1 &= 0 \\
 -\frac{4}{5}A_1^0 + \frac{12}{11}A_2^0 + \frac{6}{5}\zeta A_2^1 &= 0 \\
 -\frac{6}{5}A_1^1 - \frac{6}{5}\zeta A_2^0 + \frac{36}{11}A_2^1 + \frac{12}{5}A_2^2 &= 0 \\
 -\frac{12}{5}\zeta A_2^1 + \frac{144}{11}A_2^2 &= 0.
 \end{aligned} \tag{4.56}$$

This set of equations is remarkably simple. It could be easily extended to the time dependent problem and the resulting linear dynamical system could be easily studied. Solving the above equations results in the expressions

$$\begin{aligned}
 A_1^0 &= \frac{825}{4\pi} \frac{5589 + 2420\zeta^2}{1098075\zeta^4 + 2363735\zeta^2 + 2772144} \\
 A_1^1 &= \frac{1815\zeta}{4\pi} \frac{1887 + 1210\zeta^2}{1098075\zeta^4 + 2363735\zeta^2 + 2772144}
 \end{aligned}$$

$$\begin{aligned}
 A_2^0 &= \frac{605}{8\pi} \frac{11178 - 4235\zeta^2}{1098075\zeta^4 + 2363735\zeta^2 + 2772144} \\
 A_2^1 &= \frac{2495625}{4\pi} \frac{\zeta}{1098075\zeta^4 + 2363735\zeta^2 + 2772144} \\
 A_2^2 &= \frac{1830125}{16\pi} \frac{\zeta^2}{1098075\zeta^4 + 2363735\zeta^2 + 2772144}.
 \end{aligned} \tag{4.57}$$

These expressions, together with Equations (4.15) and (4.21), will be used in the non-linear analysis of Chapter 5. The order three approximation is also sufficiently simple to express here. The nine equations are

$$\begin{aligned}
 \frac{20}{33}A_1^0 + \frac{2}{3}\zeta A_1^1 + \frac{4}{15}A_2^0 - \frac{1}{3\pi} &= 0 \\
 -\frac{2}{3}\zeta A_1^0 + \frac{20}{33}A_1^1 + \frac{2}{5}A_2^1 &= 0 \\
 -\frac{4}{5}A_1^0 + \frac{12}{11}A_2^0 + \frac{6}{5}\zeta A_2^1 + \frac{12}{35}A_3^0 &= 0 \\
 -\frac{6}{5}A_1^1 - \frac{6}{5}\zeta A_2^0 + \frac{36}{11}A_2^1 + \frac{12}{5}A_2^2 + \frac{48}{35}A_3^1 &= 0 \\
 -\frac{12}{5}\zeta A_2^1 + \frac{144}{11}A_2^2 + \frac{48}{7}A_3^2 &= 0 \\
 -\frac{24}{35}A_2^0 + \frac{120}{77}A_3^0 + \frac{12}{7}\zeta A_3^1 &= 0 \\
 -\frac{96}{35}A_2^1 - \frac{96}{35}A_2^2 + \frac{720}{77}A_3^1 + \frac{60}{7}A_3^2 &= 0 \\
 -\frac{96}{7}A_2^2 - \frac{60}{7}A_3^1 + \frac{7200}{77}A_3^2 + \frac{360}{7}\zeta A_3^3 &= 0 \\
 -\frac{360}{7}\zeta A_3^2 + \frac{43200}{77}A_3^3 &= 0.
 \end{aligned} \tag{4.58}$$

This has solutions for the first two coefficients of

$$\begin{aligned}
 A_1^0 &= \frac{33}{4\pi} \left( \frac{12152908460\zeta^6 + 454816501139\zeta^4 + 2112839412992\zeta^2 + 3718545506304}{\mathcal{D}(\zeta)} \right) \\
 A_1^1 &= \frac{363\zeta}{20\pi} \left( \frac{6076454230\zeta^6 + 222850909897\zeta^4 + 893263682080\zeta^2 + 1354356023296}{\mathcal{D}(\zeta)} \right)
 \end{aligned} \tag{4.59}$$

where

$$\begin{aligned}
 \mathcal{D}(\zeta) &= 220575288549\zeta^8 + 8220314088833\zeta^6 + 37561155901808\zeta^4 \\
 &\quad + 80481969512384\zeta^2 + 71589467955200.
 \end{aligned} \tag{4.60}$$

Figures (4.2) and (4.3) show the graphs of  $A_1^0$  and  $A_1^1$  after truncating at orders 2, 3 and 4. It can be seen that orders 3 and 4 are almost indistinguishable (and all higher orders) and that even the second order approximation captures the essential behaviour

of the system. This is also true for the coefficients  $A_2^0, A_2^1$  and  $A_2^2$  (Figures 4.4 to 4.6). However, the size of the algebraic expressions for the coefficients vary markedly. The expressions quickly become cumbersome and unmanageable after the fourth order.

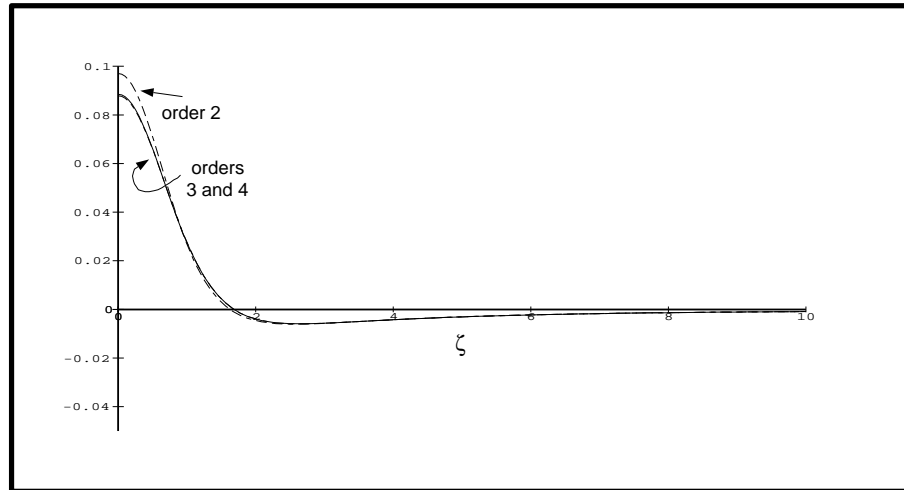


Figure 4.4: Graph of the coefficient  $A_2^0$  with  $\zeta$  for orders of approximation of 2, 3 and 4.

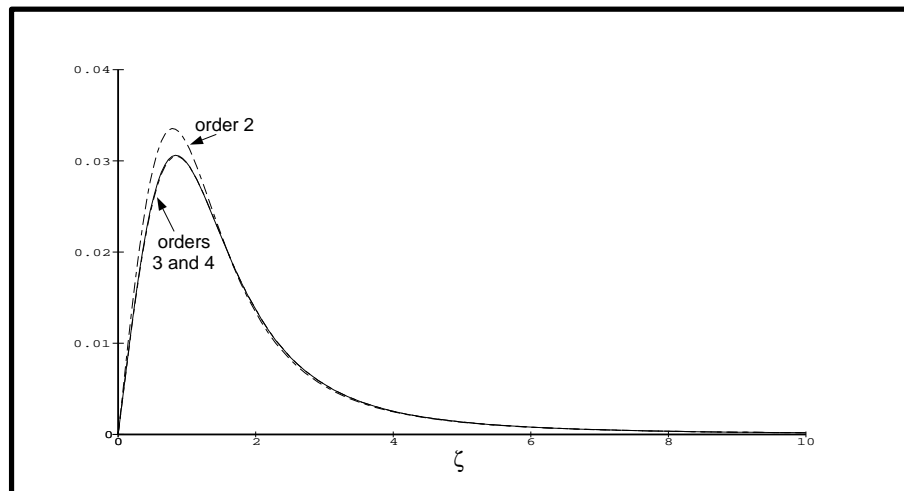


Figure 4.5: Graph of the coefficient  $A_2^1$  with  $\zeta$  for orders of approximation of 2, 3 and 4.

Section 4.3 above shows that  $A_1^1$  represents the  $x$  component of the average swimming direction and  $A_1^0$  the  $z$  component. Figures (4.7) to (4.10) show how the probability distribution,  $f$ , varies for increasing vorticity. It is straightforward to see that the results are as expected. Note that the line  $\theta = 0$  stands for a single point on the

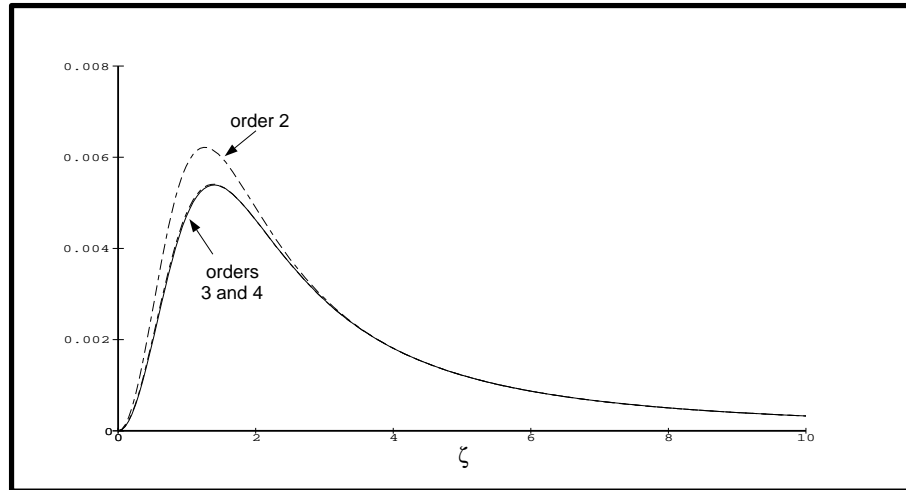


Figure 4.6: Graph of the coefficient  $A_2^2$  with  $\zeta$  for orders of approximation of 2, 3 and 4.

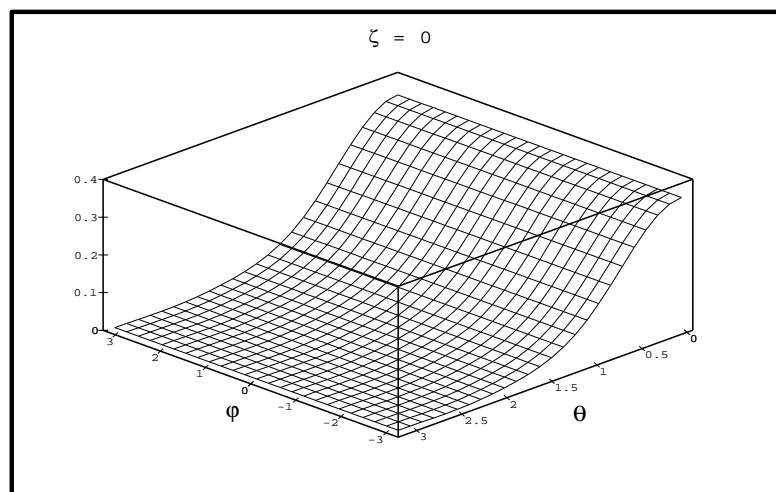


Figure 4.7: A third order approximation to the probability density function,  $f(\theta, \phi)$  for  $\alpha_0 = 0$  when  $\zeta = 0$ ,  $\xi = 0$  and  $\chi = 0$ .

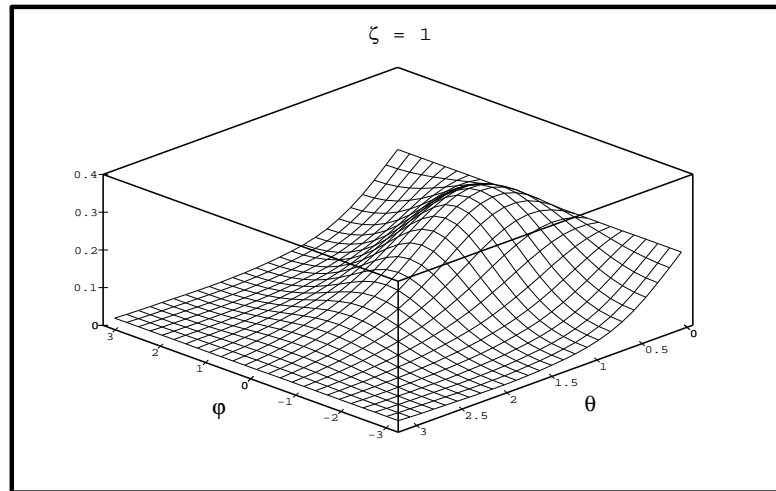


Figure 4.8: A third order approximation to the probability density function,  $f(\theta, \phi)$  for  $\alpha_0 = 0$  when  $\zeta = 1$ ,  $\xi = 0$  and  $\chi = 0$ .

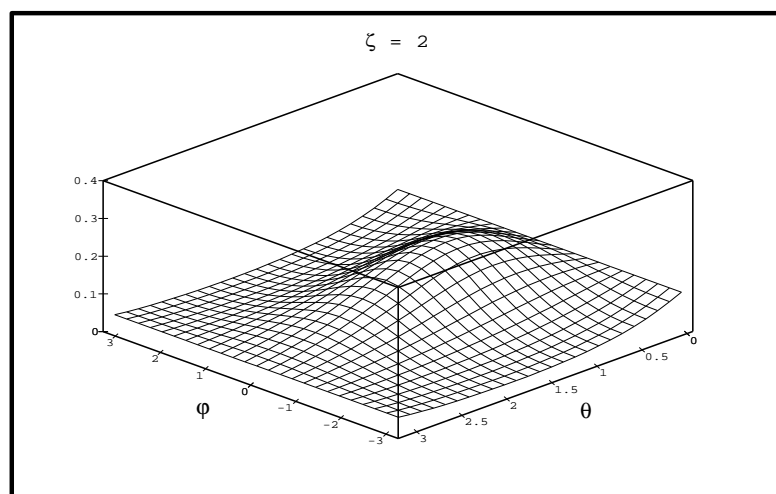


Figure 4.9: A third order approximation to the probability density function,  $f(\theta, \phi)$  for  $\alpha_0 = 0$  when  $\zeta = 2$ ,  $\xi = 0$  and  $\chi = 0$ .

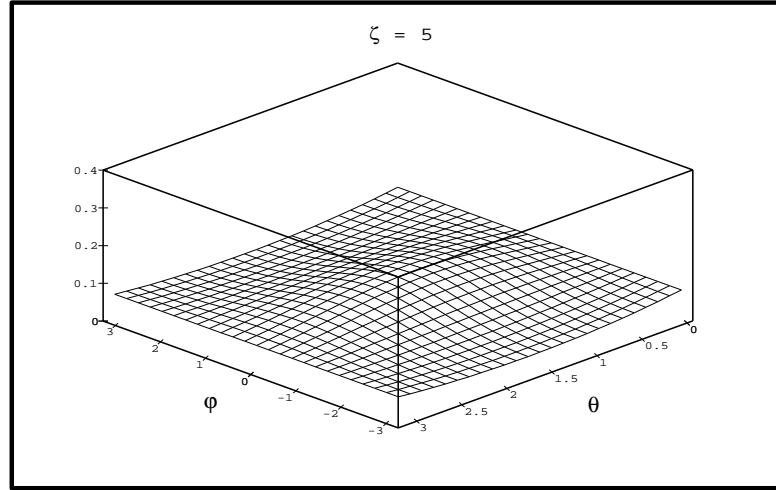


Figure 4.10: A third order approximation to the probability density function,  $f(\theta, \phi)$  for  $\alpha_0 = 0$  when  $\zeta = 5$ ,  $\xi = 0$  and  $\chi = 0$ .

sphere as does  $\theta = \pi$ .

Convergence is rapid in this case. There are no physical mechanisms that result in sharply peaked distributions which may cause resolution problems for  $\lambda = 2.2$ . This is not typically the case for  $\alpha_0 \neq 0$  as described in the next section. Here, we have chosen a typical value of the parameter  $\lambda$ , and in general as  $\lambda$  increases (i.e. either  $D_r$  or  $B$  decreases) the distribution becomes more sharply peaked.

## 4.9 Results for $\alpha_0 \neq 0$

We consider, first, the individual terms in  $\xi$  ( $= \alpha_0 \eta e_{11}$ ) and  $\chi$  ( $= \alpha_0 \eta e_{13}$ ) before combining them in Section 4.9.3.

### 4.9.1 $\xi$ varies while $\zeta = 0$ and $\chi = 0$

We find that the approximation to the cell orientation distribution function, in which  $\chi$  and  $\zeta = 0$ , converges rapidly close to  $\xi = 0$ . Otherwise, for low orders of the approximation, we find spurious singularities in the values of the coefficients  $A_1^0(\xi)$ ,  $A_1^1(\xi)$ ,  $A_2^0(\xi)$ ,  $A_2^1(\xi)$  and  $A_2^2(\xi)$ , all of which share the same denominator. As the order of approximation,  $R$ , increases, the singularities get further from the origin (see Figures 4.11, 4.12 and 4.13). When  $R = 10$  the approximation is well behaved in the region  $|\xi| \leq 10$  but singularities still exist in the region  $|\xi| \geq 10$ . None of the

coefficients are symmetric functions of  $\xi$  about the origin and this is because of the very different flow fields, with respect to gravity, for positive or negative  $e_{11}$  (see Figure 4.14). Negative values of  $e_{11}$  reinforce the upswimming of the cell whereas positive values destabilize it. The existence of spurious singularities leads us to the conclusion that

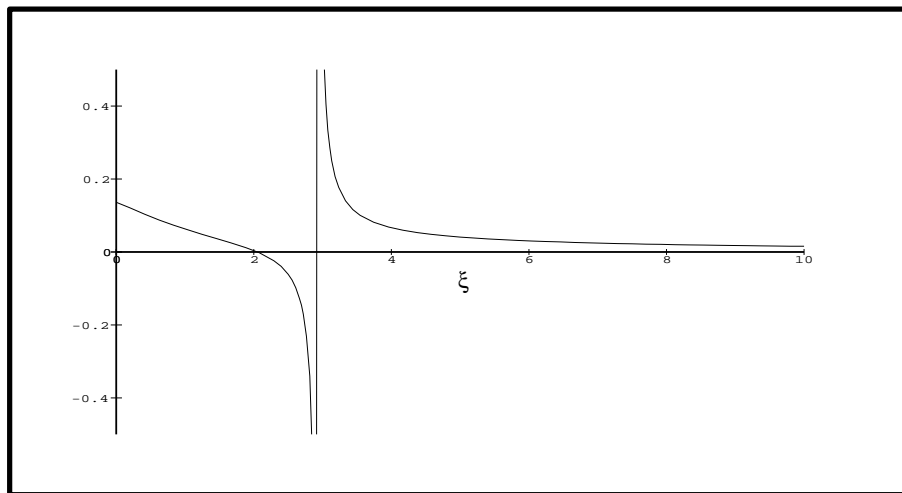


Figure 4.11: Graph of the coefficient  $A_1^0$  versus  $\xi$  for a third order approximation.  $\zeta = \chi = 0$ .

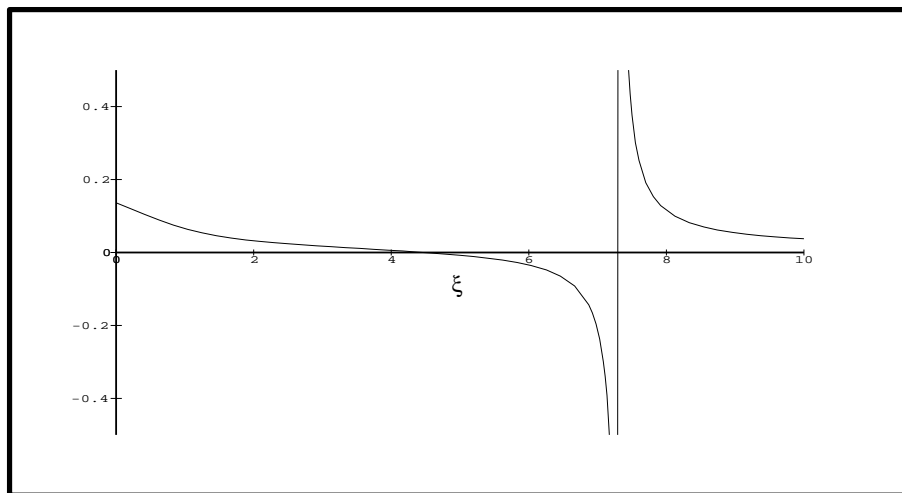


Figure 4.12: Graph of the coefficient  $A_1^0$  versus  $\xi$  for a seventh order approximation.  $\zeta = \chi = 0$ .

there is a physical problem in trying to represent the solutions as spherical harmonics. If  $e_{11}$  increases (implying  $e_{33}$  decreases, see Figure 4.14) then the cell swimming direction becomes more and more likely to be along the  $x$  axis and less random. This implies

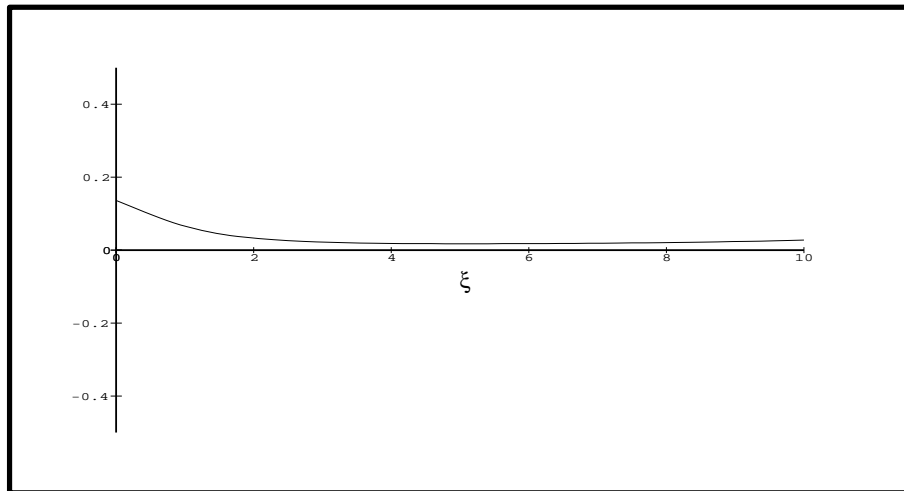


Figure 4.13: Graph of the coefficient  $A_1^0$  versus  $\xi$  for a tenth order approximation.  $\zeta = \chi = 0$ .

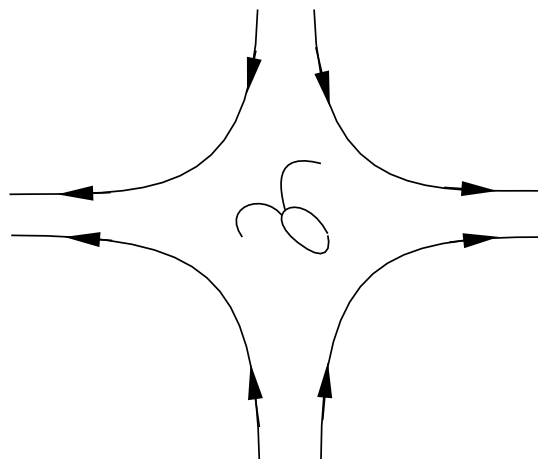


Figure 4.14: Streamlines at the stagnation point of a pure straining flow, acting on a swimming cell (where  $\omega = e_{13} = 0$ ). Here,  $e_{11}$  is positive and, hence,  $e_{33}$  is negative.

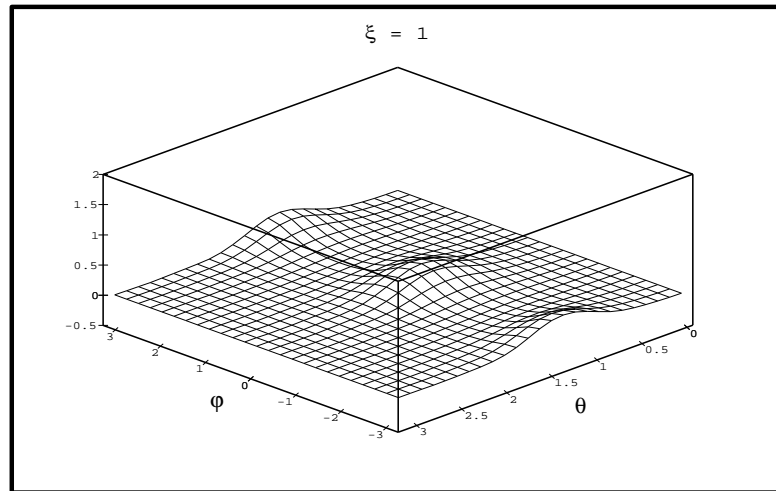


Figure 4.15: A seventh order approximation to the probability density function,  $f(\theta, \phi)$  for  $\alpha_0 = 0$  when  $\zeta = 0$ ,  $\xi = 1$  and  $\chi = 0$ .

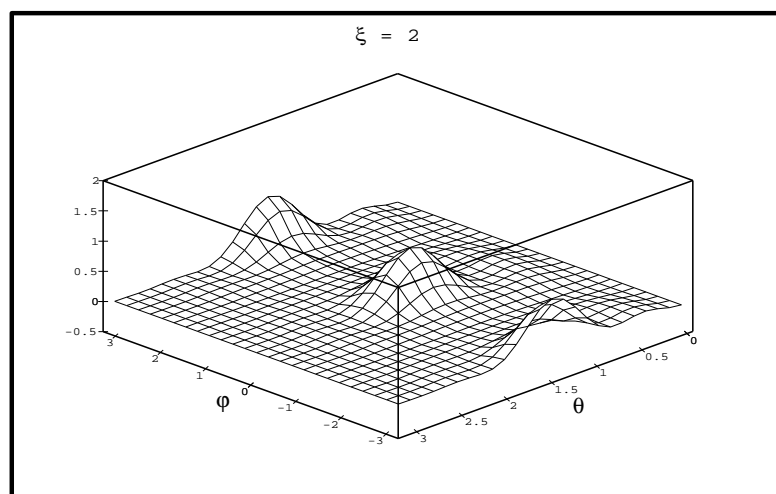


Figure 4.16: A seventh order approximation to the probability density function,  $f(\theta, \phi)$  for  $\alpha_0 = 0$  when  $\zeta = 0$ ,  $\xi = 2$  and  $\chi = 0$ .

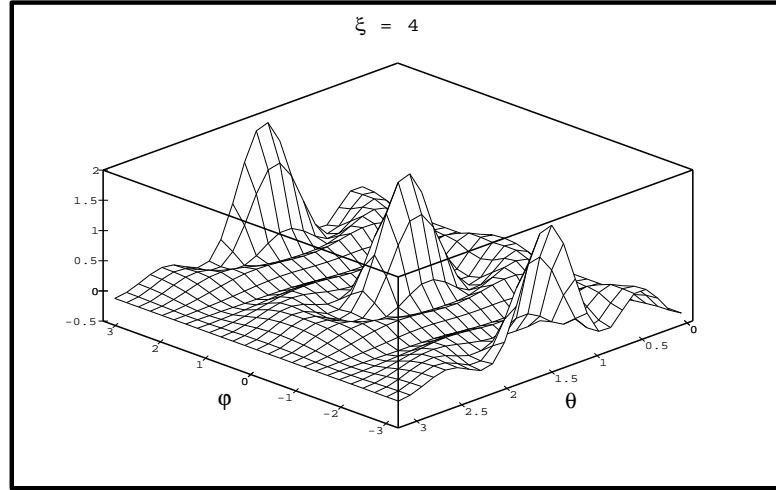


Figure 4.17: A seventh order approximation to the probability density function,  $f(\theta, \phi)$  for  $\alpha_0 = 0$  when  $\zeta = 0$ ,  $\xi = 4$  and  $\chi = 0$ .

that the distribution becomes more peaked and the number of spherical harmonics may be insufficient to represent it. As the order of approximation increases, the problem is alleviated. Figures (4.15) to (4.17) are plots of the probability distribution,  $f$ , with increasing  $e_{11}$  when  $\omega = e_{13} = 0$  and  $R = 7$ . It is clear that the distribution becomes more peaked with the increase in  $e_{11}$ . In fact in Figure (4.17) the approximation becomes negative as the spherical harmonics attempt to resolve  $f$ . This is where the approximation breaks down and is a manifestation of the Gibbs phenomenon in which the approximation overshoots the probability density function when it sharply varies. For  $R > 10$  the computer time and space required becomes excessive, and the solutions become unmanageable.

#### 4.9.2 $e_{13}$ varies where $\omega = 0$ and $e_{11} = 0$

In the same way, we can deal with the case where  $e_{13}$  is the parameter. If  $\omega = e_{11} = 0$  then the streamlines are similar to Figure (4.14) but rotated through  $45^\circ$ . A similar argument as before applies, and consequently the cell swimming direction distribution becomes more and more peaked with  $e_{13}$ . A limited range of  $e_{13}$  space has convergent solutions and this region increases with the approximation order. However,  $A_1^0(\chi)$  is seen to be symmetric about the origin, indicating that the vertical component of the swimming direction is unaffected by the sign of  $\chi$ .

### 4.9.3 Combining vorticity and rate-of-strain

Consider, for simplicity, the case where  $e_{13}$  is zero but  $\omega$  and  $e_{11}$  are allowed to vary. One can imagine the situation in which we fix  $\omega$  to be sufficiently large that the cell tumbles, and allow  $e_{11}$  or  $\alpha_0$  to increase from zero (see Figure 4.18). For reasonably

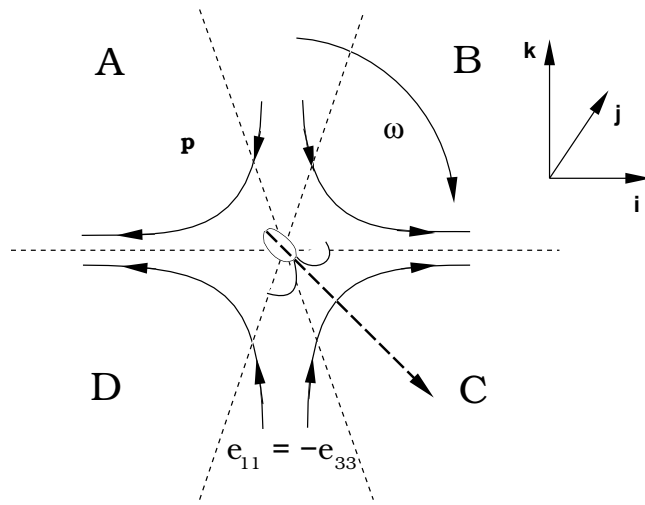


Figure 4.18: Graphical representation of a combined straining flow with vorticity.

small values of  $e_{11}$  the cell will continue to tumble but will favour pointing in the direction of the fluid efflux, i.e. along the  $x$  axis. As  $e_{11}$  increases, the cell will spend more time in the regions marked  $A$  and  $C$  and less in the regions marked  $B$  and  $D$ . This

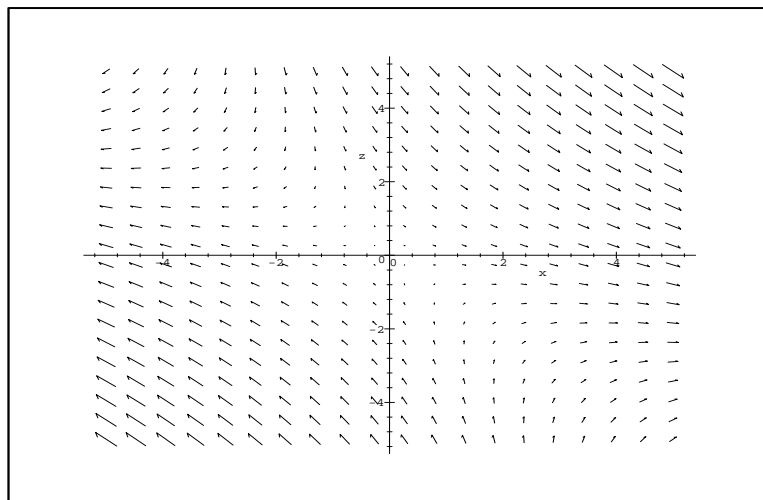


Figure 4.19: Streamlines for a combination of a straining flow with vorticity. Here  $e_{11} = \omega$ . Doubling  $\omega$  would give a pure shear flow.

process will continue to occur until  $e_{11}$  becomes large enough to prevent the cell from pointing along the  $z$  axis and, hence, from tumbling. The gravitational torque acts such

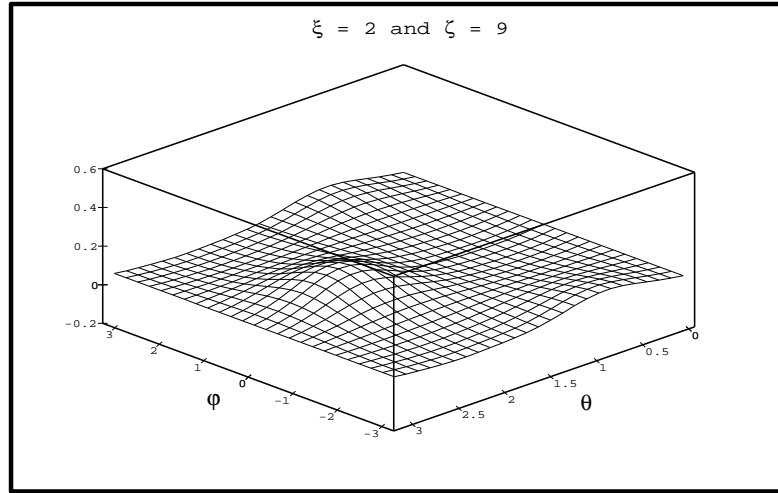


Figure 4.20: A seventh order approximation to the probability density function,  $f(\theta, \phi)$  for  $\alpha_0 = 0$  when  $\zeta = 9$ ,  $\xi = 2$  and  $\chi = 0$ .

that it is easier for the cell to escape region  $A$  than  $C$ . As  $e_{11}$  increases still further, the cell will be constrained in region  $C$  or less so in region  $A$ . This will lead to a sharply peaked distribution and, thus, for low orders of the approximation, the method will fail and produce unreliable results. As the order of approximation increases, the spherical harmonics have more of a chance to resolve the true distribution for higher values of  $e_{11}$ . Figure (4.19) shows the two dimensional streamlines for a typical shear flow (or a balance between viscosity and rate-of-strain), and Figures (4.20) to (4.22) show an example of the distribution becoming peaked, using a seventh order approximation (in this case for negative  $\xi$ ). Figure (4.22) shows that the probability distribution becomes negative for some values of  $\theta$  and  $\phi$ , in an attempt to resolve the true distribution  $f$ .

In the absence of vorticity, the solutions behave as in Section 4.9.1, but a small amount of vorticity broadens the distribution and increases the critical value of  $\xi$ , above which problems of resolution occur. Figures (4.23) and (4.24) show an approximation of order five with  $\chi$  and  $\zeta$  as parameters. One can clearly see that the solution breaks down in different regions, with the coefficient  $A_1^0$  going to plus or minus infinity. A similar picture is produced with  $\xi$  and  $\zeta$  as parameters.

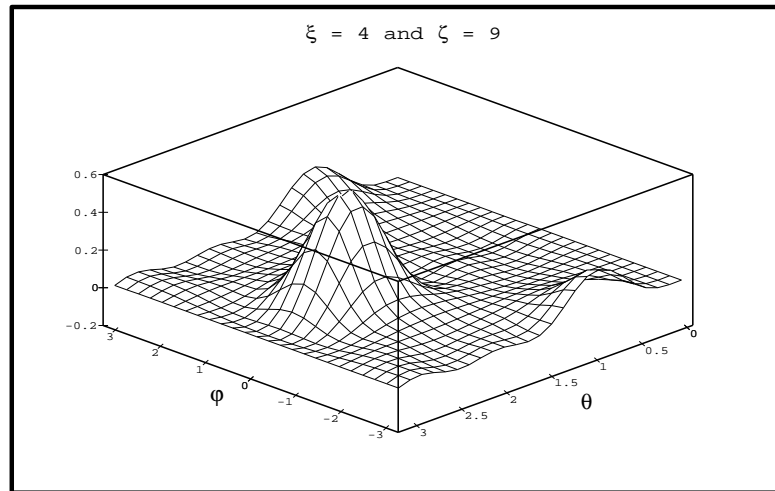


Figure 4.21: A seventh order approximation to the probability density function,  $f(\theta, \phi)$  for  $\alpha_0 = 0$  when  $\zeta = 9$ ,  $\xi = 4$  and  $\chi = 0$ . In this case, the cell is almost always pointing downwards, due to the “barrier” formed by the large values of  $\xi$ .

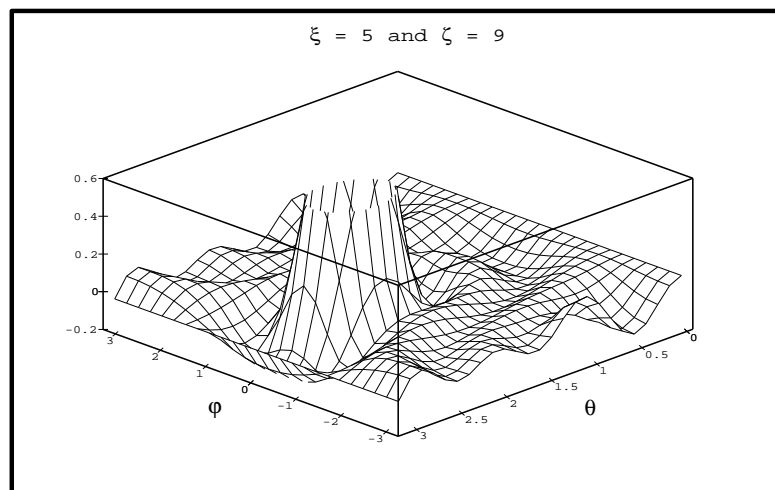


Figure 4.22: A seventh order approximation to the probability density function,  $f(\theta, \phi)$  for  $\alpha_0 = 0$  when  $\zeta = 9$ ,  $\xi = 5$  and  $\chi = 0$ . There are regions where  $f$  has become negative and the method has broken down.

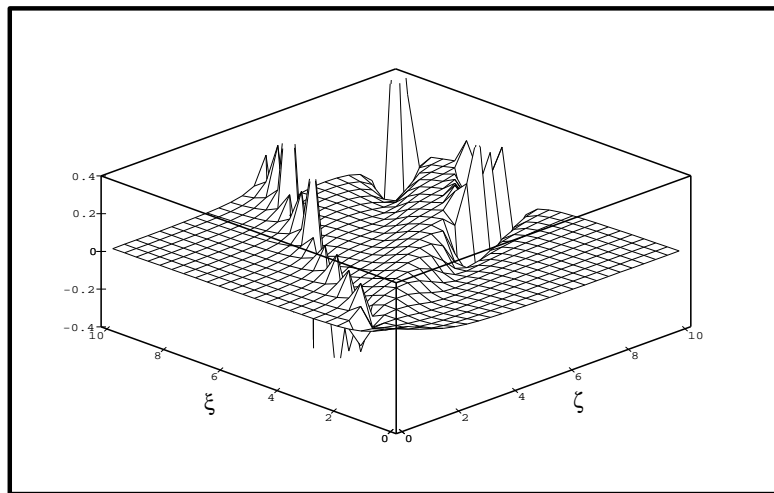


Figure 4.23: A fifth order approximation of  $A_1^0(\zeta, \xi)$  with  $\chi = 0$  ( $\propto e_{13}$ ).

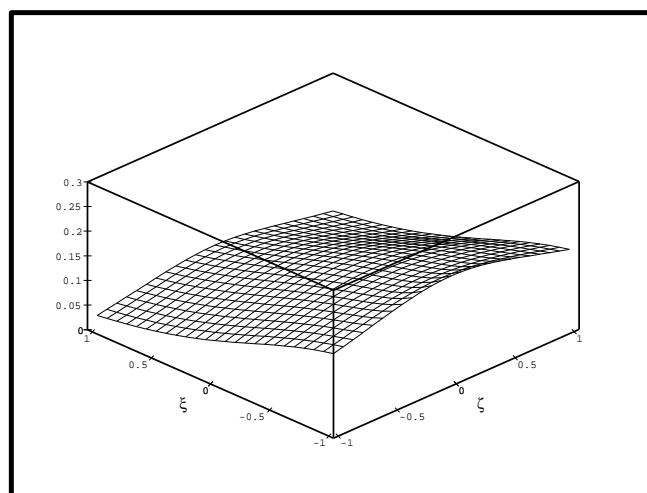


Figure 4.24: A close up, at the origin, of Figure (4.23). A fifth order approximation of  $A_1^0(\zeta, \xi)$  with  $\chi = 0$  ( $\propto e_{13}$ ) showing the smooth solution surface close to the origin.

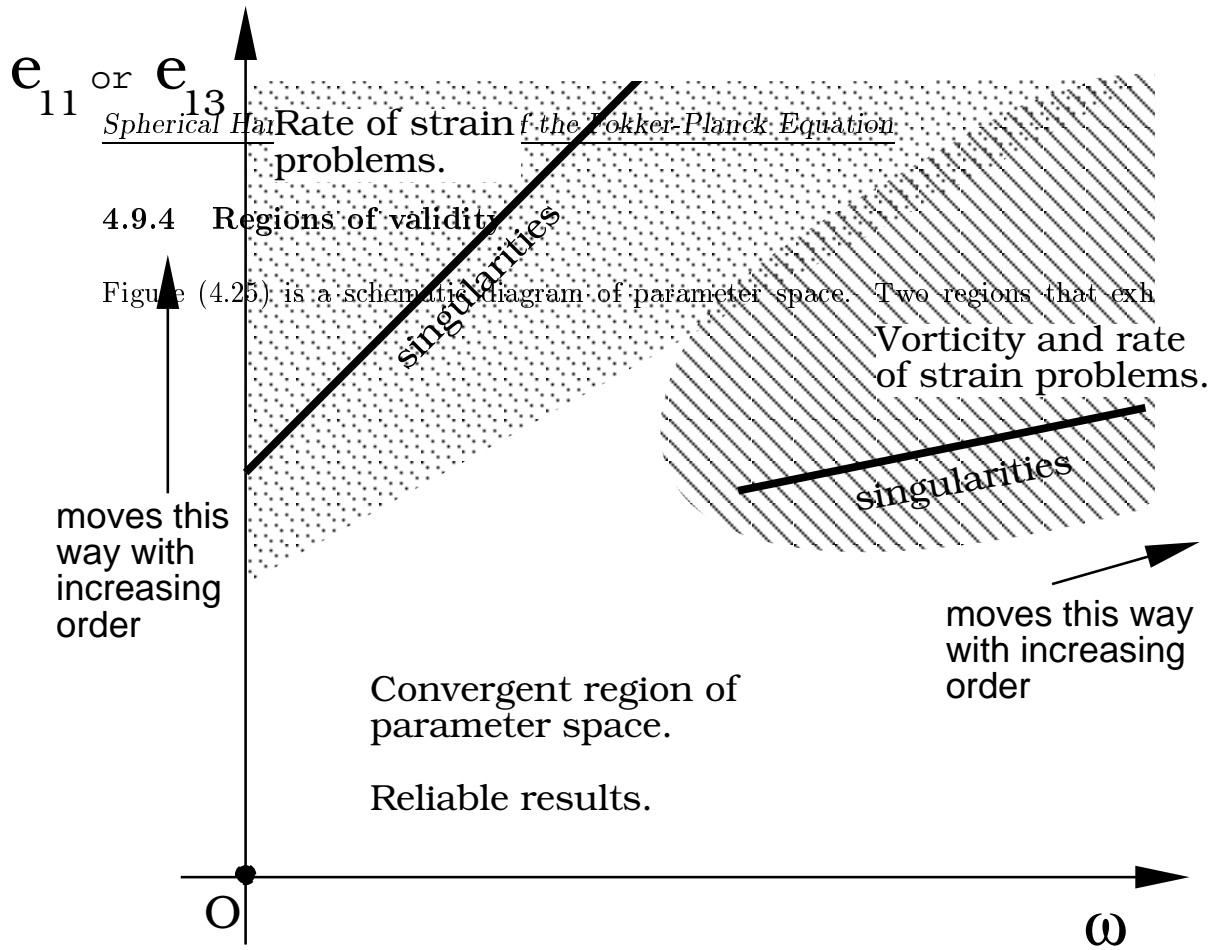


Figure 4.25:  $\omega$  and  $e_{11}$  space - highlighting the regions of validity. The solid lines indicate the possibility of spurious singularities and the surrounding shaded regions indicate unreliable results.

resolving problems are identified and a region where reliable results are obtained is proposed. Although Figures (4.23) and (4.25) seem to imply that the function is highly discontinuous for most realistic values of  $N$ , it does not imply that the method is a failure. The coefficient  $A_1^0(\zeta, \xi, \chi)$  converges to the real distribution for reasonably large regions of parameter space. But what are realistic/experimental values for the parameters? Using the definition of  $\eta$  as  $B\Omega$  (Equation 3.9), where  $\Omega$  is a typical scale for vorticity and rate-of-strain and  $B$  is the gyrotaxis orientation parameter (see Table 3.2), we get

$$\xi = \alpha_0 B E_{11}, \quad (4.61)$$

where  $E_{11}$  is a dimensional component of the rate-of-strain tensor. From observations, a typical fluid velocity will not exceed  $1 \text{ mm/s}$  and will change over a distance of  $1 \text{ mm}$ . This indicates that in experiments  $E_{11} \leq O(1)$ . Hence,  $\xi \leq O(1)$ . Hence, in normal situations, the fourth order approximation should be valid.

#### 4.9.5 Including swimming speed as a random variable

If we also include the effects of a random swimming speed, we can calculate the diffusion tensor using Equation (4.21) but in a similar manner to Section 3.7. Figure (4.26) displays a second order approximation for  $\mathbf{D}_{xx}$  versus  $\zeta$ , in which  $\xi = \chi = 0$ , with different values of  $\mathcal{N}$  ( $\mathcal{N}$  is defined in Section 3.7). Figures (4.27) and (4.28) display  $\mathbf{D}_{yy}$  and  $\mathbf{D}_{zz}$  respectively. From Figures (4.26) to (4.29) we see that the diffusion varies

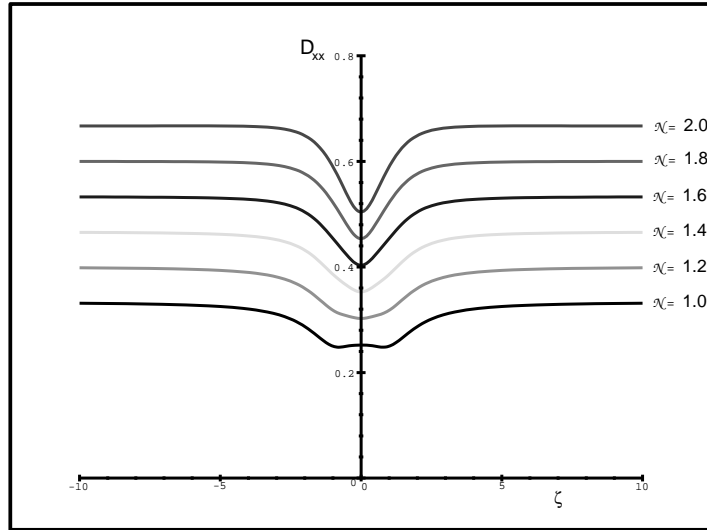


Figure 4.26: A graph of  $D_{xx}$  with varying  $\zeta$  and  $\mathcal{N}$  for a second order approximation to  $f(\theta, \phi)$  with  $\alpha_0 = 0$ .  $\mathcal{N}$  increases with  $D_{xx}(0)$  from 1.0 to 2.0.

only a small amount and perhaps an isotropic diffusion is justified, however, notice the differences in behaviour between  $D_{xx}$ ,  $D_{yy}$  and  $D_{zz}$  around  $\zeta = 0$ . The value of  $\mathcal{N}$  of 1.3, for which  $P_6$  vanishes in the linear analysis, also has a significant effect on the type of stationary point of  $D_{zz}$  and the sign of the gradient of  $D_{xy}$  at  $\zeta = 0$ . In fact  $D_{xy}$  looks very flat, at this value of  $\mathcal{N}$ , for all  $\zeta$ . Otherwise, increasing  $\mathcal{N}$  increases the size of the diagonal terms in the diffusion tensor. The linear analysis of the Fokker-Planck equation (Chapter 3) gave values for the diffusion tensor of  $D_H = 0.26$  and  $D_V = 0.16$  for zero flow. The spherical harmonic approximation at second order provides values of  $D_H \equiv D_{xx}(\zeta = 0) = D_{yy}(\zeta = 0) = 0.2520$  (4 d.p.) and  $D_V \equiv D_{zz}(\zeta = 0) = 0.1886$  (4 d.p.). Better agreement is obtained for higher orders of approximation. The expressions for the diffusion coefficients, for  $\alpha_0 = 0$ , will be used in the non-linear analysis of the next chapter.

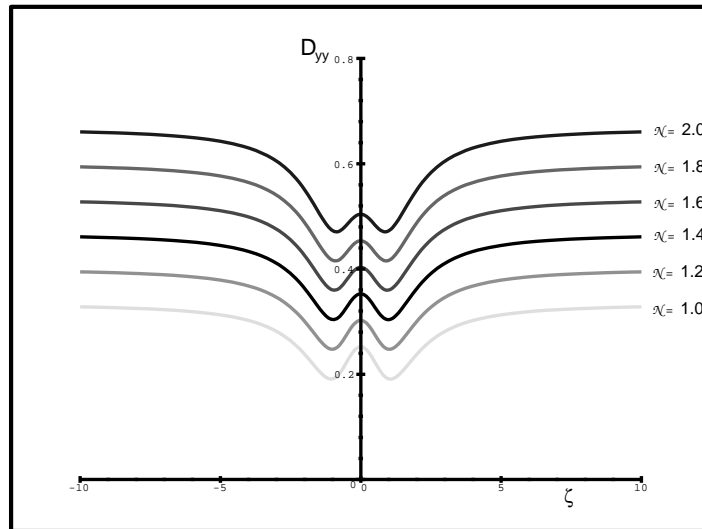


Figure 4.27: A graph of  $D_{yy}$  with varying  $\zeta$  and  $\mathcal{N}$  for a second order approximation to  $f(\theta, \phi)$  with  $\alpha_0 = 0$ .  $\mathcal{N}$  increases with  $D_{yy}(0)$  from 1.0 to 2.0.

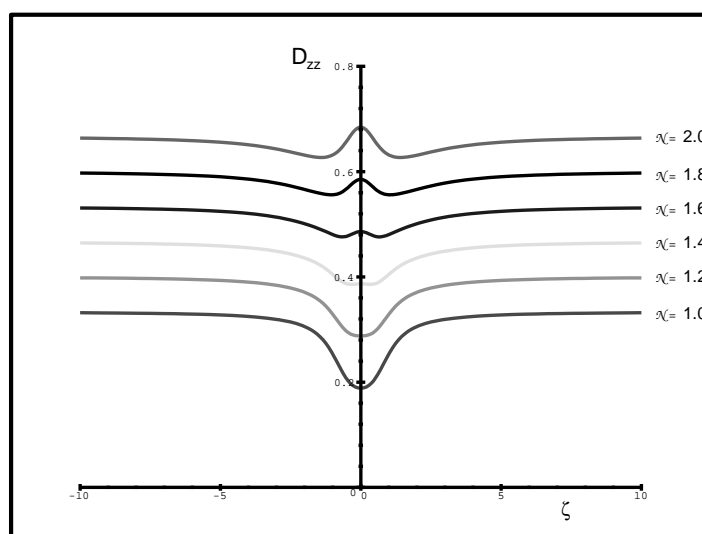


Figure 4.28: A graph of  $D_{zz}$  with varying  $\zeta$  and  $\mathcal{N}$  for a second order approximation to  $f(\theta, \phi)$  with  $\alpha_0 = 0$ .  $\mathcal{N}$  increases with  $D_{zz}(0)$  from 1.0 to 2.0.

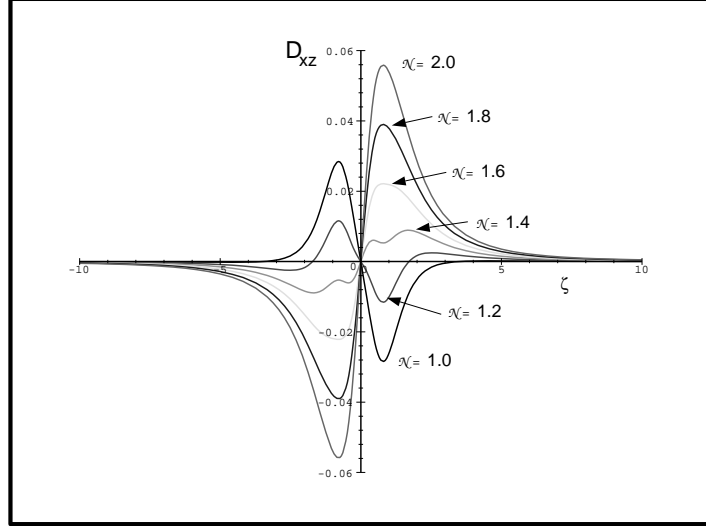


Figure 4.29: A graph of  $D_{xz}$  with varying  $\zeta$  and  $\mathcal{N}$  for a second order approximation to  $f(\theta, \phi)$  with  $\alpha_0 = 0$ .  $\mathcal{N}$  increases from 1.0 to 2.0.

#### 4.10 Extension to a three dimensional flow field

In this section we assume that  $\alpha_0 = 0$  and, hence, the rate-of-strain in the fluid does not affect the cell orientation. It is reasonable to assume also, owing to the symmetries of the patterns observed in experiments, that there is no component of vorticity in the  $z$  direction. In doing so we can construct an approximation to the diffusion tensor, in a similar manner to the previous sections, with the aim of using the results in a non-linear analysis in order to explore the three-dimensional structure of bioconvection. In particular, the flow field can be written in terms of a poloidal velocity field (see Section 5.8.2).

We rotate the “plane of solution” about a vertical axis, such that  $\boldsymbol{\omega}$  will be perpendicular to the plane  $\phi = 0$ . The Fokker-Planck equation can be expanded in terms of surface spherical harmonics, as before, and can then be rotated back to its original coordinate system within the integral definitions of  $\langle \mathbf{p} \rangle$  and  $\mathbf{D}$ .

We define the angle of rotation,  $\psi$ , to be

$$\psi = \arctan \left( \frac{\omega_1}{\omega_2} \right), \quad (4.62)$$

where

$$\boldsymbol{\omega} = \begin{pmatrix} \omega_1 \\ \omega_2 \\ 0 \end{pmatrix} \quad (4.63)$$

and put  $\omega^2 = \omega_1^2 + \omega_2^2$ . Then

$$\langle \mathbf{p} \rangle = \int_S f(\theta, \phi - \psi) \mathbf{p} dS. \quad (4.64)$$

Putting  $\bar{\phi} = \phi - \psi$  then

$$\langle \mathbf{p} \rangle = \int_S f(\theta, \bar{\phi}) \begin{pmatrix} \sin \theta \cos (\bar{\phi} + \psi) \\ \sin \theta \sin (\bar{\phi} + \psi) \\ \cos \theta \end{pmatrix} dS, \quad (4.65)$$

where we can expand  $\cos (\bar{\phi} + \psi) = \cos \bar{\phi} \cos \psi - \sin \bar{\phi} \sin \psi$  and  $\sin (\bar{\phi} + \psi) = \sin \bar{\phi} \cos \psi + \cos \bar{\phi} \sin \psi$ . Hence,

$$\langle \mathbf{p} \rangle = \int_S f(\theta, \bar{\phi}) \begin{pmatrix} Q_1^1 \cos \psi \\ Q_1^1 \sin \psi \\ Q_1^0 \end{pmatrix} dS \quad (4.66)$$

which, when  $f$  is written as a sum of spherical harmonics as in Section 4.3, implies

$$\langle \mathbf{p} \rangle = \frac{4}{3} \pi \begin{pmatrix} A_1^1 \cos \psi \\ A_1^1 \sin \psi \\ A_1^0 \end{pmatrix}. \quad (4.67)$$

In a similar way

$$\langle \mathbf{pp} \rangle = \int_S f(\theta, \bar{\phi}) \mathbf{M} dS \quad (4.68)$$

where  $\mathbf{M}$  is equal to

$$\begin{pmatrix} \sin^2 \theta \cos^2 (\bar{\phi} + \psi) & \sin^2 \theta \cos (\bar{\phi} + \psi) \sin (\bar{\phi} + \psi) & \cos \theta \sin \theta \cos (\bar{\phi} + \psi) \\ \sin^2 \theta \cos (\bar{\phi} + \psi) \sin (\bar{\phi} + \psi) & \sin^2 \theta \sin^2 (\bar{\phi} + \psi) & \cos \theta \sin \theta \sin (\bar{\phi} + \psi) \\ \cos \theta \sin \theta \cos (\bar{\phi} + \psi) & \cos \theta \sin \theta \sin (\bar{\phi} + \psi) & \cos^2 \theta \end{pmatrix}. \quad (4.69)$$

Substituting the surface spherical harmonics for  $f$ , expanding and evaluating, gives

$$\langle \mathbf{pp} \rangle = \pi \begin{pmatrix} \frac{4}{3} A_0^0 - \frac{4}{15} A_2^0 + \frac{8}{5} A_2^2 \cos 2\psi & \frac{8}{5} A_2^2 \sin 2\psi & \frac{4}{5} A_2^1 \cos \psi \\ \frac{8}{5} A_2^2 \sin 2\psi & \frac{4}{3} A_0^0 - \frac{4}{15} A_2^0 - \frac{8}{5} A_2^2 \cos 2\psi & \frac{4}{5} A_2^1 \sin \psi \\ \frac{4}{5} A_2^1 \cos \psi & \frac{4}{5} A_2^1 \sin \psi & \frac{8}{15} A_2^0 + \frac{4}{3} A_0^0 \end{pmatrix}. \quad (4.70)$$

The  $A$ 's are all functions of  $\omega = \sqrt{\omega_1^2 + \omega_2^2}$  and by using  $\tan \psi = \left(\frac{\omega_1}{\omega_2}\right)$  we can write

$$\begin{aligned}\cos \psi &= \frac{\omega_2}{\omega}, \\ \sin \psi &= \frac{\omega_1}{\omega}, \\ \cos 2\psi &= \frac{\omega_2^2 - \omega_1^2}{\omega^2}, \\ \sin 2\psi &= \frac{2\omega_1\omega_2}{\omega^2}.\end{aligned}\tag{4.71}$$

## 4.11 Discussion

In this Chapter we have demonstrated that exact expressions can be obtained, in terms of the first five coefficients of the spherical harmonics, for the mean cell swimming direction and the approximation to the diffusion tensor.

For the case of spherical cells, where  $\alpha_0 = 0$ , the coefficients converge very rapidly. The second order approximation captures all of the behaviour (see Figure 4.2), and yet is sufficiently simple to be used in the non-linear analysis of Chapter 5. We also show that these results can easily be extended to a three-dimensional flow field in which there is no vertical vorticity. This will aid future analysis on non-linear planform selection (see Section 5.8).

For the case of non-spherical cells where  $\alpha_0 \neq 0$  the method may not be the most efficient means of obtaining a solution, as we require the expressions to be large in order to obtain reliable results. This is due to the appearance of spurious singularities for low orders of approximation, related to the physical interaction of vorticity and rate-of-strain. Methods such as finite differences may produce more reliable results. However, there are regions in parameter space where convergence is rapid and it may be possible to patch or smooth over irregularities. This may be particularly straightforward if we assume that there are no additional, unexpected features of the coefficients associated with the interactions of the external couples. Simple, smooth functions could be constructed from the convergent regions of the coefficients and known asymptotes for dominant flow conditions (see Brenner & Weissmann 1972 [12] and Pedley & Kessler 1992 [86]).

Finally, the methods described in this Chapter are sufficiently flexible such that solutions could be obtained for combinations of taxes. In particular, the interaction of

geotaxis, gyrotaxis and phototaxis (see Kessler *et al.* 1992 [67]) could be investigated.

## Chapter 5

# Non-Linear Analysis

### 5.1 Introduction

There are many papers on constructing weakly nonlinear theories in terms of amplitude modulations for solutions close to the neutral curve (see Fauve 1985 [31]). The bioconvection equations do not exhibit Boussinesq symmetry, the reflective symmetry about a horizontal plane due to the application of the Boussinesq approximation, as in the standard Rayleigh-Bénard problem so the analysis is more difficult. Childress & Spiegel (1978) [21] have obtained an amplitude equation for the weakly non-linear non-gyrotactic bioconvection model of Childress *et al.* (1975) [19], with a zero most unstable wavenumber, and their methods have been used in other contexts (e.g. Chapman & Proctor (1980) [16], Proctor (1981) [90]). They show that, in their case, the bifurcation to instability is subcritical and, hence, the linear analysis cannot always be used to predict the wavelength of the initial disturbance. Poyet (1981) [88] and Depassier & Spiegel (1981) [28] have extended these methods for situations in which there is a double minimum of the neutral stability curve. With finite depth gyrotactic bioconvection, however, this process would be very time consuming and may not be an efficient method of analysis. The difficulties arise from the complexity of the equations and the uncertainty of the existence of a unique most unstable wavenumber, i.e. there could exist a balance between a zero and a non-zero most unstable wavenumber, see Chapter 3. We have instead opted to investigate the non-linear mechanisms for gyrotaxis in “deep” gyrotactic bioconvection. Purely upswimming models ([19]) are not unstable for suspensions of infinite depth, unlike models incorporating gyrotaxis. Fig-

ure (5.1) contains pictures of suspensions of *Chlamydomonas nivalis* being cultured in flasks under a bright white light source and shows evidence of long plume structures in deep suspensions. The figure also displays evidence of vertically travelling pulses that move down the plumes. Observations indicate that larger pulses travel faster than smaller pulses. The larger pulses can catch the smaller pulses, whereupon they merge (also see Kessler 1985 [62] where pulses are observed in the focusing experiment in Figure 1.5).

In this chapter, we consider the fully non-linear equations for infinite depth and use the expressions obtained from the spherical harmonic expansion of the Fokker-Planck equation in Chapter 4. Initially, in Section 5.2, we explore the linear analysis considered by Pedley *et al.* (1988) [83], which highlights the scalings required for the weakly non-linear analysis of Section 5.4. Then, in Section 5.3, we consider the experimentally realisable case of long vertical wavelengths in deep suspensions in order to simplify the equations. This provides us with a set of non-linear partial differential equations, the first of which involves  $z$  in a passive manner. Section 5.4 considers the weakly non-linear analysis of deep bioconvection for long vertical wavelengths and aims to characterize the bifurcation to instability, thus determining whether the linear analysis can be used to predict the initial pattern wavelengths. In Section 5.5 we consider the horizontal steady state solutions for long vertical wavelengths by numerically integrating the equations and in Section 5.6 time dependence is included in the form of horizontally travelling vertical plumes subject to a small forcing flow field. Section 5.7 derives an equation for variations in the  $z$  direction and calculates the wavespeed of small amplitude vertically travelling pulses. Eventually, improvements of the present system are discussed, such as the inclusion of vertical dependence in the weakly non-linear analysis and possible extensions to three-dimensional space.

We begin by stating the main equations governing the flow and concentration fields in an infinite domain (see Chapter 1):

$$\nabla \cdot \mathbf{u} = 0, \tag{5.1}$$

$$\rho \left( \frac{\partial \mathbf{u}}{\partial t} + \mathbf{u} \cdot \nabla \mathbf{u} \right) = -\nabla p_e + nv\Delta\rho\mathbf{g} + \mu\nabla^2 \mathbf{u} \tag{5.2}$$

and

$$\frac{\partial n}{\partial t} = -\nabla \cdot [n(\mathbf{u} + V_s \langle \mathbf{p} \rangle) - \mathbf{D} \cdot \nabla n]. \tag{5.3}$$

Figure 5.1: *Chlamydomonas nivalis* being cultured in flasks. Plumes with long vertical scales can be clearly seen. Pulses are generally observed travelling down the plumes.

Non-dimensionalising time with  $\tau$ , velocity with  $V_s$ , length with  $V_s\tau$  and concentration with  $n_0$  (following Pedley *et al.* 1988 [83], but see Equations 3.92 where we used the suspension depth to scale distance) then

$$\nabla \cdot \mathbf{u} = 0, \quad (5.4)$$

$$\partial_t \mathbf{u} + \mathbf{u} \cdot \nabla \mathbf{u} = -\nabla p_e - \text{Ra} n \mathbf{k} + \frac{1}{\text{Re}} \nabla^2 \mathbf{u} \quad (5.5)$$

and

$$\partial_t n = -\nabla \cdot [n(\mathbf{u} + \langle \mathbf{p} \rangle)] - \mathbf{D} \cdot \nabla n \quad (5.6)$$

where

$$\text{Ra} = \frac{n_0 v \Delta \rho g \tau}{\rho V_s} \quad (5.7)$$

is a Rayleigh number and

$$\text{Re} = \frac{\tau V_s^2}{\nu} \quad (5.8)$$

is a type of micro-organism Reynolds number. The non-dimensional gyrotaxis parameter is now given by

$$\eta = \frac{B}{\tau} \quad (5.9)$$

(which is a form of Péclet number),  $\lambda$  is still given by

$$\lambda = \frac{1}{2BD_r} \quad (5.10)$$

and the diffusion tensor is  $O(1)$ . For the subsequent analysis the problem will be simplified by assuming  $\alpha_0 = 0$ . Analytic solutions to the gyrotactic Fokker-Planck equation, as determined in Chapter 4, will be used throughout this chapter. In particular, we introduce the shorthand for the expressions for  $\langle \mathbf{p} \rangle^x$  and  $\mathbf{D}^{xx}$  of Chapter 4, which are non-linear in  $\eta$  and  $\omega$ .

$$E(\eta\omega) \equiv -\langle \mathbf{p} \rangle^x = -\frac{a_1^1 + b_1^1 \eta^2 \omega^2}{\mathcal{R}(\eta\omega)} \eta\omega \quad (5.11)$$

and

$$A(\eta\omega) \equiv \mathbf{D}^{xx} = \frac{\left(\frac{1}{3}\mathcal{R}^2 - (a_2^0 - (b_2^0 + b_2^2)\eta^2\omega^2)\mathcal{R} - (a_1^1 + b_1^1\eta^2\omega^2)^2\eta^2\omega^2\right)}{\mathcal{R}^2(\eta\omega)} \quad (5.12)$$

where

$$\mathcal{R}(\eta\omega) = 1 + r_2\eta^2\omega^2 + r_4\eta^4\omega^4 \quad (5.13)$$

and the  $a$ 's,  $b$ 's and  $r$ 's are constants which were determined in Chapter 4 (see Table 5.2).

parameter name	expression	typical value
CASE 1: $\tau = 1.3\text{s}$ and $B = 3.4\text{s}$		
Re	$\frac{\tau V_s^2}{\nu}$	$5.2 \times 10^{-5}$
Ra	$\frac{n_0 v \Delta \rho g \tau}{\rho V_s}$	$5.2 \times 10^{-6} n_0$
$\eta$	$\eta = \frac{B}{\tau}$	2.6
CASE 2: $\tau = 5\text{s}$ and $B = 6.3\text{s}$		
Re	$\frac{\tau V_s^2}{\nu}$	$2 \times 10^{-4}$
Ra	$\frac{n_0 v \Delta \rho g \tau}{\rho V_s}$	$2 \times 10^{-5} n_0$
$\eta$	$\eta = \frac{B}{\tau}$	1.3

Table 5.1: Parameter expressions and estimates.

Name	Value
$a_1^1$	0.41182
$a_2^0$	0.081317
$b_1^1$	0.26407
$b_2^0$	0.030809
$b_2^2$	0.066018
$r_2$	0.85267
$r_4$	0.39611

Table 5.2: Table of constants for the mean cell swimming direction vector and diffusion tensor (to 5 s.f.).

## 5.2 Linear analysis

On perturbing the uniform solution in a suspension of infinite depth and making the substitutions  $\mathbf{u} = \delta \mathbf{u}^1$  and  $n = 1 + \delta n^1$  in Equations (5.4) to (5.6), where  $\delta \ll 1$ , we can establish the linear stability of the uniform solution. We use the analysis of Chapter 3, where we make allowances for the different scalings in Equation (3.115), to obtain an equation for the  $z$  component of  $\mathbf{u}^1$ ;

$$\partial_t (\nabla^2 u_3^1) = \frac{1}{\text{Re}} \nabla^4 u_3^1 - \text{Ra} \nabla^2 n^1 + \text{Ra} \partial_3 \partial_3 n^1. \quad (5.14)$$

Equation (5.6) becomes

$$\partial_t n^1 + \langle \mathbf{p} \rangle^{0z} \partial_z n^1 - \mathbf{D}^{0xx} \partial_x^2 n^1 - \mathbf{D}^{0zz} \partial_z^2 n^1 = \eta \langle \mathbf{p} \rangle^{1x} (0) \nabla^2 u_3^1, \quad (5.15)$$

where  $D^{0zz}$  and  $D^{0xx}$  are vertical and horizontal diffusivities for the zero flow solution and

$$\langle \mathbf{p} \rangle^x = \langle \mathbf{p} \rangle^{0x} + \delta \eta \omega \langle \mathbf{p} \rangle^{1x}. \quad (5.16)$$

Consider solutions of the form

$$u_3^1 = C_u e^{\sigma t + i(kx + mz)} \quad (5.17)$$

and

$$n^1 = C_n e^{\sigma t + i(kx + mz)}, \quad (5.18)$$

where  $C_u$  and  $C_n$  are constants to be eliminated. Then

$$\begin{aligned} & \sigma^2 + \left( im \langle \mathbf{p} \rangle^{0z} + D^{0xx} k^2 + D^{0zz} m^2 + \frac{k^2 + m^2}{\text{Re}} \right) \sigma \\ & + \frac{k^2 + m^2}{\text{Re}} (im \langle \mathbf{p} \rangle^{0z} + D^{0xx} k^2 + D^{0zz} m^2) - \text{Ra} \eta k^2 \langle \mathbf{p} \rangle^{1x} = 0. \end{aligned} \quad (5.19)$$

This is a rewritten form of the equations found by Pedley *et al.* (1988) [83] and the subsequent analysis in this section can be compared with their results. Writing  $\sigma = \sigma_R + i\sigma_I$  and solving for  $\sigma_R$  and  $\sigma_I$  gives

$$\sigma_I = - \left( \frac{\frac{k^2 + m^2}{\text{Re}} m \langle \mathbf{p} \rangle^{0z} + m \langle \mathbf{p} \rangle^{0z} \sigma_R}{D^{0xx} k^2 + D^{0zz} m^2 + \frac{k^2 + m^2}{\text{Re}} + 2\sigma_R} \right) \quad (5.20)$$

and

$$\sigma_R^2 - F_4^2 \frac{(F_2 + \sigma_R)^2}{(F_1 + F_2 + 2\sigma_R)^2} + F_4 \frac{(F_2 + \sigma_R)}{(F_1 + F_2 + 2\sigma_R)} + (F_1 + F_2) \sigma_R + F_1 F_2 - F_3 = 0 \quad (5.21)$$

where  $F_1 = D^{0xx}k^2 + D^{0zz}m^2$ ,  $F_2 = \frac{k^2+m^2}{\text{Re}}$ ,  $F_3 = \text{Ra}\eta k^2 \langle \mathbf{p} \rangle^{1x}$  and  $F_4 = m \langle \mathbf{p} \rangle^{0z}$ . The neutral curve for modes with zero linear growth is given by  $\sigma_R = 0$ . This implies

$$(F_1 + F_2)^2(F_1F_2 - F_3) + F_4^2F_1F_2 = 0. \tag{5.22}$$

For no vertical variation  $m = 0$ , and then

$$k_c^2 = \frac{K \langle \mathbf{p} \rangle^{1x}}{D^{0xx}}, \tag{5.23}$$

where

$$K = \text{Ra Re } \eta \tag{5.24}$$

(see Figure 5.2). But if  $m \neq 0$  then the neutral curve is given by the relationship

$$K = \frac{(k^2 + m^2)(D^{0xx}k^2 + D^{0zz}m^2)}{k^2 \langle \mathbf{p} \rangle^{1x}} \left( 1 + \frac{m^2 \langle \mathbf{p} \rangle^{0z}}{\left( \frac{k^2+m^2}{\text{Re}} + D^{0xx}k^2 + D^{0zz}m^2 \right)^2} \right), \tag{5.25}$$

and on this curve  $\sigma$  has an imaginary part given by Equation (5.20) and thus the perturbation is oscillatory. Hence, the curve in Figure (5.2) represents a Hopf bifurcation and it is apparent that the modes become more unstable as  $m$  decreases to zero. The

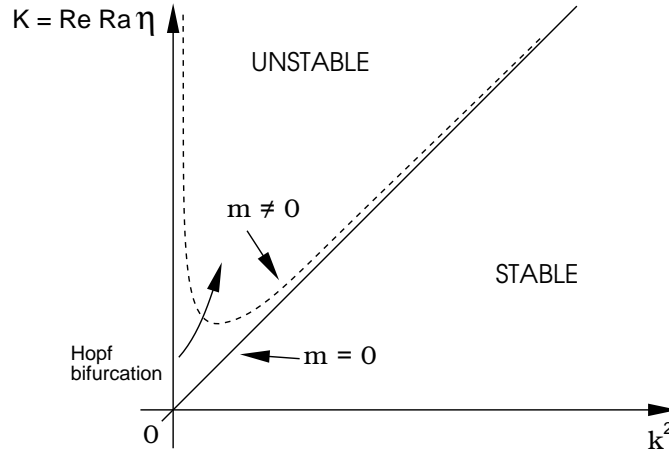


Figure 5.2: Curves of marginal stability for a homogeneous suspension of large depth. Two cases are indicated. If  $m = 0$  then the bifurcation is stationary and the growth rate is zero along the solid diagonal line and the line  $k = 0$ . If  $m \neq 0$  then we have a Hopf bifurcation in which the real part of the linear growth rate is zero along the dotted line.

most unstable mode occurs when  $m = 0$  and here the neutral curve represents a stationary bifurcation. In this case, the linear growth rate of a slightly supercritical mode

may be rewritten, using Equations (5.11) and (5.12), as

$$\sigma = -\frac{k^2}{2} \left( \frac{A(0)\text{Re} + 1}{\text{Re}} \right) \pm \frac{k}{2\text{Re}} \sqrt{k^2 (A(0)\text{Re} - 1)^2 - 4\text{Re}KE'(0)}. \quad (5.26)$$

and is plotted in Figure (5.3). This expression will be expanded in Section 5.4 to

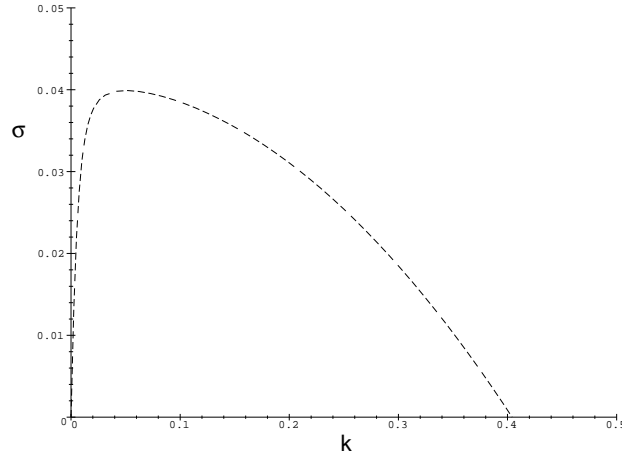


Figure 5.3: A plot of the linear growth rate for a mode with  $m = 0$  and horizontal wavenumber  $k$ , for a value of the parameter  $K$  slightly above the critical value of 0. Here,  $\text{Re} = 10^{-3}$  and  $K = 0.1$ .

motivate the scalings for a weakly non-linear analysis.

### 5.3 Long vertical wavelength approximation ( $m \sim \epsilon$ ) for 2-d non-linear solutions

We can make use of the long length scale in the  $z$  direction by scaling  $z$  with a small parameter,  $\epsilon$ . First, consider a two dimensional solution in the  $xz$ -plane and put  $\mathbf{u} = \text{curl}(-\psi\mathbf{j})$ , where  $\psi$  is the stream function. Then  $u = \partial_z\psi$ ,  $w = -\partial_x\psi$  and  $\omega = \nabla^2\psi$ . Equations (5.4) to (5.6) give

$$\partial_t \nabla^2 \psi - \frac{1}{\text{Re}} \nabla^4 \psi + J(\nabla^2 \psi, \psi) = \text{Ra} \partial_x n \quad (5.27)$$

and

$$\partial_t n + J(n, \psi) + \nabla \cdot (n\langle \mathbf{p} \rangle) - \nabla \cdot (\mathbf{D} \cdot \nabla n) = 0 \quad (5.28)$$

where  $J$  is the Jacobian defined by

$$J(n, \psi) = \partial_x n \partial_z \psi - \partial_z n \partial_x \psi. \quad (5.29)$$

Putting  $Z = \epsilon z$  we obtain

$$\partial_t(\partial_x^2 + \epsilon^2 \partial_Z^2)\psi - \frac{1}{\text{Re}}(\partial_x^2 + \epsilon^2 \partial_Z^2)^2\psi + \epsilon \partial_Z \psi (\partial_x^2 + \epsilon^2 \partial_Z^2) \partial_x \psi - \epsilon \partial_x \psi (\partial_x^2 + \epsilon^2 \partial_Z^2) \partial_Z \psi = \text{Ra} \partial_x n \quad (5.30)$$

and

$$\partial_t n + \epsilon \partial_Z \psi \partial_x n - \epsilon \partial_x \psi \partial_Z n + \begin{pmatrix} \partial_x \\ \epsilon \partial_Z \end{pmatrix} \cdot \langle n(\mathbf{p}) \rangle - \begin{pmatrix} \partial_x \\ \epsilon \partial_Z \end{pmatrix} \cdot \left[ \mathbf{D} \cdot \begin{pmatrix} \partial_x \\ \epsilon \partial_Z \end{pmatrix} n \right] = 0 \quad (5.31)$$

where  $\langle \mathbf{p} \rangle$  and  $\mathbf{D}$  are both functions of  $\eta\omega = \eta(\partial_x^2 + \epsilon^2 \partial_Z^2)\psi$ . We write

$$n(x, Z, t) = n^0(x, Z, t) + \epsilon n^1(x, Z, t) + \dots \quad (5.32)$$

and

$$\psi(x, Z, t) = \psi^0(x, Z, t) + \epsilon \psi^1(x, Z, t) + \dots \quad (5.33)$$

where  $n^i$  and  $\psi^i$  ( $i = 0, 1, \dots$ ) are in general determined by non-linear partial differential equations in terms of the dependent variables. To zero order in  $\epsilon$

$$\partial_t \partial_x^2 \psi^0 - \frac{1}{\text{Re}} \partial_x^4 \psi^0 = \text{Ra} \partial_x n^0 \quad (5.34)$$

and

$$\partial_t n^0 + \partial_x (\langle \mathbf{p} \rangle^{0x} n^0) - \partial_x (\mathbf{D}^{0xx} \partial_x n^0) = 0 \quad (5.35)$$

where we have used

$$\langle \mathbf{p} \rangle^x = \langle \mathbf{p} \rangle^{0x} + \epsilon \langle \mathbf{p} \rangle^{1x} + O(\epsilon^2) \quad (5.36)$$

and similarly for  $\mathbf{D}^{xx}$ . Here, the superscript 0 means zeroth order in  $\epsilon$  and  $x$  means the  $x$  component. These equations are the same as if we had just assumed no vertical variation, but all the functions of integration in the solution will depend on  $Z$  and can be determined from the solvability conditions at higher orders. Rewriting these equations with

$$p = \eta \partial_x^2 \psi^0 = \eta\omega + O(\epsilon) \quad (5.37)$$

gives

$$\text{Re} \partial_t p = \partial_x (\partial_x p + K n^0) \quad (5.38)$$

and

$$\partial_t n^0 = \partial_x (A(p) \partial_x n^0 + E(p) n^0) \quad (5.39)$$

where

$$K = \text{RaRe}\eta. \tag{5.40}$$

The linear analysis of the previous section could be repeated here by further expanding in the  $x$  direction.

## 5.4 Amplitude equations for the non-linear saturation of initial disturbances from the homogeneous solution

As unstable linear disturbances grow in an exponential fashion, non-linear terms become more and more significant. Translational invariance in space,  $x \rightarrow x + \hat{x}$ , implies that the evolution equation of any instability of the amplitude,  $A$ , of a solution must be invariant under the transformation  $A \rightarrow Ae^{i\hat{k}\hat{x}}$ , and hence the first translationally invariant term to appear up to third order is  $|A|^2A$ . Eventually, the third order terms are of a comparable order to the first order terms and may affect the growth of the solution. If third order terms counteract the linear growth then the bifurcation to instability is said to be supercritical. If, however, the third order terms aid the growth of the linear disturbance then the bifurcation is said to be subcritical and one must look to higher orders in order to saturate the growth of the leading order terms. Subcritical bifurcations imply the existence of stable bioconvecting solutions below the critical parameter value and, hence, below the neutral curve. (See Coulet & Fauve 1985 [24] and Fauve 1985 [31] for discussions on amplitude equations, and Buzano & Golubitsky (1983) [13] and Golubitsky *et al.* (1984) [36] for the general form of amplitude equations on a hexagonal lattice). It is possible, in most systems, to generate a long wavelength theory of the evolution of initial disturbances close to the critical point (see Childress & Spiegel 1978 [21], Chapman & Proctor 1980 [16] and Knobloch 1990 [69]). However, for this model we are unable to find such an amplitude equation and, at best, the linear theory is recovered at each attempt. We choose instead to derive a Landau equation (Schlüter *et al.* 1965 [101]) which describes the weakly non-linear behaviour of the system close to a general point on the neutral curve, for which  $k \neq 0$ , and to investigate the nature of the bifurcation to instability close to the critical point at  $k = K = 0$ .

First we will motivate our scaling by expanding the growth rate of Equation (5.26)

in terms of  $(K - K_c)$  and  $(k - k_c)$ ,

$$\sigma = \left( \frac{\partial \sigma}{\partial K} \right)_c (K - K_c) + \left( \frac{\partial \sigma}{\partial k} \right)_c (k - k_c) + h.o.t. \quad (5.41)$$

where the subscript  $c$  implies that the function is evaluated at a point on the neutral curve. We find that

$$\sigma = \left( -\frac{E'(0)}{A(0)\text{Re} + 1} \right) (K - K_c) + \left( -\frac{2A(0)k_c}{A(0)\text{Re} + 1} \right) (k - k_c) + h.o.t. \quad (5.42)$$

where  $k_c$  is found from the linear analysis to be  $k_c = \sqrt{\frac{-K_c E'(0)}{A(0)}}$ . Supposing that the amplitude of a solution on the neutral curve is modulated by  $f(X, T)$ , for long length and time scales  $X$  and  $T$ , then multiplying Equation (5.42) by  $\hat{f}$  and taking the inverse Fourier transform gives the leading order form of the amplitude equation for small but finite amplitude disturbances (see Fauve 1985 [32]). Hence,

$$f_T = \left( -\frac{E'(0)}{A(0)\text{Re} + 1} \right) (K - K_c)f + \left( \frac{2A(0)k_c}{A(0)\text{Re} + 1} \right) i \frac{\partial f}{\partial X} + h.o.t. \quad (5.43)$$

This indicates that we should scale time,  $1/(K - K_c)$  and  $x$  by the same small scale. We also need to scale  $p$  such that the higher order terms appear in the equations at the same order as the terms in Equation (5.43) above. Defining our small parameter  $\delta$  (where  $1 \gg \delta \gg \epsilon$ ) by

$$\delta^2 K_2 = (K - K_c) + O(\delta^3) \quad (5.44)$$

where  $K_2$  measures the distance from criticality, then this leads us to the scalings and expansions

$$\begin{aligned} T &= \delta^2 t \\ X &= \delta^2 x \\ \partial_x &\mapsto \partial_x + \delta^2 \partial_X \\ n^0(x, X, T) &= 1 + \delta n_1(x, X, T) + \delta^2 n_2(x, X, T) + \dots \\ p(x, X, T) &= \delta p_1(x, X, T) + \delta^2 p_2(x, X, T) + \dots \end{aligned} \quad (5.45)$$

and, for now, consider

$$K = K_c + \delta K_1 + \delta^2 K_2 + \delta^3 K_3 + \dots \quad (5.46)$$

where we shall show that  $K_1 = 0$ . As  $E$  is odd and  $A$  is even, we can write

$$E(p) = (\delta p_1 + \delta^2 p_2 + \dots) E'(0) + \frac{1}{3!} (\delta^3 p_1^3 + \dots) E'''(0) + \dots \quad (5.47)$$

and

$$A(p) = A(0) + \frac{1}{2} (\delta^2 p_1^2 + 2\delta^3 p_1 p_2 + \delta^4 p_2^2 + \dots) A''(0) + \dots \quad (5.48)$$

Hence, substituting these expansions and scalings into Equations (5.38) and (5.39) gives

$$\begin{aligned} \text{Re} \delta^3 \partial_T (p_1 + \delta p_2 + \dots) &= \delta (\partial_x^2 + 2\delta^2 \partial_x \partial_X + \delta^4 \partial_X^2) (p_1 + \delta p_2 + \dots) \\ &+ \delta (K_c + \delta K_1 + \delta^2 K_2 + \dots) (\partial_x + \delta^2 \partial_X) (n_1 + \delta n_2 + \delta^2 n_3) \end{aligned} \quad (5.49)$$

and

$$\begin{aligned} \delta^3 \partial_T (n_1 + \delta n_2 + \dots) &= \delta (\partial_x + \delta^2 \partial_X) [E'(0) (p_1 + \delta p_2 + \dots) (1 + \delta n_1 + \delta^2 n_2 + \dots) \\ &+ \left( A(0) + \frac{1}{2} A''(0) (\delta^2 p_1^2 + \dots) \right) (\partial_x + \delta^2 \partial_X) (n_1 + \delta n_2 + \delta^2 n_3 + \dots)] \end{aligned} \quad (5.50)$$

The lowest orders of Equations (5.49) and (5.50) are

$$\partial_x^2 p_1 + K_c \partial_x n_1 = 0 \quad (5.51)$$

and

$$E'(0) \partial_x p_1 + A(0) \partial_x^2 n_1 = 0 \quad (5.52)$$

which imply that

$$\begin{pmatrix} p_1 \\ n_1 \end{pmatrix} = f(X, T) \begin{pmatrix} -\frac{A(0)ki}{E'(0)} \\ 1 \end{pmatrix} e^{ikx} + c.c. \quad (5.53)$$

where  $k = 0$  or  $\sqrt{\frac{-K_c E'(0)}{A(0)}}$ . This defines the piecewise continuous neutral curve seen in Figure (5.2). We choose to take the non-trivial root and, hence, consider a solution near that part of the neutral curve that gives spatial pattern. If  $K_c$  is small then this solution is close to the trivial critical solution at  $k = 0$ . The next order gives the two equations

$$\partial_x^2 p_2 + K_c \partial_x n_2 = -K_1 \partial_x n_1 \quad (5.54)$$

and

$$E'(0) \partial_x p_2 + A(0) \partial_x^2 n_2 = -E'(0) \partial_x (p_1 n_1). \quad (5.55)$$

Clearly  $\partial_x n_1$  is a secular term and  $\partial_x (p_1 n_1)$  is not. Solvability implies that the secular term is orthogonal to the solution of the homogeneous equation and, in this case, this implies that the secular term should vanish and, hence, that  $K_1 = 0$ . This is consistent

with our predicted scalings (Equation 5.44). The general solution for these equations is

$$\begin{pmatrix} p_2 \\ n_2 \end{pmatrix} = f_2(X, T) \begin{pmatrix} a \\ b \end{pmatrix} e^{ikx} + c.c. + g(X, T) \begin{pmatrix} d \\ e \end{pmatrix} e^{2ikx} + c.c. \quad (5.56)$$

We choose  $a = b = 0$  as this part of the solution can be combined with the leading order solution. Substituting Equation (5.56) back in to Equations (5.54) and (5.55), we get that

$$g(x, T) = f^2(X, T), \quad (5.57)$$

$$d = \frac{ikA(0)}{6E'(0)} \quad \text{and} \quad e = \frac{1}{3}. \quad (5.58)$$

The next orders give

$$\partial_x^2 p_3 + K_c \partial_x n_3 = Re \partial_T p_1 - K_2 \partial_x n_1 - K_c \partial_X n_1 - 2 \partial_x \partial_X p_1 \quad (5.59)$$

and

$$\begin{aligned} E'(0) \partial_x p_3 + A(0) \partial_x^2 n_3 &= \partial_T n_1 - E'(0) \partial_x (p_2 n_1) - E'(0) \partial_x (p_1 n_2) \\ &- E'(0) \partial_X p_1 - 2A(0) \partial_x \partial_X n_1 - \frac{1}{2} A''(0) \partial_x [p_1^2 \partial_x n_1]. \end{aligned} \quad (5.60)$$

The solvability condition (see Ince 1956 [51]) requires that

$$\int_0^{\frac{2\pi}{k}} \mathbf{u}^H \mathbf{N} dx = 0 \quad (5.61)$$

where  $H$  means the Hermitian,  $\mathbf{u}$  is the solution to the adjoint problem and  $\mathbf{N}$  indicates the secular terms in the inhomogeneous problem. Hence, as

$$\mathbf{u}^H \propto \left( \frac{E'(0)i}{k}, \quad 1 \right) e^{-ikx} + c.c. \quad (5.62)$$

then the solvability condition becomes

$$\begin{aligned} 0 &= \int_0^{\frac{2\pi}{k}} \left[ \frac{E'(0)}{k} \left( ie^{-ikx} - ie^{ikx} \right) \left( -Re f_T \frac{A(0)ki}{E'(0)} e^{ikx} + Re \bar{f}_T \frac{A(0)ki}{E'(0)} e^{-ikx} \right. \right. \\ &- K_2 ik f e^{ikx} + K_2 ik \bar{f} e^{-ikx} - K_c f_X e^{ikx} - K_c \bar{f}_X e^{-ikx} - 2f_X \frac{A(0)k^2}{E'(0)} e^{ikx} \\ &- 2\bar{f}_X \frac{A(0)k^2}{E'(0)} e^{-ikx} \left. \right) + \left( e^{-ikx} + e^{ikx} \right) \left( f_T e^{ikx} + \bar{f}_T e^{-ikx} \right. \\ &- E'(0) \left[ \left( \frac{2k^2 A(0)}{6E'(0)} f^2 e^{2ikx} + \frac{2k^2 A(0)}{6E'(0)} \bar{f}^2 e^{-2ikx} \right) \left( f e^{ikx} + \bar{f} e^{-ikx} \right) \right. \\ &\left. \left. + \left( \frac{-ikA(0)}{6E'(0)} f^2 e^{2ikx} + \frac{-ikA(0)}{6E'(0)} \bar{f}^2 e^{-2ikx} \right) \left( ik f e^{ikx} - ik \bar{f} e^{-ikx} \right) \right] \right] dx \end{aligned}$$

$$\begin{aligned}
 & + \left( \frac{2ikA(0)}{3E'(0)} f^2 e^{2ikx} - \frac{2ikA(0)}{3E'(0)} \bar{f}^2 e^{-2ikx} \right) \left( -\frac{A(0)ik}{E'(0)} f e^{ikx} + \frac{A(0)ik}{E'(0)} \bar{f} e^{-ikx} \right) \\
 & + \left( \frac{1}{3} f^2 e^{2ikx} + \frac{1}{3} \bar{f}^2 e^{-2ikx} \right) \left( \frac{A(0)k^2}{E'(0)} f e^{ikx} + \frac{A(0)k^2}{E'(0)} \bar{f} e^{-ikx} \right) \\
 & - A(0)ik f_X e^{ikx} + A(0)ik \bar{f}_X e^{-ikx} + 2A(0)ik f_X e^{ikx} - 2A(0)ik \bar{f}_X e^{-ikx} \Big] \\
 & - A''(0) \left( \frac{A(0)}{E'(0)} \right)^2 \left[ \left( -ik f e^{ikx} + ik \bar{f} e^{-ikx} \right) \left( k^2 f e^{ikx} + k^2 \bar{f} e^{-ikx} \right) \left( ik f e^{ikx} - ik \bar{f} e^{-ikx} \right) \right. \\
 & \left. + \frac{1}{2} \left( -ik f e^{ikx} + ik \bar{f} e^{-ikx} \right)^2 \left( -k^2 f e^{ikx} - k^2 \bar{f} e^{-ikx} \right) \right] dx. \tag{5.63}
 \end{aligned}$$

This implies that

$$f_T = \left( \frac{-K_2 E'(0)}{A(0)\text{Re} + 1} \right) f - \left( \frac{-K_c E'(0) + 9K_c^2 A''(0)}{6(A(0)\text{Re} + 1)} \right) |f|^2 f + \left( \frac{2\sqrt{-K_c E'(0)A(0)}}{A(0)\text{Re} + 1} \right) i f_X \tag{5.64}$$

(and a conjugate equation for the complex conjugate of  $f$ ) and represents the non-linear saturation of linear modes.

The  $i f_X$  term is invariant to all of the relevant symmetries and is a consequence of prescribing a periodic domain of size  $L = 2\pi/k_c$ . The term represents corrections to the amplitude equation for small variations of the wavenumber from  $k_c$  and can be removed by the transformations

$$X' = X + i\kappa T \tag{5.65}$$

and

$$T' = T, \tag{5.66}$$

where

$$\kappa = \left( \frac{2\sqrt{-K_c E'(0)A(0)}}{A(0)\text{Re} + 1} \right), \tag{5.67}$$

such that

$$f_T \longrightarrow f_{T'} + i\kappa f_{X'}. \tag{5.68}$$

For the special case at the critical point, where  $k = 0$ , the  $i f_X$  term vanishes. As  $K_c$  decreases to zero, the third order term tends to zero but, crucially, does so from below. The multiplier of the  $|f|^2 f$  term is negative provided  $K_c > 0$  and

$$-E'(0) > -9K_c A''(0). \tag{5.69}$$

$E'(0)$  is always negative and  $A''(0)$  is positive provided  $A(p)$  has a minimum at  $p = 0$ . This occurs if and only if  $\mathcal{N} > 1.0206$  (see Chapter 4 and Figure 4.26). Hence, if either

$\mathcal{N} > 1.0206$  (very likely) or  $K_c$  is small but positive, then the multiplier of the  $|f|^2 f$  term is negative. We conclude that the bifurcation to instability is supercritical (for example see Coulet & Fauve 1985 [24]; Schlüter *et al.* 1965 [101]) and is our main result in this section. This implies that the linear analysis is useful for predicting the wavenumber of the initial disturbance from equilibrium. We could go on to explore solutions and stabilities of the amplitude equation as in Fauve (1985) [32, 31], where the Eckhaus and zig-zag instabilities are investigated, but solutions of an obvious extension to the theory, where the vertical wavelength is non-zero, may be more illuminating (see the discussion in Section 5.8). In particular, we would obtain a Ginzburg-Landau equation to describe temporal and spatial evolution of the solution amplitude (see Newell & Whitehead 1969 [81]; Chaté 1994 [17]).

## 5.5 Steady state solution

We look for a steady solution to Equations (5.38) and (5.39). The time-independent equations can be integrated directly to obtain the equations

$$p_x + K (n^0 - \Lambda) = 0 \tag{5.70}$$

and

$$A(p)n_x^0 + E(p)n^0 = C_2 \tag{5.71}$$

where  $C_2$  and  $\Lambda$  are in general unknown functions of  $Z$ . Applying boundary conditions such that  $p = 0$  when  $n_x^0 = 0$  (i.e. that vorticity is zero in the centre of the plume) then  $C_2 \equiv 0$ . These are the only boundary conditions imposed. Integrating the first equation over  $x$  we find that

$$\{n^0\}^x = \Lambda(Z) \tag{5.72}$$

where  $\{\cdot\}^x$  is a space average over  $x$ . As  $n^0$  is a normalized quantity then

$$\{\{n^0\}^x\}^Z = \{\Lambda(Z)\}^Z = 1. \tag{5.73}$$

To reduce the number of parameters, we could consider the equations space averaged over the vertical direction and this would result in  $\Lambda$  being replaced by a 1 and the solutions would be vertically averaged. However, we choose instead to consider the change of variables

$$N = \frac{n^0}{\Lambda(Z)} \tag{5.74}$$

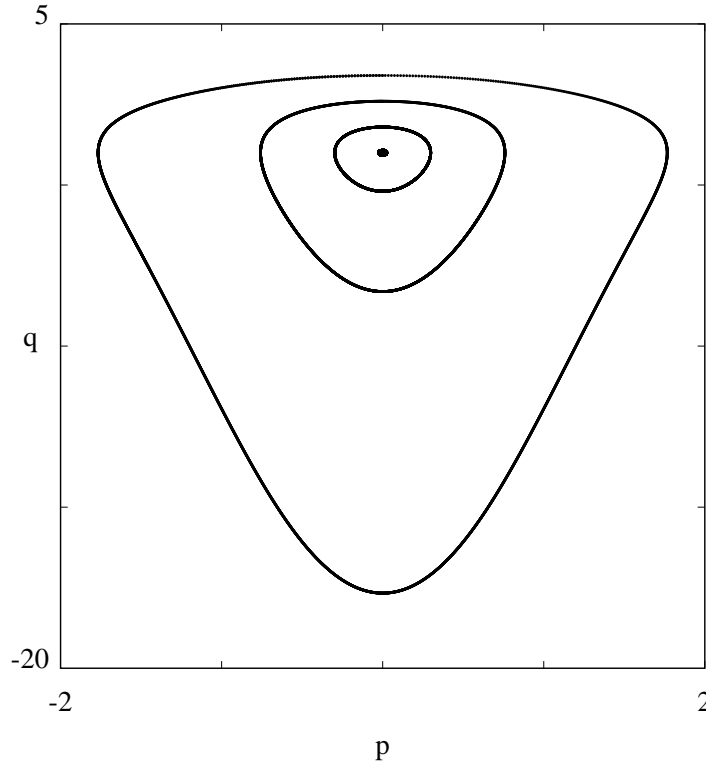


Figure 5.4: Orbits for  $K^* = 0.1$  going clockwise with increasing  $x$ .

and

$$K^*(Z) = \Lambda(Z)K. \tag{5.75}$$

This implies that the time-dependent equations become

$$\text{Re } p_t = (p_x + K^*(N - 1))_x \tag{5.76}$$

and

$$N_t = (A(p)N_x + E(p)N)_x, \tag{5.77}$$

where there is now only one parameter,  $K^*(Z)$ . Changing variables again by putting

$$q = \ln(N) \tag{5.78}$$

we find that the time dependent equations become

$$\text{Re } p_t = (p_x + K^*(e^q - 1))_x \tag{5.79}$$

and

$$e^q q_t = (e^q A(p)q_x + e^q E(p))_x. \tag{5.80}$$

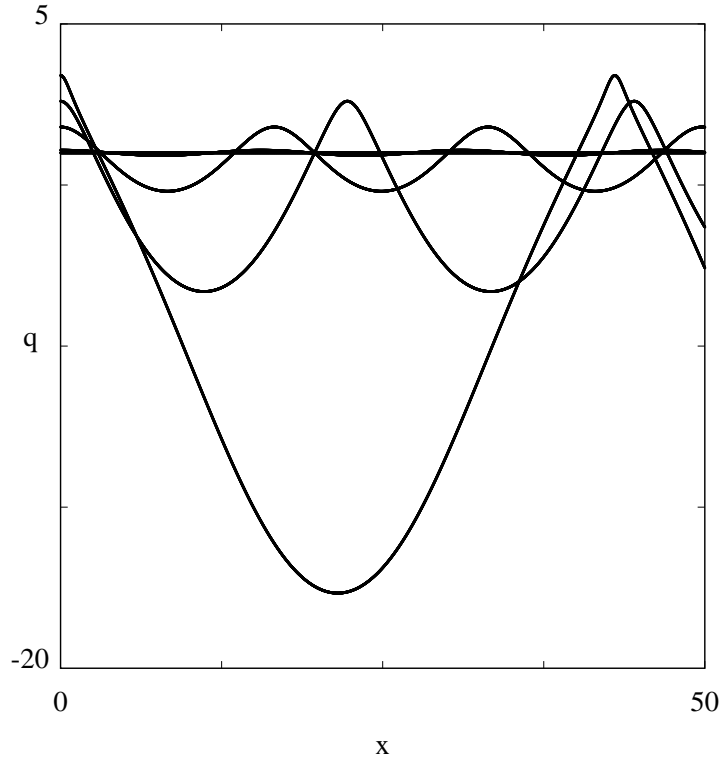


Figure 5.5: Profiles of the orbits given in Figure 5.4. Examples of  $q$  ( $= \ln(n^0)$ ) varying in the  $x$  direction for  $K^* = 0.1$ .

The new steady system is Hamiltonian and can be written as

$$\partial_x p = -\partial_q \mathcal{H} \tag{5.81}$$

and

$$\partial_x q = \partial_p \mathcal{H}, \tag{5.82}$$

where  $\mathcal{H}$  is given by

$$\mathcal{H} = K^* (e^q - q) - \int_0^p \frac{E(p')}{A(p')} dp'. \tag{5.83}$$

This system of equations can be integrated explicitly using methods such as fourth order Runge-Kutta schemes, and the easiest way to do this is to consider the equations as a dynamical system in the dependent variable  $x$  and to use one of the dynamical systems packages available, such as *DsTool2* by Guckenheimer, Myers, Wicklin & Worfolk (Cornell University, 1995). All of the orbits are closed and thus all of the solutions are periodic. Some of the closed orbits of this system are represented in Figures (5.4) and (5.6) and clearly there are an infinity of possible solutions. Their wavenumbers, however, are restricted to a small range from zero to some maximum value obtained from

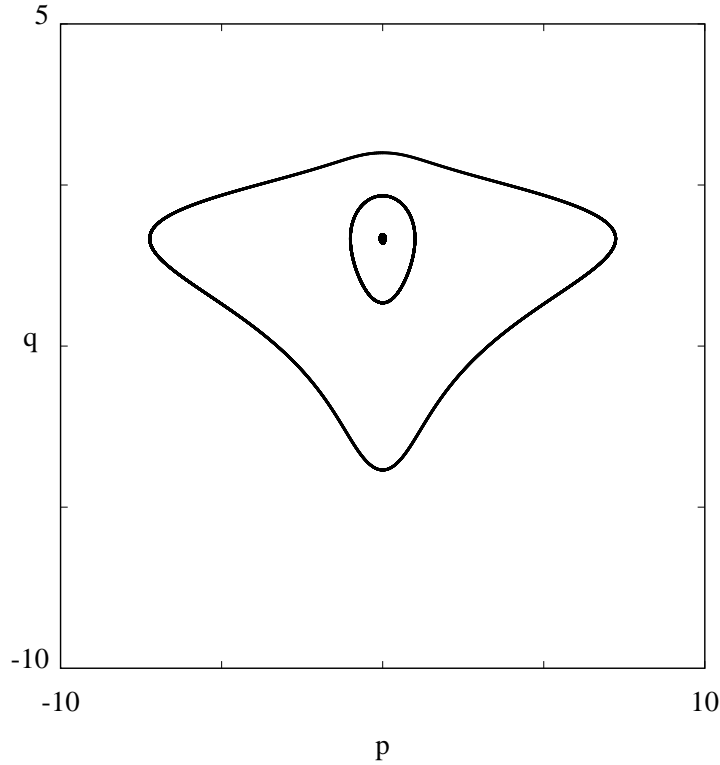


Figure 5.6: Orbits for  $K^* = 1$  going clockwise with increasing  $x$ .

the numerical solutions. Thus, in a periodic domain of a specified size, there are finitely many steady state solutions. Figures (5.4) and (5.5) display the periodic curves of  $p(x)$  and  $q(x)$  for  $K^* = 0.1$ , and shows how they increase their wavelength with increasing amplitude. Figures (5.6) and (5.7) describe the system when  $K^*$  is raised to 1. For all values of  $K^*$  the pattern wavelength increases with its amplitude. Therefore, small amplitude solutions give the maximum wavenumber. The small amplitude solutions are precisely those given by the linear analysis of Section 5.2. Hence, the maximum wavenumber is given by

$$k_c = \sqrt{\frac{-K_c E'(0)}{A(0)}}, \tag{5.84}$$

from Equation (5.23). This is consistent with the form of the amplitude equation given in Section 5.4. However, the system is structurally unstable in that if a small perturbation displaces a solution from one trajectory to another then it will stay on the new trajectory (see an example of a similar system, by Lotka and Volterra, in Murray, 1990 [80]). We do not know the final pattern unless we know every perturbation from the homogeneous state. It is thus necessary to consider higher orders in order to

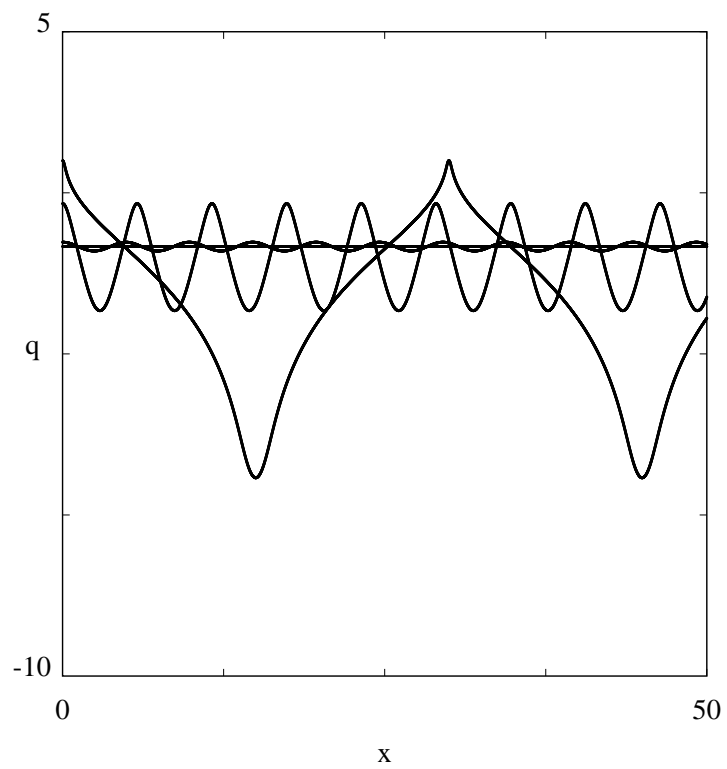


Figure 5.7: Profiles of the orbits given in Figure 5.6. Examples of  $q (= \ln(n^0))$  varying in the  $x$  direction for  $K^* = 1$ .

establish the stability of the greater system.

We have shown, here, that it is possible to construct steady state solutions from the first order equations, non-linear in  $x$ , describing a horizontal balance between diffusion and gyrotaxis. These solutions are only dependent on  $Z$  through the functions of integration, and will be used in later sections when investigating the system at higher orders.

## 5.6 Travelling wave solution

In certain special situations it is possible to obtain time dependent solutions. In Section 5.8 we shall discuss the construction of similarity solutions for the time dependent problem and in this section we shall describe a class of solutions that provide horizontally travelling waves. In particular we shall investigate a travelling wave solution that leaves in its path a regular array of travelling plumes. It is first necessary to break the symmetry of the system and impose a “background vorticity”, in which we simply enforce that  $p = p_0$  at  $x = \infty$  where  $p_0$  is a positive constant. For example, a constant fluid velocity gradient in the horizontal direction would be sufficient.

Consider  $\Xi = x - ct$ , where without loss of generality we assume  $c \geq 0$ , then

$$-c \operatorname{Re} p' = (p' + K^* N)' \tag{5.85}$$

and

$$-c N' = (A(p)N' + E(p)N)' \tag{5.86}$$

where  $'$  means differentiation with respect to  $\Xi$ . This implies that

$$p' = K^*(1 - N) - c \operatorname{Re} p + C_1 \tag{5.87}$$

and

$$N' = -\frac{E(p)N + cN + C_2}{A(p)}. \tag{5.88}$$

For a rightward travelling wave, we require that  $N = 1$ ,  $p = p_0$  and  $N' = p' = 0$  at  $\Xi = \infty$  where  $p_0$  is our background vorticity. As  $N$  represents the concentration of cells, then we need to enforce  $N \geq 0 \quad \forall \Xi \in \mathbb{R}$ . That is to say that no trajectory that asymptotes to  $(p, N) = (p_0, 1)$  should cross the line in phase space given by  $N = 0$ .

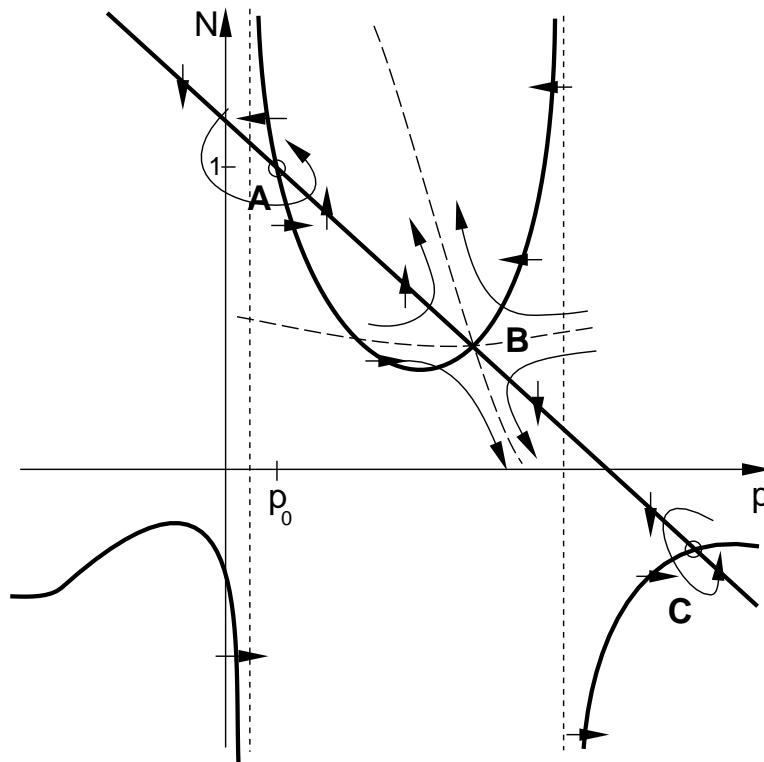


Figure 5.8: Nullclines for a typical travelling wave system where  $c + E(p_0) \leq 0$ . The saddle point, B, allows the possibility of a homoclinic orbit around the focus, A, and as the focus, A, changes stability a limit cycle can develop. This ensures the existence of a Hopf bifurcation. The equilibrium point C is not within the region of realistic cell concentrations.

Applying the boundary conditions to Equation (5.85) implies that  $C_1 = c\text{Re}p_0$ . The boundary conditions applied to Equation (5.86) imply that

$$c + C_2 = -E(p_0). \tag{5.89}$$

This enables us to rewrite the equations as

$$p' = c\text{Re}(p_0 - p) + K^*(1 - N) \tag{5.90}$$

and

$$N' = \frac{[c(1 - N) + (E(p_0) - E(p)n)]}{A(p)}. \tag{5.91}$$

Hence, there is a point of equilibrium at  $(p_0, 1)$ . Linearizing about this point and calculating the eigenvalues,  $\lambda$ , corresponding to the principal linear growth rates, we find

$$\lambda = -\frac{1}{2} \left( c\text{Re} + \frac{c + E(p_0)}{A(p_0)} \right) \pm \frac{1}{2} \sqrt{\left( c\text{Re} - \frac{c + E(p_0)}{A(p_0)} \right)^2 + 4K^* \frac{E'(p_0)}{A(p_0)}} \tag{5.92}$$

and this implies that we have either a stable (with respect to  $\Xi$ ) focus or node or a saddle point. We are particularly interested in the stable focus as it represents growing oscillations travelling to the right. The other two possibilities allow unbounded cell concentrations and will not be considered further. For the stable focus to exist we require  $\Re(\lambda) < 0$ , which implies

$$c > \frac{-E(p_0)}{A(p_0)\text{Re} + 1} \geq 0, \tag{5.93}$$

and  $\Im(\lambda) \neq 0$ , which implies

$$c_- < c < c_+ \tag{5.94}$$

where

$$c_{\pm} = \frac{E(p_0)}{A(p_0)\text{Re} - 1} \pm \frac{2A(p_0)}{A(p_0)\text{Re} - 1} \sqrt{\frac{-K^*E'(p_0)}{A(p_0)}}. \tag{5.95}$$

Hence, we require

$$E'(p_0) < 0 \tag{5.96}$$

for real, non-zero values of  $c_{\pm}$ . The nullclines for this system are given by

$$n = \frac{c\text{Re}}{K^*}(p_0 - p) + 1 \tag{5.97}$$

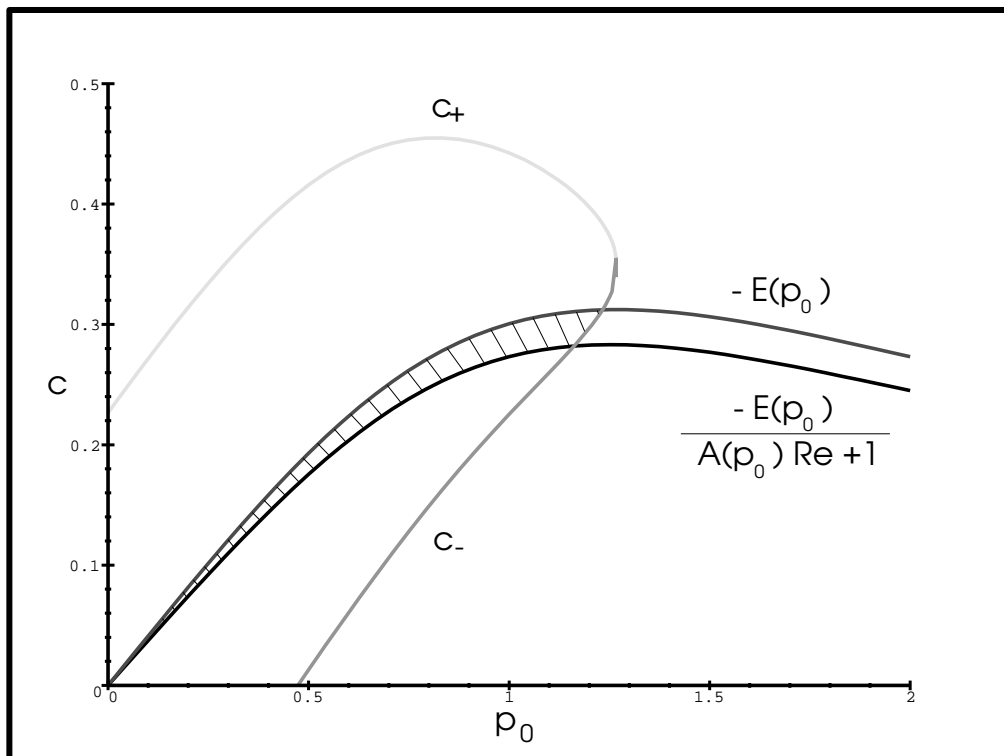


Figure 5.9: Travelling wave solutions exist for a small range of wavespeeds,  $c$ , given the parameters  $Re$ ,  $K^*$  and  $p^0$ . Here  $K^* = 0.1$ ,  $Re = 0.4$  and  $p^0$  is plotted along the  $x$  axis. The hatched region indicates where travelling wave solutions exist. Here, the value of  $Re$  is artificially large in order to indicate the hatched region. Normally  $Re \sim 10^{-4}$  and the region is much smaller.

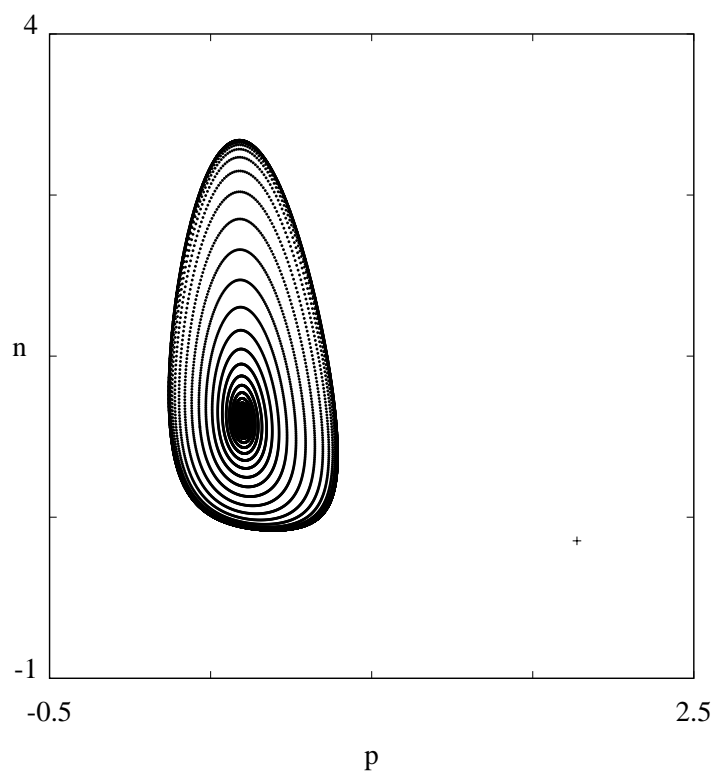


Figure 5.10: Trajectories for the travelling wave system (clockwise with  $\Xi$ ) where an unstable limit cycle is clearly observed. The + indicates the location of the saddle point.  $K^* = 0.1$ ,  $p_0 = 0.4$ ,  $\text{Re} = 0.4$  and  $c = 0.15$ .

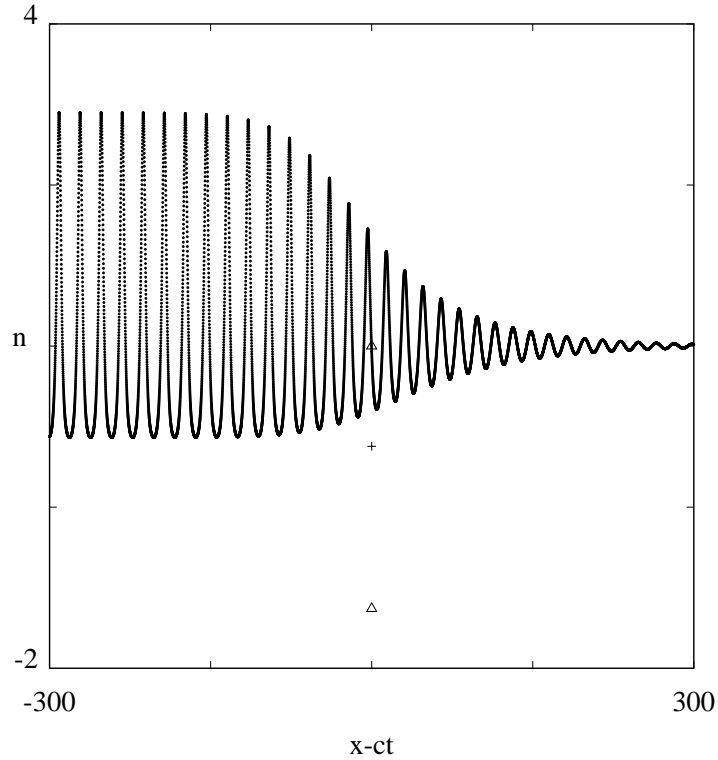


Figure 5.11: Cell concentration varying with  $x - ct$  for waves travelling to the right.  $K^* = 0.1$ ,  $p_0 = 0.4$ ,  $\text{Re} = 0.4$  and  $c = 0.15$ .

and

$$n = \frac{c + E(p_0)}{c + E(p)} \tag{5.98}$$

and are plotted in Figure (5.8). This figure enables us to see the location of two other equilibrium points and to establish their stability from geometrical considerations. The saddle point is the second most important feature and it clearly allows the possibility for the usual homoclinic orbit bifurcation to a limit cycle around the focus (see Balmforth 1995 [2]). A Hopf bifurcation potentially exists and it is the objective of the subsequent analysis to establish conditions for the existence of the Hopf bifurcation. If the trajectory starts in the neighbourhood of  $(p, N) = (p_0, 1)$ , then we also require that  $N' \leq 0$  on  $N = 0$  for  $N$  to be bounded below by at least  $N = 0$ . If  $N = 0$  then

$$N' = -\frac{C_2}{A(p)} \tag{5.99}$$

and hence we require that  $C_2$  be positive. This implies that

$$0 \leq c \leq -E(p_0). \tag{5.100}$$

The maximum wavespeed is given by  $c = -E(p_0)$  and this occurs when  $C_2 = 0$ . Clearly no travelling wave solutions exist if there is no background vorticity as  $c = 0$  if  $p_0 = 0$ . Collecting all of these necessary conditions together for a limit cycle to exist gives

$$0 \leq \frac{-E(p_0)}{A(p_0)\text{Re} + 1} < c \leq -E(p_0) \quad (5.101)$$

and

$$c_- < c < c_+, \quad (5.102)$$

where

$$c_{\pm} = \frac{E(p_0)}{A(p_0)\text{Re} - 1} \pm \frac{2A(p_0)}{A(p_0)\text{Re} - 1} \sqrt{\frac{-K^*E'(p_0)}{A(p_0)}} \quad (5.103)$$

and

$$E'(p_0) < 0 \quad (5.104)$$

(see Figure 5.9). If  $K^*$  increases then the region described by Equation (5.102) grows in size. Decreasing  $K^*$  has the opposite effect but the region only vanishes if  $K^* \leq 0$ . Similarly, if  $\text{Re}$  increases the region described by Equation (5.101) increases in size and if  $\text{Re}$  decreases the region also decreases but only vanishes if  $\text{Re} \leq 0$ . The two regions always coincide near to  $p^0 = 0$  and  $c = 0$ . A limit cycle is seen to exist for certain limited choices of  $c$  by direct integration of the governing equations (see Figures 5.10 and 5.11) which corresponds exactly with the region given in Figure 5.9. This implies that if the pattern nucleates at a point then plumes will spread out, where the wave speed is confined to a small range, and increase in amplitude until a regular pattern is reached. This theoretical prediction for a small range of values of  $c$  could be compared with experiments once a suitable experimental arrangement has been formulated.

## 5.7 Vertical variation of the steady state solutions

In this section we develop a theory to help explain the pulses that travel down the long plume structures, as seen in Figure (5.1). Consider the steady state solutions of Section 5.5 and allow these solutions to vary slowly with time and in the vertical direction. If we rescale time with the small parameter  $\epsilon$ , such that  $T = \epsilon t$ , then we can use the equations of Section 5.3 to obtain the leading order equations for a small variation in the  $z$  direction. Hence, the first order equations are

$$p_x + K(n^0 - \Lambda(Z, T)) = 0 \quad (5.105)$$

and

$$n_x^0 + \frac{E(p)}{A(p)}n^0 = 0, \quad (5.106)$$

and at second order we get

$$\frac{1}{\text{Re}}(\partial_x^4 \psi^1) + \text{Ra} \partial_x n^1 = \partial_T(\partial_x^2 \psi^0) + \partial_Z \psi^0 \partial_x^3 \psi^0 - \partial_x \psi^0 \partial_x^2 \partial_Z \psi^0 \quad (5.107)$$

and

$$\begin{aligned} \partial_x (n^1 \langle \mathbf{p} \rangle^x (\eta \partial_x^2 \psi^0) + \eta \partial_x^2 \psi^1 n^0 \langle \mathbf{p} \rangle^{x'}) (\eta \partial_x^2 \psi^0) - \mathbf{D}^{xx} (\eta \partial_x^2 \psi^0) \partial_x n^1 - \eta \partial_x^2 \psi^1 \partial_x n^0 \mathbf{D}^{xx'} (\eta \partial_x^2 \psi^0) \\ = -\partial_T n^0 + \partial_x (\mathbf{D}^{xz} (\eta \partial_x^2 \psi^0) \partial_Z n^0) + \partial_Z (\mathbf{D}^{xz} (\eta \partial_x^2 \psi^0) \partial_x n^0 - \langle \mathbf{p} \rangle^z (\eta \partial_x^2 \psi^0) n^0) \\ + \partial_x \psi^0 \partial_Z n^0 - \partial_Z \psi^0 \partial_x n^0 \end{aligned} \quad (5.108)$$

where

$$\mathbf{D}^{xz} (\eta \partial_x^2 \psi^0) = \frac{4}{5} A_2^1 (\eta \partial_x^2 \psi^0) - \frac{16\pi}{9} A_1^1 (\eta \partial_x^2 \psi^0) A_1^0 (\eta \partial_x^2 \psi^0), \quad (5.109)$$

$$\langle \mathbf{p} \rangle^z (\eta \partial_x^2 \psi^0) = \frac{4\pi}{3} A_1^0 (\eta \partial_x^2 \psi^0) \quad (5.110)$$

and the  $A_j^i$  are given in Equation (4.57). The solvability condition can be found by integrating the second of these equations over a horizontal wavelength. If  $\{\cdot\}^x$  represents a space average in the  $x$  direction, as before, then

$$\partial_T \{n^0\}^x = \partial_Z \left\{ \mathbf{D}^{xz}(p) \partial_x n^0 - \langle \mathbf{p} \rangle^z(p) n^0 + \frac{p^2}{K\eta} \right\}^x \quad (5.111)$$

where  $p = \eta \partial_x^2 \psi^0$ . We can simplify this equation to be in terms of  $p$  and  $\Lambda$ , using the first order equations. Hence,

$$\partial_T \Lambda(Z, T) = \partial_Z \left\{ B(p) \Lambda(Z, T) + \frac{p^2}{K\eta} \right\}^x. \quad (5.112)$$

where

$$B(p) = \langle \mathbf{p} \rangle^z(p) - \mathbf{D}^{xz}(p) \frac{E(p)}{A(p)}. \quad (5.113)$$

Clearly this equation possesses travelling wave solutions and is similar to the equations discussed by Whitehead (1988) [121] where soliton like pulses were discovered travelling up magma ducts in a viscous matrix. It is the purpose of the following analysis to investigate small amplitude solutions where we will be able to derive the wave speed but not its form.

First, we write

$$\Lambda(Z, T) = 1 + M(Z, T), \quad (5.114)$$

where  $|M(Z, T)| \ll 1$ , and expand  $p$  and  $n^0$  in terms of  $M(Z, T)$  such that

$$p(x, Z, T) = p_0(x) + M(Z, T)p_1(x) + O(M^2) \quad (5.115)$$

and

$$n^0(x, Z, T) = n_0(x) + M(Z, T)n_1(x) + O(M^2). \quad (5.116)$$

At first order we regain the non-linear equations for solutions in the horizontal direction with zero vertical variation, i.e.

$$p_{0x} + K(n_0 - 1) = 0 \quad (5.117)$$

and

$$n_{0x} + \frac{E(p_0)}{A(p_0)}n_0 = 0. \quad (5.118)$$

The next order in  $M(Z, T)$  provides a set of linear equations for the perturbations to the steady state solutions which are both independent of  $M(Z, T)$ ,  $Z$  or  $T$ . Namely,

$$p_{1x} + K(n_1 - 1) = 0 \quad (5.119)$$

and

$$n_{1x} + \frac{E(p_0)}{A(p_0)}n_1 + \left(\frac{E(p_0)}{A(p_0)}\right)' n_0 p_1 = 0. \quad (5.120)$$

This last system describes a forced oscillator (see Thompson & McRobie 1993 [107] for a discussion of the complexities of driven oscillators) and potentially has solutions with wavelengths that are quotient multiples of the unperturbed system. We can explicitly find solutions with a multiple of the wavenumber of the unperturbed system such that they abide by the same boundary conditions. Hence, more than one closed orbit is possible for  $p_1$  and  $n_1$  given  $p_0$  and  $n_0$ .

Hence, using Equations (5.114) and (5.115) in Equation (5.112) gives

$$\partial_T M(Z, T) = \left\{ B'(p_0)p_1 + \frac{2p_0 p_1}{K\eta} \right\}^x \partial_Z M(Z, T) + O(M^2). \quad (5.121)$$

If we look for a travelling wave solution (see Figure 5.1) and put  $\Xi = Z - ct$  then

$$\partial_{\Xi} M(\Xi) (B + c) = 0 \quad (5.122)$$

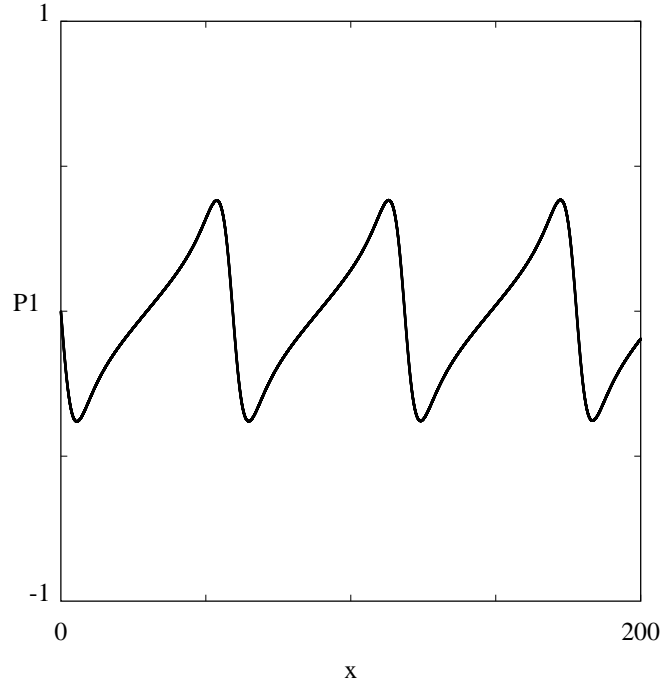


Figure 5.12: Perturbation,  $p_1$ , to  $p_0$  varying with  $x$  for a vertically travelling pulse. Here  $K^* = 0.01$  with the initial conditions  $n_0 = 5$ ,  $p_0 = 0$ ,  $n_1 = 13.8$  and  $p_1 = 0$ .

where

$$\mathcal{B} = \left\{ B'(p_0)p_1 + \frac{2p_0p_1}{K\eta} \right\}^x \tag{5.123}$$

and, thus, we can determine the wave speed,  $c = -\mathcal{B}$ , but not the wave form. The full problem in Equation (5.112) is sufficient to determine the waveform. As an example, we find a particular solution for  $n_1$ ,  $p_1$  and  $c$  given the parameter  $K = 0.01$  and the conditions  $n_0 = 5$  when  $p_0 = 0$  (i.e. just one of an infinite number of possible orbits). We find a closed orbit with the initial conditions  $p_1 = 0$  and  $n_1 = 13.8$ , as illustrated in Figures (5.12) and (5.13), which has the same wavelength as the unperturbed solution. Hence, we can use the functions  $p_0$  and  $p_1$  to calculate  $c$ .

To compare the theory with the experiments we should measure in the experiments the minimum and maximum concentration profiles. Linear theory (Equation 5.116) gives  $n_0$  as the average of the two and  $n_1$  as half of their difference. Substituting  $n_0$  and  $n_1$  into Equations (5.118) and (5.120), solving for  $p_0$  and  $p_1$  and substituting in Equation (5.123) gives the wavespeed,  $c$ . This should be compared with the observed wavespeed.

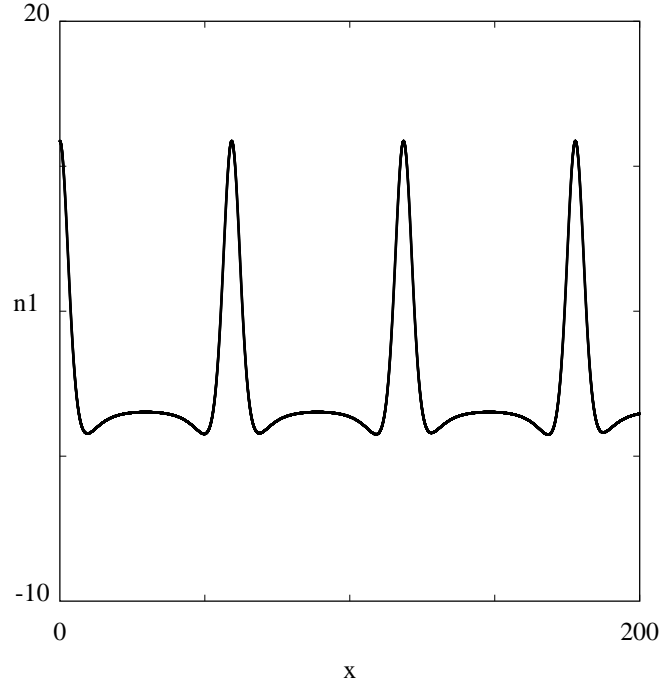


Figure 5.13: Perturbation,  $n_1$ , to the cell concentration,  $n_0$ , varying with  $x$  for a vertically travelling pulse. Here  $K^* = 0.01$  with the initial conditions  $n_0 = 5$ ,  $p_0 = 0$ ,  $n_1 = 13.8$  and  $p_1 = 0$ .

## 5.8 Discussion and future improvements

In this section we shall discuss the work from the whole chapter paying particular attention to areas of possible future research. Some detail of the theories for two likely advances will be given explicitly.

We have shown that it is possible to expand the full non-linear equations for stochastic, gyrotactic bioconvection in the vertical direction, guided by experimental observations of plumes and the linear analysis. At first order, we obtain a set of partial differential equations in  $x$  and  $t$  for which we derive a Landau equation for the non-linear saturation of linear modes close to the curve of neutral stability. We show that the bifurcation to instability is supercritical and, hence, that the linear theory is useful for predicting the wavenumber of the initial instability from equilibrium in a deep chamber. This analysis should be repeated on the full non-linear equations allowing for the Hopf bifurcation resulting from non-zero vertical variation. The finite depth of a realistic suspension may indicate that we should investigate the system for a small, but

non-zero, fixed value of the vertical wavenumber,  $m$ , and we would therefore obtain a non-zero critical wavenumber and a non-zero critical parameter,  $K$  (see Figure 5.2).

From the long vertical wavelength expansion we have obtained, at first order, a Hamiltonian system which describes steady state solutions. These solutions are dependent on a function of integration,  $K^*$ , which is itself dependent on  $z$ .

We go on to consider a horizontally travelling vertical plume solution of the first order non-linear partial differential equations. We obtain a set of waveforms and a very small range of possible wavespeeds. These results could be directly compared with experiments once a suitable experimental arrangement has been formulated.

Finally, we investigate the second order equations for the long vertical wavelength approximation and obtain an amplitude equation from a solvability condition that describes vertically travelling pulse solutions on top of the steady state solutions already derived. We then assume that the vertical variation is itself small and obtain a set of four ordinary differential equations independent of  $z$ . We use the solutions of these to calculate the wavespeed. However, for this approximation, we cannot calculate the waveform. A future improvement would be to investigate the weakly non-linear theory of this amplitude equation and, hence, solve for the waveform. Again, these results could be compared with experiments once careful measurements have been obtained for both wavespeeds of small amplitude pulses and profiles of the plume concentrations. This is necessary as the wavespeed is dependent on the cell concentration profile of the plume.

### 5.8.1 Similarity solutions

Similarity solutions for Equations (5.38) and (5.39) describing zero vertical variation cannot be obtained for the general forms of the diffusion,  $A(p)$  (Equation 5.12), and the gyrotaxis,  $E(p)$  (Equation 5.11), terms. Following a suggestion of Dr. Peter Hydon (personal communication, 1996) a simplification of  $A(p)$  and  $E(p)$  could lead to similarity solutions with a similar behaviour to the original system. The diffusion term,  $A(p)$ , is plotted in Figure (4.26) and it can be seen that it is rather flat. Therefore, we assume that

$$A(p) = a_0, \tag{5.124}$$

where  $a_0$  is a constant. Equation (5.11) implies that for small  $p$

$$E(p) \sim e_0 p, \tag{5.125}$$

for constant  $e_0$ , and if  $p$  is large then  $E(p) \sim e_1/p$  (see Figure 4.3). Thus, we consider the diffusion to be constant and  $E(p)$  to be made up of a piecewise continuous function of a linear part and a decay. For small  $p$  we have the set of equations

$$\text{Re} p_t = (p_x + K n)_x \tag{5.126}$$

and

$$n_t = (a_0 n_x + e_0 p n)_x \tag{5.127}$$

with particular solutions

$$n = \frac{1}{t} N(\Xi) \tag{5.128}$$

and

$$p = \frac{1}{\sqrt{t}} P(\Xi), \tag{5.129}$$

where

$$\Xi = \frac{x}{\sqrt{t}}. \tag{5.130}$$

This leads to the two ordinary differential equations

$$P'' + K N' = -\frac{\text{Re}}{2}(P + \Xi P') \tag{5.131}$$

and

$$a_0 N'' + e_0 (N' P + N p') = -\left(N + \frac{\Xi}{2} N'\right). \tag{5.132}$$

We can integrate the first to give

$$P' = -K(N - 1) + \frac{\text{Re}}{2} \Xi P. \tag{5.133}$$

Hence we have a three-dimensional non-autonomous dynamical system or, by introducing a new parameter,  $Q$ , such that  $Q' = 1$ , a four-dimensional autonomous dynamical system.

Similarly, for large  $p$  we have the system

$$\text{Re} p_t = (p_x + K n)_x \tag{5.134}$$

and

$$n_t = (a_1 n_x + e_1 \frac{n}{p})_x \quad (5.135)$$

where we may assume the diffusion to be a different constant to the one above. This has particular solutions

$$n = N(\Xi) \quad (5.136)$$

and

$$p = \sqrt{t}P(\Xi), \quad (5.137)$$

where

$$\Xi = \frac{x}{\sqrt{t}}. \quad (5.138)$$

This leads to the two ordinary differential equations

$$P'' + KN' = \frac{\text{Re}}{2}(P - \Xi P') \quad (5.139)$$

and

$$a_1 N'' + e_1 \left(\frac{N}{P}\right)' = -\frac{\Xi}{2}N'. \quad (5.140)$$

Both of these systems could display complex behaviour and should be studied in detail. Time and space do not permit that here.

### 5.8.2 Extension to a three-dimensional flow field

Another possibility for future work would be to investigate the three-dimensional structure of deep bioconvection. It may be assumed, from observations, that the vorticity in the vertical direction is zero. Hence, we can use the spherical harmonic approximations developed in Section 4.10 for a three-dimensional flow field in the absence of vorticity in the vertical direction. Therefore, we propose the purely poloidal velocity field,  $F$ , such that

$$\mathbf{u} = \nabla \wedge \nabla \wedge (F\mathbf{k}) \quad (5.141)$$

which gives

$$\nabla \wedge (F\mathbf{k}) = \begin{pmatrix} \partial_y F \\ -\partial_x F \\ 0 \end{pmatrix}, \quad (5.142)$$

$$\mathbf{u} = \begin{pmatrix} \partial_x \partial_z F \\ \partial_y \partial_z F \\ \nabla_H^2 F \end{pmatrix} \quad (5.143)$$

and

$$\boldsymbol{\omega} = \nabla \wedge \mathbf{u} = \begin{pmatrix} -\partial_y \nabla^2 F \\ \partial_x \nabla^2 F \\ 0 \end{pmatrix}, \quad (5.144)$$

where  $\nabla_H^2$  is the horizontal Laplacian. We again make use of the method used to derive Equation (3.115) and apply Equations (5.142) to (5.144) which gives

$$-\partial_t \nabla^2 \nabla_H^2 F = -\mathcal{A}_1(F) - \mathcal{A}_2(F) + \text{Ra} \nabla_H^2 n + \frac{1}{\text{Re}} \nabla^4 \nabla_H^2 F \quad (5.145)$$

and

$$\partial_t = -\partial_x n \partial_x \partial_z F - \partial_y n \partial_y \partial_z F + \partial_z n \nabla_H^2 F - \nabla \cdot (n \langle \mathbf{p} \rangle - \mathbf{D} \cdot \nabla n), \quad (5.146)$$

where the non-linear operators,  $\mathcal{A}_1(F)$  and  $\mathcal{A}_2(F)$ , are given in Appendix D. We can proceed as in Section 5.3 by introducing a long vertical wavelength,  $Z = \epsilon z$  where  $\epsilon \ll 1$ , to obtain

$$\partial_t \nabla_H^4 F^0 = \text{Ra} \nabla_H^2 n^0 + \frac{1}{\text{Re}} \nabla_H^6 F^0 \quad (5.147)$$

and

$$\partial_t n^0 = -\nabla_H \cdot (n^0 \langle \mathbf{p} \rangle (\nabla_H^2 F^0) - \mathbf{D} (\nabla_H^2 F^0) \cdot \nabla_H n^0), \quad (5.148)$$

where

$$n(x, Z, t) = n^0(x, Z, t) + \epsilon n^1(x, Z, t) + \dots \quad (5.149)$$

and

$$F(x, Z, t) = F^0(x, Z, t) + \epsilon F^1(x, Z, t) + \dots \quad (5.150)$$

As before, these equations are not explicitly dependent on  $Z$  but the functions of integration will be.

We can now use the expressions given in Section 4.10 for the terms  $\langle \mathbf{p} \rangle$  and  $\mathbf{D}$ . To proceed further we will have to consider particular forms for  $n^0$  and  $\nabla_H^2 F^0$ , for example we may introduce hexagonal or square planforms (see Buzano & Golubitsky 1983 and Golubitsky *et al.* 1984). These equations may be used in future analysis to predict the three-dimensional patterns in gyrotactic bioconvection and to analyse their stability.

## Chapter 6

# Conclusions

Bioconvection occurs as a result of the passive or active orientation mechanisms of many microscopic swimming individuals and is realised as the bulk motion of suspensions on much larger scales than the individuals involved. Therefore, it requires modelling at every scale to fully understand the system.

In this thesis we have shown that it is possible to perform controlled experiments on bioconvection and to develop theoretical techniques to analyse mathematical models of stochastic, gyrotactic bioconvection. We have also compared the experiments with theoretical predictions. In this way, we hope to have highlighted the strengths and weaknesses of the models.

In Chapter 2 we described robust and reliable experiments, measuring the dominant pattern wavenumber with cell concentration, suspension depth and time. It was found that, for some regions of parameter space, the initially observed patterns were highly dependent on the initial conditions. The method of mixing the suspension had a strong influence on the initial pattern wavenumber. In general, roll patterns were the first to appear but quickly became unstable to three-dimensional modes. The well developed patterns were not sensitive to the initial conditions and eventually evolved into steady patterns of dots in either square or hexagonal arrays. Fourier analysis was used to extract the dominant unstable wavelengths. It was found that the initial most unstable wavelength increased with depth but hardly varied at all with concentration. In contrast, the final most unstable wavelength decreased with increasing concentration and slightly decreased with increasing depth. In general, the pattern wavelength decreased with time from the initial to the final states. The transient patterns were

also investigated and annular patterns were seen in some cases of shallow, concentrated suspensions. Observations of the pattern evolution showed a mechanism whereby descending plumes reach the lower boundary and spread out. Clear fluid is entrained in the plume and an annulus pattern is formed when this fluid reaches the lower boundary. The structures of the transient patterns were then studied using techniques from surface geometry. The images were associated with surfaces in Euclidean three-space where the intensity at a point on the image signified the height of the surface. Thus, the surface curvatures could be analysed such that the local surface topography could be identified. It was found that two-dimensional patterns were unstable to three-dimensional patterns, as expected. Other features of the images that were not immediately obvious were highlighted by the method. Linear structures were seen to persist for long periods of time during the evolution of the pattern and may not altogether disappear. Hence, the method provides a good measure of the quantitative pattern evolution and could be used to study the patterns in greater detail. Some experiments using an unreactive agent, which was denser than the cell culture medium, to vary the effects of geotaxis and gyrotaxis were unsuccessful. Further studies should be conducted using a selection of agents. Finally, other experiments were discussed that could lead to a greater understanding of the pattern forming capabilities of suspensions of swimming micro-organisms.

In Chapter 3 we completed a linear analysis for the stochastic, gyrotactic bioconvection model (Pedley & Kessler 1990 [85]) in a suspension layer of finite depth. We found the general results below which can be compared with the deterministic, gyrotactic finite depth model (Hill *et al.* 1989 [42]) and the purely upswimming finite depth model (Childress *et al.* 1975 [19]) in the following ways.

- For very shallow layers the model predicts a non-zero most unstable wavenumber, in a similar manner to Hill *et al.* (1989) [42], given sufficiently large values of the gyrotactic orientation parameter.
- Otherwise a zero most unstable wavenumber is predicted, as in Childress *et al.* (1975) [19].
- The Rayleigh number, based on suspension depth, was shown to behave like a constant for small wavenumbers in shallow layers and like  $d^4$  for deep layers where

$d$  is the ratio between layer and sub-layer depth.

- Double minimums of the neutral curve were shown to exist, where the minimums occurred at long and finite wavelengths.
- Increasing the suspension depth increased the predicted most unstable wavelength, as found in the experiments of Chapter 2.

We proposed that the model should contain the effects of the random nature of the cells swimming speed as well as its direction. This was shown to affect the nature of the first order perturbation to the diffusion tensor and, thus, affect the shape of the neutral curve. We found that increasing the variance of the cell swimming speed, destabilized modes with small wavenumbers until the most unstable wavenumber became zero. Experiments by Hill & Häder (1996) [41] provide a range of values for the variance of the cell swimming speed. Using updated parameter values from Jones (1995) [54] and above, we obtained the same general conclusions as before but different quantitative predictions. Comparisons with the experiments of Chapter 2 suggested that the updated parameter values were an improvement. Good agreement for the predicted Rayleigh numbers was obtained but the predicted wavenumbers were an order larger. It was found that better agreement could be obtained by adjusting some of the parameters. Therefore, it was suggested that more accurate, independent measurements of sensitive parameters should be a priority.

However, in most of the experiments the cells did not always have sufficient time to swim upwards and form the exponential equilibrium distribution, assumed in the linear analysis, before the onset of an instability. In some cases (such as for deep chambers) the stability analysis of a uniform distribution may be more appropriate.

In Chapter 4 we performed a surface spherical harmonic expansion of the steady gyrotactic Fokker-Planck equation, which describes the probability density function for the orientation of the micro-organisms, in order to obtain solutions for the whole range of vorticities and strain-rates expected in the fluid. Analytic expressions were found for the mean cell swimming direction and diffusion tensors in terms of the first five coefficients of the spherical harmonics for a two-dimensional flow field. Exact computer algebra was employed to minimize errors and deal with the large quantity of standard operations. The expansion was truncated at a particular order, providing

analytic expressions for the desired quantities. Later, these solutions were extended to a three-dimensional flow field when there is no vertical component of vorticity. The expansion converged rapidly for spherical cells but spurious singularities occurred in the solutions for spheroidal cells at high rates of strain. However, a relatively low order of approximation was required, for all cells, to obtain convergent expressions for the range of flow parameters expected in standard bioconvection experiments. For parameters outside this range it may be necessary to use other numerical methods to obtain solutions.

The analytic expressions from Chapter 4 were used in Chapter 5 in the first non-linear analyses of the gyrotactic instability in a suspension of infinite depth. A weakly non-linear analysis with zero variation in the vertical direction demonstrated that this instability is supercritical. A plan for future research is to conduct a similar weakly non-linear analysis with a non-zero vertical wavenumber which may be physically realisable in a suspension of large but finite depth. A long vertical wavelength approximation was used to obtain partial differential equations describing long vertical plume structures. Analysis showed that a horizontally travelling wave of plumes of finite concentration could exist in the presence of a small background vorticity. Consideration of realistic concentration profiles confined the possible wavespeeds to a very small range of values. The theoretical predictions should be compared with future experiments once a suitable apparatus has been designed. A solvability condition was obtained at a higher order of the small vertical variation approximation that described the  $z$  dependence of the horizontally space averaged cell concentration. Pulses travelling down steady state plumes were shown to exist. Consideration of this equation for small amplitude variations gave a set of ordinary differential equations which could be solved to give the wavespeed, the predictions of which could in principle be compared with suitable experiments. These last theories help to explain some of the more complex bioconvection structures observed in deep suspensions. Finally, we discussed the possibility of constructing similarity solutions describing the time and space evolution of two-dimensional structures for slightly modified equations. We derived two, four-dimensional dynamical systems for the asymptotic behaviours, that need to be matched together to describe the full system. We also derived some of the governing equations for a three-dimensional flow field that could be used in future analysis to study pattern selection.

# Appendix A

## Special functions

### A.1 Identities for associated Legendre polynomials

Legendre's associated equation is defined as

$$((1-x^2)y')' + \left[ n(n+1) - \frac{\mu^2}{(1-x^2)} \right] y = 0, \quad (\text{A.1})$$

where  $x \in [-1, 1]$ ,  $y(x)$  is finite at the end points and  $0 \leq n, \mu \in \mathbb{Z}$ . Making the substitution  $y(x) = (1-x^2)^{\frac{\mu}{2}} u(x)$  and dividing by  $(1-x^2)^{\frac{\mu}{2}}$ , gives Legendre's equation differentiated  $\mu$  times. Hence

$$y(x) = P_n^\mu(x) = (1-x^2)^{\frac{\mu}{2}} \frac{d^\mu}{dx^\mu} P_n(x), \quad (\text{A.2})$$

where  $P_n(x)$  are Legendre polynomials and  $P_n^\mu$  are called associated Legendre polynomials. Rodrigues' formula for associated Legendre polynomials is

$$P_n^\mu(x) = \frac{(1-x^2)^{\frac{\mu}{2}}}{2^n n!} \frac{d^{\mu+n}}{dx^{\mu+n}} (x^2-1)^n. \quad (\text{A.3})$$

Associated Legendre polynomials are orthogonal in the lower index;

$$\int_{-1}^1 P_n^k P_m^k dx = \delta_n^m \frac{2}{2n+1} \frac{(n+k)!}{(n-k)!} \quad (\text{A.4})$$

where  $0 \leq k \leq n, m$ . They are also orthogonal in the upper index;

$$\int_{-1}^1 \frac{P_k^n P_k^m}{1-x^2} dx = \delta_n^m \frac{1}{m} \frac{(k+m)!}{(k-m)!} \quad (\text{A.5})$$

where  $1 \leq n \leq m \leq k$ . Arfken (1985) [1] gives a list of recurrence relations (page 660):

$$P_n^{m+1} - \frac{2mx}{(1-x^2)^{\frac{1}{2}}} P_n^m + [n(n+1) - m(m-1)] P_n^{m-1} = 0, \quad (\text{A.6})$$

$$(2n+1)xP_n^m = (n+m)P_{n-1}^m + (n-m+1)P_{n+1}^m, \quad (\text{A.7})$$

$$(2n+1)(1-x^2)^{\frac{1}{2}}P_n^m = P_{n+1}^{m+1} - P_{n-1}^{m+1}, \quad (\text{A.8})$$

$$(2n+1)(1-x^2)^{\frac{1}{2}}P_n^m = (n+m)(n+m-1)P_{n-1}^{m-1} - (n-m+1)(n-m+2)P_{n+1}^{m-1}, \quad (\text{A.9})$$

and

$$(1-x^2)^{\frac{1}{2}}P_n^{m'} = \frac{1}{2}P_n^{m+1} - \frac{1}{2}(n+m)(n-m+1)P_n^{m-1}. \quad (\text{A.10})$$

## A.2 The gamma function

The incomplete gamma function is defined as

$$\Gamma(z) = \int_0^\infty e^{-t}t^{z-1}dt, \quad \text{Re}(z) < 0. \quad (\text{A.11})$$

In particular,

$$\Gamma(n) = (n-1)!, \quad n = 1, 2, 3, \dots, \quad (\text{A.12})$$

$$\Gamma\left(\frac{1}{2}\right) = \pi^{\frac{1}{2}} \quad (\text{A.13})$$

and

$$\Gamma\left(n + \frac{3}{2}\right) = \frac{\pi^{\frac{1}{2}}(2n+1)!!}{2^{n+1}} \quad n = 0, 1, 2, 3, 4, \dots \quad (\text{A.14})$$

where the  $n!! = n(n-2)(n-4)\dots 1$  (the last number being 2 if  $n$  is even). Also

$$\Gamma(\sigma+1) = \sigma\Gamma(\sigma). \quad (\text{A.15})$$

## Appendix B

### An integral identity

Consider the evaluation of

$$\int_{-1}^1 \frac{1}{1-x^2} P_p^m(x) P_q^m(x) dx. \quad (\text{B.1})$$

Gradshteyn & Ryzhik (1980) [38] give

$$\int_{-1}^1 \frac{1}{1-x^2} P_p^m(x) P_q^m(x) dx = \frac{1}{m} \frac{(p+m)!}{(p-m)!} \quad \text{if } p = q \quad (\text{B.2})$$

but what if  $p \neq q$ ?

**Theorem B.1** *If  $p, q \geq m > 0$  and  $p, q, m \in \mathbb{Z}$  then*

$$\int_{-1}^1 \frac{1}{1-x^2} P_p^m(x) P_q^m(x) dx = \begin{cases} \frac{1}{m} \frac{(\min(p,q)+m)!}{(\min(p,q)-m)!} & p+q \text{ even} \\ 0 & \text{otherwise.} \end{cases} \quad (\text{B.3})$$

The proof below is similar to the standard orthogonality proof in Arfken (1985) [1] using Rodrigues' formula

$$P_n^m(x) = \frac{1}{2^n n!} (1-x^2)^{\frac{m}{2}} D^{n+m} (x^2-1)^n, \quad (\text{B.4})$$

where  $D \equiv \frac{d}{dx}$ . However, in the orthogonality proof, when integrating by parts, the integrated parts vanish. In this case, this is not true.

**Proof B.1** *Define  $X \equiv x^2 - 1$  and put  $A \equiv \frac{(-1)^{m-1}}{2^{p+q} p! q!}$  where  $m > 0$ , then*

$$\int_{-1}^1 \frac{P_p^m P_q^m}{-X} dx = A \int_{-1}^1 X^{m-1} D^{p+m} X^p D^{q+m} X^q dx. \quad (\text{B.5})$$

Integrating by parts  $q + m$  times and denoting the integrated parts by  $\mathcal{I}$  ( $\mathcal{I}$  will be considered later) implies

$$\int_{-1}^1 \frac{P_p^m P_q^m}{-X} dx = \mathcal{I} + A(-1)^{q+m} \int_{-1}^1 X^q D^{q+m} (X^{m-1} D^{p+m}) X^p dx. \quad (\text{B.6})$$

Expanding the integrand on the right hand side using the Leibnitz formula gives

$$X^q D^{q+m} (X^{m-1} D^{p+m} X^p) \equiv X^q \sum_{i=0}^{q+m} \frac{(q+m)!}{i!(q+m-i)!} D^{q+m-i} X^{m-1} D^{p+m+i} X^p. \quad (\text{B.7})$$

Since  $X^{m-1}$  contains no power of  $x$  greater than  $x^{2(m-1)}$  we must have

$$q + m - i \leq 2(m - 1) \quad (\text{B.8})$$

or the derivative will vanish. Similarly

$$p + m + i \leq 2p. \quad (\text{B.9})$$

Thus,  $i \geq q - m + 2$  and  $i \leq p - m$ . Hence,

$$p \geq q + 2. \quad (\text{B.10})$$

By exchanging the indices  $p$  and  $q$  we also have the requirement for a non-zero integrand that

$$q \geq p + 2. \quad (\text{B.11})$$

Hence, the integral must vanish  $\forall p, q$ . Now consider the integrated parts,  $\mathcal{I}$ , and assume without loss of generality that  $p \leq q$ .

$$\mathcal{I} = \left[ A \sum_{j=0}^{q+m-1} (-1)^j D^j (X^{m-1} D^{p+m} X^p) D^{q+m-j-1} X^q \right]_{-1}^1. \quad (\text{B.12})$$

We have that  $D \equiv \frac{d}{dx} \equiv \frac{dX}{dx} \frac{d}{dX}$  and clearly  $D^{p+q} X^p$  will always produce some terms independent of  $X$  and, hence, will not affect the lowest order of  $X$  in  $D^j (X^{m-1} D^{p+m} X^p)$ . Hence,  $D^j (X^{m-1} D^{p+m} X^p)$  will contain a term independent of  $X$  if  $j \geq m - 1$ . Similarly  $q + m - j - 1 \geq q$  which implies  $j \leq m - 1$ . If a term is dependent on  $X$  then it will vanish at  $\pm 1$ . This implies that

$$\mathcal{I} = [A(-1)^{m-1} D^{m-1} (X^{m-1} D^{p+m} X^p) q!(2x)^q]_{-1}^1. \quad (\text{B.13})$$

By the Leibnitz formula

$$D^{m-1} (X^{m-1} D^{p+m} X^p) = \sum_{j=0}^{m-1} \frac{(m-1)!}{j!(m-1-j)!} D^j X^{m-1} D^{(m-1)-j+(p+m)} X^p. \quad (\text{B.14})$$

The necessary condition for  $D^j X^{m-1}$  to be independent of  $X$  is that  $j \geq m-1$  which implies  $j = m-1$ . Hence,

$$\begin{aligned} D^{m-1} (X^{m-1} D^{p+m} X^p) &= (m-1)!(2x)^{m-1} D^{p+m} X^p \\ &= (m-1)!(2x)^{m-1} 2^p p! \frac{d^m}{dx^m} P_p(x). \end{aligned} \quad (\text{B.15})$$

Thus,

$$\begin{aligned} \mathcal{I} &= \frac{(-1)^{2(m-1)}}{2^{p+q} p! q!} \left[ q! 2^q x^q (m-1)! 2^{m-1} x^{m-1} 2^p p! \frac{d^m}{dx^m} P_p(x) \right]_{-1}^1 \\ &= \left[ (m-1)! x^{q+m-1} 2^{m-1} \frac{d^m}{dx^m} P_p(x) \right]_{-1}^1. \end{aligned} \quad (\text{B.16})$$

This implies that for  $p \leq q$

$$\int_{-1}^1 P_p^m(x) P_q^m(x) \frac{1}{1-x^2} dx = \begin{cases} (m-1)! 2^m \frac{d^m}{dx^m} P_p(x) \Big|_{x=1} & p+q \text{ is even} \\ 0 & p+q \text{ is odd} \end{cases}. \quad (\text{B.17})$$

For a non-trivial solution  $p+q$  must be even, for which the right hand side is independent of  $q$ . In this case, the right hand side must be equal to the result when  $p=q$  (i.e. Equation B.2). Hence, the theorem is proved.

This is quite an unusual result as it is independent of the associated Legendre polynomial of the higher order. As far as we are aware, this result has not been proved previously.

## Appendix C

# Maple program for the spherical harmonic expansion of the Fokker-Planck equation

The following Maple program is used in the spherical harmonic analysis of Chapter 4. See Chapter 4 for an explanation.

```
'Function definitions';

B := (mmm,nnn) -> if (mmm <= nnn and mmm >= 0 and nnn <= order)
                  then C(mmm,nnn) else 0 fi:

N := (w,x,y,z) -> if (w > x or x < 0 or w < 0) then 0 else
                  (delta(w,0)+1) * delta(w,y)
                  * delta(x,z) * (x+w)! / ((2*x+1) * (x-w)!) fi:

delta := (z,y) -> if evalf(z) = evalf(y) then 1 else 0 fi:

xc := proc(e,m,n) local c,d:integer:
      sbsq := {seq(seq(Q[m+c,n+d] = (m+c+n+d) * Q[m+c,n+d-1]
```

```

        / (2*(n+d)+1) + (n+d-m-c+1) * Q[m+c,n+d+1]
        / (2*(n+d)+1) , d=-5..5), c=-3..3}):
    subs(sbsq,e)
end:

xss := proc(e,m,n)
    e - xc(xc(e,m,n),m,n)
end:

xssp := proc(e,m,n) local c,d:integer:
    sbsq := {seq(seq(Q[m+c,n+d] = (m+c+n+d) * (n+d+1) * Q[m+c,n+d-1]
        / (2*(n+d)+1) - (n+d) * (n+d-m-c+1) * Q[m+c,n+d+1]
        / (2*(n+d)+1), d=-5..5), c=-3..3}):
    subs(sbsq,e)
end:

xsu := proc(e,m,n) local c,d:integer:
    sbsq := {seq(seq(Q[m+c,n+d] = Q[m+c+1,n+d+1] / (2*(n+d)+1)
        - Q[m+c+1,n+d-1] / (2*(n+d)+1), d=-5..5), c=-3..3}):
    subs(sbsq,e)
end:

xsd := proc(e,m,n) local c,d:integer:
    sbsq := {seq(seq(Q[m+c,n+d] = (m+c+n+d) * (m+c+n+d-1)
        * Q[m+c-1,n+d-1] / (2*(n+d)+1) - (n+d-m-c+1) * (n+d-m-c+2)
        * Q[m+c-1,n+d+1] / (2*(n+d)+1) , d=-5..5), c=-3..3}):
    subs(sbsq,e)
end:

'Spherical Harmonics';
h := proc(m,n,t,p) local xx;

```

```

    p.m.n.order * cos(m*p) * qq(m,n,xx);
    xx := cos(t);
    ""
end;

'Associated Legendre polynomials';
qq := proc(m,n,x) if m = 0 then P(n,x) else
        (1-x^2)^(m/2)*diff(P(n,x),x$m) fi
end;

'Approximation to f';
g := proc(t,p) local j,k;
    s := 0;
    for k from 0 to order do
        for j from 0 to k do
            s := s + h(j,k,t,p)
        od:
    od:
end;

# User defined flow parameters
# zeta := 0;
# xi := 1;
chi := 0;

l := 10/22;          #l = 1 / lambda

'Main Program';

```

```

for order from 3 to 5 do

    print('');
    print('order = '+order);

    print('Fokker-Planck Equation for m = 0 (special case)');

    eq1a := A(0,n)*( 1*n*(n+1)*Q[0,n] + xssp(Q[0,n],0,n) -
    2*xc(Q[0,n],0,n) + zeta * (-Q[1,n] )
    -2*xi*( xc(xsu(Q[1,n],0,n),0,n)/2 +
    3*xsu(xsu(Q[0,n],0,n),0,n)/2 + 3*xss(Q[0,n],0,n)/2 -
    3*xc(xc(Q[0,n],0,n),0,n) +
    3/(2*(2*n+1)) *xc(n*(n+1)*Q[0,n-1] - n*(n+1)*Q[0,n+1],0,n))
    -2*chi*(xc(xc(2* Q[1,n],0,n),0,n) -
    Q[1,n] + 6*xc(Q[1,n+1] - Q[1,n-1] ,0,n) / (2*n+1) ) ) :

    print('Fokker-Planck Equation for m = 1 (special case)');

    eq1b := A(1,n)*( 1*n*(n+1)*Q[1,n] + xssp(Q[1,n],1,n) -
    2*xc(Q[1,n],1,n) + zeta/2 * (-Q[2,n] + n*(n+1)*Q[0,n])
    -2*xi*(-(n)*(1+n)*xc(xsu(Q[0,n],1,n),1,n)/4 +
    (3-1)*xss(Q[1,n],1,n)/4 + xc(xsu(Q[2,n],1,n),1,n)/4 +
    (3+1)*xsu(xsu(Q[1,n],1,n),1,n)/4 + 3*xss(Q[1,n],1,n)/2 -
    3*xc(xc(Q[1,n],1,n),1,n) +
    3/(2*(2*n+1)) *xc((n+1)*(n+1)*Q[1,n-1] - n*(n)*Q[1,n+1],1,n))
    -2*chi*(xc(xc(-(n)*(n+1)*Q[0,n] + Q[2,n],1,n),1,n) -
    (-(n)*(n+1)*Q[0,n] + Q[2,n])/2 -
    xc(xsd(Q[1,n],1,n)-xsu(Q[1,n],1,n) ,1,n) +
    3*xc((n+1)*(n)*Q[0,n-1]- (n)*(n+1)*Q[0,n+1] +
    Q[2,n+1] - Q[2,n-1] ,1,n) / (2*n+1) ) ) :

```

```

print('Fokker-Planck Equation m > 1');

eq1 := A(m,n)*( 1*n*(n+1)*Q[m,n] + xssp(Q[m,n],m,n) -
2*xc(Q[m,n],m,n) + zeta/2 * (-Q[m+1,n] + (n-m+1)*(n+m)*Q[m-1,n])
-2*xi*(-(n-m+1)*(m+n)*xc(xsd(Q[m-1,n],m,n),m,n)/4 +
(3-m)*xsd(xsd(Q[m,n],m,n),m,n)/4 + xc(xsu(Q[m+1,n],m,n),m,n)/4 +
(3+m)*xsu(xsu(Q[m,n],m,n),m,n)/4 + 3*xss(Q[m,n],m,n)/2 -
3*xc(xc(Q[m,n],m,n),m,n) +
3/(2*(2*n+1)) *xc((n+m)*(n+1)*Q[m,n-1] - n*(n-m+1)*Q[m,n+1],m,n))
-2*chi*(xc(xc(-(n-m+1)*(n+m)*Q[m-1,n] + Q[m+1,n],m,n),m,n) -
(-(n-m+1)*(n+m)*Q[m-1,n] + Q[m+1,n])/2 -
m*xc(xsd(Q[m,n],m,n)-xsu(Q[m,n],m,n),m,n) +
3*xc((n+m)*(n+m-1)*Q[m-1,n-1]-(n-m+1)*(n-m+2)*Q[m-1,n+1] +
Q[m+1,n+1] - Q[m+1,n-1],m,n) / (2*n+1) ) ):

print('Summing equations');

SS := sum(sum(eq1,m=2..n),n=2..order+3)+ sum(eq1b,n=1..order+3) +
sum(eq1a,n=0..order+3):

sq5 := seq(seq(A(mm,nn)=B(mm,nn),mm=-3..order+6),nn=-3..order+6):

for r from 0 to order do
  for q from 0 to r do
    QES := {seq(seq(Q[i,j]=N(i,j,q,r),
i=-2..order+6),j=-2..order+6)};
    tot := subs(QES, SS);
    tot := subs(sq5,tot);
    eq.q.r := simplify(tot, factorial):
  end do
end do

```

```
od:
od:

print('Solving equations');

parlist := seq(seq(C(mm,nn),mm=0..nn),nn=1..order);
eqlist  := seq(seq(eq.mm.nn = 0,mm=0..nn),nn=0..order);

sols := (solve({eqlist},{parlist}));

C(0,0) := 1/(4*Pi);
p00.order := C(0,0);

for r from 1 to order do
  for q from 0 to r do
    p.q.r.order := subs(sols,C(q,r));
  od:
od:

od:

save p013,p014,p015, p113,p114,p115, p023,p024,p025,
p123,p124,p125 ,p223,p224,p225,
'output.m';

'END';
```

## Appendix D

### Some operator expressions

Below are the definitions for the operators  $\mathcal{A}_1(F)$  and  $\mathcal{A}_2(F)$  used in Section 5.8.

$$\begin{aligned}\mathcal{A}_1(F) &= \nabla^2 ((\mathbf{u} \cdot \nabla) \nabla_H^2 F) \\ &\equiv (\partial_x^2 + \partial_y^2 + \partial_z^2) (\partial_x \partial_z F \partial_x \nabla_H^2 F + \partial_y \partial_z F \partial_y \nabla_H^2 F - \nabla_H^2 F \partial_z \nabla_H^2 F)\end{aligned}\quad (\text{D.1})$$

and

$$\begin{aligned}\mathcal{A}_2(F) &= \partial_z \nabla \cdot ((\mathbf{u} \cdot \nabla) \mathbf{u}) \\ &\equiv \partial_z \partial_x (\partial_x \partial_z F \partial_x^2 \partial_z F + \partial_y \partial_z F \partial_x \partial_y \partial_z F - \nabla_H^2 F \partial_z^2 \partial_x F) \\ &\quad + \partial_z \partial_y (\partial_x \partial_z F \partial_x \partial_y \partial_z F + \partial_y \partial_z F \partial_y^2 \partial_z F - \nabla_H^2 F \partial_z^2 \partial_y F) \\ &\quad - \partial_z^2 (\partial_x \partial_z F \partial_x \nabla_H^2 F + \partial_y \partial_z F \partial_y \nabla_H^2 F - \nabla_H^2 F \partial_z \nabla_H^2 F),\end{aligned}\quad (\text{D.2})$$

where

$$\mathbf{u} = \nabla \wedge \nabla \wedge (F \mathbf{k}). \quad (\text{D.3})$$

# Bibliography

- [1] G. Arfken. *Mathematical methods for Physicists*. Academic Press Inc., London, 3rd ed., 1985.
- [2] N. J. Balmforth. Solitary waves and homoclinic orbits. *Annual Review of Fluid Mechanics*, 27:335–373, 1995.
- [3] G. K. Batchelor. The stress system in a suspension of force-free particles. *Journal of Fluid Mechanics*, 41:545–570, 1970.
- [4] G. K. Batchelor. Sedimentation in a dilute dispersion of spheres. *Journal of Fluid Mechanics*, 52(2):245–268, 1972.
- [5] M. A. Bees. The Birds and Bees: A mathematical model of speciation. Technical report, Woods Hole Oceanographic Institute, Woods Hole, Massachusetts MA02543, 1994.
- [6] M. A. Bees and E. A. Spiegel. Bifurcations in evolution. *In preparation*, 1997.
- [7] E. O. Bingham. *The Fast Fourier Transform*. Englewood Cliffs, NJ : Prentice Hall, 1974.
- [8] H. C. Bold and M. J. Wynne. *Introduction to the algae. Structure and reproduction*. Prentice Hall, New Jersey, 1978.
- [9] J. S. Boscov and M. A. Feinlieb. Phototactic responses of *Chlamydomonas* to flashes of light. ii. response of individual cells. *Journal of Photochemistry and Photobiology*, 30:499–505, 1979.
- [10] H. Brenner. Suspension rheology. *Progress in Heat Mass Transfer*, 5:89–129, 1972.

- [11] H. Brenner. Rheology of a dilute suspension of axisymmetric Brownian particles. *International Journal of Multiphase Flow*, 1:195–341, 1974.
- [12] H. Brenner and M. H. Weissmann. Rheology of a dilute suspension of dipolar spherical particles in an external field. II. effects of rotary brownian motion. *Journal of Colloid and Interface Science*, 41(3):499 – 531, December 1972.
- [13] E. Buzano and M. Golubitsky. Bifurcation of the hexagonal lattice and the planar Bénard problem. *Philosophical Transactions of the Royal Society of London*, 308:617–667, 1983.
- [14] J. R. Cash and D. R. Moore. A high order method for the numerical solution of two-point boundary value problems. *BIT*, 20:44–52, 1980.
- [15] S. Chandresekar. *Hydrodynamic and Hydromagnetic Stability*. Clarendon, Oxford University Press, 1961.
- [16] C. J. Chapman and M. R. E. Proctor. Nonlinear Rayleigh-Bénard convection between poorly conducting boundaries. *Journal of Fluid Mechanics*, 101:759–782, 1980.
- [17] H. Chaté. Spatiotemporal intermittency regimes of the one-dimensional complex Ginzburg-Landau equation. *Nonlinearity*, 7(1):185–204, 1994.
- [18] S. Childress. *Mechanics of swimming and flying*. Cambridge University Press, Cambridge, 1981.
- [19] S. Childress, M. Levandowsky, and E. A. Spiegel. Pattern formation in a suspension of swimming micro-organisms: equations and stability theory. *Journal of Fluid Mechanics*, 69:595–613, 1975.
- [20] S. Childress and R. Peyret. A numerical study of two-dimensional convection patterns. *Journal de Mécanique*, 15:753–779, 1976.
- [21] S. Childress and E. A. Spiegel. Pattern formation in a suspension of swimming microorganisms: Nonlinear aspects. Unpublished, 1978.
- [22] R. K. Clayton. Patterns of accumulation resulting from taxes and changes in motility of micro-organisms. *Archive für Mikrobiologie*, 27:311–319, 1957.

- [23] J. W. Cooley and J. W. Tuckey. An algorithm for the machine calculation of complex Fourier series. *Mathematics of Computation*, 19, 1965.
- [24] P. Couillet and S. Fauve. *Collective modes of periodic structures, combustion and non-linear phenomena*. Les Editions de Physique, 1985.
- [25] H. C. Crenshaw. Orientation by helical motion – i. kinematics of the helical motion of organisms with up to six degrees of freedom. *Bulletin of Mathematical Biology*, 55:197–212, 1993.
- [26] N. A. C. Cressie. *Statistics for spatial data*. John Wiley & sons inc., New York, revised edition, 1993.
- [27] R. Dawkins. *The selfish gene*. Oxford University Press, new edition, 1989.
- [28] M. C. Depassier and E. A. Spiegel. The large scale structure of compressible convection. *Astronomical Journal*, 86(3):496–512, 1981.
- [29] M. P. do Carmo. *Differential Geometry of Curves and Surfaces*. Prentice Hall, 1976.
- [30] J. C. Eilbeck. The pseudo-spectral method and path following in reaction-diffusion bifurcation studies. *SIAM Journal of Scientific and Statistical Computation*, 7(2), April 1986.
- [31] S. Fauve. GFD lecture notes. Technical report, Woods Hole Oceanographic Institute, Woods Hole, Massachusetts MA02543, 1985.
- [32] S. Fauve. Large scale instabilities of cellular flows. Technical report, Woods Hole Oceanographic Institute, Woods Hole, Massachusetts MA02543, 1985.
- [33] K. W. Foster and R. D. Smyth. Light antennas in phototactic algae. *Microbiological Reviews*, 44(4):572–630, December 1980.
- [34] D. J. Futuyma. *Evolutionary Biology*. Sinauer Associates, Inc, Sunderland, Massachusetts, second edition, 1994.
- [35] H. F. Goldstein, E. Knobloch, I. Mercader, and M. Net. Convection in a rotating cylinder i: Linear theory for moderate Prandtl numbers. *Journal of Fluid Mechanics*, 248:583–604, 1993.

- [36] M. Golubitsky, J. W. Swift, and E. Knobloch. Symmetries and pattern selection in Rayleigh-Bénard convection. *Physica D*, 10:249–276, 1984.
- [37] C. M. Goodess and J. P. Palutikof. The development of regional climate scenarios and the ecological impact of greenhouse gas warming. In F. I. Woodward, editor, *The Ecological Consequences of global climate change*, volume 22, pages 33–62. Academic Press, 1992.
- [38] I. S. Gradshteyn and I. M. Ryzhik. *Tables of Integrals, Series and Products*. Academic Press Inc., English ed., 1980.
- [39] J. Happel and H. Brenner. *Low Reynolds Number Hydrodynamics*. Prentice-Hall, 1965.
- [40] A. Harashima, M. Watanabe, and I. Fujishiro. Evolution of bioconvection patterns in a culture of motile flagellates. *Physics of Fluids*, 31(4), April 1988.
- [41] N. A. Hill and D. P. Häder. A biased random walk model for the trajectories of swimming micro-organisms. *Journal of Theoretical Biology (in press)*, 1997.
- [42] N. A. Hill, T. J. Pedley, and J. O. Kessler. Growth of bioconvection patterns in a suspension of gyrotactic micro-organisms in a layer of finite depth. *Journal of Fluid Mechanics*, 208:509 – 543, 1989.
- [43] N. A. Hill and R. V. Vincent. A simple model and strategies for orientation in phototactic microorganisms. *Journal of Theoretical Biology*, 163:223–235, 1993.
- [44] A. J. Hillesdon. *Pattern formation in a suspension of swimming bacteria*. PhD thesis, University of Leeds, 1994.
- [45] A. J. Hillesdon, T. J. Pedley, and J. O. Kessler. The development of concentration gradients in a suspension of chemotactic bacteria. *Bulletin of Mathematical Biology*, 57:299–344, 1995.
- [46] E. J. Hinch and L. G. Leal. The effect of Brownian motion on the rheological properties of a suspension of non-spherical particles. *Journal of Fluid Mechanics*, 52:683–712, 1972a.

- [47] E. J. Hinch and L. G. Leal. Note on the rheology of a dilute suspension of dipolar spheres with weak Brownian couples. *Journal of Fluid Mechanics*, 56:803–813, 1972b.
- [48] S. Holmes. *Henderson's dictionary of biological terms*. Longman, London and New York, ninth edition edition, 1985.
- [49] D. W. Hughes and M. R. E. Proctor. Magnetic fields in the solar convection zone. *Annual Review of Fluid Mechanics*, 20:187–223, 1988.
- [50] D. W. Hughes and M. R. E. Proctor. Nonlinear three-wave interaction with non-conservative coupling. *Journal of Fluid Mechanics*, 244:583–604, 1992.
- [51] E. L. Ince. *Integration of ordinary differential equations*. Oliver & Boyd, Edinburgh and London, seventh edition, 1956.
- [52] D. E. James. Culturing algae. Algae Department, Carolina Biological Supply Company, Burlington, North Carolina 27215, 1978.
- [53] G. B. Jeffrey. The motion of ellipsoidal particles immersed in a viscous fluid. *Proceedings of the Royal Society of London*, A102:161–179, 1922.
- [54] M. S. Jones. *Hydrodynamics of Bi-flagellate Locomotion*. PhD thesis, University of Leeds, 1995.
- [55] M. S. Jones, L. le Baron, and T. J. Pedley. Biflagellate gyrotaxis in a shear flow. *Journal of Fluid Mechanics*, 281:137 – 158, 1994.
- [56] D. D. Joseph. Stability of convection in containers of arbitrary shape. *Journal of Fluid Mechanics*, 47:257–282, 1971.
- [57] B. I. Justusson. Median filtering: Statistical properties. In T. S. Huang, editor, *Two Dimensional Digital Signal Processing II*, volume 43 of *Topics in Applied Physics*, pages 161–196. Springer, New York, 1981.
- [58] J. O. Kessler. Algal cell harvesting. U.S. Patent No. 4,324,067, 1982.
- [59] J. O. Kessler. Algal cell growth, modification and harvesting. U.S. Patent No. 4,438,591, 1984.

- [60] J. O. Kessler. Gyrotactic buoyant convection and spontaneous pattern formation in algal cell cultures. In M. G. Velarde, editor, *Non-equilibrium cooperative phenomena in physics and related fields*, pages 241–248. New York: Plenum, 1984.
- [61] J. O. Kessler. Co-operative and concentrative phenomena of swimming micro-organisms. *Contemporary Physics*, 26(2):147–166, 1985.
- [62] J. O. Kessler. Hydrodynamic focussing of motile algal cells. *Nature*, 313:218–220, 1985.
- [63] J. O. Kessler. The external dynamics of swimming micro-organisms. volume 4 of *Progress in Phycological Research*, pages 257–307, Bristol, 1986. Biopress.
- [64] J. O. Kessler. Individual and collective dynamics of swimming cells. *Journal of Fluid Mechanics*, 173:191–205, 1986.
- [65] J. O. Kessler. Path and pattern - the mutual dynamics of swimming cells and their environment. *Comments in Theoretical Biology*, 1:85–108, 1989.
- [66] J. O. Kessler. Individual and collective dynamics of swimming cells. *Advanced space research*, 12:33–42, 1992.
- [67] J. O. Kessler, N. A. Hill, and D. P. Häder. Orientation of swimming flagellates by simultaneously acting external factors. *Journal of Phycology*, 28:816–822, 1992.
- [68] S. Kim and C. J. Lawrence. Similarity solutions for the orientation distribution function and rheological properties of suspensions of axisymmetric particles with external couples. *Journal of Non-Newtonian Mechanics*, 24:297 – 310, 1987.
- [69] E. Knobloch. Pattern selection in long-wavelength convection. *Physica D*, 41:450–479, 1990.
- [70] L. G. Leal and E. J. Hinch. The effect of weak Brownian rotations on particles in shear flow. *Journal of Fluid Mechanics*, 46:685–703, 1971.
- [71] L. G. Leal and E. J. Hinch. The rheology of a suspension of nearly spherical particles subject to Brownian rotations. *Journal of Fluid Mechanics*, 55:745–765, 1972.

- [72] M. Lebert and D. P. Häder. How *Euglena* tells up from down. *Nature*, 379, 15th February 1996.
- [73] T. B. Lennie, D. P. McKenzie, D. R. Moore, and N. O. Weiss. The breakdown of steady convection. *Journal of Fluid Mechanics*, 188:47–85, 1988.
- [74] M. Levandowsky, W. S. Childress, E. A. Spiegel, and S. H. Hutner. A mathematical model of pattern formation by swimming microorganisms. *Journal of Protozool*, 22(2):296–306, 1975.
- [75] S. A. Levin and L. A. Segel. Pattern generation in space and aspect. *SIAM Review*, 27(1), March 1985.
- [76] M. J. Lighthill. *Mathematical biofluidynamics*. CBMS - NSF Regional conference series in applied mathematics. SIAM, 1975.
- [77] J. B. Loeffler and R. B. Mefferd. Concerning pattern formation by free-swimming microorganisms. *The American Naturalist*, 86(830):325–329, 1952.
- [78] W. V. R. Malkus and G. Veronis. Finite amplitude cellular convection. *Journal of Fluid Mechanics*, 4:225–260, 1958.
- [79] K. Mardia. *Statistics of directional data*. Academic Press, 1972.
- [80] J. D. Murray. *Mathematical Biology*. Springer-Verlag, second edition, 1990.
- [81] A. C. Newell and J. A. Whitehead. Finite bandwidth, finite amplitude convection. *Journal of Fluid Mechanics*, 38:279–303, 1969.
- [82] W. Nultsch and E. Hoff. Investigation on pattern formation in *Euglenae*. *Archive für Protistenk*, 115:336–352, 1973.
- [83] T. J. Pedley, N. A. Hill, and J. O. Kessler. The growth of bioconvection patterns in a uniform suspension of gyrotactic micro-organisms. *Journal of Fluid Mechanics*, 195:223 – 237, 1988.
- [84] T. J. Pedley and J. O. Kessler. The orientation of spheroidal micro-organisms swimming in a flow field. *Proceedings of the Royal Society of London series B*, 231:47 – 70, 1987.

- [85] T. J. Pedley and J. O. Kessler. A new continuum model for suspensions of gyrotactic micro-organisms. *Journal of Fluid Mechanics*, 212:155 – 182, 1990.
- [86] T. J. Pedley and J. O. Kessler. Hydrodynamic phenomena in suspensions of swimming micro-organisms. *Annual Review of Fluid Mechanics*, 24:313 – 358, 1992.
- [87] M. S. Plesset and H. Winet. Bioconvection patterns in swimming micro-organism cultures as an example of Rayleigh-Taylor instability. *Nature*, 248:441–443, 1974.
- [88] J. P. Poyet. *Problems of Time Dependent Convection*. PhD thesis, University of Columbia, New York, 1981.
- [89] W. H. Press, S. A. Teukolsky, W. T. Vetterling, and B. P. Flannery. *Numerical Recipes in FORTRAN. The art of scientific computing*. Cambridge University Press, second edition, 1992.
- [90] M. R. E. Proctor. Planform selection by finite-amplitude thermal convection between poorly conducting slabs. *Journal of Fluid Mechanics*, 113:469–485, 1981.
- [91] E. M. Purcell. Life at low Reynolds number. *American Journal of Physics*, 45:3–11, 1977.
- [92] J. M. Rallison. The effects of Brownian rotations in a dilute suspension of rigid particles of arbitrary shape. *Journal of Fluid Mechanics*, 84(2):237–263, 1978.
- [93] M. Ramia. Numerical-model for the locomotion of *Spirilla*. *Biophysical Journal*, 60(5):1057–1078, 1991.
- [94] M. Ramia and M. A. Swan. The swimming of unipolar cells of *Spirillum volutans* - theory and observations. *Journal of Experimental Biology*, 187:75–100, 1994.
- [95] M. Ramia, D. L. Tullock, and N. Phan-Thien. The role of hydrodynamic interaction in the locomotion of microorganisms. *Biophysical Journal*, 65(2):755–778, 1993.
- [96] H. Risken. *The Fokker-Planck equation*. Springer Verlag, Berlin, 2nd edition, 1989.

- [97] A. M. Roberts. The external dynamics of swimming micro-organisms. *Nature*, 828:375–376, 1970.
- [98] A. M. Roberts. The biased random walk and the analysis of micro-organism movement. In T. Y. T. Wu, C. J. Brokaw, and C. Bennis, editors, *Swimming and Flying in Nature*, number 1, pages 377–393, New York, London, 1975. Plenum Press.
- [99] U. Ruffer and W. Nultsch. High speed cinematographic analysis of the movement of *Chlamydomonas*. *Cell Motility*, 5:251–263, 1985.
- [100] M. Schienbein and H. Gruler. Langevin equation, Fokker-Planck equation and cell migration. *Bulletin of Mathematical Biology*, 55:585–608, 1993.
- [101] A. Schlüter, D. Lortz, and F. Busse. On the stability of steady finite amplitude convection. *Journal of Fluid Mechanics*, 23:129–144, 1965.
- [102] A. R. Solow and J. H. Steele. Scales of plankton patchiness: biomass versus demography. *Journal of Plankton research*, 17(8):1669–1677, 1995.
- [103] E. A. Spiegel and S. Zaleski. Reaction-diffusion instability in a sheared medium. *Physics Letters*, 106A(7):335–338, 1984.
- [104] J. H. Steele and E. W. Henderson. Spatial pattern in North Sea plankton. *Deep-Sea Research*, 26A:955–963, 1979.
- [105] M. A. Stephens. Use of the Kolmogorov-Smirnov, Cramér-von Mises and related statistics without extensive tables. *Journal of the Royal Statistical Society, Series B*, 32:115–122, 1970.
- [106] S. R. Strand and S. Kim. Dynamics and rheology of a dilute suspension of dipolar nonspherical particles in an external field: Part 1. steady shear flows. *Rheological Acta*, 31:94 – 117, 1992.
- [107] J. M. T. Thompson and F. A. McRobie. Indeterminate bifurcations and the global dynamics of driven oscillators. In E. Kreuzer and G. Schmidt, editors, *First European Nonlinear Oscillations Conference, Hamburg*, pages 107–128, Berlin, August 1993. Akademie Verlag.

- [108] A. M. Tomson and R. Demets. *Sexual communication in the green algae Chlamydomonas eugametos*. PhD thesis, University of Amsterdam, 1989.
- [109] J. E. Truscott and J. Brindley. Equilibrium, stability and excitability in a general class of plankton population models. *Philosophical Transactions of the Royal Society. London (A)*, 347(7):703–718, 1994.
- [110] J. W. Tukey. *Exploratory data analysis*. Addison-Wesley, New York and Jonathan Cape, London, 1977.
- [111] A. M. Turing. The chemical basis of morphogenesis. *Philosophical Transactions of the Royal Society (B)*, 237:37–72, 1952.
- [112] S. G. Tyan. Median filtering: Deterministic properties. In T. S. Huang, editor, *Two Dimensional Digital Signal Processing II*, volume 43 of *Topics in Applied Physics*, pages 197–217. Springer, New York, 1981.
- [113] T. G. M. van de Ven. *Colloidal Hydrodynamics*. Academic Press, 1989.
- [114] M. van Dyke. *Perturbation methods in Fluid mechanics*. Academic Press, New York, 1964.
- [115] G. Veronis. Penetrative convection. *The Astrophysical Journal*, 137, 1963.
- [116] R. V. Vincent. *Mathematical modelling of phototaxis in motile micro-organisms*. PhD thesis, University of Leeds, 1995.
- [117] R. V. Vincent and N. A. Hill. Bioconvection in a suspension of phototactic algae. *submitted to Journal of Fluid Mechanics*, 1996.
- [118] R. von Mises. *Mathematical theory of probability and statistics*. Academic Press, New York, 1972.
- [119] H. Wager. The effect of gravity upon the movements and aggregation of *Euglena viridis*, Ehrb., and other micro-organisms. *Philosophical Transactions of the Royal Society of London*, B201:333–390, 1911.
- [120] J. Weiner. *The Beak of the Finch*. Knopf, New York and Jonathan Cape, London, 1994.

- [121] J. A. Whitehead. Fluid models of geological hotspots. *Annual Review of Fluid Mechanics*, 20:61–87, 1988.
- [122] J. J. Wille and C. F. Ehret. Circadian rhythm of pattern formation in populations of a free-swimming organism, *Tetrahymena*. *Journal of Protozool*, 15(4):789–792, 1968.
- [123] G. B. Witman. *Chlamydomonas* phototaxis. *Trends in Cell Biology*, 3:403–408, 1993.